8-2021

A Study of Systematic Uncertainties for a Photon-like Low Energy Excess Search at MicroBooNE

Gray Yarbrough
gyarbrou@vols.utk.edu

To the Graduate Council:

I am submitting herewith a dissertation written by Gray Yarbrough entitled "A Study of Systematic Uncertainties for a Photon-like Low Energy Excess Search at MicroBooNE." I have examined the final electronic copy of this dissertation for form and content and recommend that it be accepted in partial fulfillment of the requirements for the degree of Doctor of Philosophy, with a major in Physics.

Sowjanya Gollapinni, Major Professor

We have read this dissertation and recommend its acceptance:

Stefan M Spanier, Nadia Fomin, David C Donovan

Accepted for the Council:

Dixie L. Thompson

Vice Provost and Dean of the Graduate School

(Original signatures are on file with official student records.)

A Study of Systematic Uncertainties for a Photon-like Low Energy Excess Search at MicroBooNE

A Dissertation Presented for the

Doctor of Philosophy

Degree

The University of Tennessee, Knoxville

Gray Yarbrough

August 2021

Dedicated to all of those who helped me along the way

Acknowledgments

Thanks to the many people who supported me from University of Tennessee Knoxville. My advisor, Dr. Sowjanya Gollapinni, deserves particular praise for the guidance in introducing me to the MicroBooNE collaboration and her immeasurable support in my dissertation work. Also, particular thanks to my doctoral committee for their support in the dissertation process. Finally, my appreciation is immeasurable to all the professors and staff who supported me at UTK. I would also like to thank the Fermilab and MicroBooNE communities for welcoming me and supporting through my stay at the lab, both in my work and in my life. Finally, thanks to my family for their unwavering support in my career. To my mother and father, the fact that I knew I could always call on you in times of stress was a great comfort. To my grandfather, you could always be relied upon to hear my problems and make me laugh. Thank you all, truly.

Abstract

The premise of this dissertation is the study of and reduction of systematic uncertainties in the MicroBooNE experiment at the Fermi National Accelerator Laboratory. MicroBooNE is a short-baseline oscillation experiment using the innovative liquid argon time projection chamber technology to study, with unprecedented detail, neutrino interactions. The primary goal of MicroBooNE is the investigation of the MiniBooNE low energy excess (LEE) of electron neutrino events, a result which raised fundamental questions on the existence of sterile neutrinos with broad implications to the field of particle physics. The principal study of this dissertation is a study of systematics as part of the LEE search seeking an explanation to the MiniBooNE low energy excess anomaly via neutrino-induced single photon events. A detailed knowledge of uncertainties is necessary to achieve the required precision, and the work presented in this thesis allowed for an estimated three times reduction of systematic uncertainties in the single photon analysis. In addition, a study of beamline properties and systematics on the source beam for MicroBooNE, the Booster Neutrino Beam, with a method of recovering data deemed unfit due to beamline related issues has been performed. Significance of beam-related measurements depends on the protons on target collected and, as such, this result could potentially increase the neutrino data received by MicroBooNE. Overall, these studies have significantly contributed to the precision and confidence of the single photon analysis along with potential for improvements to future analyses in MicroBooNE.

Table of Contents

List of Tables

List of Figures

Chapter 1

Overview of Thesis

A series of accelerator neutrino experimental results has led to a search for novel physics in what is known as the short-baseline region. The principle subject of this thesis is to investigate the Mini Booster Neutrino Experiment (MiniBooNE) [11] measurement of ν_e-like excess at low energies or the Low Energy Excess (LEE) [11]. The Micro Booster Neutrino Experiment (MicroBooNE) [1] at Fermi National Accelerator Lab (Fermilab) is the most modern data collecting experiment in this direction. While efforts to define theories accounting for the LEE are being developed, including sterile neutrinos, which do not interact via the weak force, with broad implications to Standard Model particle physics, MicroBooNE investigates the MiniBooNE anomaly experimentally with new tools to reduce backgrounds and produce more accurate measurements. MicroBooNE is in the process of examining neutrino interactions with unprecedented detail compared to what MiniBooNE performed using a mineral oil Cherenkov detector. As a liquid argon time projection chamber (LArTPC), the MicroBooNE detector can reconstruct events in three dimensions via signals on wire planes and drift time with greater precision. Properties measured in the MicroBooNE detector also have broad implications to future LArTPCs including the Deep Underground Neutrino Experiment (DUNE) and the Short Baseline Neutrino (SBN) program.

MicroBooNE must account for uncertainties from both its neutrino beam flux prediction and underlying cross-section assumptions for interactions within the detector. My work, therefore, covers several approaches towards estimating and reducing MicroBooNE's systematic uncertainties. Several concurrent analyses exist in MicroBooNE investigating the

Low Energy Excess and measuring more generic neutrino-argon cross section properties. My principle analysis is therefore tied specifically to the Single Photon or gamma LEE analysis effort investigating an explanation to the LEE involving misidentified photons or unexplored backgrounds leading to new physics. My work has largely focused on implementation of tools developed in the MicroBooNE collaboration to the specific single photon analysis and subsequent investigation. This implementation is crucial to determining the significance level of the gamma LEE results and confidence intervals.

There is also accompanying work on the Booster Neutrino Beamline (BNB) which applies to MicroBooNE more generically. Investigations were attempted to improve the knowledge of the BNB neutrino flux by analyzing beam instrumentation data and studying secondary proton re-interactions in the beamline. Results here may allow increasing the amount of usable data via new instrumentation data analysis. The significance of MicroBooNE results depends on the quantity of data, therefore data recovery could be invaluable.

In the remainder of the text, chapter organization is discussed with an overview of the individual chapters of this dissertation. Ch. refch:neutrinos briefly outlines the properties of neutrinos with a focus on properties relevant to our experimental goals. It also covers open-questions in the field including those investigated by MicroBooNE. Ch. 3 describes the MicroBooNE detector in detail along with its physics goals and status of the operations of the experiment. Ch. 4 covers the methods of data extraction, reconstruction, and simulation in the MicroBooNE experiment necessary for discussion of my analysis methods. Ch. 5 gives an introduction to the Single Photon or gamma Low Energy Excess analysis for which I performed a complete evaluation of systematic uncertainties crucial to determining significance levels and precision of final measurements. Ch. 6 covers this systematics work including several approaches to calculating uncertainties. It also covers sensitivity projections towards our final fit significance given the current state of systematic uncertainties. Ch. 7 briefly covers the field of accelerator neutrino experiments, and describes the BNB and Neutrinos at the Main Injector (NuMI) beamlines which contribute to neutrino flux received by MicroBooNE. Ch. 8 covers my specific analysis of the Booster Neutrino Beamline and related systematics. It includes efforts to better model the neutrino flux prediction from the

beamline, and to improve our knowledge of the beam status via instrumentation data. Ch. 9 summarizes the results of this thesis and gives an outlook towards future work.

Chapter 2

Neutrino Physics

This chapter introduces the Standard Model (SM) of particle physics and explains basic neutrino concepts to serve as reference for the rest of the thesis. It also states the open questions in neutrino physics as motivation for the dissertation work presented here. Sec. 2.1 gives a brief overview of the Standard Model and neutrinos' place therein. Sec. 2.2 gives an overview of neutrino history. Sec. 2.3 explains key properties of neutrino oscillations. Sec. 2.4 explains the types and mechanics of neutrino interactions. Sec. 2.5 goes over open questions in the field of neutrino physics. Finally, Sec. 2.6 gives an overview of neutrino experiments.

2.1 Standard Model

The Standard Model or Glashow-Weinberg-Salam [26, 27, 28] model developed in the 1970s aims to describe interactions in the small distance and high energy regime. It currently stands as a complete quantum field theory that describes nearly all physical interactions. It is defined by the gauge group $SU(3)_C \times SU(2)_L \times U(1)_Y$ where C, L, and Y stand for chirality, left handed, and hypercharge respectively. These groups have symmetries such that under particular transformations physical phenomena will be unchanged, but which can be broken under certain conditions. With the Higgs symmetry breaking (in vacuum), the model is converted to $SU(3)_C \times U(1)_Q$ where $U(1)_Q$ is the gauge symmetry group corresponding to conservation of charge. Interactions are determined via the generators of each group referred

to as bosons. These bosons and particles together make up the components of the Standard Model as seen in Fig. 2.1.

Fundamental particles are assumed to be point-like with no internal structure, and are separated into fermions with half-integer spin and bosons with integer spin. Also each particle has a corresponding anti-particle. Fermions are the fundamental building blocks of matter separated into six quarks and six leptons. They are grouped into three generations each, including two quarks and two leptons as seen in Tab. 2.1. Quarks and leptons are distinguished by the properties that strong force only applies to quarks, and quarks cannot exist independently.

As stated, bosons are the generators of the Standard Model groups with five bosons that have been predicted and detected as shown in Fig. 2.1. Bosons mediate force by acting as propagators that transmit quantities (charge, mass, lepton number, energy) between fermions. Boson exchange can be characterized by a propagator term proportional to $(q^2 \pm m^2)^{-1}$ where q^2 is the scalar product of the interaction 4-momentum $(E/c, p_x, p_y, p_z)$ and m is the mass of the boson.

Quantum electrodynamics (QED) is defined by the $U(1)_Y$ charge group with its generator being the photon (γ). The photon is massless and chargeless as demanded by theory. Due to its massless nature, electromagnetic interactions mediated via the photon remain strong over significantly larger distances than the weak or strong forces. However, electromagnetic forces are significantly weaker at small distances than weak or strong forces.

Weak interactions are mediated via the generators of the $SU(2)_L$ group including three massive gauge bosons W^+, W^-, and Z^0. These interactions can be unified with the electromagnetic for electroweak theory of the $SU(2)_L \times U(1)_Y$ group. Chirality is defined by how particles transform under a Lorentz boost, and it is identical to helicity for massless particles and in the high-energy regime. Helicity is defined by the projection of the spin vector onto the momentum vector. When helicity and chirality are identical, positive helicity (aligned) becomes right-handed chirality and negative helicity (unaligned) becomes left-handed chirality. Left handed particles interact as doublets [27] based on generations of particles described in Fig. 2.1 i.e.

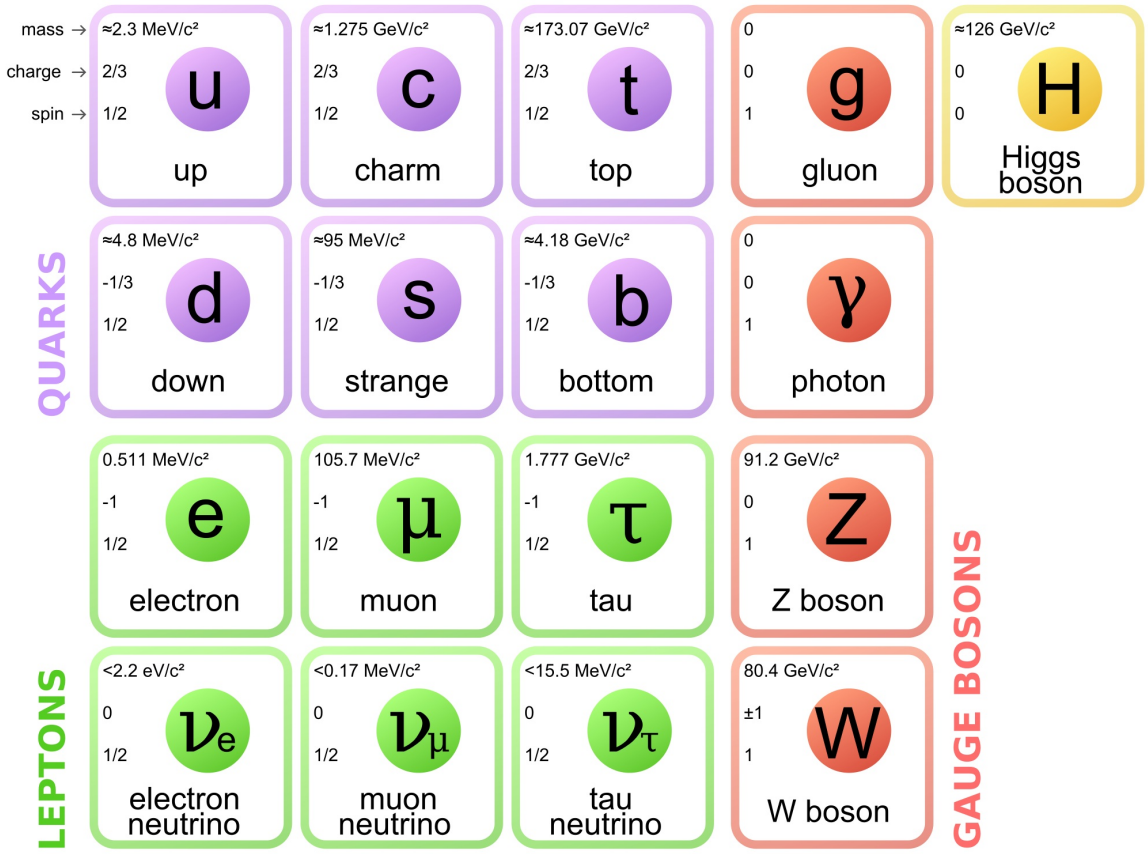

Figure 2.1: The Standard Model of particle physics.

Table 2.1: Generational description of quarks and leptons.

	1st generation	**2nd generation**	**3rd generation**
quarks	u (up) d (down)	c (charm) s (strange)	t (top) b (bottom)
leptons	ν_e (electron neutrino) e (electron)	ν_μ (muon neutrino) μ (muon)	ν_τ (tau neutrino) τ (tau)

$$L_L = \begin{pmatrix} \nu_{eL} \\ \mathrm{e}_L, \end{pmatrix}, \; Q_L = \begin{pmatrix} \mathrm{u}_L \\ \mathrm{d}_L \end{pmatrix}.$$

Right handed particles are then singlets u_R and e_R and are unaffected by charged current weak interactions. However, as will be elaborated upon in Sec. 2.5, the nature of right handed neutrinos is unknown. Weak conversions between neutrinos and charged leptons are thus transformations on these doublets. Flavor lepton number conservation is a consequence of the electroweak formulation where the number of each flavor of lepton is conserved in weak interactions (and consequently the total lepton number as well). But while the Standard Model demands flavor conservation, neutrinos notably do not conserve flavor while oscillating which will be discussed in Sec. 2.3.

Quantum Chromodynamics (QCD) is defined via the eight generators of the $SU(3)_C$ defined as eight gluons, and the strong force acts only between quarks and gluons. Color charge is a property necessary to allow quarks to exist within hadrons without possessing identical quantum states. These were designated as red, green, and blue with corresponding anti-colors. Free particles must have a neutral color charge. Neutral color charge can be achieved either by combining a quark and anti-quark i.e. the combination of a red and anti-red quark to form a meson, or by combining each of the three colors (or anti-colors) i.e. a combination of a red quark, green quark, and blue to form a baryon.

Neutrinos in the Standard Model make up three neutral leptons of spin 1/2 with flavor states corresponding to each charged lepton. Neutrinos interact only weakly i.e. in beta decay $n \to p + e^- + \bar{\nu_e}$. It has been shown that neutrinos propagate as mass states which are superpositions of flavor states, but the Higgs mechanism, responsible for generating mass in the Standard Model, seems incompatible with neutrino nature. The Higgs mechanism generates mass of W and Z gauge bosons and fermions. The mechanism is based on spontaneous symmetry breaking by the scalar Higgs Field when applied to the fields of fundamental fermions and gauge vector bosons in the Standard Model. The Higgs was defined by Francois Englert and Peter Higgs [29] as a $SU_L(2)$ doublet

$$\phi(x) = \begin{pmatrix} \phi_+(x) \\ \phi_-(x) \end{pmatrix}.$$

This generates a potential term in the Lagrangian ultimately breaking the $SU(2)_L \times U(1)_Y$ to a $U(1)_Q$ group. It should be noted this symmetry breaking only occurs in vacuum otherwise the $SU(2)_L \times U(1)_Y$ group remains symmetrical. The Higgs mechanism generates lepton mass via the Lagrangian $L_Y^{lep} = -\Sigma_{l_1,l_2} \bar{l}'_{1L} Y_{l1,l2} l'_{2R}(\nu + H)$ [30]. Here $\bar{l}'_{1L}$ is a left-handed lepton field, $Y_{l1,l2}$ is the Yukawa mixing matrix, and l'_{2R} is a right handed lepton field. ν is the lepton mass term and H is the Higgs field. So the Higgs mechanism depends on a mixing of right and left handed fields, and in the absence of right handed fields it cannot generate mass.

While long theorized, the Higgs was finally detected in 2012 by the ATLAS and CMS detectors at the Large Hadron Collider (LHC) [31]. A Nobel Prize would be awarded jointly in 2013 to the co-founders of the theory, Francois Englert and Peter W. Higgs.

2.2 Neutrino history

The first hint at a neutrino-like particle was the measured energy spectrum of outgoing electrons in Beta decay in 1914. The experiment assumed the decay $n \rightarrow p + e^-$ would necessitate a discrete value, but the measured spectrum was continuous as illustrated in Fig. 2.2. Pauli would make a, so called, desperate prediction to save the theory of conservation of energy. He predicted a chargeless particle of spin 1/2 to carry the resulting energy missing in the measured continuous spectrum.

It would not be until 1956 that neutrinos were actually observed by Reines and Cowan. Their experiment consisted of a hydrogenous liquid scintillator receiving neutrino flux from a nuclear reactor which detected interactions of ν_e [2]. Event displays from this experiment can be seen in Fig. 2.3. In 1957, Bruno Pontecorvo would predict the oscillatory property of neutrinos [32]. In 1962, the ν_μ was detected by Leon M. Lederman, Melvin Schwartz, and Jack Steinberger at Brookhaven National Lab in the Alternating Gradient Synchrotron (AGS) beamline neutrino experiment [33]. The group would receive the Nobel Prize for this

in 1988. In 1965, the Homestake [34] experiment would first observe the oscillatory properties of neutrinos via a deficit in the flux of solar neutrinos compared to the prediction of the Standard Solar Model [35]. In 2002, the founder of this experiment, Raymond Davis, Jr., would receive part of a Nobel prize for this work. The Nobel prize was shared with Masatoshi Koshiba who designed Kamiokande [21] and Super-Kamiokande [36] which expanded the study of solar neutrinos. While it was then logical to conclude the existence of a third flavor, corresponding to the τ lepton, the tau neutrino (ν_τ) would not be detected until 2001 in the DONUT experiment [37] finally completing the three flavor model experimentally.

2.3 Neutrino Oscillations

Neutrinos interact as flavor states corresponding to each lepton, but propagate as mass states that are superpositions of flavor states. The formulation of mass eigenstates implies the property of neutrino oscillations where a neutrino interacting as one flavor can be measured or interact as another flavor after being propagated. Mixing between flavors was formalized theoretically in 1962 by Ziro Maki, Masami Nakagawa, and Shoichi Sakata [38] to explain the neutrino oscillations previously predicted by Bruno Pontecorvo [32]. Oscillations were first observed by the atmospheric neutrino experiment Super-Kamiokande [39] in 1998, then in the solar experiment (SNO) [40] in 2001, and in 2015, a Nobel Prize would be awarded jointly to the two experiments. After this, the first reactor experiment to investigate neutrino oscillations was KamLAND [41] in 2005. The three flavor formulation mixing is defined by

$$\nu_{lL}(x) = \sum_{i=1}^{3} U_{li}\nu_{iL}(x) \tag{2.1}$$

where ν_{iL} represents the neutrino mass states, ν_{lL} represents flavor states, and $\nu_{iL}(x) = e^{-iE_it}\nu_{iL}(0)$. U is the Pontecorvo–Maki–Nakagawa–Sakata (PMNS) mixing matrix [38], a 3×3 unitary matrix defining the transfer from mass state basis to flavor state basis [30]

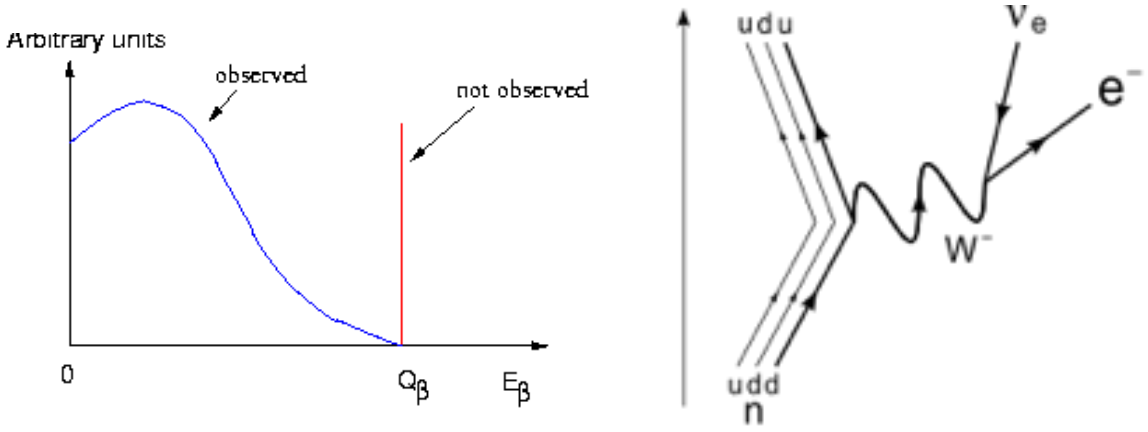

Figure 2.2: The left figure shows an illustration of the measured exiting beta energy spectrum vs the expected discrete spectrum. The right figure shows a beta decay Feynman diagram.

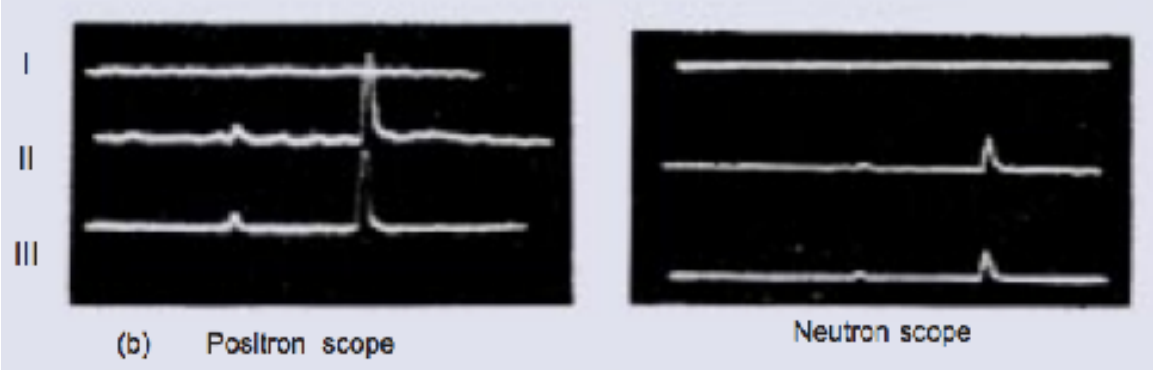

Figure 2.3: Oscilloscope traces from the Reines and Cowan experiment for first measurement of neutrinos [2]. The left figure shows the signals for positron annihilation and the right figure for neutron capture, on each of three detectors.

given by

$$\begin{bmatrix} \nu_e \\ \nu_\mu \\ \nu_\tau \end{bmatrix} = \begin{bmatrix} U_{e1} & U_{e2} & U_{e3} \\ U_{\mu 1} & U_{\mu 2} & U_{\mu 3} \\ U_{\tau 1} & U_{\tau 2} & U_{\tau 3} \end{bmatrix} \begin{bmatrix} \nu_1 \\ \nu_2 \\ \nu_3 \end{bmatrix}, \tag{2.2}$$

or more explicitly

$$U = \begin{bmatrix} c_{12}c_{13} & s_{12}c_{13} & s_{13}e^{-i\delta_{CP}} \\ -s_{12}c_{23} - c_{12}s_{23}s_{13}e^{i\delta_{CP}} & c_{12}c_{23} - s_{12}s_{23}s_{13}e^{i\delta_{CP}} & s_{23}c_{13} \\ -s_{12}s_{23} - c_{12}c_{23}s_{13}e^{i\delta_{CP}} & -c_{12}s_{23} - s_{12}c_{23}s_{13}e^{i\delta_{CP}} & c_{23}c_{13} \end{bmatrix}. \tag{2.3}$$

It is defined by three mixing angles where $c_{ab} = \cos\theta_{ab}$, $s_{ab} = \sin\theta_{ab}$, for which $a, b = 1, 2, 3$, $a \neq b$, and phase factor δ. These mixing angles have been well defined by experiments. The Charge Parity (CP) violating phase δ_{CP} is not yet known and will be discussed in Sec. 2.5.5. Note that this matrix assumes neutrinos are Dirac instead of Majorana, but Majorana nature is not expected to have any impact on transition probabilities. The evolution of a given neutrino flavor state is therefore determined by projecting to the mass state, propagating, then reconverting to flavor states

$$|\nu\rangle_t = e^{-iH_0 t} |\nu_l\rangle_t = \sum_{l'} |\nu_{l'}\rangle \, (\sum_{l} U_{l'i} e^{-iE_i t} U^*_{li}) \tag{2.4}$$

The transition probability between two flavors is then

$$P(\nu_l \to \nu_{l'}) = \left| \delta_{l'l} + \sum_{i \neq p} U_{l'i} (e^{-i(E_i - E_p)t} - 1) U^*_{li} \right|^2 \tag{2.5}$$

where p is an arbitrarily fixed index. If the neutrino is ultra-relativistic, the following approximation can be made

$$E_i = \sqrt{p_i^2 + m_i^2} \approx p_i + \frac{m_i^2}{2E} \tag{2.6}$$

such that

$$(E_i - E_p)t \approx \frac{\Delta m^2_{pi} L}{2E} \gtrapprox 1 \tag{2.7}$$

with $\Delta m^2_{pi} = m^2_i - m^2_p$ [30].

A two flavor model is sufficient for the transition region of most neutrino experiments. The simplified two flavor model is then

$$P_{\alpha \rightarrow \beta} = sin^2(2\theta) sin^2(1.27 \frac{\Delta m^2 L}{E}) \tag{2.8}$$

Oscillations of this region are illustrated in Fig. 2.4.

Thus transition probabilities depend upon the mixing angle θ, the distance between the neutrino source and detector, referred to as baseline L, the neutrino energy E, and the mass squared differences of neutrino mass states Δm^2. Therefore neutrino experiments can tune their baseline and energy to maximize a given oscillation probability. Short baseline experiments have L/E less than any estimated Δm^2 and so seek to estimate neutrino interaction properties or search for exotic physics. Long baseline experiments consist of two detectors such that neutrino flavor conversions are measured at two locations with the distance between them tuned with the neutrino energy to the region of the desired Δm^2 values. The latest measurements of the mixing properties are listed in Tab. reftab:neutrino$_p$*roperties* [42].

2.4 Neutrino Interactions

Neutrino events can be divided into neutral current (NC) and charged current (CC) interaction channels defined by whether the exchanged boson carries charge. Feynman diagrams for these are seen in Fig. 2.5. Note that only CC interactions allow flavor detection through the outgoing corresponding charged lepton. Therefore flavor of neutrinos in NC interactions cannot be determined by the interaction itself. NC events with the same outgoing particles can be mis-identified as CC events, but cannot be used to make measurements on particular flavors making them a problematic background. These categories can be further divided into Charged Current Quasi-Elastic (CCQE), Resonant (RES), Deep Inelastic Scattering (DIS), and Coherent (COH) interactions. The energy regimes of the first three are shown in Fig. 2.6.

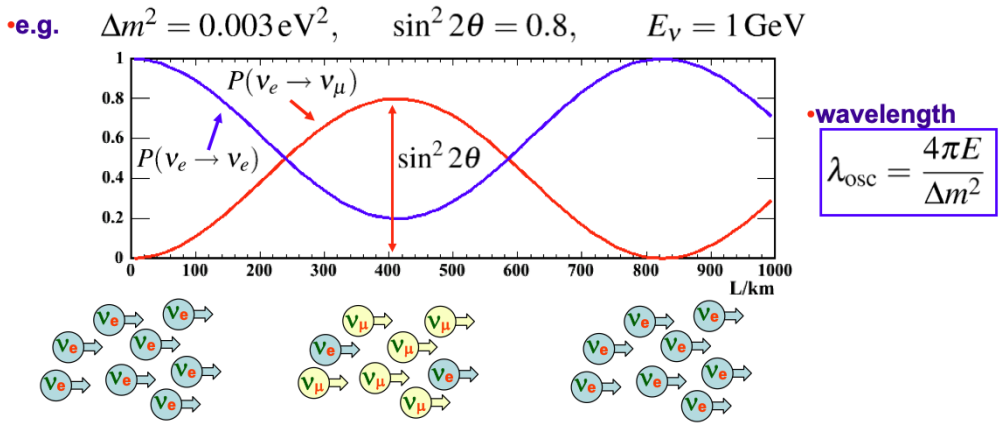

Figure 2.4: Shown is a 2 flavor neutrino oscillation illustration. The oscillation probability as a function of the baseline, L, for a given set of mixing parameters.

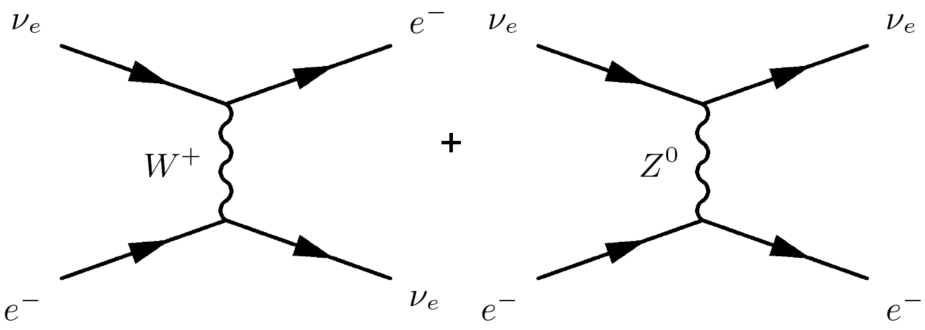

Figure 2.5: Feynman diagrams for elastic neutrino-electron scattering with charged current (CC) on the left and neutral current (NC) on the right. Note the outgoing particles are identical despite being different processes.

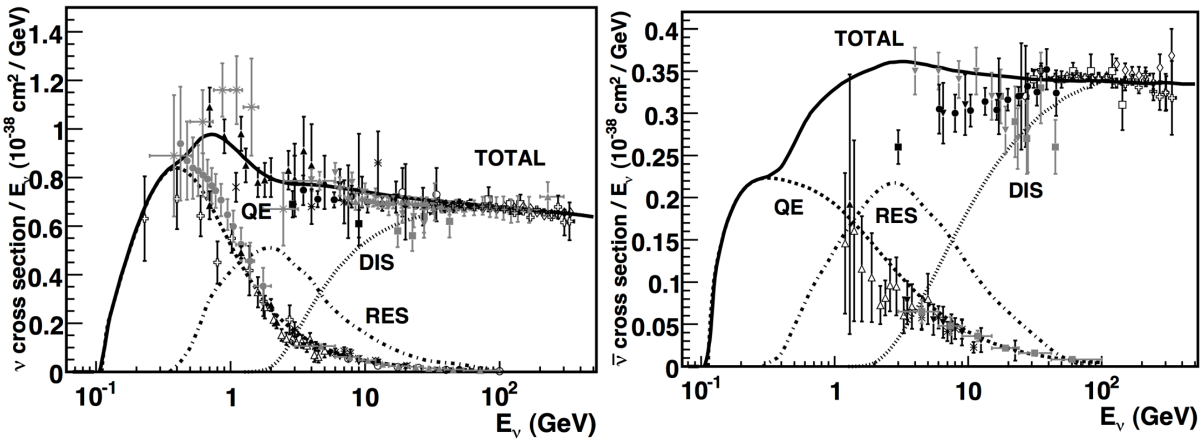

(a) (b)

Figure 2.6: Total neutrino and anti-neutrino per nucleon charged current cross sections (for an isoscalar target) [3] divided by neutrino energy and plotted as a function of energy for neutrinos (left) and anti-neutrinos (right). Also shown are the various contributing processes including quasi-elastic scattering (dashed), resonance production (dot-dash), and deep inelastic scattering (dotted). Data points are represented by triangle [4], asterisk [5], square [6], and star [7] symbols.

.

As will be elaborated on in Ch. 3, the MicroBooNE receives neutrino flux with average energy of ∼1 GeV. Neutrino interactions occur in liquid argon, chosen for its relatively heavy nuclei, scintillation, and other useful properties. The primary focus of my work, the single photon Analysis, focuses on resonance productions but has significant background from other pion-producing interactions as will be discussed in Ch. 5.

2.4.1 Charge Current Quasi-Elastic Interactions

Quasi-elastic scattering is the most prominent interaction process in the energy region ∼100 MeV to 1 GeV. It is quasi-elastic as the energy transfer is small compared to the incident energy of the scattered particles. This positions the interactions between the two regimes of inelastic where the energy transfer is larger and elastic where it is negligible. Interaction channels include

$$\nu_l + n \rightarrow p + l^- \tag{2.9}$$

$$\nu_l + p \rightarrow n + l^+ \tag{2.10}$$

where l corresponds to lepton flavors, the n and p are neutron and proton respectively. Charge current quasi-elastic (CCQE) events which include an electron or positron can be misidentified as our single photon signal, but are distinguishable by the electron-photon separating power of the MicroBooNE detector. CCQE modelling uses the Llewellyn Smith formalism as described in [43]. However, an improved model is the Nieves [44] CCQE model which includes a correction for long-range nucleon correlations and an approximation of the Coulomb interaction of outgoing charged leptons from the nucleus.

2.4.2 Deep Inelastic Interactions

Deep Inelastic Scattering (DIS) occurs largely at higher neutrino energies but can occur at neutrino energies as low as ∼2 GeV. In this regime, the incident neutrino wavelength is sufficiently small to induce hadronization including the processes

$$\nu_l + N \rightarrow l + X \tag{2.11}$$

$$\nu_l + N \rightarrow \nu_l + X \tag{2.12}$$

where N is a proton or neutron and X is a hadron shower. MicroBooNE uses The Bodek-Yang [45] model for DIS interactions.

2.4.3 Resonant Interactions

Resonant pion production dominates the few-GeV energy range. It occurs when neutrino interactions in target nucleon cause a resonance excitation creating an excited baryon state. This excited baryon state then decays emitting a pion. There are three CC channels and four NC channels for this process including

$$\nu_l + p \rightarrow l + p + \pi^+ \tag{2.13}$$

$$\nu_l + n \rightarrow l + p + \pi^0 \tag{2.14}$$

$$\nu_l + n \rightarrow l + n + \pi^+ \tag{2.15}$$

for CC, and

$$\nu_l + p \rightarrow \nu_l + p + \pi^0 \tag{2.16}$$

$$\nu_l + p \rightarrow \nu_l + n + \pi^+ \tag{2.17}$$

$$\nu_l + n \rightarrow \nu_l + n + \pi^0 \tag{2.18}$$

$$\nu_l + n \rightarrow \nu_l + p + \pi^- \tag{2.19}$$

$$\tag{2.20}$$

for NC. Note the interactions are listed with resulting pions and nucleons, but this is because these are the most common decays of the baryon which are produced. The single photon selected signal is composed of resonance events where a delta particle decays instead directly into a photon and nucleon. However, pion decays will produce photons which will pair convert into electron-positron pairs producing ionization showers in the detector resulting in a very similar signal, as will be discussed in Ch. 5. Modeling for these processes is commonly

done via the Rein-Sehgal model [46]. MicroBooNE uses the improved Berger-Sehgal model which was updated to include the effects of lepton mass.

2.4.4 Coherent Interactions

In this process, neutrinos scatter elastically off a nucleus in its entirety (instead of individual nucleons) producing pions. Both CC and NC channels exist including

$$\nu_l + A \rightarrow l + A + \pi^+ \tag{2.21}$$

$$\nu_l + A \rightarrow \nu_l + A + \pi^0. \tag{2.22}$$

This occurs largely with low momentum transfer. Coherent pion production is also modeled with a Berger-Sehgal formulation. Pions produced in coherent processes are a sub-dominant contribution in our single photon selections.

2.4.5 Neutrino-Argon Interactions Developement

Historically, neutrino detectors used lighter nuclei such as Hydrogen and Deuterium, but with the advent of Liquid Argon Time Projection Chamber detectors, determining the properties of the much denser Argon nuclei has become crucial. Future experiments of the Short Baseline Neutrino (SBN) program [47] and the Deep Underground Neutrino Experiment [48] will depend on modern measurements of neutrino-argon properties. MicroBooNE is well positioned to provide high statistics neutrino cross section measurements on argon.

2.5 Open Questions in Neutrino Physics

Although neutrinos have been studied by a diverse set of experiments for over 70 years, many questions about neutrino properties and their interactions remain unanswered. This section will provide a brief overview of open questions in neutrino physics along with current experimental efforts underway to address them.

2.5.1 Neutrino Mass Hierarchy

Solar and atmospheric neutrino experiments have estimated two of the neutrino mass squared differences Δm^2_{21} and Δm^2_{31} therefore referred to as Δm^2_{sol} and Δm^2_{atm} respectively. However, the absolute masses of neutrinos have yet to be precisely determined. Therefore two possibilities exist for the order of neutrino mass states referred to as "normal" and "inverted" hierarchies, as can be seen in Fig. 2.7. The difference is in the position of m^2_3 which is either heavier or lighter than the other two. This is because, while Δm^2_{31} has been measured, the sign of Δm_{31} is unknown [8].

The sign of these mass differences can be probed via matter effects in flavor conversion. For example enhancement of electron neutrinos due to matter effects in the sun determined the sign of $\Delta m_{21} > 0$ [49]. For Δm^2_{31}, enhancement of ν_e would indicate normal ordering while enhancement of $\bar{\nu}_e$ would indicate inverted mass ordering [49]. Tokai to Kamiokande (T2K) [21] and NuMI Off-axis ν_e Appearance (NOνA) [50] experiments are both evaluating sensitivities to this effect while the upcoming Deep Underground Neutrino Experiment (DUNE) [48] and Taiko to Hyper-Kamiokande (T2HK) [51] should both have enhanced sensitivity.

2.5.2 Absolute Masses of Neutrinos

The measurement of absolute mass of neutrino states is difficult due to their (estimated) incredibly low value and the fact that neutrinos only interact weakly. An upper bound on the combined mass of the three mass states was determined by considering their contribution to the universal known mass density using cosmological data. It was determined as $\Sigma_i m_i <$ 14 eV [52].

There is an effort to measure absolute neutrino masses via distortion of the β decay spectrum in Tritium experiments. Two experiments which have attempted this are Mainz [53] which placed an upper bound on the ν_e mass of $m \leq 2.3$ eV/c^2 and Troitsk [54] which gave an upper bound value of ν_μ mass of $m < 2.12$ eV/c^2, both at 95% confidence level. In 2019, the KATRIN experiment announced a reduction of the upper bound of ν_e to $m < 1.1$ eV at 90% confidence level, and it continues to collect data for more precision [55].

Other future experiments are Project 8 [56], ECHO [57] and HOLMES [58] which are all aiming for sub-eV sensitivity.

2.5.3 Additional Neutrino States

As will be elaborated in Ch. 3, both LSND [10] and MiniBooNE [11] saw results indicating the potential of oscillation in a region, $\Delta m^2 \approx 1$ eV^2, where it should be forbidden. This has led to the theory of an intermediary sterile neutrino $\nu_\mu \rightarrow \nu_s \rightarrow \nu_e$ that allows for the oscillation and does not interact via the weak force. This would align them with the properties of right-handed neutrinos as will be discussed Sec. 2.5.4. MicroBooNE is the principal investigator of the anomaly observed by MiniBooNE with the goal to evaluate the sterile neutrino interpretation. MicroBooNE is also part of the more extensive short-baseline neutrino (SBN) [59] program which is exploring existing hints for sterile neutrinos. In addition, JSNS^2 [60] at JPARC [61] (Japan) has just started taking data and aims for a direct test of LSND.

2.5.4 Majorana or Dirac Nature

The three charged fermions are known to be Dirac fermions which have distinct antiparticles. However, it is unknown if neutrinos are Dirac or Majorana, where Majorana nature implies that neutrinos are their own anti-particles. Neutrinos unlike charged leptons possess no charge or other conserved quantity that would distinguish a particle from an antiparticle. Results from the Large Electron-Positron (LEP) collider [62] concluded that a theoretical right-handed neutrino could not couple with weak bosons, so lack of observation of right-handed neutrinos does not forbid their existence. However, experiments have determined that produced neutrinos have negative helicity which equates to left-handedness in the high energy regime. The Goldhaber Experiment [63] first proved the negative helicity of neutrinos via resonant scattering of gamma rays following orbital electron capture.

Another aspect to consider is generation of mass, which as discussed requires left and right-handed fields for the Higgs mechanism. Upper bounds for neutrino mass from cosmological data [30] put neutrino at ~6 orders of magnitude below the smallest known

scale of the electron mass. This indicates neutrinos do not receive mass by the typical Brout-Englert-Higgs mechanism that generates Dirac masses. No Standard Model interaction exists to give Majorana mass implying that neutrino masses must come from beyond the Standard Model physics.

Confirmation of the Majorana neutrino could be accomplished via neutrinoless double beta decay. Here a virtual neutrino (antineutrino) is exchanged in two simultaneous beta decay interactions such that no neutrinos are emitted (shown in Fig. 2.8). This is only possible if the neutrino and antineutrino are interchangeable. Measurement is difficult both due to the general difficulty in measuring neutrino production with precision and the low expected likelihood of such an interaction.

CUORE [64] is an ongoing effort to measure neutrinoless double beta decay with a series of detectors. The experiment placed a limit on the half-life of neutrinoless double beta decay of $T_{1/2} > 3.0 \times 10^{25}$ years in ^{130}Te and many detectors in the future (e.g. LEGEND [65], SuperNEMO [66], nEXO [67], DARWIN [68]) hope to contribute to the study using different isotopes and experimental techniques.

2.5.5 Charge Parity Violation

As discussed before, a transformation being symmetrical means that all physical laws and processes should remain unchanged following the transformation. Foundational symmetries to the Standard Model are charge conjugation (C) where each particle is replaced with its anti-particle, parity transformation (P) which flips chirality, and time reversal (T), although each is broken under different circumstances. The charge conjugation symmetry carries the implication that matter and antimatter should be of equivalent abundance in the universe, but this does not seem to be the case. There is also the issue that charge conjugation would transform a left-handed neutrino into a left-handed antineutrino, the nature of which is unknown. Parity was believed to be an unbroken symmetry until 1956 when Tsung-Dao Lee and Chen-Ning Yang [69] documented that the symmetry was as yet unconfirmed in weak interactions and proposed experiments for such a verification. Wu E. Ambler would lead an experiment in 1957 proving non-conservation in beta decay of Cobalt-60 [70]. However, the parity symmetry remains unbroken in strong and electromagnetic interactions.

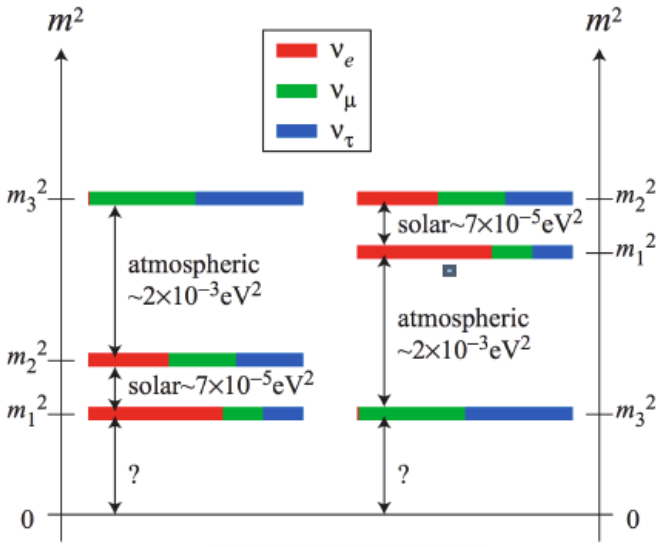

Figure 2.7: Neutrino mass ordering with normal (left) and inverted (right) hierarchies. The coloration represent the flavor composition of each state. As the absolute masses are not precisely determined, the distance from m^2=0 is not defined on the diagram [8].

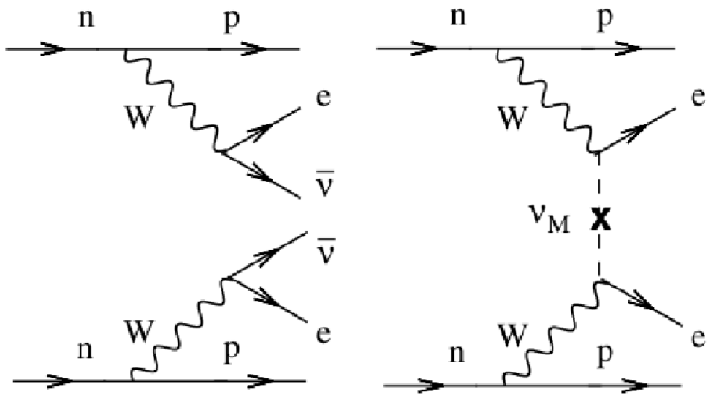

Figure 2.8: Feynman diagrams for normal (left) and neutrinoless (right) double beta decay processes.

It was determined that a combination of charge and parity transformations would restore symmetry in the experimental interactions leading to the concept of CP symmetry. C symmetry would be broken in weak interactions to cancel out the asymmetries of a parity transformation. In 1964, indirect CP violation was observed by James Cronin and Val Fitch [71] by measuring the transformation of kaons. Transformation rates of kaons involving transformation of their component quarks to anti-quarks (and vice-versa) were found to have differing probabilities in different directions. This is considered indirect proof as it could be explained by either CP violation or T violation. Direct CP violation would not be conclusively demonstrated until 1999 from the KTeV [72] experiment at Fermilab and NA48 [73] experiment at CERN by measuring a difference in CP symmetric decays of kaons to pions.

CPT is a combination of symmetries that remains unbroken and has strong theoretical backing established in 1954 by Gerhat Luders and Wolfgang Pauli [74]. This symmetry implies violations of CP symmetry must be cancelled by violations in the T symmetry. CP violation could explain the matter-antimatter asymmetry of the universe, but the measured rate in kaons is not large enough to work as a sole explanation. Measurements in the neutrino sector could expand this theory. CP violations have yet to be confirmed in neutrino experiments, but the theoretical factor δ_{CP} has been incorporated into the PMNS matrix with relation to the reactor mixing angle θ_{13}.

Long baseline experiments such as NOvA [50] and T2K [21] experiments have some sensitivity to δ_{CP} but are limited. Next generation long-baseline experiments such as DUNE [48] and Hyper-K [51] are designed to provide discovery sensitivities to δ_{CP}. Both experiments are expected to take physics data in late 2020s.

2.6 Neutrino Experiments

Neutrino experiments are divided into several categories based on their neutrino source. These each probe neutrinos at different energies as can be seen in Fig. 2.9. Initial experiments searching for the existence of the neutrino could be small-scale and rely on event counting requiring less precision. To more properly measure neutrinos, larger and higher-precision

detectors are necessary. Bubble chambers were initially favored, such as those at Argonne National Laboratory [75] and Brookhaven National Laboratory [76]. Their working principle is to have an ionizing particle produce microscopic bubbles on a material and to reconstruct the interactions via photographic images. Bubble chambers boast high precision but have a number of limitations including their photogenic output and difficulty of construction at larger sizes. Liquid argon time projection chambers (LArTPCs) have emerged as a balance of precision and ability to be scaled to large sizes as can be seen in Fig. 2.10. LArTPCs possess other advantages such as digitized outputs for ease of analysis. As has been noted, the focus of this dissertation is MicroBooNE, an accelerator LArTPC experiment which will be more thoroughly explained in Ch. 3.

2.6.1 Neutrino Accelerator Experiments

Accelerator neutrino experiments can be divided into the categories of long baseline (∼1000 km) and short baseline (∼1 km). The baseline indicates how far the neutrinos will travel after production before passing through the (final) detector. This is primarily for defining the L/E ratio, where L denotes baseline and E the neutrino energy, which corresponds to a certain region of Δm^2 in the neutrino oscillation spectrum as defined in Sec. 2.3. Long baseline experiments utilize near and far detectors to precisely measure the rates of neutrino appearance or disappearance, as flavor states mix over the travel distance. These measurements can be used to address the question of neutrino mass hierarchy as well as investigate other questions like CP violation relating to the matter-antimatter asymmetry and precision measurements of neutrino oscillation parameters. Short baseline experiments, on the other hand, investigate the potential for novel physics unsupported by current models (e.g. sterile neutrinos). Detectors are set in a region of Δm^2 that does not fit with current mass-hierarchy predictions, but has been indicated by several short baseline experiments as a region of interest for sterile neutrinos or other novel physics. Both short and long baseline experiments provide opportunities to perform R&D and measure interaction cross sections as well as other properties in the detector, which can be beneficial to future neutrino experiments.

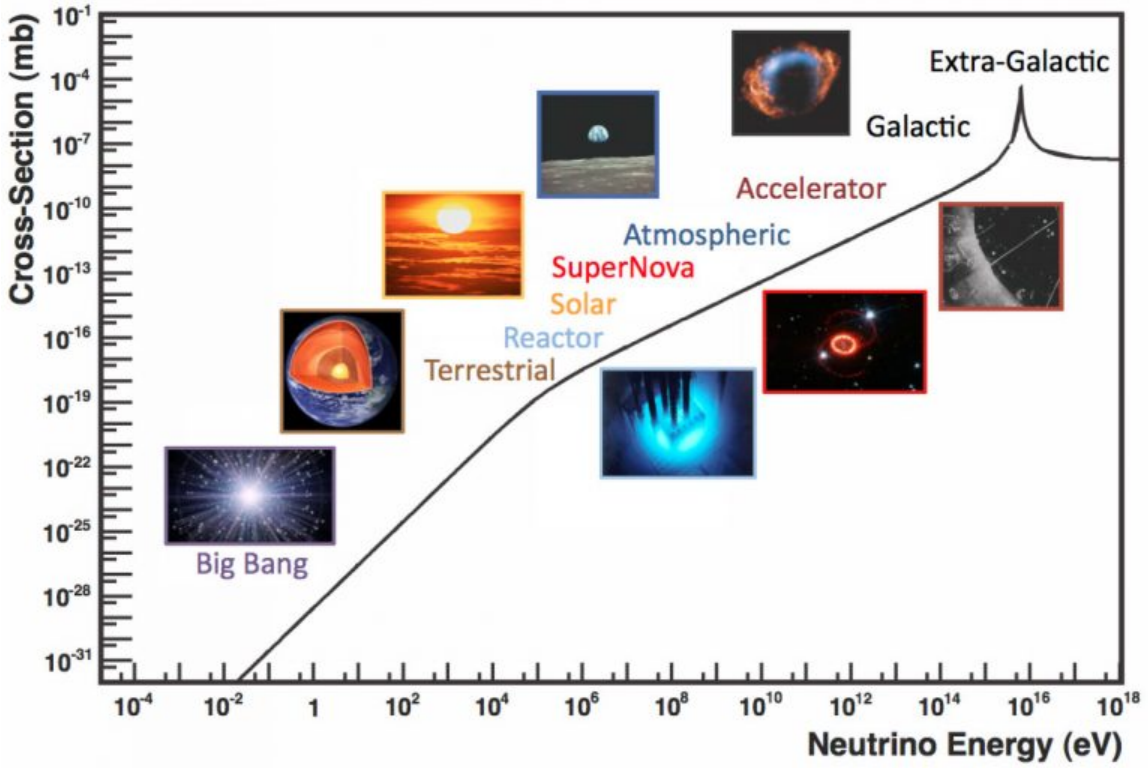

Figure 2.9: Representative example of various neutrino sources across decades of energy. The electroweak cross-section for $\nu_e e^- \to \bar{\nu}_e e^-$ scattering on free electrons as a function of neutrino energy (for a massless neutrino) is shown for comparison [3].

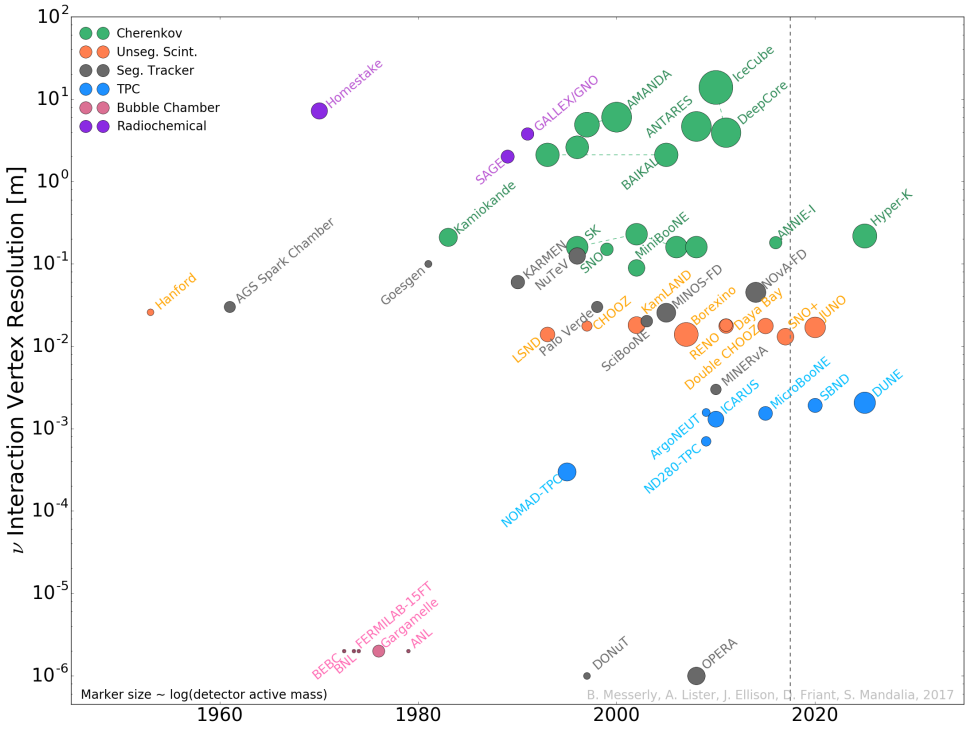

Figure 2.10: Detectors interaction vertex resolution plotted by year built. The size of the marker scales logarithmically with detector mass. The detectors are roughly separated by the technology they used. In some cases detectors fall into multiple categories. For example, MiniBooNE uses both scintillation light and Cherenkov light. When experiments have had multiple runs in different configurations, a dashed line connects the runs. The vertical grey line indicates the year 2019 [9].

2.6.2 Long Baseline Experiments

Current long baseline experiments taking data include Tokai to Kamioka Experiment (T2K) [21] in Japan and NuMI Off-axis ν_e Appearance Experiment (NOνA) [50] in the United States. The first to begin was T2K experiment so named since it uses a beam of neutrinos produced in the Japan Proton Accelerator Research Complex (J-PARC) then detected in the Super-KamioKande (Super-K) detector in Kamioka (see Fig. 2.11). The beamline consists of majority of muon neutrinos produced on a graphite target and is used to investigate muon to electron and muon to tau conversions at a baseline of 295 km and energy of 600 MeV. There is a near detector, ND280, 280 m from the target and the far detector is the Super-K detector, a massive Cherenkov detector of ultra-pure water. The detector is 2.5 degrees off the center of the neutrino beam which leads to a narrower set of energies.

The next major experiment would be at Fermilab in the United States with the NOνA experiment. The beamline it uses (NuMI)is explained in greater detail in App. C. NoνA uses a pair of detectors, with similar designs, but different scales. These include a 300 metric-ton near detector at Fermilab and a 14 metric-kiloton far detector in Minnesota. The detector utilizes cells of highly reflective plastic PVC each filled with liquid scintillator. Another long baseline search was the Main Injector Neutrino Oscillation Search (MINOS, MINOS+) [77] long baseline experiment in the NuMI beam at Fermilab. This sent neutrinos 450 miles away to the Soudan Underground Mine in northern Minnesota, and has been taking data since 2005 and recently ended operations.

Finally the Deep Underground Neutrino Experiment (DUNE) [48] is planned along a new beamline at Fermilab using the NuMI and BNB via the planned Proton Improvement Project (PIP-II) accelerator. The DUNE beamline is shown in Fig. 2.12. The Long Baseline Neutrino Facility (LBNF) will provide the infrastructure and facilities at both near and far sites. The experiment uses a pair of detectors, one of which will be placed at Fermilab and the other at Sanford Underground research Facility (SURF) in South Dakota. The DUNE far detector will be a liquid argon time projection chamber (LArTPC) with 40 kilotons of active liquid argon mass. DUNE is the next generation long baseline experiment and is the ultimate

experiment to measure remaining properties of neutrinos. MicroBooNE and other short baseline LArTPC experiments will provide valuable input to DUNE both technologically and through physics measurements.

2.6.3 Short Baseline Experiments

LSND or Liquid Scintillator Neutrino Detector [10] is the start of the chain of measurements which lead to the MicroBooNE detector. LSND was located at Los Alamos National Laboratory (LANL) running from 1993−1998. The beam was produced via the Los Alamos Neutron Science Center accelerator (LANSCE) which outputs a highly concentrated beam of low energy neutrinos. In 1993−1995, it used a 30 cm long water target with water-cooled Cu beam dump, but in 1996 it was replaced for "a close packed, high-Z target". The accelerator is a linear accelerator with proton current of 1 mA at 798 MeV making it ideal for producing and studying low energy neutrinos. Questions posed by the LSND measurement led to the MiniBooNE experiment on the Booster Neutrino Beam (BNB) at Fermi National Laboratory (Fermilab). The Booster Neutrino Beamline will be discussed in detail in Sec. 3.3, but, for reference, produces neutrinos with an energy peak of ∼800 MeV. To produce a similar L/E ratio to that of LSND, the baseline of MiniBooNE was set to 541 m. As discussed, the MiniBooNE detector was a mineral oil detector that works by collecting Cherenkov light. While it did not report the same excess as LSND, it did report an excess in $\bar{\nu}_e$ appearance in the low energy region (<500 MeV). This is now commonly referred to as the low energy excess (LEE). Additional statistics collected since then have shown an increasing discrepancy between data and prediction over the range of 200−475 MeV [78]. MiniBooNE is unable to distinguish between signal electron events and background photon pair conversions, and investigation of this would be the primary motivation for construction of the MicroBooNE detector described in Ch. 3. MiniBooNE and LSND will be further discussed in Sec. 3.1.

The Short Baseline Neutrino Detector (SBND) is under construction as part of the Short-Baseline Neutrino (SBN) Program at Fermilab (see Fig. 2.13). It is located on the Booster Neutrino Beam utilizing existing experiments, MicroBooNE and ICARUS-T600, as intermediate and far detectors respectively. The SBN program with the three detector arrangement is aimed at more definitively addressing the sterile neutrino question where

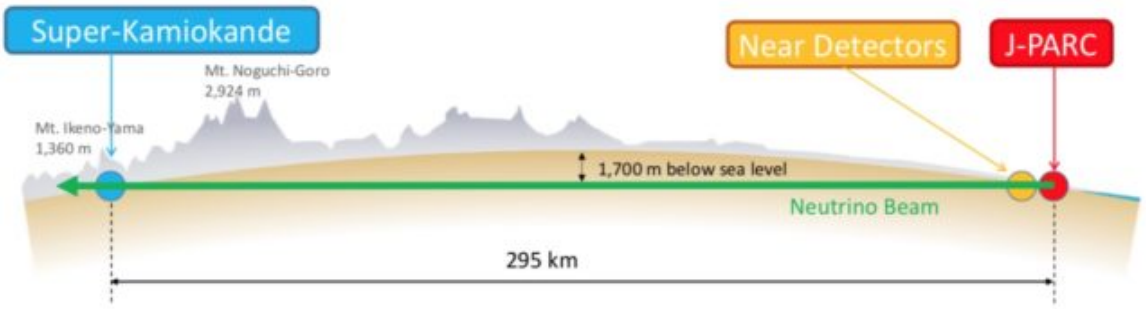

Figure 2.11: T2K beamline in Japan.

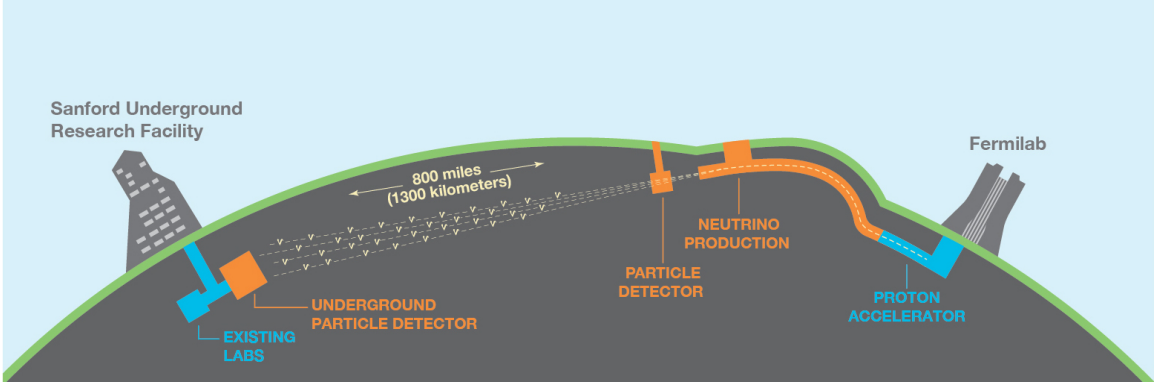

Figure 2.12: DUNE Beamline in the United States.

there are existing hints. While the detectors are not identical, as desired by near and far detectors, each is a liquid argon time projection chambers with comparable properties and being on the same beam line significantly reduces systematic uncertainties across the three detectors.

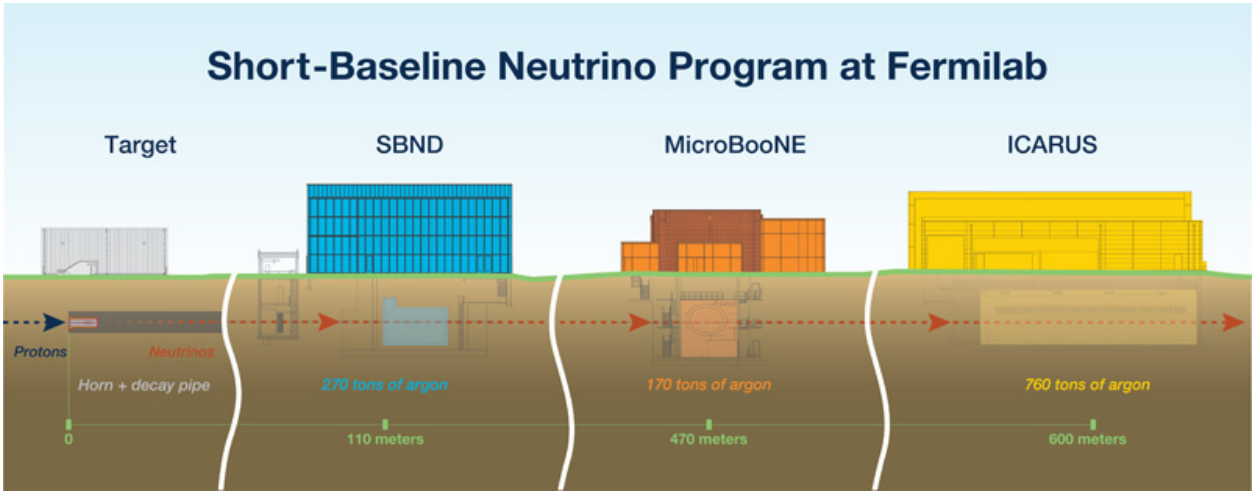

Figure 2.13: Fermilab Short-Baseline Neutrino program with three LArTPC detectors: MicroBooNE, SBND and ICARUS.

Chapter 3

The MicroBooNE Experiment

This chapter describes the physics motivation and concepts of the MicroBooNE experiment. Sec. 3.1 covers the predecessor experiments, LSND and MiniBooNE, as motivation for MicroBooNE. Sec. 3.2 establishes the goals of the MicroBooNE experiment. Sec.3.3 covers necessary information on the primary flux source of MicroBoooNE, the Booster Neutrino Beamline. Sec. 3.4 describes the construction and operation of the detector. The MicroBooNE detector is also introduced in detail along with component sub-systems. Finally, Sec. 3.5 gives an overview of MicroBooNE's run time and collected data.

3.1 Experimental Motivation

As discussed before, the Liquid Scintillator Neutrino Detector (LSND) showed an excess of appearance of $\bar{\nu_e}$ events above what was expected at that baseline, 30 m, and energy $0 - 250$ MeV of $\bar{\nu_\mu}$ as shown in Fig. 3.1. This would imply a Δm^2 of $0.2 - 10$ eV^2/c^4 implying one neutrino state has a mass greater than 0.4 eV/c^2 well above what current models predict [10]. This observation led to many theories involving additional neutrino states referred to as sterile neutrinos. Model agreement with data actually favors a 2-sterile neutrino model [79, 80].

To investigate this anomalous result, MiniBooNE was commissioned in the same Δm^2 region as LSND. MiniBooNE is a surface-based mineral oil Cherenkov detector (see Fig 3.2a). Cherenkov light is produced by particles moving through a dielectric medium with velocity

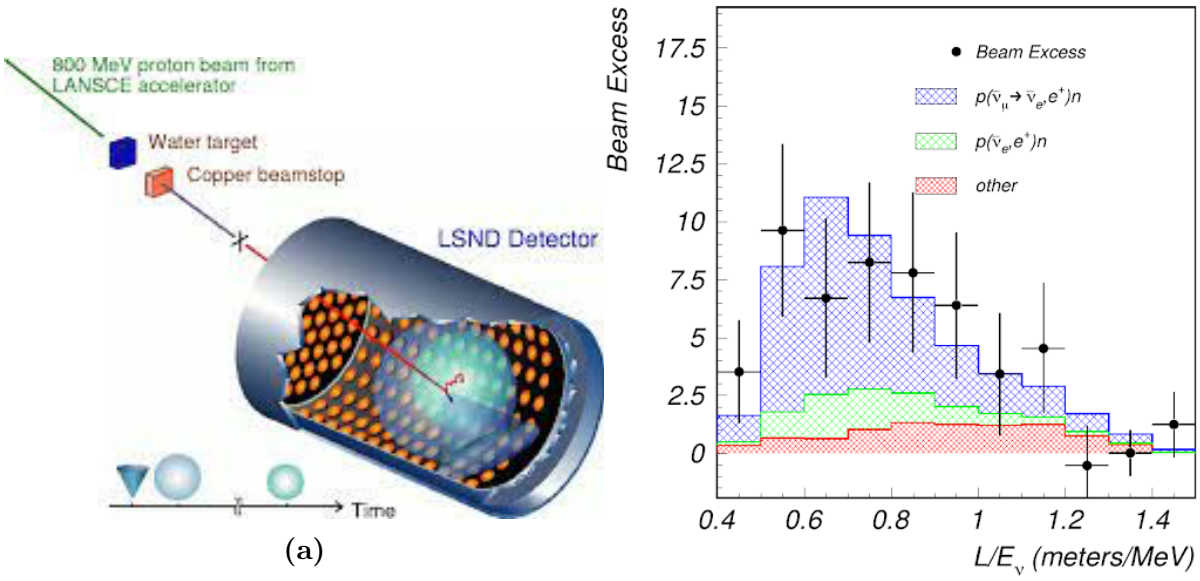

(a) **(b)**

Figure 3.1: (Left) Basic design of the LSND experiment. (Right) LSND result of selected events versus L/E_ν where L is the distance traveled by the neutrino and E_ν is the neutrino energy [10]. The red and green portions of the histogram represent the expected background. The blue histogram represents an additional neutrino state oscillation with $\Delta m^2 \sim 1$ eV^2.

greater than the phase velocity (speed of propagation of photons) in that medium. Polarized particles returning to the ground state will then emit photons in a pattern comparable to sound emitted in a sonic boom. In the MiniBooNE detector, light is collected on photo-multiplier tubes, which is used to reconstruct particle interactions. MiniBooNE began operation in 2002 and stopped running in 2017 after collecting about 18.75×10^{20} POT worth of neutrino data. While it did not exactly replicate the LSND excess exactly, it instead reported an excess in $\bar{\nu}_e$ appearance in the low energy region (<500 MeV). The most recent data results of the excess is shown in Fig. 3.2b [11], and a side by side comparison with LSND is shown in Fig 3.3b. This is now commonly referred to as the low energy excess (LEE). Additional statistics collected since then have shown an increasing discrepancy between data and prediction over the range of $200-475$ MeV with a significance of 4.8σ [78]. MiniBooNE being a Cherenkov detector has difficulty distinguishing signal electron events and background photon pair conversions. This is illustrated in Fig. 3.4. The issue is photons from π^0 can be reconstructed as electrons (the primary signal of a ν_e interaction) if one photon ring is not reconstructed or if they significantly overlap to appear as one ring. The source of this excess remains an open mystery so investigation of the MiniBooNE result would be the primary motivation for construction of the MicroBooNE detector as described in Sec. 3.2.

3.2 MicroBooNE and Physics Goals

The primary physics goal of Micro Booster Neutrino Experiment (MicroBooNE) is to measure short baseline neutrino oscillations with a focus on examining the excess of low energy electron-like events observed by the MiniBooNE experiment. MiniBooNE was unable to distinguish signal electrons from the background of photon conversions and it is expected that MicroBooNE's superior capability to separate electrons from photons can resolve questions on the MiniBooNE LEE. This resolution power comes from the MicroBooNE detector's construction as a Liquid Argon Time Projection Chamber (LArTPC). The detector is surface-based, with a volume of ~100 tonnes, and is located on the Booster Neutrino Beam (BNB) with a baseline at 470 m similar to that of MiniBooNE (541 m). The

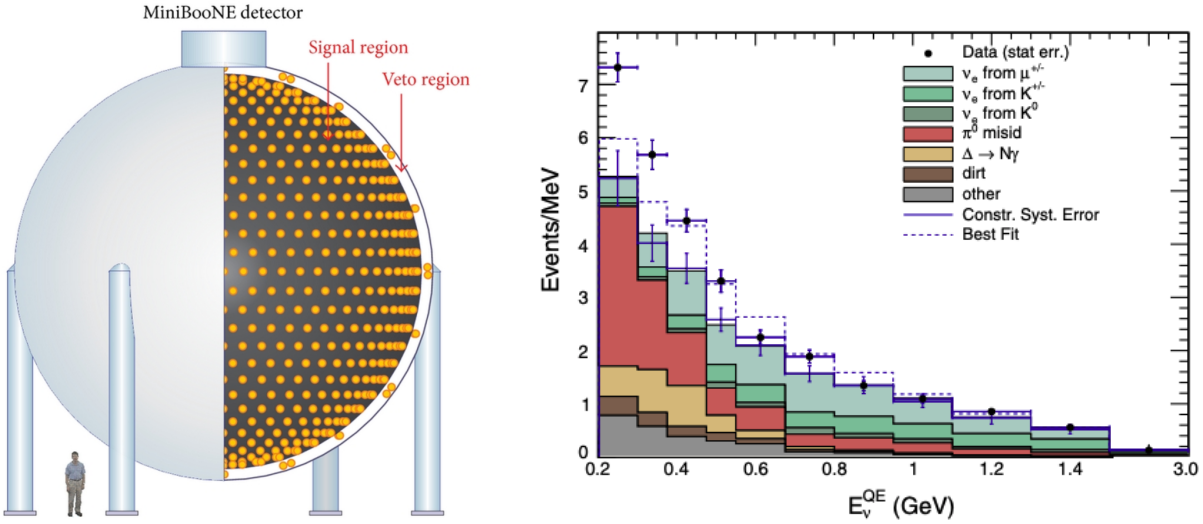

(a) MiniBooNE scale and active region

(b) MiniBooNE excess

Figure 3.2: (Left) The MiniBooNE detector diagram. (Right) The MiniBooNE neutrino mode E_ν^{QE} distributions [11], which corresponds to to a total 18.75 $\times 10^{20}$ POT data for ν_e CCQE data (points with statistical errors) with included. predicted backgrounds (colored histograms). A constrained background is shown as additional points with systematic error bars. The dashed histogram shows the best fit to the neutrino-mode data assuming the known two-neutrino oscillation model.

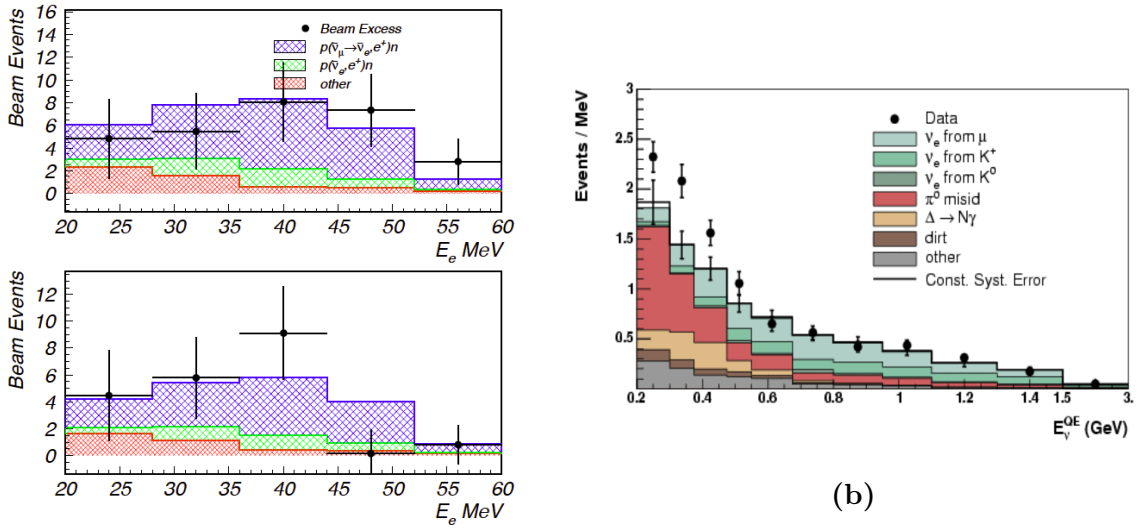

(a) **(b)**

Figure 3.3: Comparison of LSND excess (left) vs MiniBooNE excess (right) plotted with neutrino energy. In the case of LSND, the top plot is from the 1993-1995 run span and the bottom is from the 1996-1998 following a change of the beam target as discussed in Ch. 7.

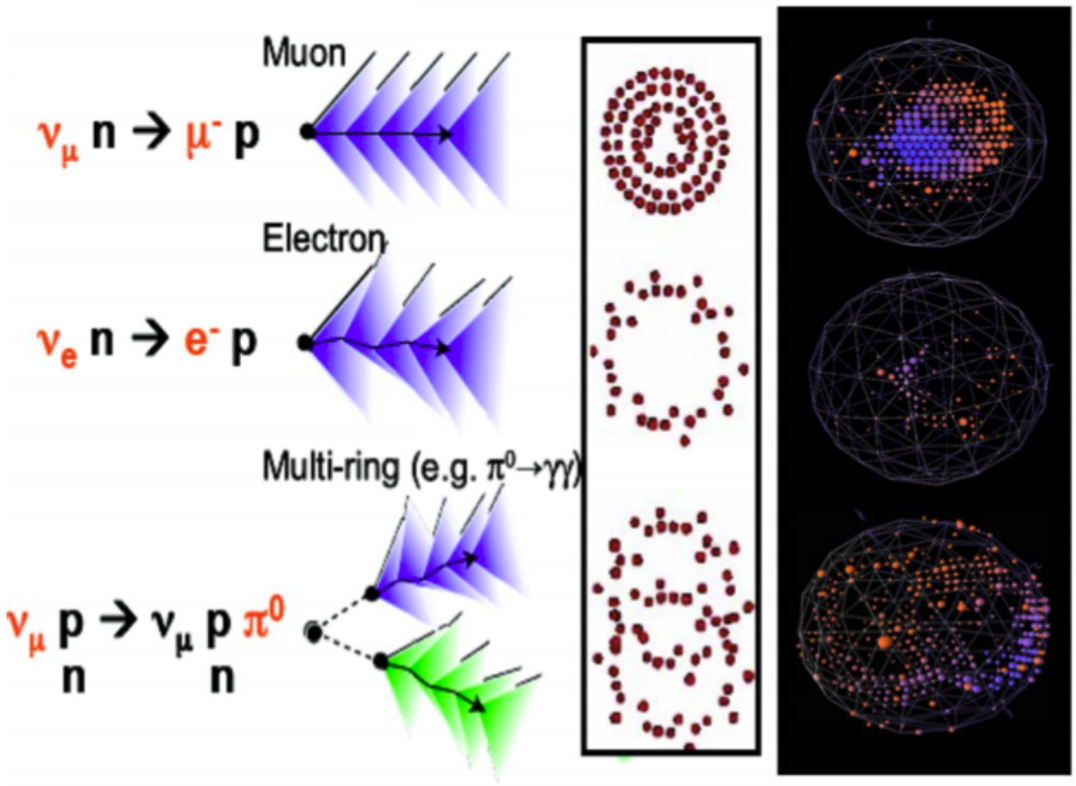

Figure 3.4: An illustration of the signals seen in MiniBooNE. Note the similarity in electron and photon signals. From top to bottom, a muon neutrino charged-current quasi-elastic (CCQE) interaction, an electron neutrino CCQE interaction, and a neutral current, neutral pion production interaction. For each interaction the expected Cherenkov rings are shown on the right along with a candidate event.

Booster Neutrino Beam delivers a beam of predominantly muon neutrinos produced primarily from pion decays, with energies peaking around 700 MeV as shown in Sec. 3.3.2 and Fig. 3.6. Further details of the operation of this beam will be provided in Ch. 8. MicroBooNE is also exposed to an off-axis component of the NuMI beam produced from pion and kaon decays with average neutrino energies of about 0.25 GeV and 2 GeV respectively. MicroBooNE observed its first cosmic ray tracks in August 2015 and began collecting neutrino beam data in October 2015.

MicroBooNE has several supplemental goals in supporting other ongoing experiments and making measurements for next generation detectors. In particular, MicroBooNE is performing a range of analyses on neutrino-argon cross sections as well as important R&D for future multi-kiloton LArTPC experiments like the Deep Underground Neutrino Experiment (DUNE). Due to nuclear effects in neutrino interactions on argon, a great variety of nucleon emission and event topologies can be observed within the detector. The single photon analysis actually includes both an effort to explain the LEE and also efforts to measure cross-sections for neutrino interactions on argon.

MicroBooNE also serves as the mid detector in the Fermilab short baseline neutrino (SBN) program along with two other LArTPCs: ICARUS and the Short Baseline Neutrino Detector (SBND) with the goal of a highly sensitive search for sterile neutrino oscillations in the region $L/E \sim 1$ km/GeV where there are existing hints for sterile neutrinos. Finally, the detector is capable of contributing to supernova analysis and proton decay. While MicroBooNE itself does not have enough active volume to enable a competitive sensitivity to proton decay, it is capable of doing a proof of concept for larger detectors and can do background measurements [1].

3.3 Booster Neutrino Beam

The Booster Neutrino Beam is the primary source of flux for the MicroBooNE experiment. The secondary source NuMI is not considered for my analyses (and can be disregarded given the difference in beam timing). Secs. 3.3.1 and 3.3.2 cover the relevant information to the

Single Photon analysis. Further discussion of the accelerator and beamline will be included in Ch. 7 and Ch. 8.

3.3.1 Beam Target and Horn

Production of mesons is done via a beryllium target surrounded by a magnetic horn which focuses the mesons produced before they decay. It can be switched between neutrino-mode where it focuses π^+ that decay as $\pi^+ \rightarrow \mu^+ + \nu_\mu$ and diverts π^- that would decay to $\pi^- \rightarrow \mu^- + \bar{\nu_\mu}$ and anti-neutrino mode which reverses this. Focused mesons go through the collimator which blocks particles that do not contribute to neutrino flux and reduces radiation levels. The mesons arrive in a 50 m decay region (open air) where mesons decay producing the neutrino beam. A beam stop blocks nearly all non-neutrino particles and the neutrinos propagate through dirt to the detector. A simple diagram of the path from the booster to the detector can be seen in Fig. 3.5.

3.3.2 Booster Neutrino Beam MicroBooNE Era

MiniBooNE already had a well developed GEANT4 [81] framework when MicroBooNE entered operation which included techniques for systematic uncertainty which will be expanded in Ch. 6 and 8. As discussed in Sec. 3.3.1, the magnetic focusing horn focuses pions for a dominant ν_μ signal. However, sub-dominant electron neutrino component from unfiltered kaon decays, $K^+ \rightarrow \nu_e + e^+ + \pi^0$ and $K^0_L \rightarrow \nu_e + e^+ + \pi^0$, remains. Improvements in flux prediction were made using SciBooNE's [82] measurement of $p + Be \rightarrow K^+$ and the Hadron Production Experiment (HARP) [83] pion production data. In 2018, adaptions were made for a prediction at MicroBooNE's location [84]. Figure 3.6 shows a comparison of the booster neutrino flux at MiniBooNE and MicroBooNE.

Beamline instrumentation is used to monitor the beam on a spill-by-spill basis keeping the uncertainty due to POT to $\sim$2%. Other beam systematic uncertainties are small when compared to those from modeling interactions and those having to do with detector effects, which will be elaborated in Ch. 6. MicroBooNE also has a neutrino flux contribution from

the the Neutrino at Main Injector (NuMI) beamline, but as these events do not contribute to this dissertation, its properties are discussed in App. C.

3.4 MicroBooNE Construction

Liquid argon time projection chambers (LArTPCs) are prominent in neutrino research with experiments around the world utilizing them to detect neutrino interactions. LArTPCs are time projection chambers that consist of liquid argon in an electric field provided by anode and cathode planes. The TPC is enclosed in a cryostat (see Fig. 3.7) with a purification and re-circulation system in order to keep the liquid argon ultra pure. Charged particles produced in neutrino-argon interactions propagate through the detector and ionize the surrounding medium along their trajectory, causing released electrons to drift towards the anode. Charged particles also create prompt vacuum ultraviolet (VUV) scintillation photons which can be detected by a light collection system. The working principle of a LArTPC can be seen in Fig. 3.8.

3.4.1 TPC

The MicroBooNE detector is surface-based with an 89-ton active volume (total volume of 170 tons). It consists of a drift chamber with a cathode plane at -70 kV and anode plane with a 2.56 m drift distance between them, resulting in an electric field of strength 273 V/cm. A field cage made up of 64 stainless steel tubes is placed between cathode and anode planes across which a resistor chain is installed to gradually step down the voltage to ensure a uniform electric field along the drift distance. An image of the TPC while it was being constructed can be seen in Fig. 3.9. Measurement of drift electrons is done by finely segmented anode wire planes, two induction planes and one collection plane, with a 3 mm pitch and 3 mm wire plane spacing. An overview of TPC properties is given in Tab. 3.1. The TPC volume is described in a right-handed Cartesian coordinate system, with the origin defined to be located on the upstream face of the LArTPC, centered halfway up the vertical height of the active volume and horizontally centered on the innermost anode plane closest to the cathode. In this system, x ranges from 0.0 m at the innermost anode plane to +2.56

m at the cathode, y ranges from −1.15 m on the bottom of the active volume to +1.15 m at the top of the active volume, and z ranges from 0.0 m at the upstream end of the active volume to +10.4 m at the downstream end.

The Cathode

The cathode is composed of 9 individual stainless steel sheets framed by round stainless steel tubes on the edge. To ensure field uniformity, the cathode plane sheets are shimmed ensuring it is parallel to within 0.0413° to the anode plane. Maximum deviations are low with best fit +6.6 mm and −6.5 mm, with 90% of 10,000 survey points within 5 mm deviation of the best fit plane. The Cathode has been set to −70 kV for the entire data collection run-span of the experiment.

The Field Cage

The field cage encloses the TPC active volume that being the volume between the cathode plane and anode plane. The field cage structure consists of 64 rectangular loops of thin-walled stainless steel tubes around the perimeter of the active volume parallel to the cathode and anode planes. They are linked via a resistor chain step down voltage to ensure a uniform electric field. The steps have been set to 1.09 kV for a drift field of 273 V/cm. A diagram of the field cage can be seen in Fig. 3.10.

The Anode Planes

The anode section consists of three wire planes, one collection plane and two induction planes which are angled vertically, and at ±60° to the vertical, respectively. A bias voltage of −200 V, 0 V, and +440 V is applied to the U, V, and Y planes respectively to allow electrons to drift past the U and V induction planes to the Y collection plane. Ionization electrons produce bipolar waveforms on induction planes and unipolar waveforms on the collection plane. A picture of the anode section prior to installation can be seen in Fig. 3.11. An example of induction and collection plane waveforms can be seen in Fig. 3.12.

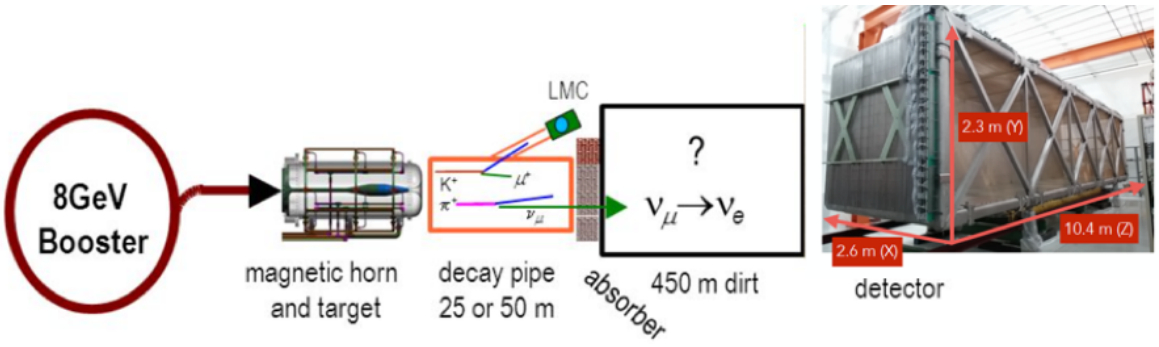

Figure 3.5: Diagram of the beam path beginning in the Booster and ending at the MicroBooNE detector.

Table 3.1: A list of construction properties of the MicroBooNE TPC [1].

Parameter	Value
Anode planes spacing	3 mm
Wire pitch	3 mm
Wire pitch	3 mm
Wire diameter	150 μm
Wire coating	2 μm Cu, 0.1 μm Ag
Design Wire tension	6.9N $\pm$ 1.0 N
Number Wires (total)	8256
Number Induction plane U wires	2400
Number Induction plane V wires	2400
Number Collection plane Y wires	3456
Wire orientation (w.r.t. vertical)	$+60, -60, 0$ (U, V, Y)

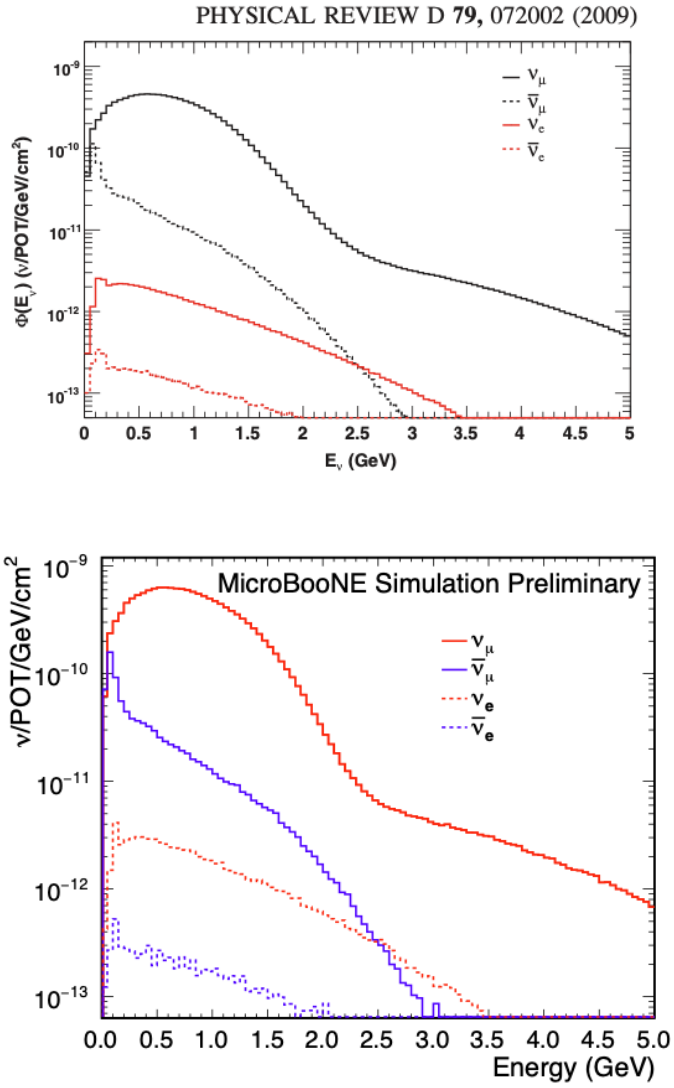

Figure 3.6: Total flux of Booster Neutrino Beam in the neutrino mode at MiniBooNE (top) and MicroBooNE (bottom). Flux is averaged through detector volume and each neutrino flavor is shown.

3.4.2 Light Collection

The light collection system consists of an array of 32 Hamamatsu cryogenic photomultiplier tubes (PMTs) and four light-guide paddles. It is located directly behind the anode planes on beam-right, facing the detector volume through the anode planes. Light collection is vital for cosmic ray rejection and event selection. Each PMT is located behind a wavelength shifting plate coated in tetraphenyl-butadiene (TPB) to shift the difficult to detect $\sim$128 nm scintillation light to wavelengths closer to the detection peak in the 350$-$450 nm region. The resulting shifted spectrum is 425$\pm$20 nm. Quantum efficiency values in the peak region are $\sim$20% [1]. The four light paddles or acrylic light guides were a test of concept, as they provide more coverage for the same number of electronics channels, cables, and feed-throughs. However, they are not currently used in data collection. The PMTs are connected via a splitter circuit, located outside of the cryostat which separates the high voltage (HV) of the PMT from its output signal. This is subsequently split into a high-gain (HG) and a low-gain (LG) channel which carry 18% and 1.8% of the total signal amplitude respectively.

All electronics here work submerged in the liquid argon within the single-walled cryostat. Signals are passed out of the cryostat via front-end electronics mounted directly on the LArTPC which amplify the signals on the wires and pass the signals to disk storage.

3.4.3 Cryogenic System

The cryogenic system consists of three major systems: argon purification, nitrogen refrigeration, and monitoring system. Minimizing contaminants such as oxygen, water and nitrogen are crucial for preventing attenuation of ionization charge signals and quenching as well as absorption of scintillation light. Two pumps allow for circulation of the Argon even while one is being serviced. Two identical filter units are each referred to as filter skids. Each consists of two subfilters, one a molecular sieve largely to remove water contamination and the other a pelletized material of copper impregnated on a high-surface-area alumina [1] to remove oxygen. The nitrogen contamination cannot be purified and is purchased with needed purity from the manufacturer. Cooling is performed via a liquid nitrogen system of

two liquid nitrogen coils which can handle a heat load of ∼9.5 kW per day. These maintain a consistent liquid argon temperature of 89.2±0.3 K.

In 2017, the O_2-equivalent contamination was measured to be 17 parts per trillion (ppt) [20] using cosmic ray muons. This corresponds to a signal loss of around 12%. This indicates excellent performance from MicroBooNE in achieving required liquid argon purity.

3.4.4 Cosmic Ray Tagger

To compensate for the cosmic backgrounds MicroBooNE encounters as a surface detector, a cosmic ray tagger (CRT) was added which began operation in December 2017 (shown in Fig. 3.14). The CRT works via scintillation light produced by cosmic rays passing through its panels which include scintillating strips and photomultipliers. It has an independent readout chain, and its output is called "CRTHits" which contain a position in 3D and a time stamp with nanosecond resolution. With this, events at the same time in the detector can be compared by extending their tracks to the intersection with the CRT [85].

3.4.5 Data Acquisition

To collect data from within the cryostat, custom low-noise electronics were developed to operate in low temperature liquid Argon and surrounding space. The electronic readout can be largely divided between TPC wires and PMTs both of which are transferred from inside the cryostat (cold electronics) to outside the cryostat (warm electronics) in the Data Acquisition (DAQ) module in the detector hall. An illustration of this can be seen in Fig 3.16.

TPC DAQ

The signals from the 8256 TPC wires are collected by a CMOS-based ASIC with 516 chips designed to read in 16 wires apiece each in a separate channel. Intermediate amplifiers ∼12 dB are necessary for the transfer over 20 m long cables to the warm readout electronics. Signals are also synchronized to a common 16 MHz by a clock fanout board. This was later reduced to 2 MHz via a Stratix III Altera FPGA optimized using the expected pulse shape provided by the convolution of the cold electronics, the expected LArTPC field responses,

and the $\mathcal{O}(1\ \mu s)$ diffusion effects which govern charge drift within the liquid argon. The ultimate readout consists of 4.8 ms of data divided into four 1.6 ms frames (1.6 ms before the trigger and 3.2 ms after). This gives the best chance to reconstruct a neutrino interaction and identify cosmic ray signals occurring near the interaction time to be filtered.

PMT DAQ

The 32 PMTs follow a similar readout scheme. Each PMT signal is split between high and low gains and split again for flexibility in processing. Three PMT modules digitize them to 64 MHz. Preamplifier/shaper boards shape the signals into unipolar 60 ns peaks. As the 64 MHz sampling rate would generate too much data in the 4.8 ms window, a series of Front End Modules (FEMs) and discriminators reduce the data, but allow for a 3.4 μs exception during BNB activity.

Readout

MicroBooNE employs two types of triggers to determine when an event should be recorded: software and hardware. The Trigger Board within the PMT readout crate sends commands to systems to take data. Triggers include a BNB trigger input (maximum rate of 15 Hz), a NuMI trigger input (1.25 Hz), a Fake Beam trigger input (configurable frequency), a PMT trigger input, and two calibration trigger inputs, provided by the laser calibration system and a cosmic ray muon tracker respectively. When the hardware trigger is fired, windows for data collection open: a 4.8 ms TPC readout stream and PMT 23.4 μs readout. The hardware trigger efficiency is 99.8%. The software trigger reduces the collection of unusable data by checking for optical activity above a threshold in photo-electrons (PE) of 6.5 PE [1]. The PMT trigger must also be fulfilled for BNB data collection. Finally there is the external (EXT) trigger that is used to collect cosmic data for background studies. The completed readout data is managed by the DAQ software and saved to disks for reconstruction and analysis.

3.5 MicroBooNE Data Collection

As noted before, MicroBooNE began collecting data in 2015. During the summer time, there is usually a beam shutdown for maintenance work where no beam data is collected as can be seen in Fig. 3.17. This has led to the division of data into run spans, seen in Tab. 3.2, which are often treated distinctly given varying detector conditions and levels of investigation into each run. The measure of quantity of data collected is denoted by protons on target (POT) referring to the number of protons impinging on the BNB target. This is further described in Sec. 7.2. The POT correlates with the number of neutrinos produced through the process described in Sec. 3.3.

Figure 3.7: An image of the MicroBooNE cryostat.

Table 3.2: POT values for each run period.

Run 1	Run 2	Run 3	Run 4	Run 5
1.7×10^{20} POT	2.7×10^{20} POT	2.6×10^{20} POT	3.2×10^{20} POT	2.2×10^{20} POT

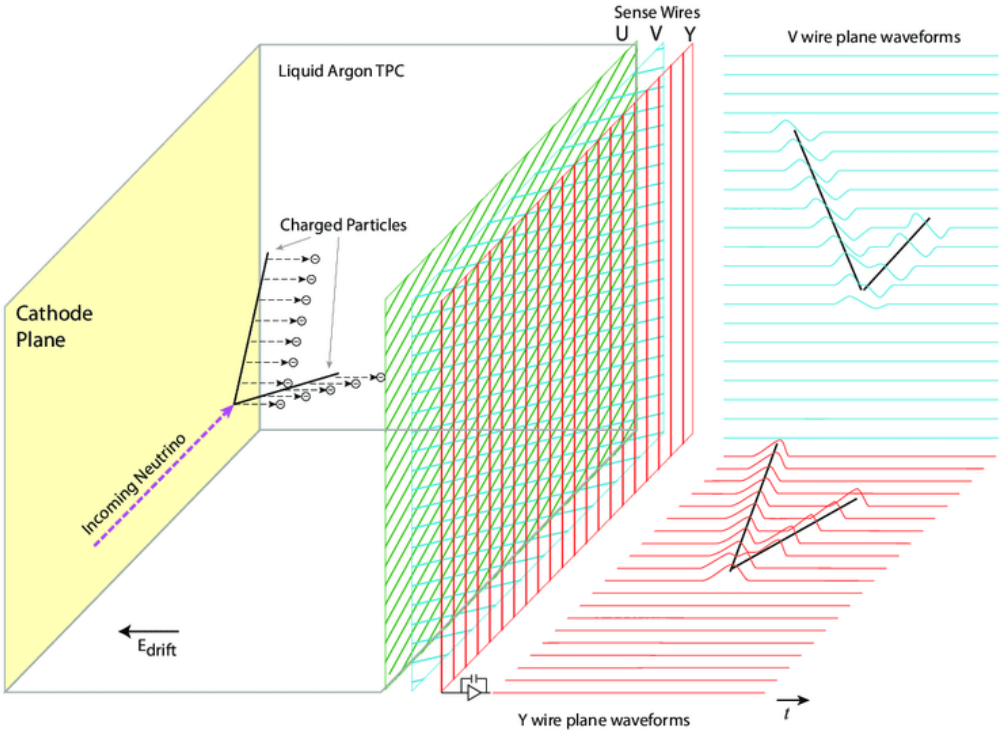

Figure 3.8: Diagram illustrating signal formation in the MicroBooNE LArTPC with three wire planes. The signal on each plane produces a 2D image of the event. For simplicity, the signal in the U induction plane is not shown.[12].

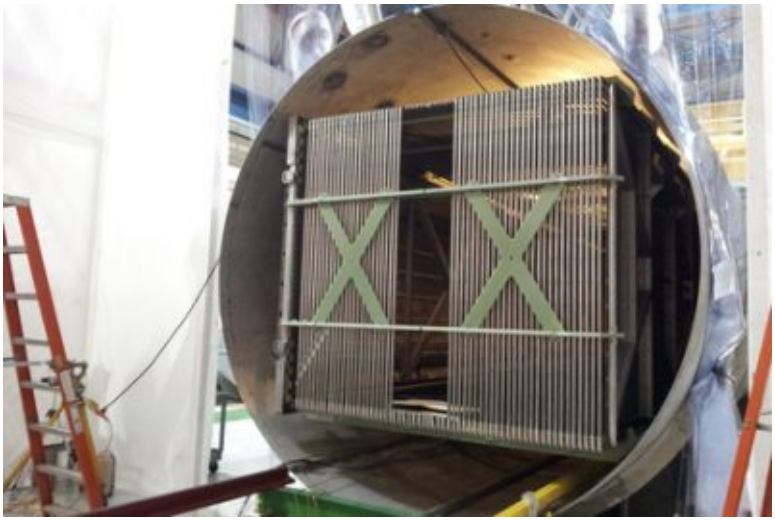

Figure 3.9: MicroBooNE TPC during construction.

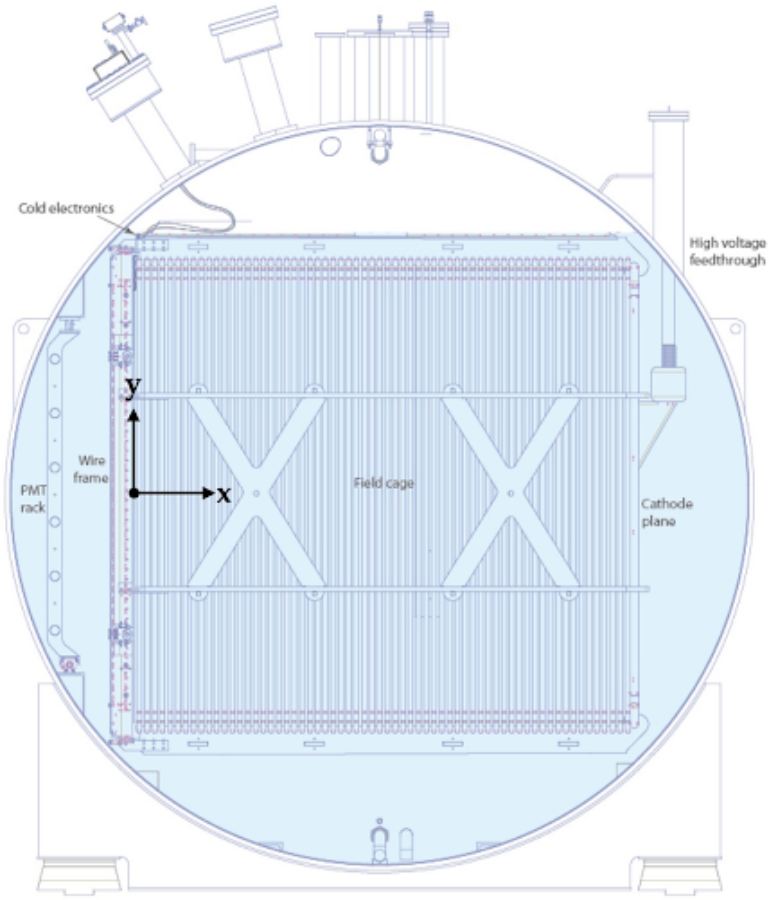

Figure 3.10: Diagram of the MicroBooNE field cage with components labelled.

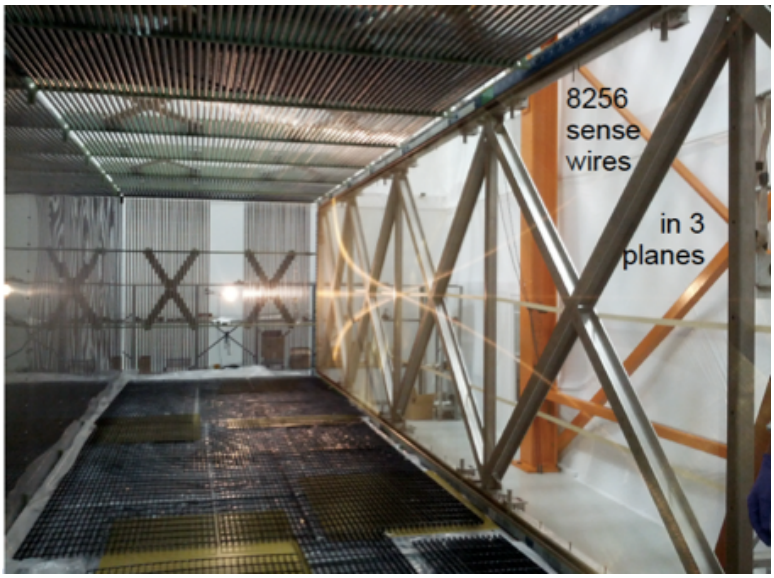

Figure 3.11: A picture of the TPC and anode wire planes prior to installation.

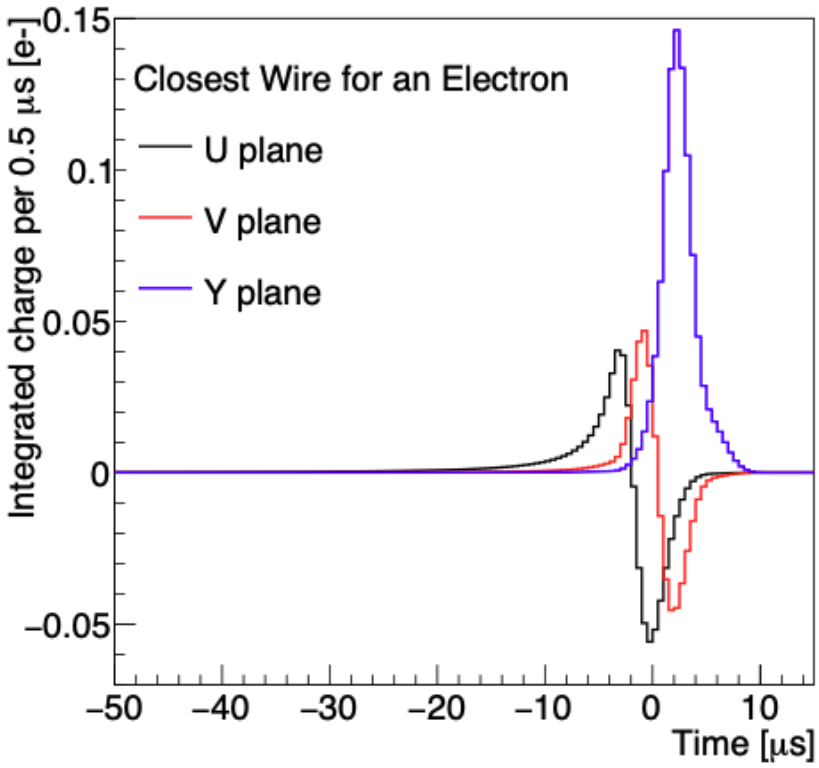

Figure 3.12: Overlaid sample wire signals from each TPC anode plane. Field responses (induced/collected-current) from various paths of a single drifting ionization electron for the three wire planes are shown. Y-axis is integrated charge over 0.5 μs [12].

(a) PMT image

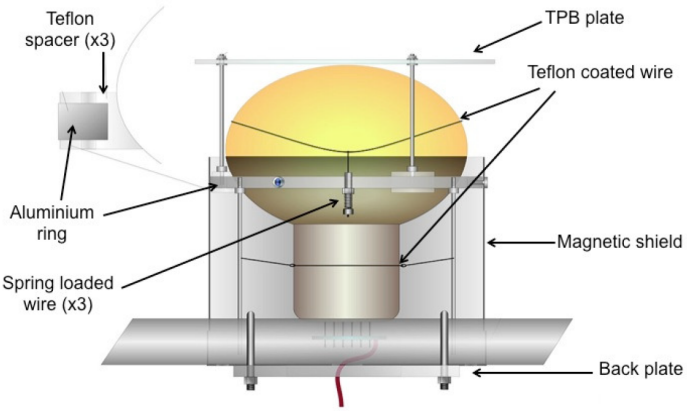

(b) PMT diagram

Figure 3.13: MicroBooNE PMT image (left) and concept (right).

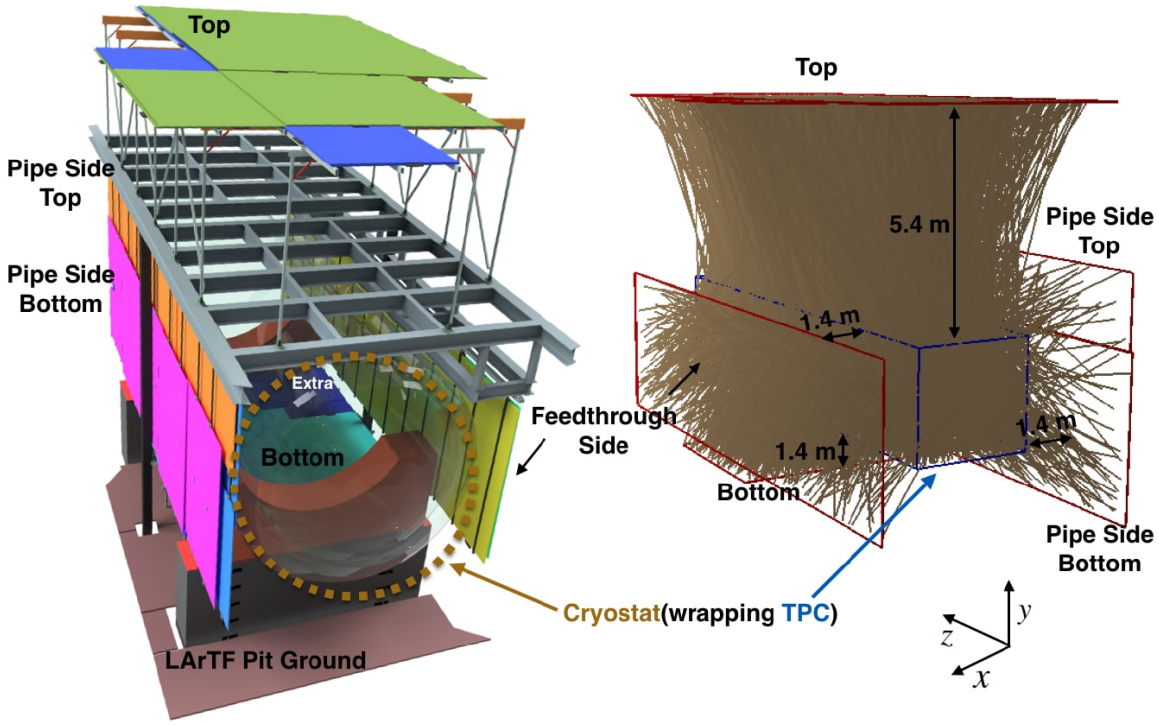

Figure 3.14: The design of CRT planes as part of the MicroBooNE detector. Simulation of cosmic rays crossing the CRT, the brown lines represent possible cosmic ray trajectories. There are four CRT planes: top plane, bottom plane, pipe side plane and feed-through side plane. In the shown coordinate system the beam direction is along the z axis [13].

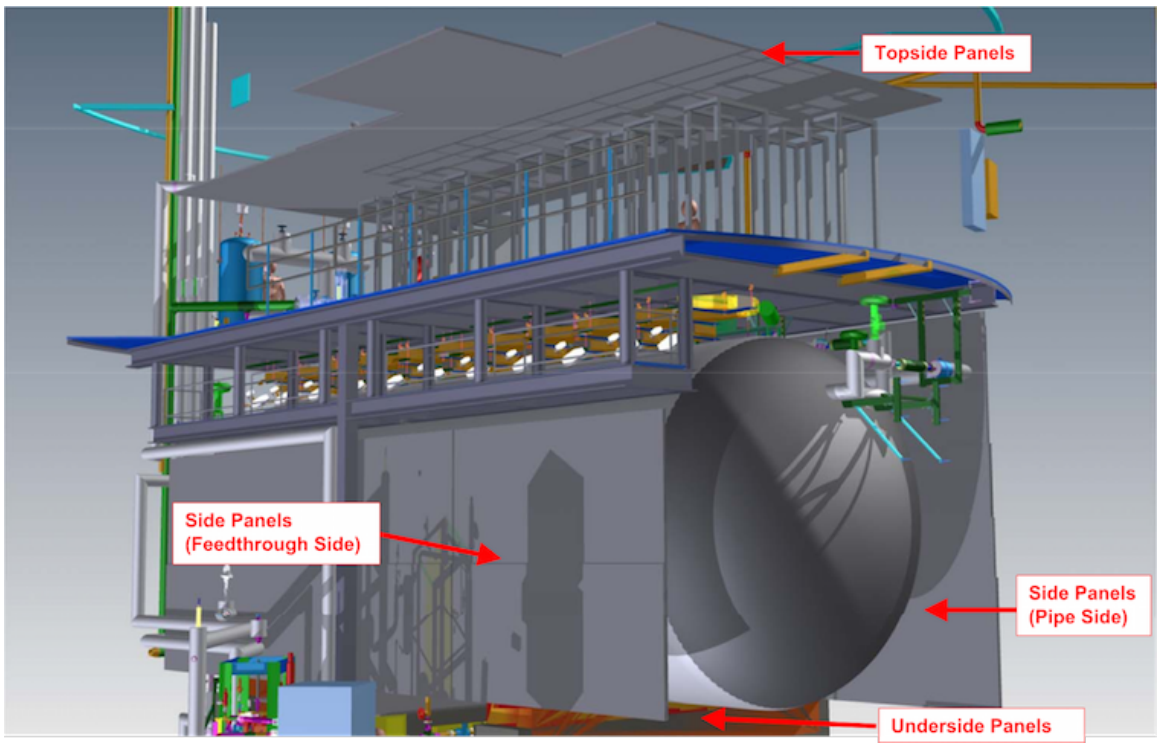

Figure 3.15: Diagram of the MicroBooNE cosmic ray tagger surrounding the cryostat.

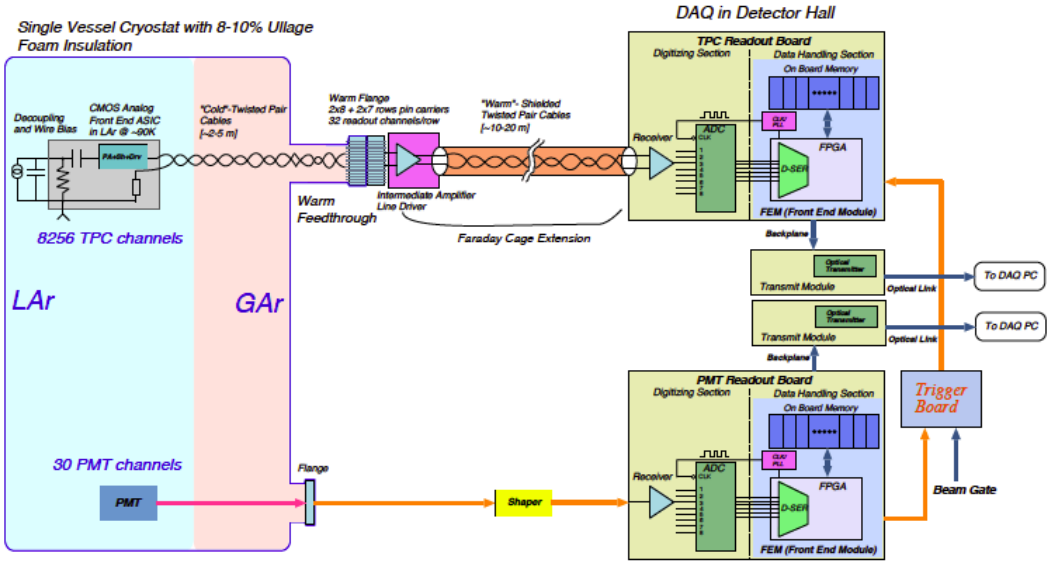

Figure 3.16: The MicroBooNE DAQ chain overview [1]. The left part of this image represents the detector, with the front end motherboards embedded in the liquid argon, while the right part of the image represents the DAQ machines in the detector hall.

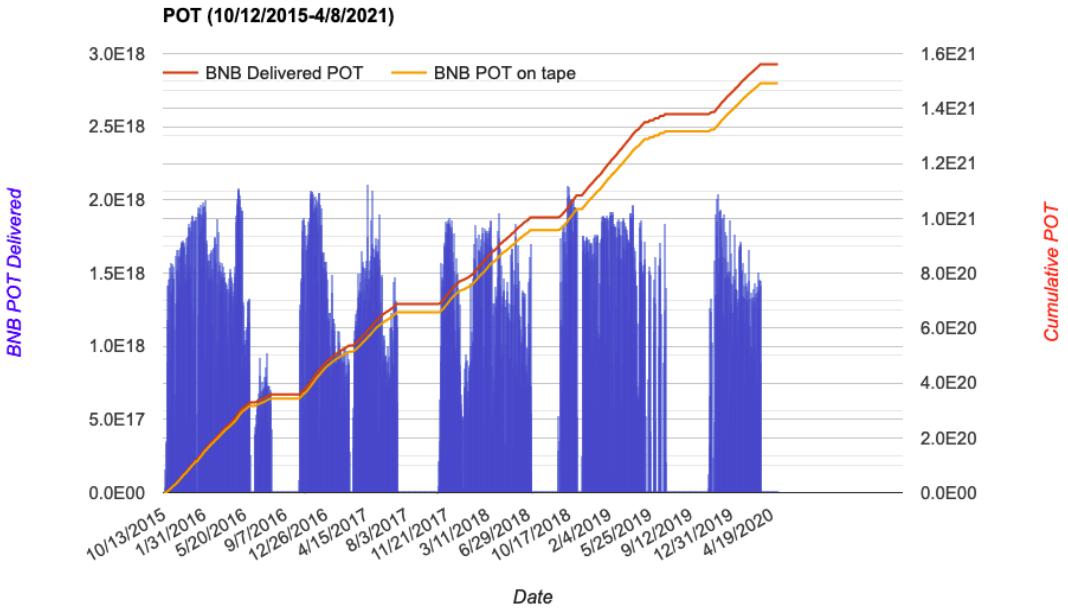

Figure 3.17: Weekly and cumulative POT received by the MicroBooNE detector.

Chapter 4

MicroBooNE Reconstruction and Simulation

This chapter describes how MicroBooNE reconstructs and simulates events. Sec. 4.1 describes MicroBooNE's simulation, and Sec. 4.2 describes the actual process of extracting signals from the detector. Then Sec. 4.3 explains the details of event reconstruction.

4.1 MicroBooNE Simulation

MicroBooNE's analysis approach is for analyses on different neutrino signals to optimize their selection procedure using simulation of events (models of what data should be collected using truth information). When simulated reconstruction reaches a threshold of capability for accuracy and completion, unboxing of actual collected data and subsequent reconstruction can be performed. In this way, MicroBooNE avoids bias towards a particular result. Thus the bulk of material in this dissertation and that MicroBooNE has presented so far is based on this simulation along with a small fraction of open data used mainly to check data-MC agreement. However, the data opening process known as unboxing has already begun as will be described in Ch. 9, and the same reconstruction techniques described here should be applicable to data. The MicroBooNE simulation is based on the Liquid Argon Software (LArSoft) [86] framework which itself utilizes the *art* event processing framework [87]. This framework allows for storing and accessing of event information for simulation and

analysis and is shared between multiple LArTPC experiments. An overview of the simulation algorithm used can be seen in Fig. 4.1. At the particle generation stage, interactions within the detector are created. In the particle tracking stage, generated particles are propagated through the detector. The detector simulation stage applies detector specific effects. After this, the generated events go through an equivalent process for data reconstruction. Pre-reconstruction includes processes like deconvolution and hit-finding as will be discussed in Sec. 4.2. Following this is the Pandora-based reconstruction [18] which will be discussed in Sec. 4.3. Finally, the data is prepared into analysis files to be delivered to analyzers.

4.1.1 Neutrino Flux Simulation

As mentioned in Sec. 3.3.2, the simulation of the Booster Neutrino Beam flux has been ported and updated from that used in MiniBooNE. The target proton interaction is simulated via a Geant4-based Monte-Carlo using version v4_10_6_p01 [81] simulating both primary interactions and subsequent decays. An important update was the shift to using the fit from the HARP [83, 82] experiment for pion production. The HARP [83, 82] experiment was an effort for precision measurement of hadrons on various targets. The double differential cross section for $\pi^{\pm}$ and K^0 production were fit to the Sanford-Wang parameterization [88]

$$\frac{d^2\sigma}{dp\ d\Omega} = c_1 \cdot p^{c_2}(1 - \frac{p}{p_{beam} - c_9})exp[-c_3\frac{p^{c_4}}{p_{beam}^{c_5}} - c_6\ \theta(p - c_7\ p_{beam}(cos\theta)^{c_8})] \tag{4.1}$$

where the proton beam momentum is p_{beam} and θ is the angle between the proton and meson. The parameters $c_1, ..., c_9$ are set via fitting. My own efforts for a Sanford-Wang fit on proton data will be described in detail in Ch. 8.

4.1.2 Cosmic Generation

As a surface-based detector, MicroBooNE has significant cosmogenic backgrounds, therefore it requires a generator for cosmic ray events. This is performed by the Cosmic Ray Simulations for Kascade (CORSIKA) [89] package using the Constant Mass Configuration. Interactions of p, He, N, Mg, and Fe are simulated in atmosphere. The FLUKA [90] package was selected for hadronic interactions below 80 GeV. FLUKA uses hadron-nucleon interaction

models based on resonance production in the few-GeV region combined with the Dual-Parton model[91].

4.1.3 Neutrino Interactions

The output of neutrinos by the beam Monte Carlo are passed into the GENIE neutrino generator [92]. GENIE version 3_00_06 is the latest version used by MicroBooNE, but some earlier versions are still relevant to the single photon analysis. A MicroBooNE tune has been developed and is in use to more properly capture the properties of the detector. A Nieves/Valencia [44] relativistic Fermi gas model (RFG) models the nuclear environment. Here, the nucleus is treated as a set of non-interacting fermions. It does not include effects of nucleon-nucleon correlations, but it does include nuclear medium correlations due to Random Phase Approximation (RPA) and Coulomb effects.

The charged current (CC) quasi-elastic (QE) cross section model also comes from Nieves [44], but is tuned to T2K [21] data. GENIE includes two meson exchange current (MEC) models, empirical and Valencia [44]. MicroBooNE elected the Valencia model which, together with the Nieves QE model, creates a coherent picture that agrees with MiniBooNE QE data. The Valencia model is also tuned to T2K for usage in MicroBooNE.

The Berger-Sehgal [93] model, an update to the Rein-Sehgal [46] model, is selected to model resonant events. This update added the effects of lepton mass and uses axial form factors from MiniBooNE fits.

Non-resonant interactions are modeled by the Bodek-Yang [45] model, but this model is intended for combined resonant and non-resonant interactions. Therefore it must be reduced in magnitude so that the sum of the resonant model (Berger-Sehgal) and Bodek-Yang add to the combined resonant and non-resonant models. This is an imperfect solution, but no other model is available. To mitigate the effect, the resonant model is used solely below W_{cut}=1.9 GeV above which the combined model, described above, is used. Fitting of these events has been done to deuterium data, but a high uncertainty is still assigned.

The coherent pion production also uses the Berger-Sehgal model, and deep inelastic scattering (DIS) also uses a Bodek-Yang model.

Neutral current (NC) interactions are poorly constrained by data. Most data is from deuterium targets in bubble chambers. Therefore NC simulation is inferred theoretically from CC models. This is the case for the above listed model for resonant events (RES) (Berger-Sehgal) and non-resonant events (Bodek-Yang combined). The DIS model applies equally well to both NC and CC. Fits have been done for these interactions in MiniBooNE for π^0 production.

The final state interaction (FSI) uses a model called *hA2018*. This model is a data-driven empirical model produced by GENIE collaborators. Total cross section components including absorption, charge exchange, inelastic, and pion absorption are taken from pion-nucleus data [94].

4.2 MicroBooNE Signal Processing

4.2.1 Time Projection Chamber Signals

As mentioned before, ionization signals are made up via ionization electrons produced by charged particles passing through the liquid argon. These ionization electrons should drift to the anode for collection, due to the constant electric field, but there are some complicating factors. Electron recombination occurs at the point of ionization where liberated electrons quickly recombine with argon ions. The size of this effect is inverse to the electric field strength as a higher strength will limit the time available for ions and electrons to recombine. Diffusion is another complicating factor, in this case referring to the modification of the shape of the cloud of ionization electrons. It is divided between longitudinal and transverse diffusion, where longitudinal is the impact on the timing resolution in the drift direction and transverse corresponds to the position resolution perpendicular to the field. Note while longitudinal diffusion does scale with the electric field strength, in our region, this scaling is minimal [14]. In 2021, MicroBooNE submitted a measurement of its longitudinal diffusion rate to the Journal of Instrumentation (JINST) stating a diffusion rate of $D_L = 3.74^{+0.28}_{-0.29}$ cm^2/s at an electric field of 273.9 V/cm [14]. Transverse diffusion is more difficult to account for, but is included in systematic uncertainties.

Figure 4.1: Overview of the MicroBooNE simulation algorithm.

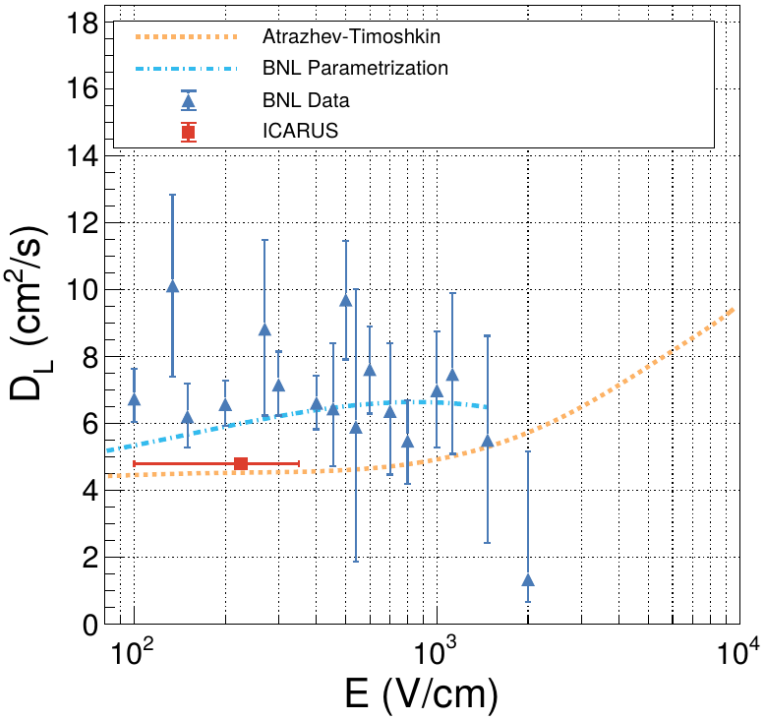

Figure 4.2: Summary of world data for longitudinal electron diffusion in liquid argon [14]. The orange dashed curve and blue dot-dashed curve shows theoretical predictions from Atrazhev-Timonshkin [15] and a parameterization from Li et al [16]. The red and dark blue points show the ICARUS [17] and Li et al. [16] measurements, respectively. Note that the ICARUS error bars (± 0.2 cm^2/s) are covered by the data point.

Optical signals are picked up via the photo-multiplier tube (PMT) array. As a bright scintillator, liquid argon will produce $\mathcal{O}(10,000)$ photons per MeV of deposited energy with peak wavelength at 128 nm. As noted in Sec. 3.4, to be sensitive to these wavelengths, a wavelength-shifting plate is used to shift the wavelength to peak at 425 nm. Quantum efficiency values in the peak region are ∼20% [1]. There are two processes for luminescence via the production of dimers. The first is self-trapping where an argon atom becomes excited by an ionizing particle and combines with a neutral argon atom. The second is recombination luminescence when an argon ion becomes excited, ionizes then combines with another argon ion to produce a charged argon dimer. After this, ionization electron thermalizes and recombines with the charged argon dimer to produce an excited argon dimer. Both processes are shown in Fig. 4.3. The photons are divided into a fast component released within 6 ns resulting from singlet states and a slow component around 1500 ns from triplet states at a later time. Some light is also produced via Cherenkov radiation. Nitrogen contamination makes liquid argon more opaque to its own light reducing the light yield.

4.2.2 Signal Extraction

The true signal of events within the detector can be modeled as a combination of $M(\omega)$ the measured signal, $R(\omega)$ the detector response, and $F(\omega)$ the Gaussian noise filter. These factors can be combined for 1D deconvolution in time

$$S(\omega) = \frac{M(\omega)}{R(\omega)}\dot{F}(\omega) \tag{4.2}$$

Functions are determined by sending known signals on the wires. However 1D convolution does not account for interactions between multiple wires. Therefore a two dimensional deconvolution is needed to account for the signal induced from the neighboring wires. Here the measured signal is defined by

$$M_i(t_0) = \int_{-\infty}^{\infty} (... + R_1(t_0 - t) \cdot S_{i-1}(t) + R_0(t_0 - t) \cdot S_i(t) + R_1(t_0 - t) \cdot S_{i+1} + ...) \cdot dt \tag{4.3}$$

where S_i is accounted for with neighboring wires S_{i-1} and S_{i+1}. R_0 and R_1 are average full response functions for ionization charge passing through the primary and secondary wires respectively. The two dimensional deconvolution in time and wire space is demonstrated in Fig. 4.4. The result is a Gaussian shaped signal waveform where the signal peak will not exceed a predefined value [12]. An image of an event on each wire plane can be seen in Fig. 4.5.

Hit finding follows deconvolution and is a relatively simple process of fitting a Gaussian function to peaks in the waveform. The time of the interaction and the charge deposited (determined by pulse area) are combined with wire plane and wire number to define a hit. These hits are then passed into reconstruction algorithms.

4.3 Reconstruction

For reconstruction, the signals on the anode wire planes provide 2 dimensions and signals on the PMT provide the third drift dimension. There is, as yet, no standard solution for automatic reconstruction in LArTPCs, so MicroBooNE investigates several methods of reconstruction. Pandora [95] and TrajCLuster [96] are each pattern recognition algorithms which cluster hits in each plane and match these clusters in three dimensions to identify particle trajectories. The WireCell [97] paradigm works more directly to cluster 3D using charge and sparsity information. Finally, there is an analysis effort to use deep learning [98] techniques to identify events via images. For the purposes of this thesis and MicroBooNE's immediate results, Pandora is the primary method used for reconstruction.

4.3.1 Pandora

The Pandora multi-algorithm pattern recognition framework uses reconstructed hits as input and produces Particle Flow Objects (PFOs) containing Particle Flow Particles (PFPs). Particle flow means each reconstructed object is related to other reconstructed objects so a PFP can be a parent or child to another PFP where parentage implies being closer to the initial neutrino vertex. In effect, parent particles lead to child particles as seen in Figs. 4.6 and 4.7.

The Pandora reconstruction consists of two algorithms which are passed over data sequentially as shown in Fig. 4.8. The first algorithm referred to as *PandoraCosmic*, is tuned to target cosmic rays which are more track oriented and downward going. It also targets their daughter delta rays which are reconstructed as showers.

The second pass referred to as *PandoraNu* is tuned to reconstruct signal neutrinos from the BNB. The candidate neutrino vertex is identified first, and subsequent interactions are reconstructed with that as the basis. Each of these passes includes two similarly formatted stages. The first stage is two-dimensional reconstruction. Hits are clustered onto each plane accepting only unambiguous straight lines of particles. For these clusters, purity (the ratio of true signals to total signals) is prioritized over completeness (the ratio of selected true signals to total true signals). To perform this, every time there is a significant change in direction or other ambiguity, a new cluster is created. Then a series of clustering algorithms are applied to merge disparate clusters to increase completeness using factors such as if the clusters are oriented towards each other or are in close proximity. The next stage is three-dimensional track reconstruction, where the clusters determined by two-dimensional reconstruction are matched across the three anode planes. The first matching variable is time which is common between the three planes. An algorithm then sorts through the matches identifying and modifying ambiguities i.e. single clusters on one plane matched to two on another. The final result is reconstructed tracks and showers.

4.3.2 Optical Reconstruction

Optical reconstruction has the same concept as wire reconstruction which is to take raw waveforms and output reconstructed objects, in this case *optical flashes* containing light information. PMTs in MicroBooNE are split between high and low gain channels: this way if the high gain channel is saturated by a particularly intense event, the low gain can be used with a gain correction factor. Otherwise, the high gain is used solely. To reconstruct optical signals, first a baseline must be established to set what level of light intensity is qualified as a hit. For the cosmic discriminator, this is established via the ADC (analog to digital converter value) of the first sample. For the beam discriminator, a rolling mean in a sliding window, and extrapolation is performed to find the baseline in the signal region. After this,

a hit peak width and area of pulse can be determined and stored. These optical hits are then grouped into an optical flash after which there is a dead time of 8 μs where no more flashes can be reconstructed.

4.3.3 Calorimetry

For defining the energy of an event, the principle factor is that the electrons liberated is proportional to the energy deposited. To reconstruct a shower, one must then combine energy of different hits collected on the wire planes. A calibration constant, as defined in Sec. 4.3.5, is needed to convert the hit integral to a total charge $Q(e^-)$ accurately. The following formulation is used to reconstruct energy,

$$E = \frac{W_f}{R_C} \times Q, \tag{4.4}$$

where W_f is the ionization work function of argon describing how many drift electrons are produced (set to 23.6×10^{-6} MeV/e$^-$), and R_C is the recombination factor also described in Sec. 4.3.5. However, there are factors that modify these theoretical values that must be accounted for as part of calorimetric reconstruction and calibration.

As a surface detector, MicroBooNE is exposed to cosmic rays which continuously interact to ionize the argon within the detector. Electrons and ions can become separated and drift to the cathode or anode respectively. This results in a build-up of Ar^+ ions near the cathode, creating a position dependant change in the electric field. This is known as the space charge effect which manifests itself by bending and/or rotating previously straight tracks. To recover true interaction topologies, it is necessary to measure observed signals as a function of drift position. For this, a calibration map must be constructed and in MicroBooNE, this is accomplished via high intense laser tracks from an external calibration system. The results of this are demonstrated in Fig. 4.9.

There are also regions in the anode wire planes where no useful information may be extracted from channels due to mechanical faults. Some regions are functional with only 2 readout planes reducing the non-reconstructable region to about 3%. This is illustrated in Fig. 4.10.

Another effect which must be accounted for is the electron drift-lifetime. This refers to the contaminants (primarily H_2O and O_2) which can capture drifting ionization electrons shortening their effective lifetime in the detector. This can be seen in Fig. 4.11. MicroBooNE has demonstrated excellent argon purity resulting in negligible contaminants during stable running. In addition, electron drift-lifetime corrections have been made as part of calibration to correct for any residual losses due to the presence of argon contaminants. The methods for calibrating these effects will be discussed in more detail in Sec. 4.3.5.

4.3.4 Particle Identification

Crucial to MicroBooNE's physics goal of analysing the MiniBooNE LEE is proper identification of particles most notably distinguishing photons and electrons. Muons, pions, and protons traversing the detector will be reconstructed as tracks, as each produces a narrow streak of energy deposition per unit length (dE/dx). Average values can be estimated via the Bethe-Bloch equation

$$-\frac{\mathrm{d}E}{\mathrm{d}x} = \rho K \frac{Z}{A}\frac{z^2}{\beta^2}\left[1/2\ln\left(\frac{2m_e c^2\beta^2\gamma^2 W_{max}}{I^2}\right) - \beta^2 - \frac{\delta(B\gamma)}{2}\right] \tag{4.5}$$

where ρ is the density of material (g/cm^3), z is the charge number of the incident particle, Z and A are the atomic number and atomic mass of the material (in g.mol^{-1}), m_e is the electron mass, I is the mean excitation energy (in eV), and β and γ are the relativistic kinematic variables. $K = 4\pi N_A r_e^2 m_e c^2$ with N_A the Avogadro's number (6.022×10^{23} mol^{-1}) and r_e the classical electron radius (2.818 fm). $\delta(\beta\gamma)$ is the density effect correction, and W_{max} is the maximum energy transfer in a single collision defined by

$$W_{max} = \frac{2m_e\beta^2\gamma^2}{1 + (2\gamma m_e)/M + (m_e/M)^2}; \tag{4.6}$$

where M is the mass of the incident particle. This formulation is valid within a few percent of uncertainty in application to a LArTPC. This formula produces an effective minimum for each particle at which point particles of that energy are referred to as minimum-ionizing

particles (MIPs). With this formula, a Bragg peak is formed for various particles as seen in Fig. 4.12.

Reconstructed proton track energy is extracted using the track length and the stopping power of protons in Argon. The NIST Standard Reference Database 124 (named PSTAR) was used to translate the measured track length to initial kinetic energy. The track mean dE/dx is reconstructed via Pandora. Protons deposit energy over a shorter distance (with a higher dE/dx), whereas muons and pions have longer tracks, therefore protons can be separated via this signature. Electrons propagating through the detector also obey Bethe-Bloch equation but lose energy primarily through photon emission (Bremsstrahlung) leading to electromagnetic showers with the resulting photons cascading into more interactions. Photons of sufficient energy can pair convert into an electron and positron producing similar showers of energy. Once again, dE/dx is a powerful discriminator as electron showers cluster around their MIP energy ($\sim$2 MeV) and photons producing two MIP particles will cluster near double this energy ($\sim$4 MeV). This is illustrated in Fig 4.13.

Another identification factor is the structure of the hits. This can be represented visually with event displays. A NC π^0 event containing photon showers is shown in Fig. 4.14a and an event containing an electron shower is shown in Fig. 4.14b. In event displays, energy is represented by coloration. Photon showers should typically have separation between the vertex and the start of the shower. This is because photons will propagate invisibly (ionizing no electrons) before undergoing pair production. Conversely, the electron shower should begin immediately at the vertex with the interacting particle.

4.3.5 Calibration

Calibration is needed to normalise the calorimetric response across the detector and reconstruct the energy deposition per unit length (dE/dx) read out from the detector. Calibration is divided between dQ/dx which makes the detector response uniform across the detector volume and dE/dx which sets the absolute energy scale of the detector. As discussed in Sec. 4.3.3, many effects introduce non uniformity in the charge density of the detector i.e. shorted regions, channel-to-channel gain variations, electron attenuation and diffusion. To calibrate dQ/dx for these effects, MicroBooNE maps the charge deposition of

cosmogenic muons in three dimensional volumes within the detector to make a correction map. Following this energy deposition, (dE/dx) calibration is done by the formula,

$$\frac{dE}{dx}^{calib.} = \frac{exp(\frac{dQ^{calib}/dx}{C}\frac{\beta_p W_{ion}}{p\epsilon} - \alpha)}{\frac{\beta_p}{\epsilon}} \tag{4.7}$$

where,

- W_{ion} is the work function of Argon (23.6 MeV/electron)
- ϵ is the electric field (0.273 kV/cm)
- ρ is the density of LAr (1.38 g/cm^3)
- α and β are the recombination constants measured by the ArgoNeut experiment at 0.481 kV/cm (α=-0.93 $\pm$ 0.002 kV/cm, β=-0.93 $\pm$ 0.02 kV/cm)
- C is the calibration constant used to convert ADC to number of electrons

The calibration constant is measured by constructing multiple dE/dx distributions built as a function of residual range (the distance from the current point to the end of the track) and are fit with a Landau-convoluted Gaussian distribution in order to extract the most probable value. An example of this methodology can be seen in Fig. 4.15.

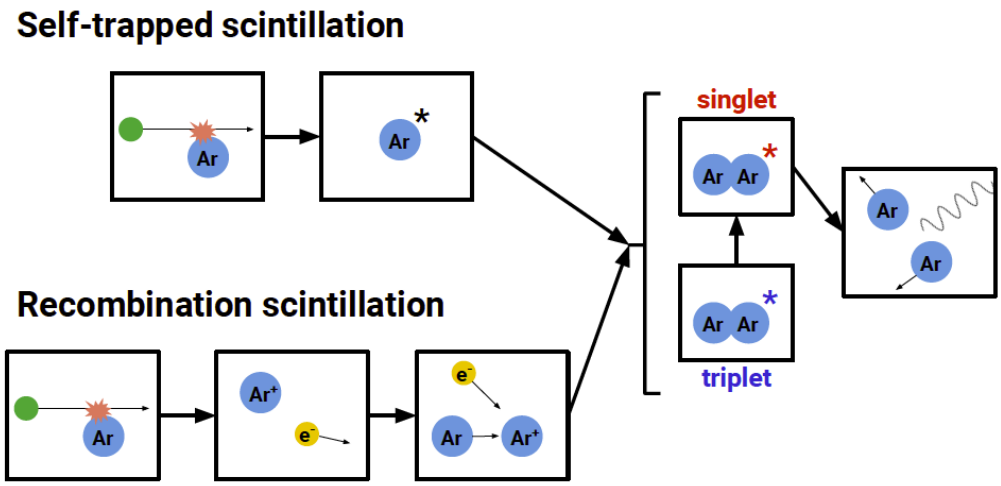

Figure 4.3: Scintillation processes in Liquid Argon. Both the self-trapped and recombination methods can produce either a singlet or triplet excited dimer state, which give rise to the fast and slow components of the scintillation light, respectively.

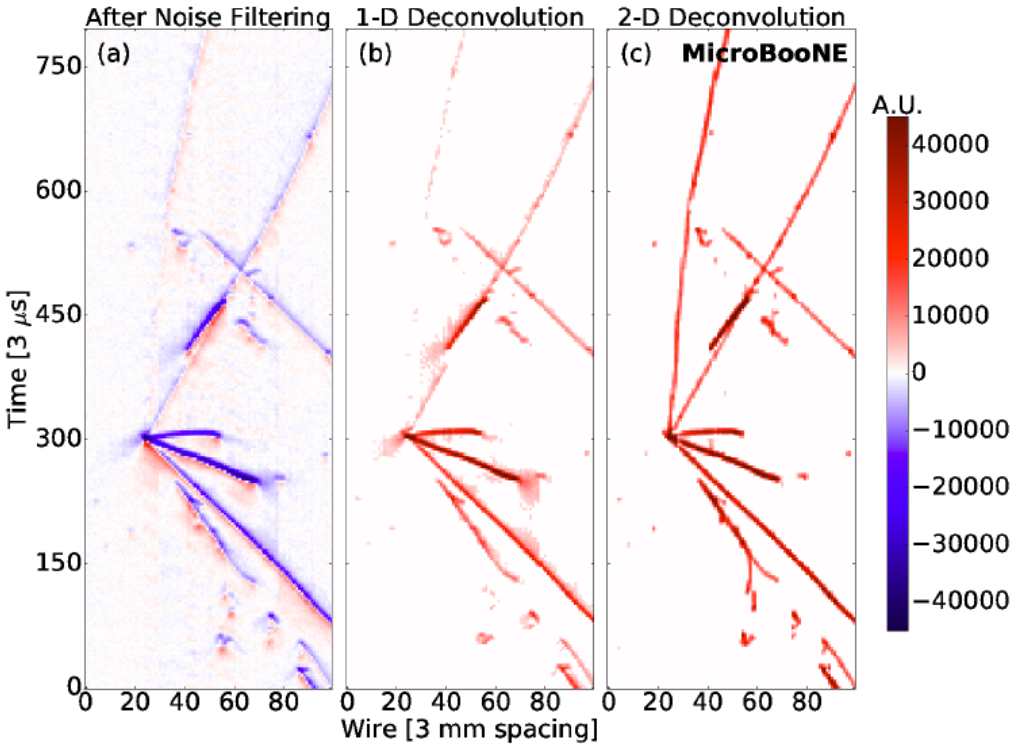

Figure 4.4: A neutrino candidate event from MicroBooNE data measured on the U plane. (a) The noise filtered raw waveform in units of average baseline and ADC scaled by 250 per 3 μs. (b) The charge spectrum given in units of electrons per 3 μs after signal processing with 1D deconvolution. (c) The charge spectrum in units of electrons per 3 μs following signal processing with 2D deconvolution [12].

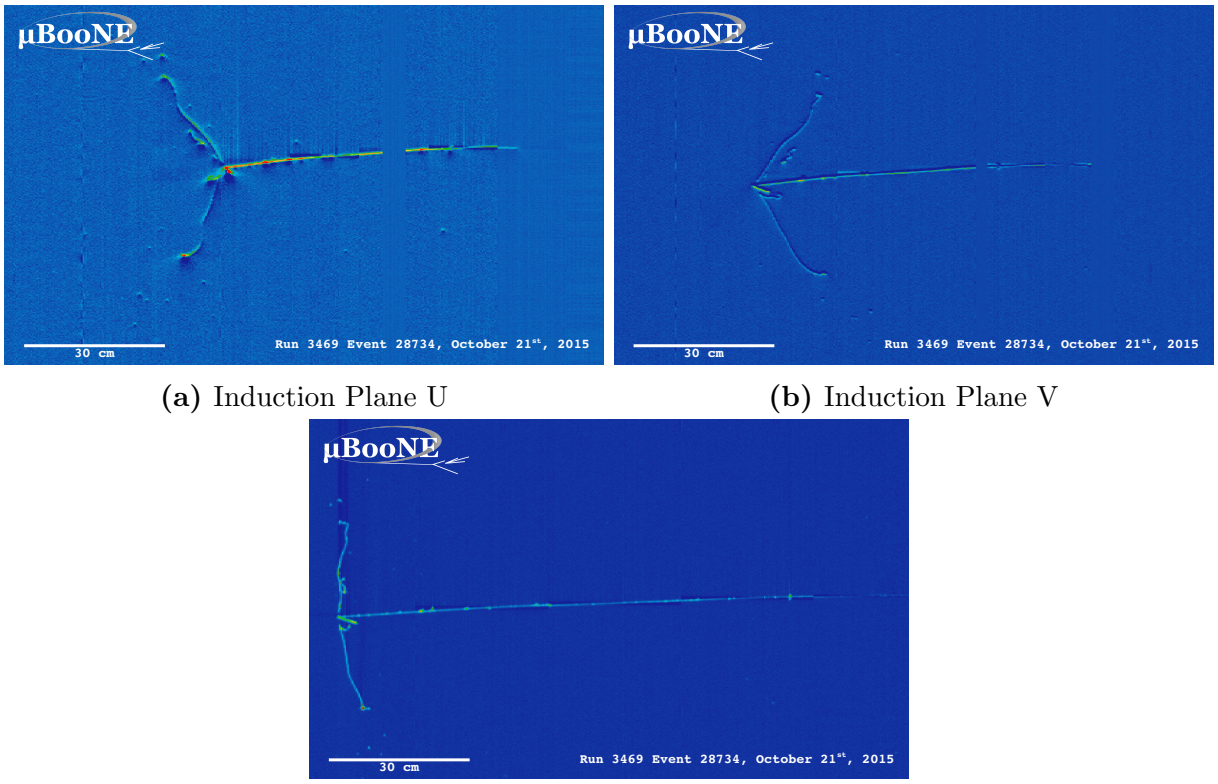

(a) Induction Plane U

(b) Induction Plane V

(c) Collection Plane Y

Figure 4.5: A neutrino interaction candidate event is displayed in all three planes of the MicroBooNE anode. It appears to be CC π^0 event as two photon showers and a muon track can be identified, with a potential smaller proton track.

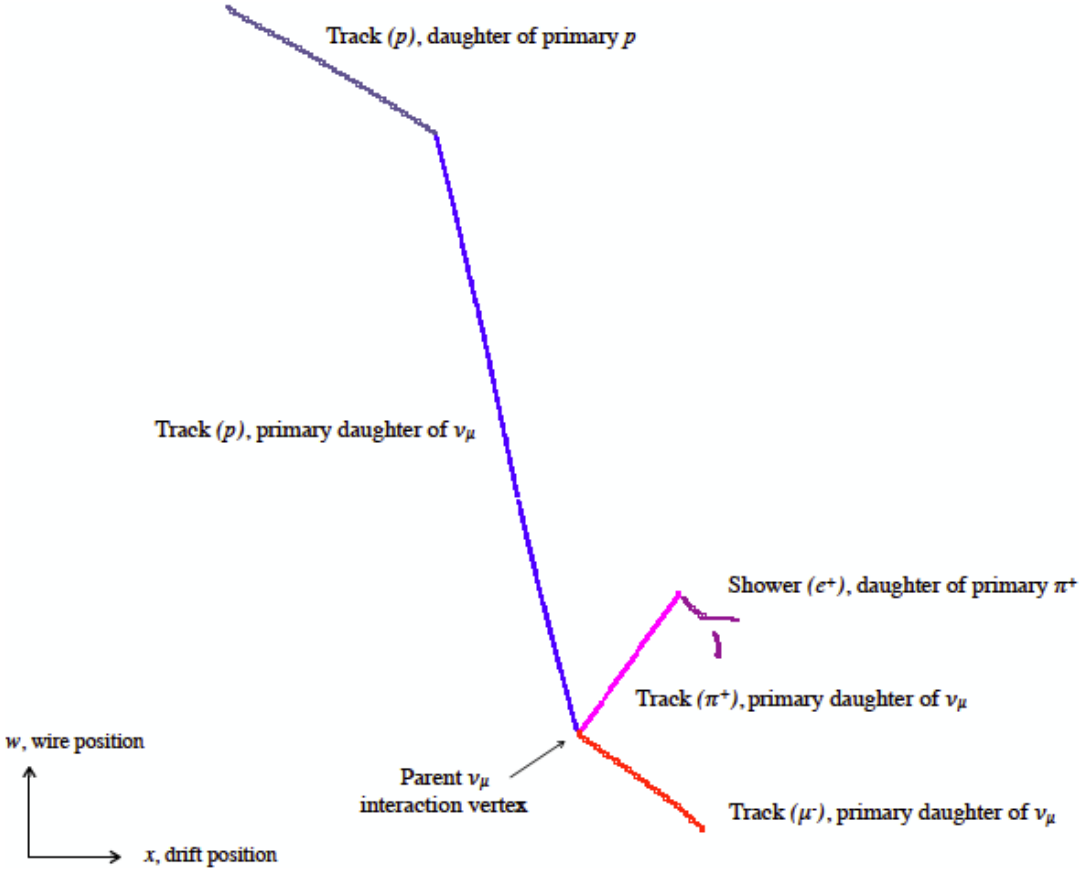

Figure 4.6: An illustration of the hierarchy of particles reconstructed for a simulated charged-current ν_μ event in MicroBooNE is shown. The visible final state includes a muon, proton and charged pion shown in separate colours. In this interaction, the neutrino particle has a reconstructed interaction vertex and three track-like primary daughter particles. The produced charged-pion decays into a μ^+, which further decays into a e^+ and is reconstructed as a shower-like secondary daughter particle. The proton later scatters off a nucleus, giving a track-like secondary daughter particle. Pandora identifies each particle as track-like or shower-like and then explicit particle types are identified using information from the simulation [18].

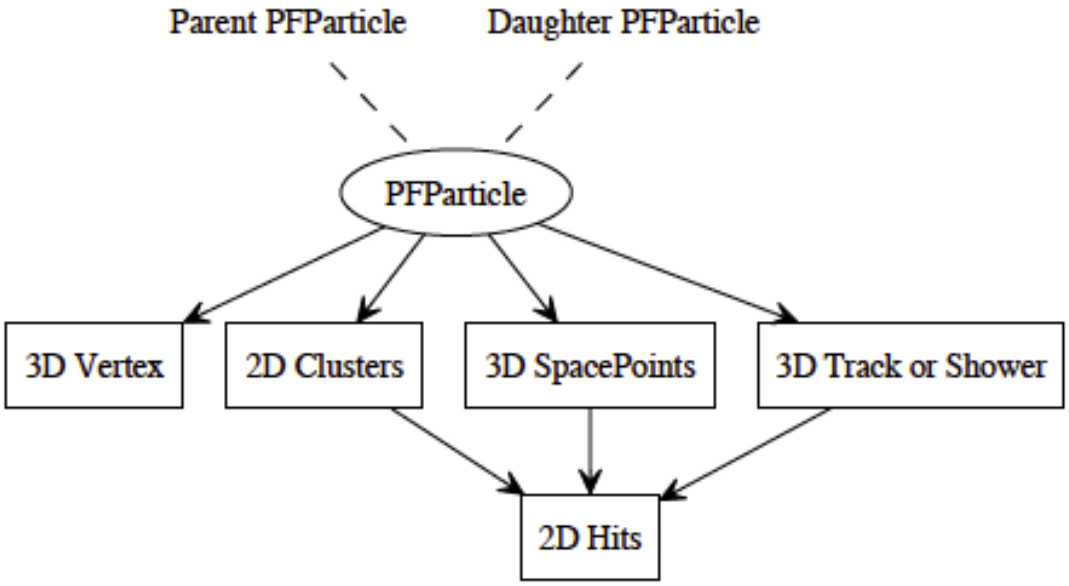

Figure 4.7: Here is shown, the Pandora output data products, as utilized in the LArSoft Event Data Model. Navigation between PFParticle hierarchies is performed by using the PFParticle interface, here represented by dashed lines. The solid lines refer to navigation from PFParticles to their associated object. [18].

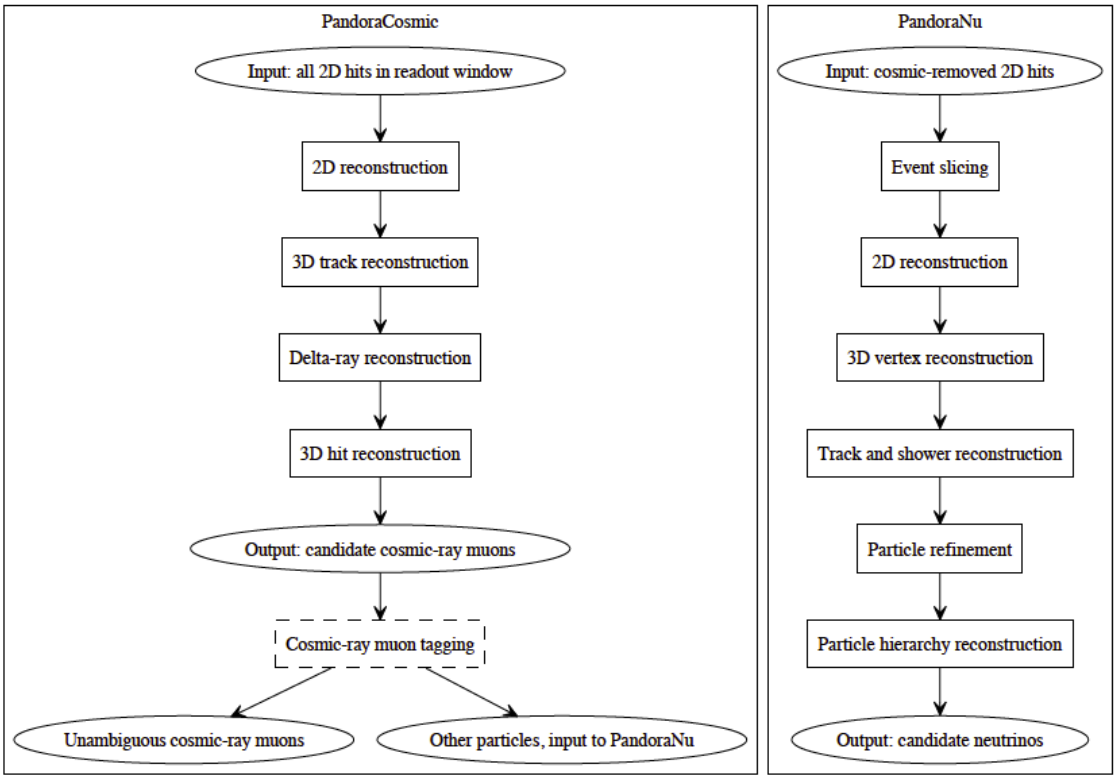

Figure 4.8: Here is shown a simple representation of the two multi-algorithm reconstruction paths used by MicroBooNE. Particles formed by the PandoraCosmic reconstruction are examined by a cosmic-ray tagging module, external to Pandora. Then, the hits associated with unambiguous cosmic-ray muons are flagged. With these hits omitted, a cosmic-removed hit collection provides the input to the PandoraNu reconstruction [18].

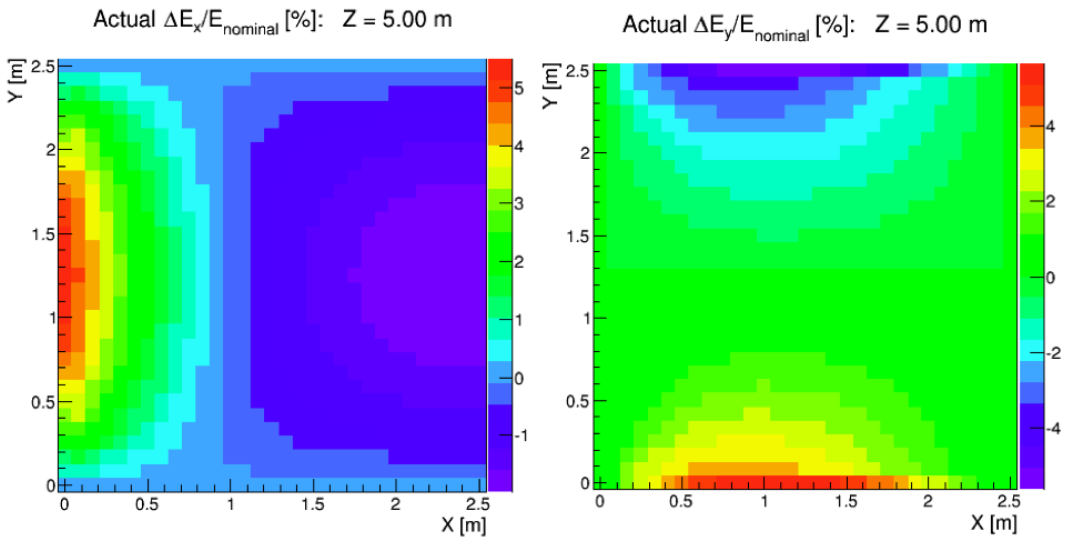

Figure 4.9: The space charge effect. Shown are plots of deviation from the nominal (constant) electric field in the X and Y plane of the detector volume. The left shows the deviation of the field in the X (drift) direction and the right shows the deviation in the Y direction [19].

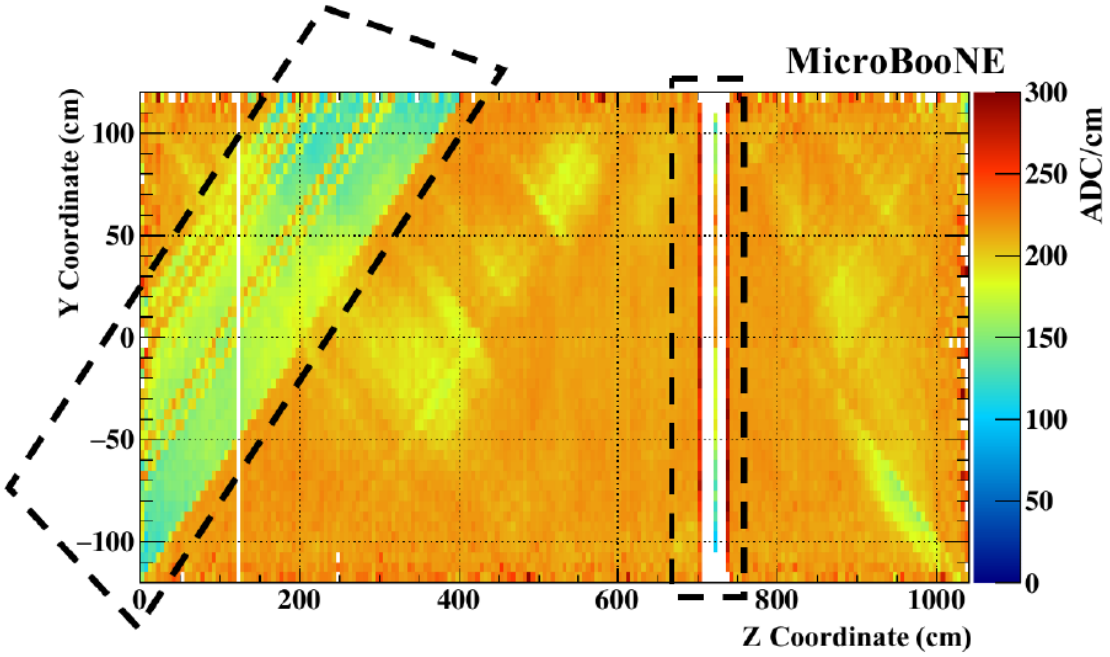

Figure 4.10: Distribution of dQ/dx in the collection plane as a function of Y and Z coordinates. The diagonal region in the dotted lines includes U plane channels which are shorted to one or more V plane channels. The vertical region in the other dotted line includes Y plane wires shorted to one or more V plane channels.

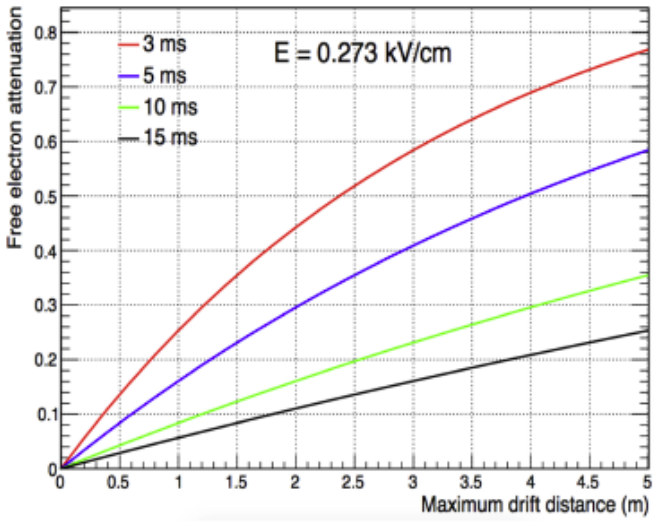

Figure 4.11: Free charge absorption as a function of drift distance and electron drift-lifetime [20].

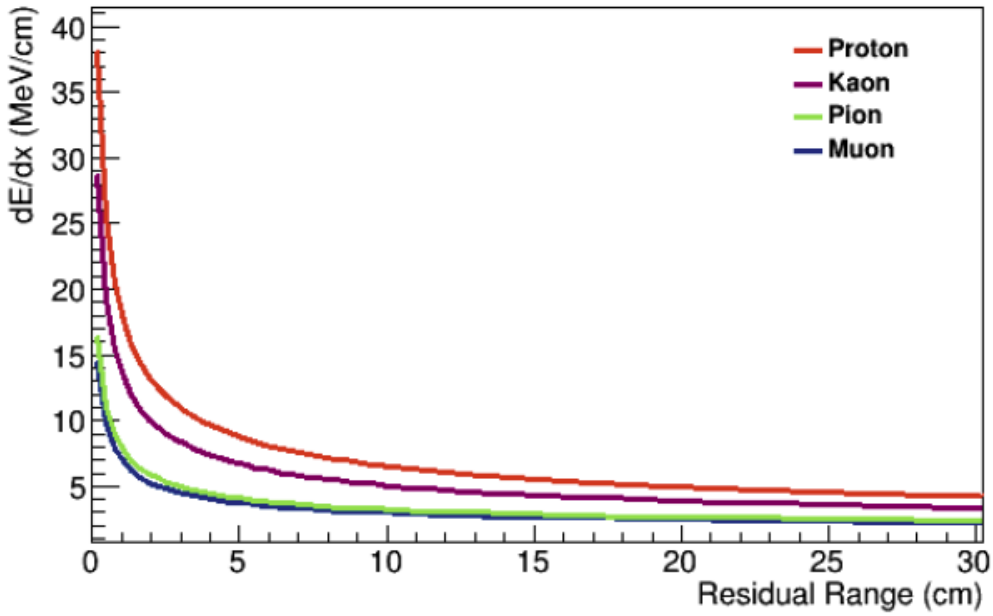

Figure 4.12: Theoretical curves for dE/dx residual range (distance from end of track) for particles inside a LArTPC. Each colored curve corresponds to a different particle.

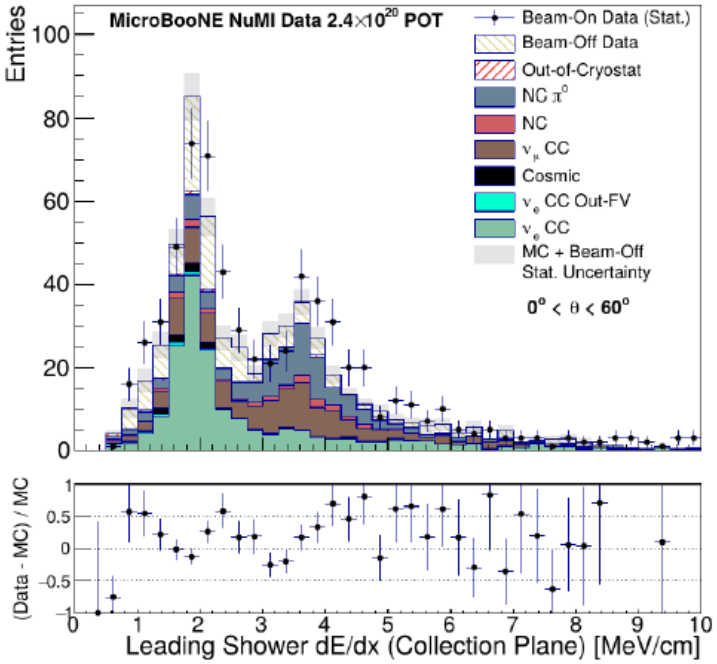

Figure 4.13: Demonstration of the separation power of the variable dE/dx. Two distinct peaks are shown with electron showers around a $\sim$2 MeV/cm peak while photons are concentrated around a 4 MeV/cm peak.

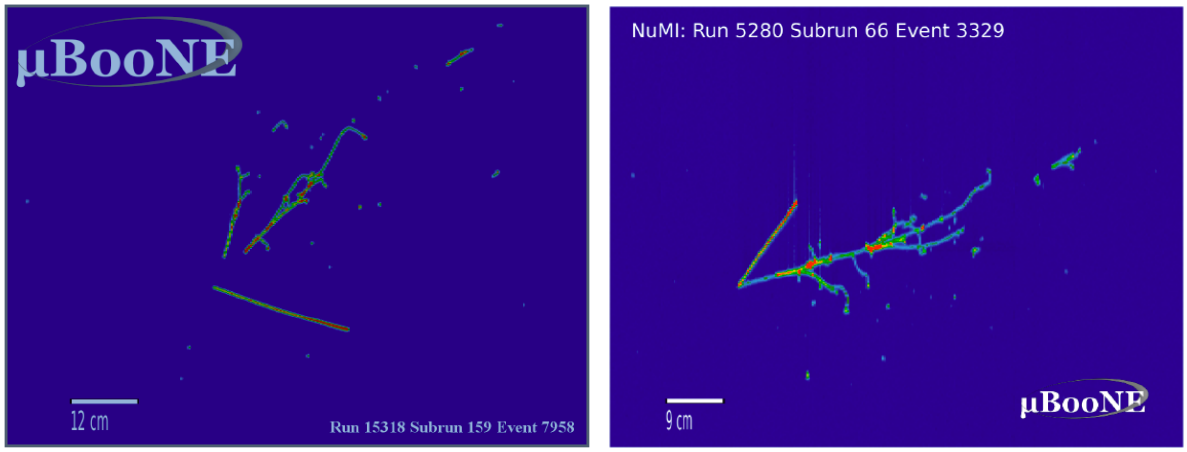

(a) **(b)**

Figure 4.14: (Left) An event display of an NC π^0candidate which includes two reconstructed photon showers and a reconstructed proton track. The event results from the BNB beam and is shown for the collection plane. (Right) An event display of an electron neutrino event including a reconstructed electron shower and a reconstructed proton. The event results from the NUMI beam where electron neutrino events are more prominent.

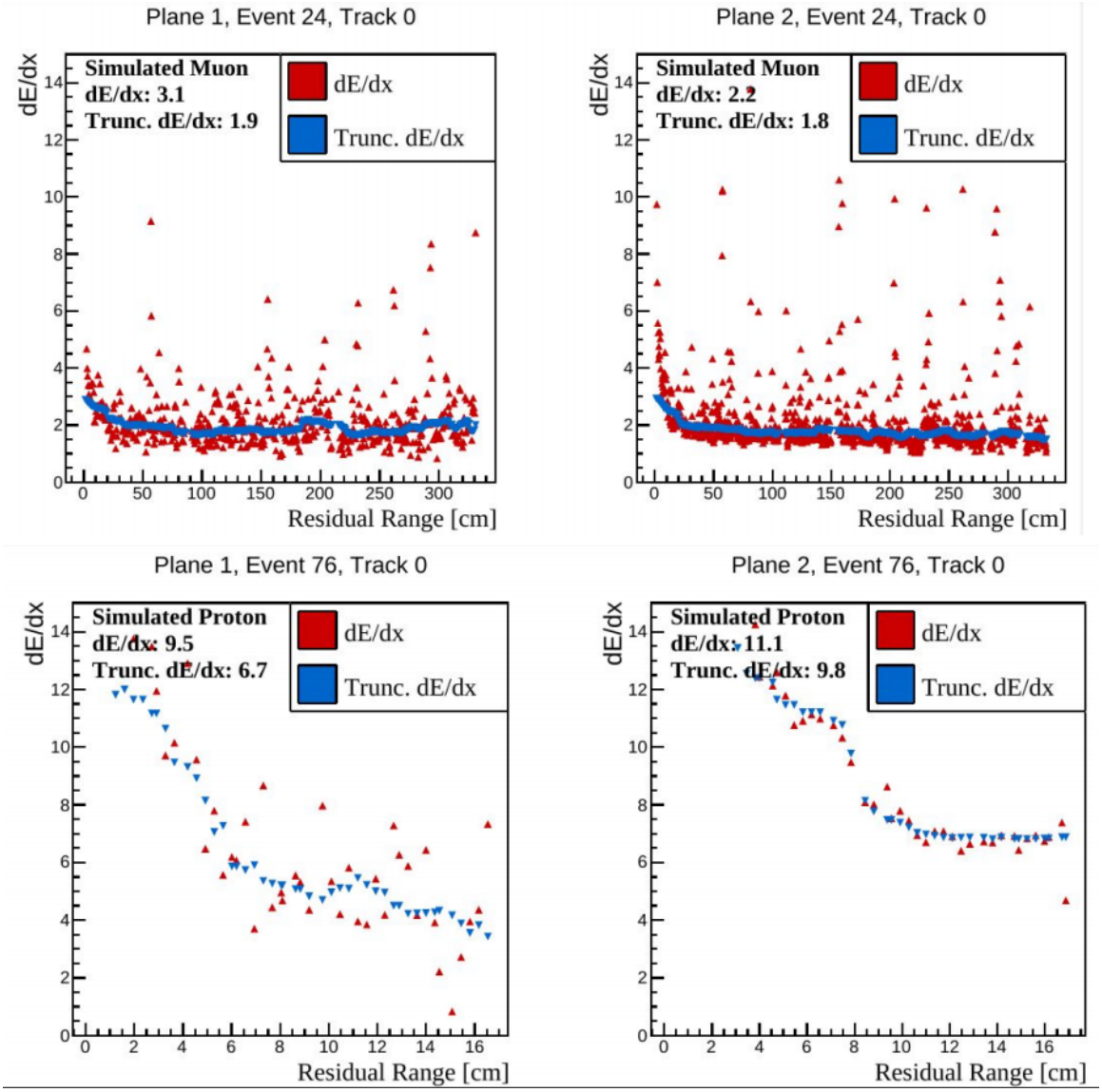

Figure 4.15: Energy loss vs residual range fitting performed on a muon (top row) and proton (bottom row) track in simulation with an induction plane on the left and an induction plane on the right. The truncated dE/dx refers to a smoothing function applied to dE/dx to remove outliers from the calculation of the mean dE/dx.

Chapter 5

Single Photon Low Energy Excess Search

This chapter gives an overview of the Single Photon Low Energy Excess search analysis. The premise of this abalysis search is covered in Sec. 5.1. An overview of the analysis methods is given in Sec. 5.2. Information on the process of selecting events is given in Sec. 5.3 and Sec. 5.4. My work on systematic uncertainties will be covered in Ch. 6.

5.1 Goals and Hypothesis

As discussed in Ch. 3, the primary physics goal of MicroBooNE is the investigation of the MiniBooNE low energy excess (LEE) of candidate electron neutrino and antineutrino charged current quasi-elastic events. One possible interpretation of the MiniBooNE LEE is that it is comprised of neutrino-induced single-photon events. This analysis is an effort to test this hypothesis via study of neutral current Δ resonance production followed by Δ radiative decay ($\Delta \rightarrow N\gamma$). A 3$\times$ standard model rate of this hypothesis would account for the excess, and this enhancement fits within the bounds of the current best measurement from the T2K experiment as seen in Fig. 5.1. To optimize selection of these events for efficiency and reduction of cosmogenic and beam-related backgrounds, a Boosted Decision Tree (BDT) framework has been developed. The result of this study should be an evaluation of the standard model (SM) predicted rate for the NC $\Delta \rightarrow N\gamma$ process and a test of the

interpretation of the previously observed MiniBooNE low energy excess as NC $\Delta \rightarrow N\gamma$ events, using the full anticipated MicroBooNE data set of 12.25×10^{20} POT.

5.2 Analysis Overview

To develop an efficient and pure selection of events with a topology consistent with neutrino-induced NC $\Delta \rightarrow N\gamma$ events, two primary topologies based on final states are examined: one with a single photon and a single proton in the final state ($1\gamma1p$), and one with a single photon and zero protons in the final state ($1\gamma0p$). In both signals, no other tracks or showers can be reconstructed as part of the interaction. In simulation, it was discovered there is a significant background to these topologies from NC π^0 events, where one of the two daughter photons of a π^0 decay is not reconstructed due to (a) leaving the detector, (b) overlapping with the primary shower, (c) pair-converting at a significant distance away thus failing to be associated with the primary neutrino interaction, or (d) failing to reconstruct due to it having too low energy. To understand and reduce these backgrounds, a concurrent analysis of π^0 rich selections has been undertaken. It defines two similar topologies: one proton and two photons ($2\gamma1p$), and zero proton and two photons ($2\gamma0p$). Once again, if there are other tracks and showers reconstructed in the final state, then the event cannot be included in these selections. These selections provide high-statistics samples for data-to-Monte Carlo comparisons used in validation of the analysis and a direct constraint on NC π^0. Feynman diagrams for the 1γ and 2γ selected signals can be seen in Fig. 5.2. More details on the Single Photon Analysis can be found in the MicroBooNE public note [22] released in concert with Neutrino 2020 conference presentations.

5.3 Single Photon Selection

The selection of NC Δ radiative events begins by using Pandora-reconstructed information to select neutrino interaction vertices that match signal topology definitions. This topological selection is defined as requiring exactly one reconstructed shower and one reconstructed track associated to the candidate vertex.

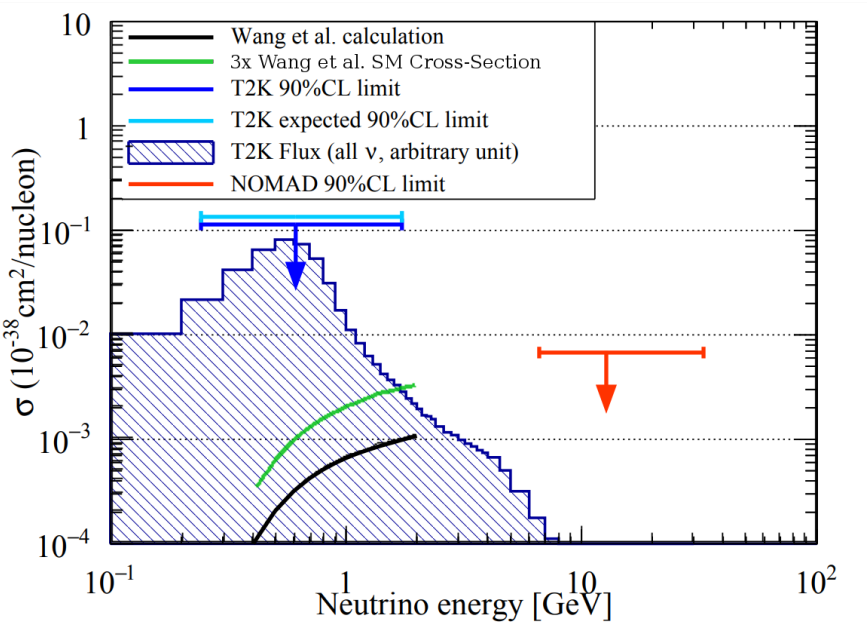

Figure 5.1: The current world's best bound on the NC Δ radiative cross-section at O(1 GeV) energy by T2K [21]. Shown also in green is the Wang et al. Standard Model (SM) cross-section scaled up by a factor of 3, which is what would be needed to explain the observed MiniBooNE low-energy excess [22].

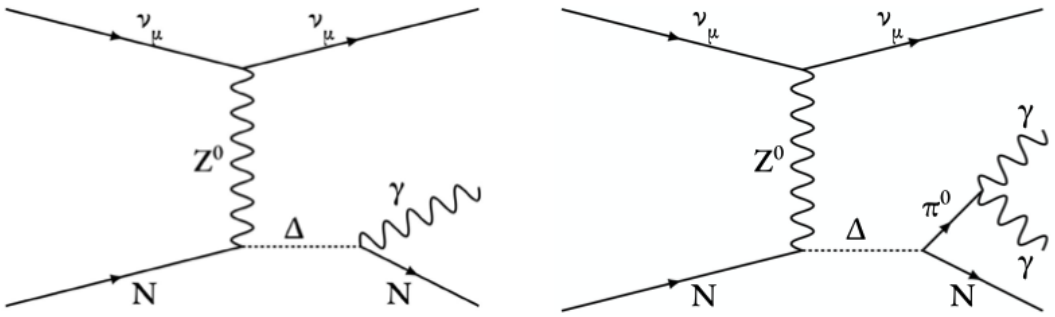

Figure 5.2: Feynaman diagrams for the 1γ (left) and 2γ (right) selected signals. Note the outgoing nucleons (N) can be a proton or a neutron which is undetectable in the MicroBooNE detector, contributing to the $0p$ variants. If a γ is missed in the 2γ output, the interaction appears very similar to the 1γ signal.

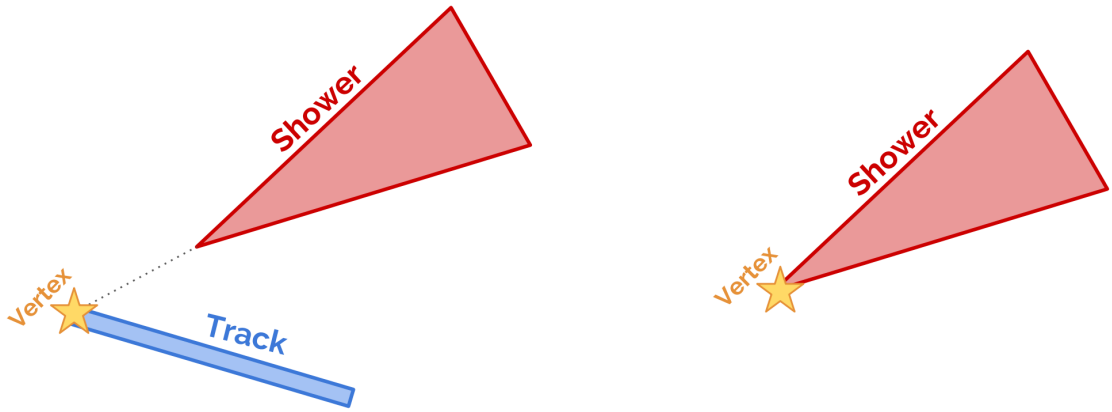

Figure 5.3: Cartoon illustrations of the two topological signatures of NC $\Delta \to N\gamma$ events targeted by the single-photon low-energy excess search. Left: $1\gamma 1p$; right: $1\gamma 0p$.

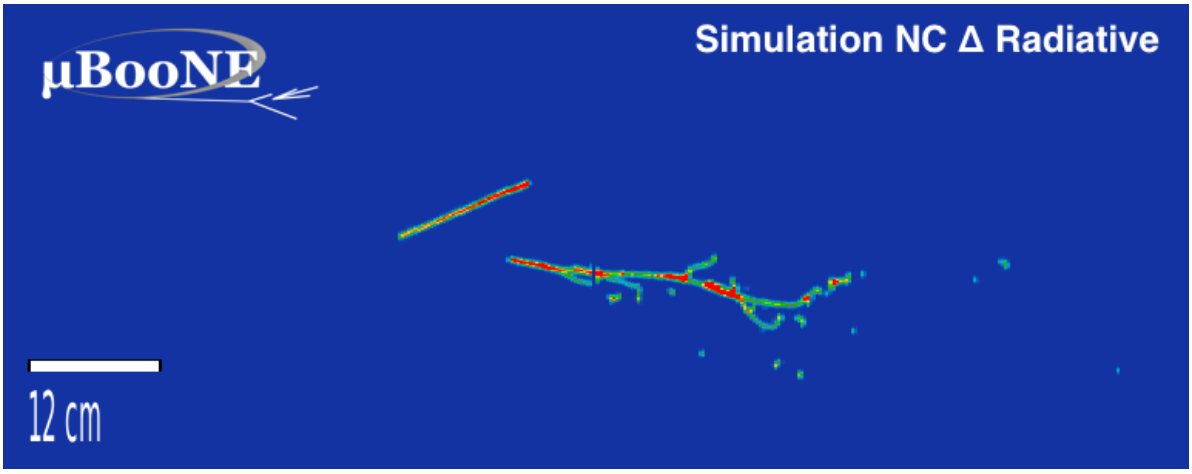

Figure 5.4: An example of simulated $\Delta^+ \to p\gamma$ event, showing a short proton track with Bragg peak, as well as non-zero conversion distance of the photon before pair-producing into an e^+e^- pair that subsequently forms an electromagnetic shower in the liquid argon. This event represents a classic example of the topology with the 1γ1p selection.

A simple illustration of these topologies is shown in Fig. 5.3, and an event display showing a Monte Carlo simulation of a $1\gamma1p$ event with a clear proton track and photon shower in the MicroBooNE LArTPC is shown in Fig. 5.4. Following topological selection, a series of cuts are applied to select the samples and reduce backgrounds. The Δ baryon energy can be reconstructed for the $1\gamma1p$ distribution from the proton and photon candidates. This is often chosen as a plotting variable for analysis because true NC Δ radiative events should be centered on the Δ mass of 1232 MeV. The distributions compare unblinded data from MicroBooNE's run period 1 (Run 1) to simulated predictions. The Run 1 data-set corresponds to approximately 5×10^{20} POT, or $< 5\%$ of the total MicroBooNE data set for Runs 1-5, although after data-quality cuts the available POT shown on subsequent plots is closer to 4.1×10^{20} POT. Data begins at the topological stage where the only requirement is meeting the topological requirements in reconstruction. Topological selection stage plots can be seen in Fig. 5.5. Plots are shown as stacked histograms of the signal and each background. To illustrate our hypothesis for the MiniBooNE LEE, NC Δ radiative decay events included both scaled to the standard model expected rate in GENIE as well as scaled to a factor of 2 enhancement (combining for the $3\times$ factor necessary to explain the LEE). Other events are sorted into categories including NC 1 π^0 Coherent, NC 1 π^0 Non-Coherent, NC $2{+}\pi^0$, CC ν_μ π^0 and CC $\nu_e/\overline{\nu}_e$ intrinsic, all representing particular sub-components of the total BNB interactions in the MicroBooNE cryostat. The remaining BNB interactions within the cryostat, that do not fit into the above six definitions, are grouped together and referred to as BNB Other, the majority of which are CC ν_μ events with no exiting π^0. The Dirt category represents all BNB neutrino-induced backgrounds that originate outside the cryostat (in the surrounding concrete, steel and dirt) but scatter inside the TPC and produce reconstructable charge.

After topological selection, a series of pre-selection cuts such as track and shower energy thresholds and fiducial volume requirements are applied in order to reduce both any obvious and clear backgrounds as well as the number of selected events with reconstruction failures. Examining the $1\gamma1p$ selection, cuts reduce the total contribution of backgrounds from $\sim$3136 events to $\sim$281 events (normalized to the open run 1 POT). The SM scaled signal is only reduced from $\sim$1.5 events to $\sim$0.9 events. However, the signal purity for the $1\gamma1p$ topology

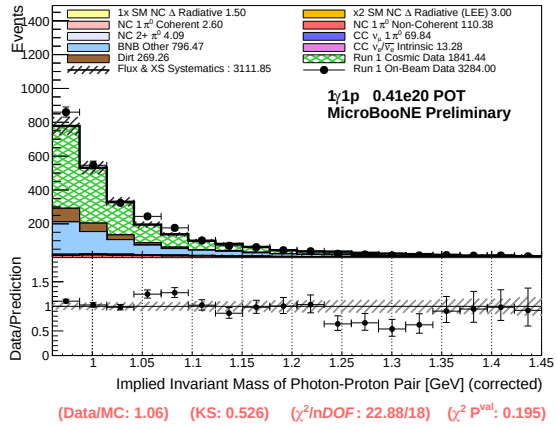

(a) $1\gamma 1p$ Selection at Topological Stage

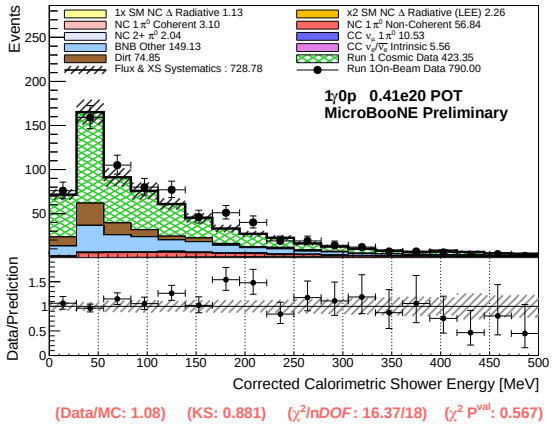

(b) $1\gamma 0p$ Selection at Topological Stage

Figure 5.5: $1\gamma 1p$ and $1\gamma 0p$ Monte Carlo predicted distributions after the topological selection stage. Predictions are scaled to and compared to the open Run 1 data set corresponding to 4.1×10^{19} POT. Here, the dominant backgrounds are cosmogenic backgrounds, in green (labeled "cosmic data", as they are directly extracted from MicroBooNE data measured in situ when the BNB is off), followed by "BNB other" and dirt induced backgrounds, in light blue. Overall, reasonable data to Monte Carlo agreement is observed, within statistical and systematic uncertainties. Note: detector systematic uncertainties have been evaluated but are omitted in these distributions.

is still $< 1\%$ of total selected events, so a stronger selection method is necessary to reduce backgrounds. The method selected was a boosted decision tree.

A decision tree is effectively a series of conditionals that are tuned to get the best efficiency (fewest true signal events removed) and accuracy (fewest backgrounds remaining). This is then boosted by having many of these trees run in parallel and combining the results. The 1γ boosted decision tree algorithm was developed with five separate multivariate BDTs that each target a different background topology: cosmic, ν_e, NC π^0, second shower veto (SSV) further targeting NC π^0 backgrounds, and other. The other category is trained on all remaining BNB neutrino backgrounds that are not directly targeted by the previous three BDTs. The trees train over a set of variables. The pre-selection data plotted via two of the top training variables can be seen in Fig. 5.6, which gives a visual representation of the separation of background and signal. Figure 5.6a shows the track truncated mean dE/dx. This gives separation power between different particles allowing us to separate μ and p tracks. Figure 5.6b shows the shower dE/dx. This variable has powerful e/γ separation due to the distinction between an initial electron vs electron-positron pair from a photon conversion as explained in Sec. 4.3. Therefore, it is valuable for discriminating ν_e backgrounds.

The same process as for 1γ1p selection can be performed for 1γ0p with only a few key changes. Here the topological signal is described as requiring exactly one reconstructed shower associated to the candidate vertex. The Δ Baryon energy cannot be reconstructed without the proton track so some BDT variables are no longer applicable (e.g. those related to a track topology). Topological selection efficiency for 1γ0p signal is at 64.3%. A BDT score[1] cut is then applied to select a given topology with desired efficiency and accuracy. The BDT response distributions for 1γ1p and 1γ0p are shown in Figs. 5.7 and 5.8, respectively. A summary of optimized BDT score cuts applied to each selection along with signal efficiencies is shown in Table 5.1.

The final selection distributions for 1γ1p and 1γ0p are shown in Fig. 5.9. Now the resulting backgrounds are reduced from $\sim$281 at precut stage to $\sim$2 events. With $\sim$0.3 signal events remaining (with SM prediction) the ratio between signal and background is

[1] A BDT score is effectively how likely the BDT thinks that the selected event is a given topology (1γ1p and 1γ0p) as desired with 1 being the maximum.

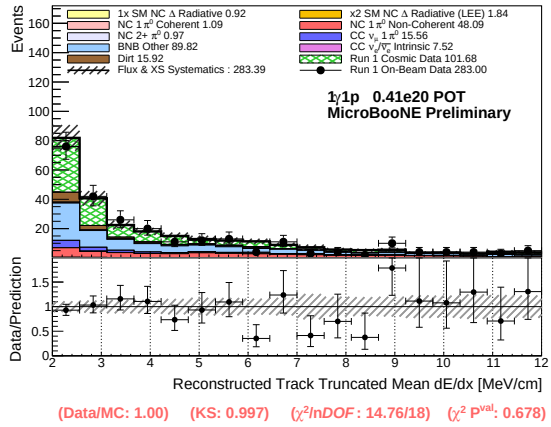

(a) Track Truncated Mean dE/dx

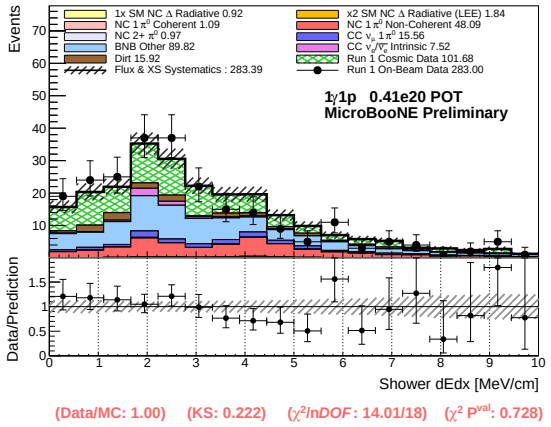

(b) Reconstructed Shower dE/dx

Figure 5.6: Monte Carlo prediction to data comparisons for two of the top training variables used for the $1\gamma1p$ BDTs, in terms of the total gain, shown at the pre-selection cut stage. Note: detector systematic uncertainties have been evaluated but are omitted in these distributions.

Table 5.1: Summary of optimized BDT score cuts applied to each selection, $1\gamma1p$ and $1\gamma0p$, and corresponding signal efficiencies. Note the lack of a proton track makes the ν_e BDT and SSV BDT inapplicable to the $1\gamma0p$.

Selection	**Cosmic BDT**	**BNB Other BDT**	**NC π^0 BDT**	**ν_e BDT**	**SSV BDT**
$1\gamma1p$ **Selection**					
Score cut:	0.975	0.963	0.467	0.571	0.522
Signal efficiency:	18.9%	15.5%	14.7%	17.9%	23.5%
$1\gamma0p$ **Selection**					
Score cut:	0.988	0.893	0.429	-	-
Signal efficiency:	55.3%	69.6%	47.4%	-	-

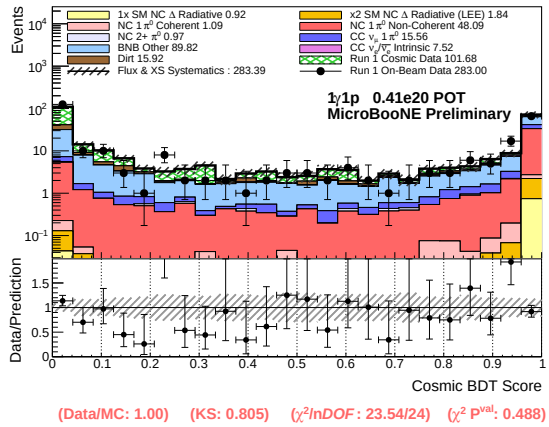

(Data/MC: 1.00) (KS: 0.805) (χ^2/nDOF: 23.54/24) (χ^2 P^{val}: 0.488)

(a) $1\gamma1p$ Cosmic BDT Response

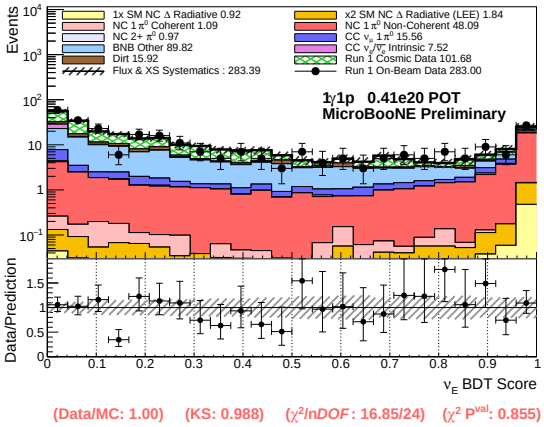

(Data/MC: 1.00) (KS: 0.988) (χ^2/nDOF: 16.85/24) (χ^2 P^{val}: 0.855)

(b) $1\gamma1p$ ν_e BDT Response

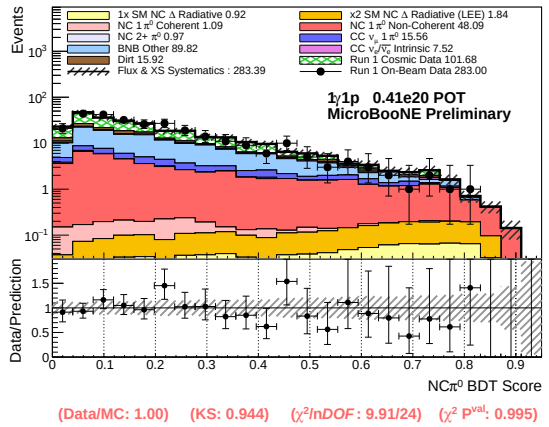

(Data/MC: 1.00) (KS: 0.944) (χ^2/nDOF: 9.91/24) (χ^2 P^{val}: 0.995)

(c) $1\gamma1p$ NC π^0 BDT Response

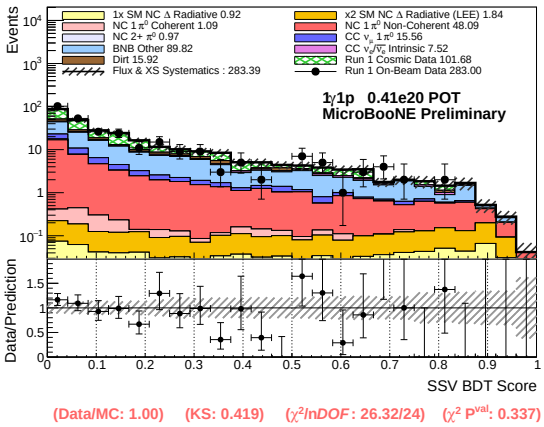

(Data/MC: 1.00) (KS: 0.419) (χ^2/nDOF: 26.32/24) (χ^2 P^{val}: 0.337)

(d) $1\gamma1p$ SSV BDT Response

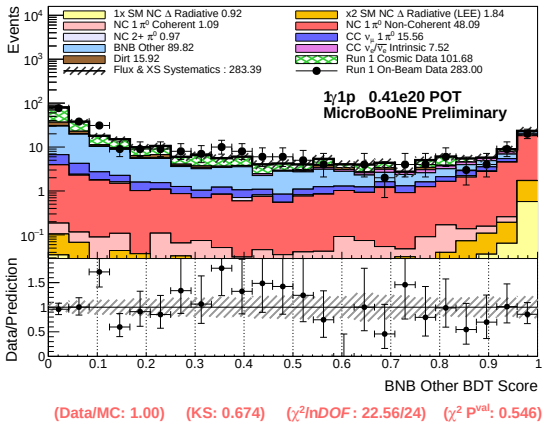

(Data/MC: 1.00) (KS: 0.674) (χ^2/nDOF: 22.56/24) (χ^2 P^{val}: 0.546)

(e) $1\gamma1p$ BNB Other BDT Response

Figure 5.7: BDT response distributions for the $1\gamma1p$ selection. The Monte Carlo predictions are scaled to 4.1×10^{19} POT, and compared to corresponding data from Run 1. The data and Monte Carlo agree reasonably within statistical and systematic uncertainties, and each BDT is capable of providing noticeable signal to background differentiation. Note: detector systematic uncertainties have been evaluated but are omitted in these distributions.

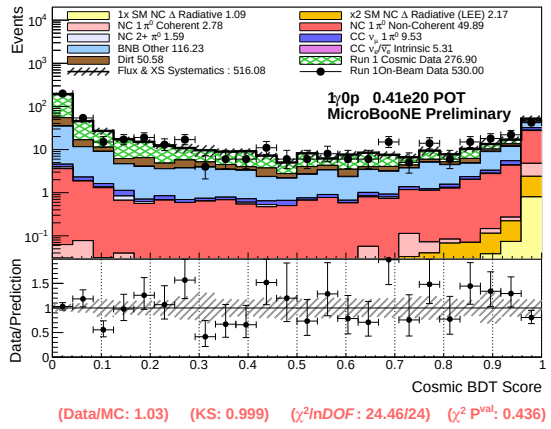

(a) $1\gamma 0p$ Cosmic BDT Response

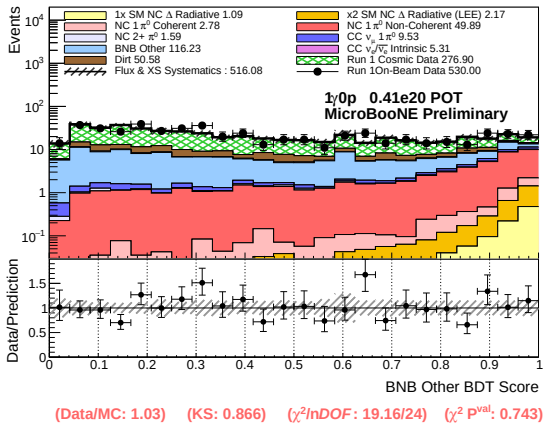

(b) $1\gamma 0p$ BNB Other BDT Response

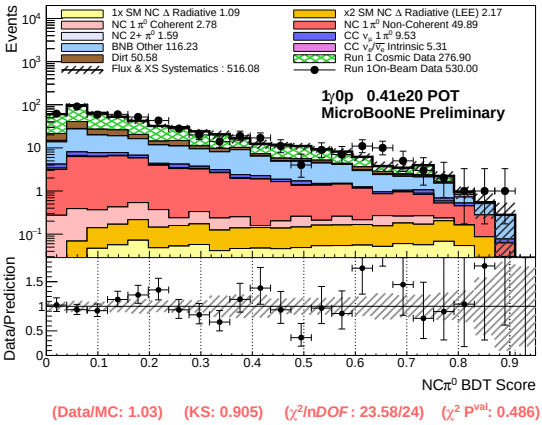

(c) $1\gamma 0p$ NC π^0 BDT Response

Figure 5.8: BDT response distributions for the $1\gamma 0p$ selection. The Monte Carlo predictions are scaled to $5{\times}10^{19}$ POT, and compared to corresponding data from Run 1. The data and Monte Carlo agree reasonably within statistical and systematic uncertainties, and each BDT is capable of providing noticeable signal to background differentiation. Note: detector systematic uncertainties have been evaluated but are omitted in these distributions.

dramatically improved. However, NC π^0 events remain the most dominant background with $\sim$1.8 events. Two data events passing the final single photon selection are shown in Fig. 5.10 which is within the uncertainties of this small data set.

5.4 Neutral Current π^0 Selection

NC π^0 forms the dominant background to the NC Δ radiative decay selection. Thus a concurrent analysis of $2\gamma 1p$ and $2\gamma 0p$ has been performed with the purpose of selecting high-purity, high-statistics sample of NC π^0 events. It also allows for reduction of systematic uncertainty on the NC π^0 background via a combined single-photon and NC π^0 fit. Efforts to quantify this constraint are discussed in Ch. 6.

The 2γ selection follows the same process as the 1γ selections beginning with topological and low-level pre-selection cuts that are run over MicroBooNE data. It is crucial to filter sufficient NC Δ signal events so blindness is maintained. This is accomplished via a dedicated filter.

Similar to 1γ, for these selections, a variable is selected for plotting. The invariant mass of the two photons is useful, because true NC π^0 events should peak at the π^0 mass of 135 MeV. At this stage, the selection is isolated mostly as CC or NC π^0 event. Once again, a BDT analysis is applied to filter the remaining cosmic contaminated events and the CC π^0. A single BDT was proven to be more efficient for this selection. The BDT is trained to select NC π^0 events using a set of calorimetric and geometric variables. Comparable to $1\gamma 0p$, with the $2\gamma 0p$ selection the lack of a proton candidate track makes it impossible to calculate variables such as the conversion distance. Therefore the selection has a reduced number of cuts. The topological stage event count isn't meaningful as NC π^0 filters are built into the algorithm. The pre-selection contains $\sim$735 NC π^0 signal events compared to $\sim$2362 background events (scaled to Runs 1-3 POT).

In 2γ, the track mean dE/dx variable remains a powerful discriminator as shown in Fig. 5.11. In this case, it is selecting highly ionizing protons over both cosmic and BNB ν_μ CC. The resulting BDT responses can be seen in Fig. 5.12, with the NC π^0 piling up on

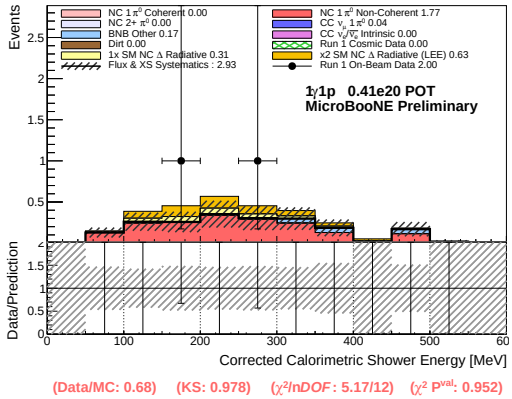

(a) $1\gamma 1p$ Run 1 Open

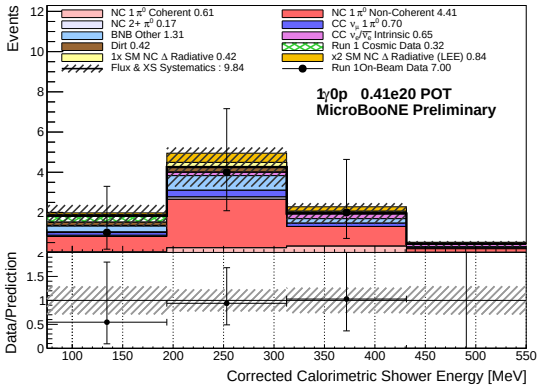

(b) $1\gamma 0p$ Run 1 Open

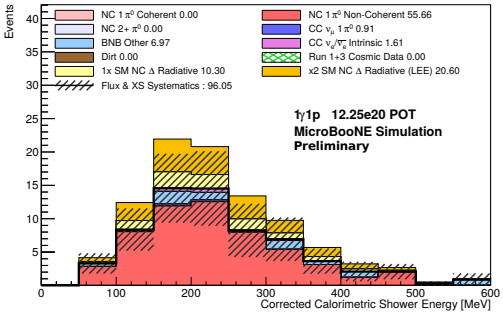

(c) $1\gamma 1p$ Runs 1-5

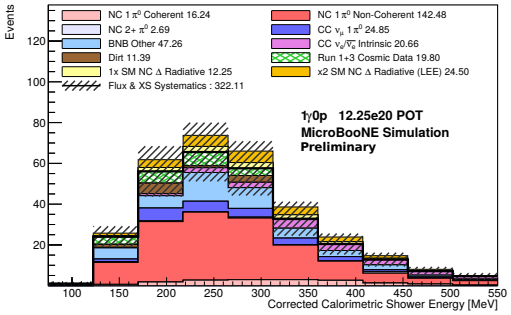

(d) $1\gamma 0p$ Runs 1-5

Figure 5.9: The top plots are $1\gamma 1p$ final selection with all cuts applied with the left for Run 1 open data and right for the full MicroBooNE data set of 12.25×10^{20} POT. The top left plot shows 2 surviving data events in the selection, with an expectation of ~ 3 Monte Carlo events. The bottom plots are the $1\gamma 0p$ final selection with the same format. The bottom left figure shows 7 surviving data events in the selection, with an expectation of ~ 9.8 Monte Carlo events. The shaded band corresponds to the combined flux, cross-section and statistical (due to finite statistics) uncertainty on the Monte Carlo. Note: detector systematic uncertainties have been evaluated but are omitted in these distributions.

the right (note that the small amount of signal on the left hand side tends to be cosmic contaminated events).

The final selection now has ∼505 true signal events compared to ∼300 background events. Matching with Runs 1-3 open data is within uncertainty, with 804.4 simulated events vs 740.1 data events from combined cosmic and beam data. Tab. 5.2 breaks down the signal events in the 2γ final selection in terms of interaction types along with respective efficiencies. Figure 5.13 shows the final selection reconstructed π^0 invariant mass distributions. Finally, Figs. 5.14 shows two example event displays of a candidate NC π^0 interaction that passes the final $2\gamma 1p$ selection.

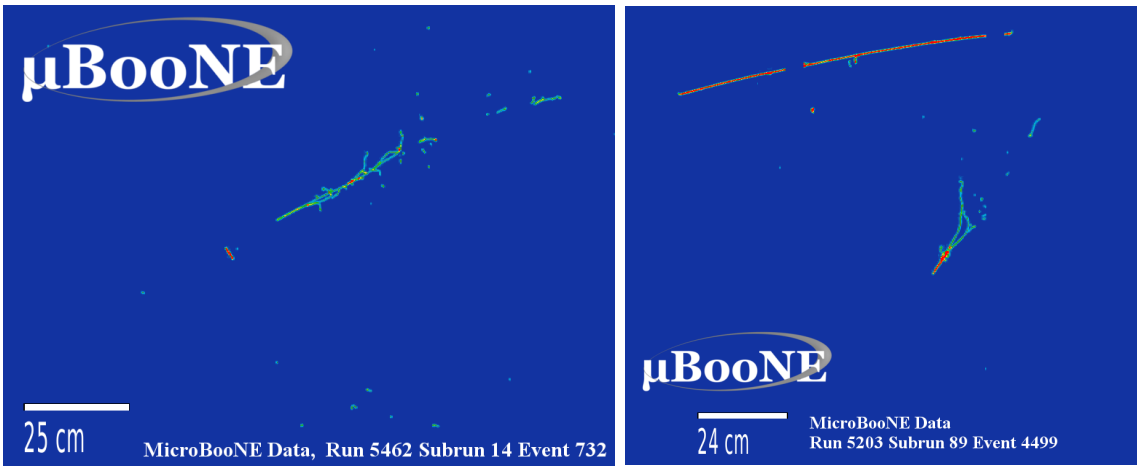

(a) $1\gamma 1p$ **(b)** $1\gamma 0p$

Figure 5.10: The two data events passing the final 1γ selection in the open Run 1 data sample. Left: $1\gamma 1p$; the first event showing clean conversion distance and no strong evidence of a secondary shower that would be suggestive of it not being NC π^0 in origin. Right: $1\gamma 0p$ shower show a large dE/dx at the shower start, with the characteristic e^+e^- pair production 'V' shape.

Table 5.2: Breakdown of interaction types in the 2γ selections, both at the pre-selection stage and final selection stage.

$2\gamma 1p$	**Resonant**	**DIS**	**QE**	**Coherent**	**MEC**
Pre-Selection	81.3%	16.3%	1.3%	1.31%	0.06%
Final Selection	85.2%	13.2%	1.2%	0.28%	0.07%
$2\gamma 0p$	**Resonant**	**DIS**	**QE**	**Coherent**	**MEC**
Pre-Selection	79.1%	14.9%	0.52%	5.5%	0.02%
Final Selection	79.2%	13.5%	0.45%	6.8%	0.00%

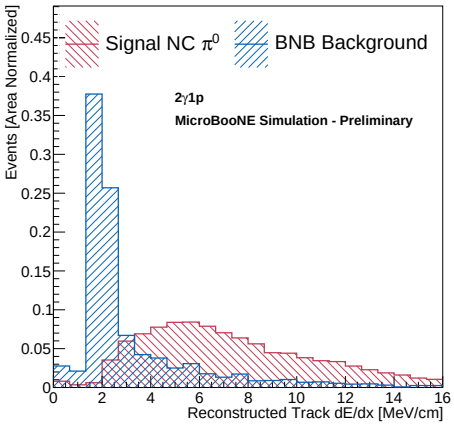

(a) MC-only Distributions (area normalized)

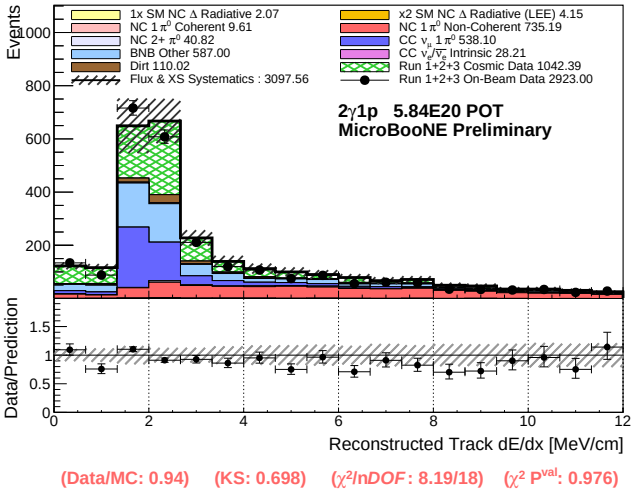

(b) Data and MC Distributions

Figure 5.11: (a) Monte Carlo predicted distribution of reconstructed track (mean truncated) dE/dx, separated between signal and BNB backgrounds. (b) Data to Monte Carlo distribution comparison for the same variable. Note: detector systematic uncertainties have been evaluated but are omitted in these distributions.

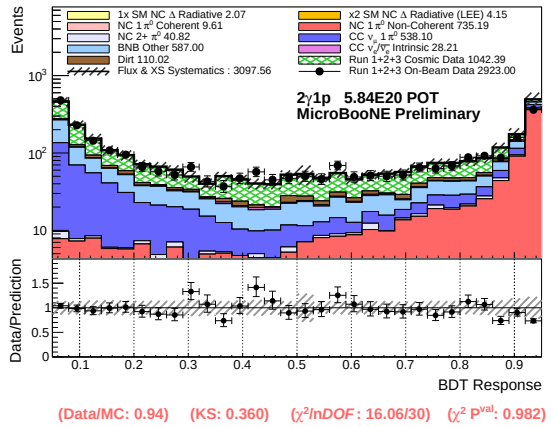

(a) $2\gamma 1p$ BDT response

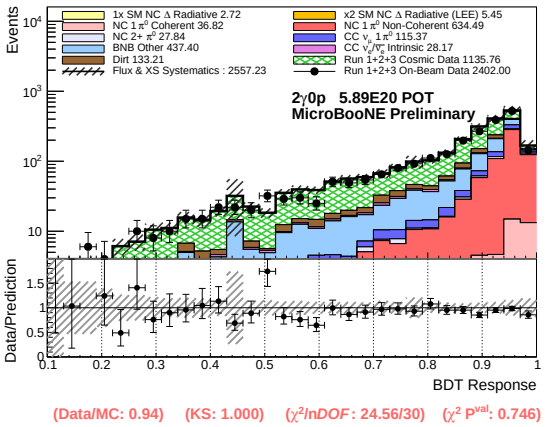

(b) $2\gamma 0p$ BDT response

Figure 5.12: Data to Monte Carlo comparisons for the $2\gamma 1p$ BDT response (left) and $2\gamma 0p$ BDT response (right). To maximize efficiency times purity in the final selection, a cut is placed at 0.854 for $2\gamma 1p$ and a cut at 0.950 for $2\gamma 0p$. Note: detector systematic uncertainties have been evaluated but are omitted in these distributions.

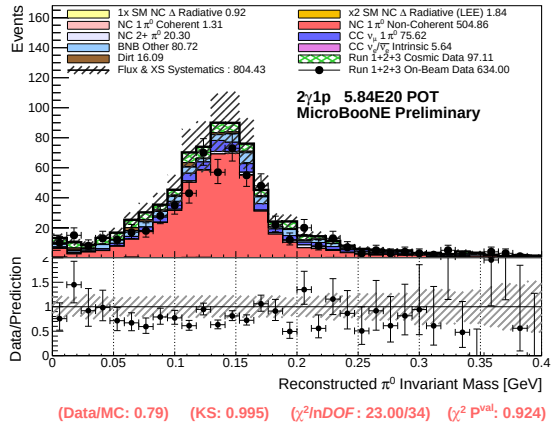

(a) $2\gamma 1p$

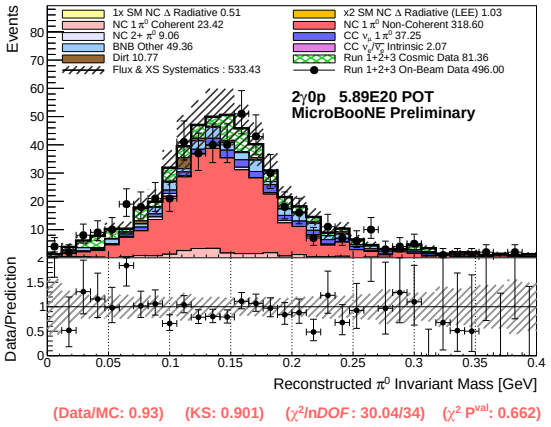

(b) $2\gamma 0p$

Figure 5.13: Final distributions show predictions scaled to 5.85×10^{20} POT, which correspond to the total POT for filtered Runs 1-3, and corresponding data. These distributions correspond to the GENIE central value (CV) prediction, i.e. no normalization correction has been applied to the NC π^0 production. Note: detector systematic uncertainties have been evaluated but are omitted in these distributions.

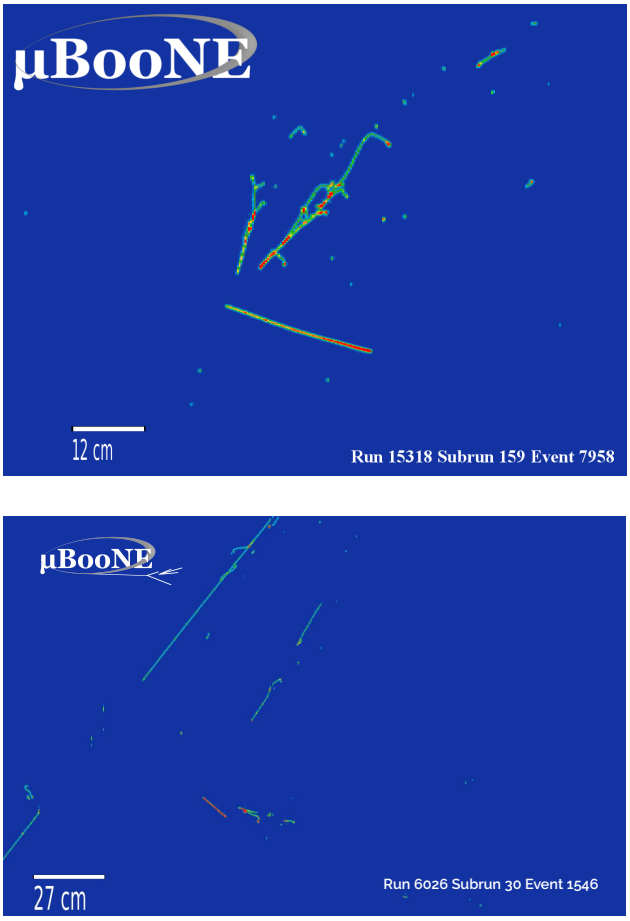

Figure 5.14: Two event displays which survive the final $2\gamma 1p$ selection. (Left) recorded during Run 3 of MicroBooNE. Leading shower energy was reconstructed as 332 MeV with a sub-leading shower energy of 98 MeV, and a corresponding invariant mass of 158.2 MeV. (Right) recorded during Run 1 of MicroBooNE. The reconstructed invariant mass is 146.2 MeV.

Chapter 6

Single Photon Systematics

This chapter describes the systematics treatment work that I have led for the single photon or gamma LEE analysis. Sec. 6.1 covers general concepts for the systematics analysis tools used in the gamma LEE analysis. Sec. 6.2 covers systematics generated via an event reweighting model, corresponding to flux and cross-section based effects. Sec. 6.3 covers systematics incompatible with these methods including detector and photo-nuclear effects. Finally, Sec. 6.4 covers efforts to reduce systematic uncertainties and their impact on the final single photon sensitivity measurement.

6.1 Systematics Frameworks

Several frameworks have been developed allowing for study of systematics on samples of the MicroBooNE simulation and following application to data measurements. These include EventWeight—an event reweighting module allowing us to obtain systematically varied distributions; Short Baseline Neutrino Fit (SBNFit)—an analysis module which produces correlation and covariance matrices; and a framework for comparing independently simulated Monte Carlo universes with varied parameters to represent sources of systematic uncertainty not included in EventWeight. Systematic uncertainties can largely be divided into 3 categories: flux, cross section, and detector systematics. Flux and cross-section effects are compatible with EventWeight, but detector effects are incompatible. There was also an

analysis to evaluate photo-nuclear absorption in a hybrid approach, as will be explained in Sec. 6.3.3.

6.1.1 Covariance Matrix Construction

The SBNFit module has been used for the creation of covariance matrices that encapsulate systematic uncertainties, including bin-to-bin and sample-to-sample systematic correlations. SBNFit [59] is a module built for the Short Baseline Neutrino (SBN) program, enabling simultaneous fitting of an arbitrarily large number of distributions corresponding to different beam running modes, detectors, and selection channels, with full accounting for their systematic correlations. Uncertainty accounting is done with the use of a fractional covariance matrix containing the statistical and systematic uncertainties and systematic correlations among different samples involved in the fit. Each sample is constructed by studying variations on selected event distributions generated from underlying systematic variations to simulation input parameters.

SBNFit calculates a series of matrices, one for each simulation input parameter variation set (referred to as systematic variation knob k). The resulting total full covariance matrix is the sum of individual covariance matrices constructed for each underlying source of systematic error k, where k might represent, e.g., π^+ production uncertainties in proton-target interactions in neutrino flux production.

Each individual covariance matrix M^k, corresponding to an underlying source of systematic uncertainty, k, is constructed by considering N = up to 1000 separate varied distributions V_n^k of the final selected samples, where $n = 1, .., N$. The varied distributions are calculated each time by varying the underlying source of uncertainty k within its associated error band. The distributions are typically broken down by sub-channels of signal, background type, etc., as a function of bin i (or j) in some reconstructed variable over which the fit is to be performed. The deviations of those varied distributions relative to the central value prediction, P, are then mapped onto the covariance matrix, constructed from the

distributions as follows

$$M_{ij} = \frac{1}{N}\sum_{n=1}^{N}(P_i - V_{i,n}^k) \times (P_j - V_{j,n}^k), \tag{6.1}$$

where i, j are bin numbers.

The varied distributions can be obtained either via reweighting of the Monte Carlo central value prediction, as described in Sec. 6.2, or via the methods described in Sec. 6.3.

The summation of the uncertainties for the single photon analysis can be described as

$$M^{total} = M^{flux} + M^{cross-section} + M^{detector}. \tag{6.2}$$

When plotting distributions, uncertainties on the bin boundaries of a given distribution are determined by the diagonal of the full systematics covariance matrix. Specifically, the elements of the full covariance matrix M_{ii} correspond to σ_{ii}^2, where σ_{ii} is the error bar on bin i.

6.2 Reweightable Systematic Uncertainties

6.2.1 EventWeight Module

The EventWeight module is used to evaluate flux and cross section systematic uncertainties on an event-by-event basis. It accepts files containing event information from any stage of selection and outputs event weight files (effectively collection of weights tied to each event), where the weights have been calculated to vary a physics parameter away from its central value according to

$$P \rightarrow P' = P(1 + x_p * (\delta P/P)), \tag{6.3}$$

where P and P' represent the central value and systematically-varied value of the physics parameter, δP represents the standard deviation of P, and x_p is the scale of the deviation drawn from a Gaussian distribution. Internal GENIE [92] calculators are used to determine how the likelihood of each event occurring would respond to the shift in P'. These new likelihoods become weights assigned to each event such that for every P', every event will

have an assigned weight. When forming selections, treating each event as a number of events equal to the weighted value forms an effective systematically varied sample. This method has a limitation in that events cannot be weighted into existence, but sufficiently large samples should negate this, and this method is most optimal given limited allocated computing resources.

Because the single photon analysis only uses artroot [87] in the initial steps of the analysis before converting to simple root files and EventWeight is designed to work with artroot files, an intermediate processing step is necessary to allow reweighting on our final samples. This intermediate step is accomplished via the TreeReader and Arborist modules, where TreeReader is designed to run EventWeight over simple root files and Arborist converts the output of TreeReader into simple root files readable by SBNfit. These will be used in conjunction with the original vertexed files which contain detailed event information for systematic analysis.

TreeReader is a module included in uboonecode[1] for which we use the version v08_00_00_40. It should be noted the accompanying GENIE version is v3_00_04_ub2, but discussions with GENIE collaborators indicate that an update to v3_00_06 was not crucial to this analysis.

6.2.2 Input Samples

The covariance matrices generated via reweighting make use of the final selections for $1\gamma1p$, $1\gamma0p$, $2\gamma1p$, and $2\gamma0p$ produced as described in Ch. 5. Covariance matrices at earlier selection stages are also generated for the purpose of including systematic error bars on distributions prior to the final selection stage. However, this section will only include final selection analysis as it is crucial to our result and more illustrative of systematic effects.

It is often instructive to break down systematic uncertainties by sub-sample. Final selected samples are often sorted using truth-level information (information assigned by the simulation instead of being reconstructed). The fractional composition of the final selections for $2\gamma1p$, $2\gamma0p$, $1\gamma1p$, and $1\gamma0p$, in terms of the above sub-sample categories, is provided in Table 6.1. Although in the following sections some of the smaller backgrounds (such as NC

[1] A combined set of MicroBooNE algorithm code base shared by most analyses.

multiple π^0s) often show large systematic uncertainties of >30%, it must be noted that these makeup less than 1% of our final 1γ backgrounds.

Note in Sec. 6.2, we show the $1\gamma 1p$ selection in six bins but for final calculations only one bin is used due to statistical limitations.

6.2.3 Flux Systematics

Standard MicroBooNE flux variations are provided by beam analysis collaborators as described in Tab. 6.2. The flux variations were tested for consistency with the MiniBooNE final flux uncertainties and have been implemented into the EventWeight framework.

Below we describe the most important (dominant) flux systematics for the analysis. Note we use the terms *unisim* and *multisim*. Traditionally unisim means a variation to a single discreet value whereas multisim is a set of variations. However, unisim in the context of flux variations refers to internal processes, and a set of variations are actually produced. The size of our combined flux systematic uncertainty on the total events in our final $2\gamma 1p$, $2\gamma 0p$, $1\gamma 1p$, and $1\gamma 0p$ selections is provided in Table 6.3. A breakdown of each individual source of uncertainty can be found in Tabs. 2 through 5 in Appendix A.

- **Skin depth**: The skin-depth flux unisim refers to the effect of time varying electric currents penetrating into the horn conductor. It is estimated by calculating weights with separate models and assuming the variations are Gaussian distributed. The effect of skin depth variations on the non-coherent π^0 component of the 2γ and 1γ final selected samples is illustrated in Figs. 6.1 and 6.2, respectively. This systematic is higher for our analysis (compared to other LEE excess analyses focusing on the electron channel) as while the reconstructed energy of the photons in our selection is near the LEE region, the parent neutrinos were of higher energy ~1 GeV, and this systematic has greater impact in that energy region. A demonstration of the energy structure of this systematic can be seen in Fig. 6.3.

- π^+ **production**: The majority of the neutrino flux at MicroBooNE comes from π^+ production in proton-Be target interactions. As such, uncertainties associated with the primary hadron Sanford Wang Central Spline parametrizing π^+ production are

Table 6.1: Fractional composition of the final selections for $2\gamma 1p$, $2\gamma 0p$, $1\gamma 1p$, and $1\gamma 0p$ samples. Highlighted in bold are the dominant categories in each of the final stage selected topology, stressing the dominance in all selections of NC 1 π^0.

Sub-sample Category	$2\gamma 1p$	$2\gamma 0p$	$1\gamma 1p$	$1\gamma 0p$
BNBExt	12.1%	14.9%	0.00%	5.5%
BNBOther	9.8%	7.5%	7.6%	10.5%
CC1π^0	9.0%	6.4%	1.5%	8.2%
Dirt (Outside TPC)	4.6%	11.1%	0.00%	21.1%
NCDeltaRad (SM)	0.1%	0.1%	15.1%	3.8%
NC1π^0Coh	0.2%	4.3%	0.00%	4.6%
NC1π^0NotCoh	**63.3%**	**55.4%**	**74.6%**	**39.7%**
NueOverlay	0.7%	0.4%	1.2%	6.6%

Table 6.2: Description of flux and cross section reweightable systematics used in final uncertainty calculations.

Flux Variation Label	**Description**
expskin_FluxUnisim	Skin Depth for electric currents penetrating conductor
horncurrent_FluxUnisim	Horn Current in magnetic focusing horn
kminus_PrimaryHadronNormalization	K^- production normalization
kplus_PrimaryHadronFeynmanScaling	K^+ Sanford Wang Central Spline Variation
kzero_PrimaryHadronSanfordWang	K^0 Sanford Wang
nucleoninexsec_FluxUnisim	Nucleon Total Inelastic cross section on Be
nucleonqexsec_FluxUnisim	Nucleon Total Quasi-elastic cross section on Be
nucleontotxsec_FluxUnisim	Nucleon Total cross section on Be
piminus _PrimaryHadronSWCentralSplineVariation	π^- Sanford Wang Central Spline Variation
pioninexsec_FluxUnisim	Pion Total Inelastic cross section on Be
pionqexsec_FluxUnisim	Pion Total Quasi-elastic cross section on Be
piontotxsec_FluxUnisim	Pion Total cross section on Be
piplus_ PrimaryHadronSWCentralSplineVariation	π^+ Sanford Wang Central Spline Variation

significant on the majority of the events in our final selections. Like other hadron production weights, uncertainties on this parameterization are propagated via multi-Gaussian smearing. The WeightCalc function of the EventWeight package contains algorithms to smear a set of parameters within a vector utilizing a covariance matrix containing the uncertainties and correlations of those parameters. As this affects the majority of events in final selection, this source of uncertainty is necessarily an important one for all of our signals and backgrounds. The effect of π^+ production variations on the NC π^0 non coherent component of the 2γ and 1γ final selected samples is illustrated in Figs. 6.4 and 6.5, respectively.

Summary of Flux Systematics

Flux systematics are sub-dominant to cross-section and well determined. The largest variations: Skin depth and π^+ Sanford Wang Central Spline Variation have been discussed and each only reaches $\sim$8% uncertainty. It is thus acceptable to apply them to our analysis without further examination. While they are included in the constraint estimation method described in Sec. 6.4.1, this is more so a matter of consistency than a real need for reduction of uncertainty.

6.2.4 Cross Section Systematics

Cross section systematic uncertainties have seen many changes in the collaboration-wide analyses move from the historical MCC8[2] to the modern MCC9 and from GENIE version 2 to GENIE version 3. The modern uncertainty is performed via the GENIE_all combined variation (with a few other variations). The GENIE_all set of variations runs a suite of variations for a number of GENIE systematic knobs simultaneously. Because it accounts for correlations between individual variation knobs, it is more appropriately used for the calculation of final uncertainties and production of covariance matrices. It is run with 1000 total multisims. The effect of cross section variations from GENIE_all is illustrated in Fig. 6.6 and Fig. 6.7, for the NC π^0 non-coherent of the 2γ and 1γ final selection stages. A list of

[2]The overarching Monte-Carlo for MicroBooNE simulation

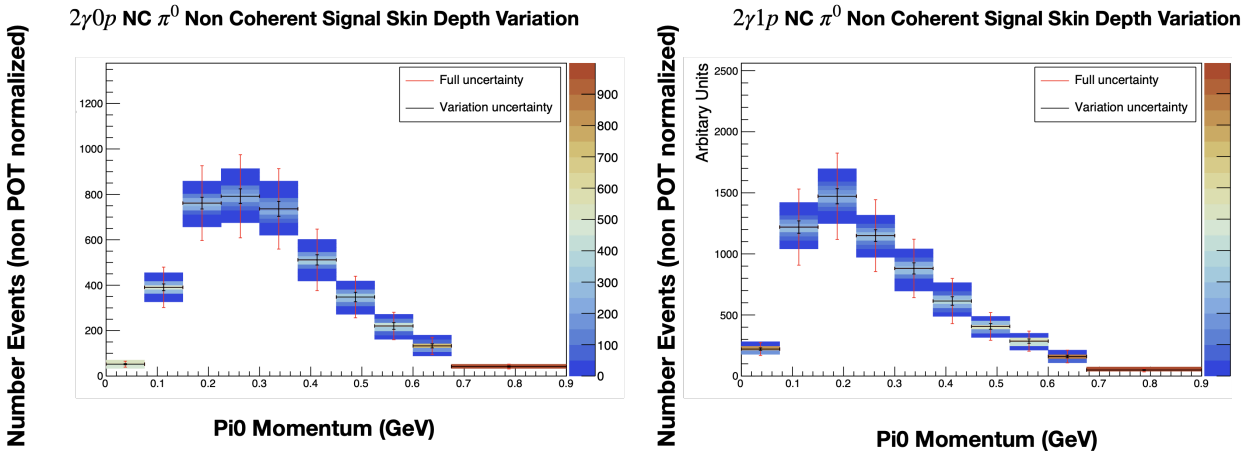

Figure 6.1: A variation plot illustrating the skin depth flux uncertainties' effect on the NC π^0 non-coherent signal in the final $2\gamma 0p$ (left) and $2\gamma 1p$ (right) selections. The color z scale represents the density of multisims or reweighted iterations that land in that particular bin thus giving a visual representation of the spread of prediction created by this underlying systematic uncertainty.

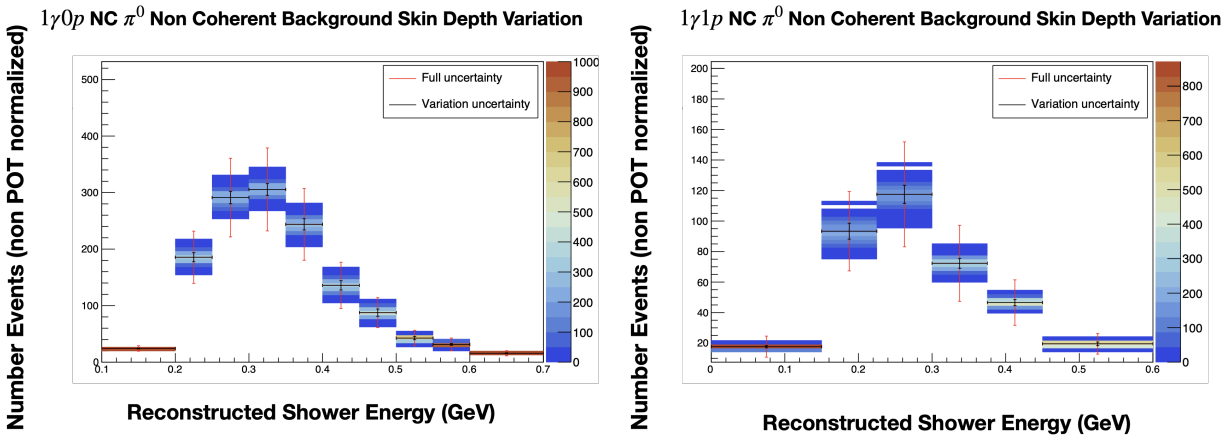

Figure 6.2: A variation plot illustrating the skin depth flux uncertainties' effect on the NC π^0 non-coherent background in the final $1\gamma 0p$ (left) and $1\gamma 1p$ (right) selections. The color z scale represents the density of multisims or reweighted iterations that land in that particular bin thus giving a visual representation of the spread of prediction created by this underlying systematic uncertainty.

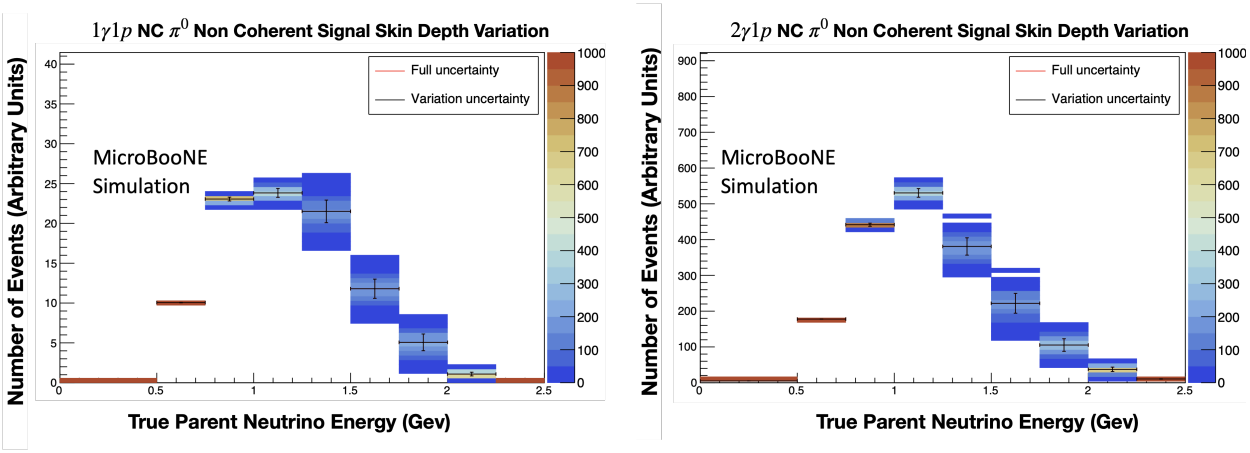

Figure 6.3: A variation plot illustrating the skin depth flux uncertainties' effect on the NC π^0 non-coherent background in the final $1\gamma1p$ (left) and $2\gamma1p$ (right) selections, but with the x axis now representing the true parent neutrino energy so that the energy dependence of the effect is visible.

Table 6.3: Table of combined flux systematics on each final selection subsample. A hyphen represents an empty sample. The OTPCinc sample in the last column refers to true neutrino events outside the TPC volume.

Variation	**BNB Other**	**CC1π^0**	**Dirt**	**NCΔRad**	**NC1π^0 Coh**	**NC1π^0 NotCoh**	**CCν_e**	**OTPCinc**
$2\gamma1p$	8.65	6.32	8.17	7.13	14.95	7.50	6.60	8.04
$2\gamma0p$	8.73	6.11	5.15	6.59	8.21	7.20	6.31	7.89
$1\gamma1p$	9.07	7.16	-	6.45	-	7.35	10.87	-
$1\gamma0p$	7.81	7.20	7.63	6.59	7.27	7.04	8.42	8.86

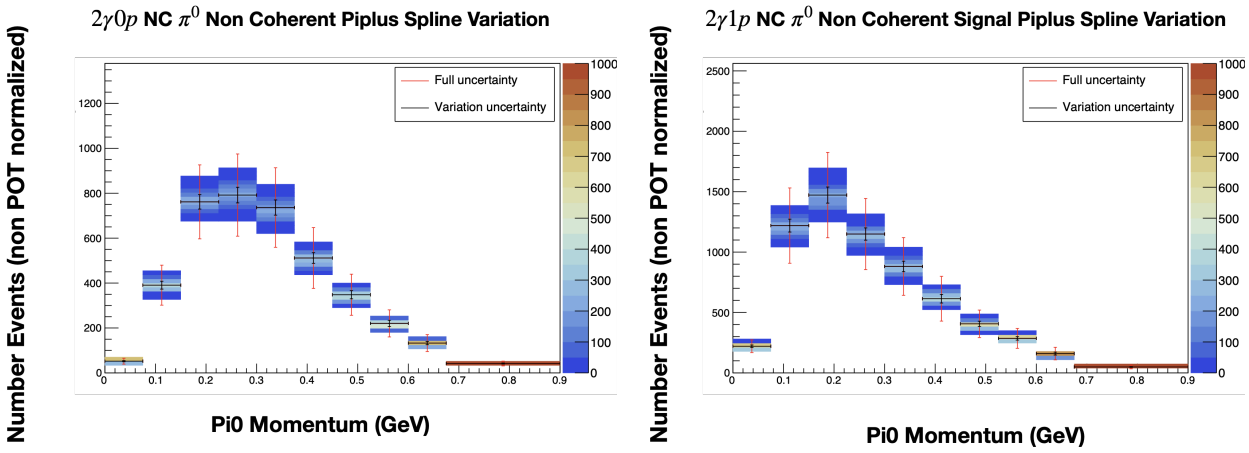

Figure 6.4: A variation plot illustrating the central Sanford Wang π^+ flux uncertainty effect on the NC π^0 non-coherent signal in the final $2\gamma 0p$ (left) and $2\gamma 1p$ (right) selection. The color z scale represents the density of multisims or reweighted iterations that land in that particular bin thus giving a visual representation of the spread of prediction created by this underlying systematic uncertainty.

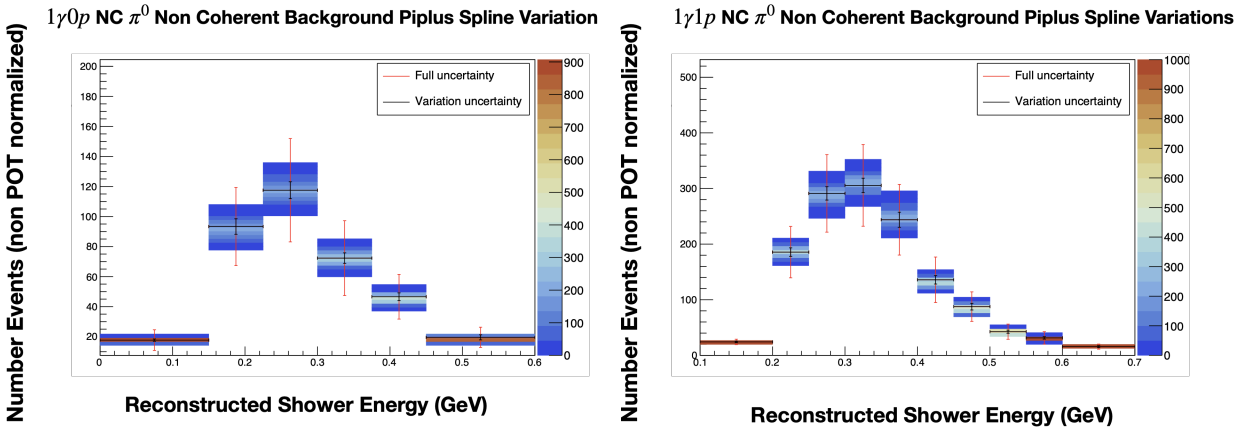

Figure 6.5: A variation plot illustrating the central Sanford Wang π^+ flux uncertainty effect on the NC π^0 non-coherent background in the final $1\gamma 0p$ (left) and $1\gamma 1p$ (right) selection. The color z scale represents the density of multisims or reweighted iterations that land in that particular bin thus giving a visual representation of the spread of prediction created by this underlying systematic uncertainty.

the final cross section knobs used is shown in Tab. 6.4. GENIE_all and the minimum and maximum variations are the only variations used for results shown in this thesis. Tab. 6 in App. A shows the components of GENIE_all individually.

A large component of the combined GENIE uncertainty is the Neutral Current Resonant Axial Mass which is an important source of systematic uncertainty as it is a variation on the form factor for our primary signal both for the 2γ and 1γ selections. It nominally has the value of $M_A^{ResAxial} = 1.07$ GeV and it enters in the cross section calculation via the form factor $1/(1 + Q^2/M_A^2)$, where Q is the four-momentum transfer in the interaction. Currently (for this analysis), it is assigned an uncertainty of $\pm 20\%$ as the formulation here was effectively copied from the CC Resonance Axial Mass which was measured in Argonne National Laboratory (ANL) and Brookhaven National Lab (BNL) bubble chambers. The factor was allowed to float freely and inherited the same uncertainty value of 20% without direct experimental justification, so it may be overestimated.

For the purpose of evaluating the size of specific cross section systematic uncertainty, individual GENIE cross section variations are run in pm1sigma[3] mode with two multisims at $+1\sigma$ and -1σ of the known uncertainty. For cross section uncertainty only the GENIE_all and these supplemental model parameters which do not lend themselves to the GENIE_all multisim approach are used for the constraint and other measurements. These parameters have been developed by the systematics and GENIE analysis groups to account for various effects. For each of these, one of the two (minimum or maximum) variations stored by EventWeight corresponds to the tuned central value (CV). Therefore there is only one weight value distinct from the CV. The only exception is the RPA_CCQE_UBGENIE variation where both minimum and maximum are distinct from the central value. The XSecShape_CCMEC_UBGENIE variation was removed upon discovery of some issues in its calculation[4]. In this mode, the uncertainty is defined as the absolute difference between two extremes rather than relative to a particular CV. The uncertainty of the combined GENIE variation can be found in Table 6.5, and the combined uncertainty of the supplemental

[3]EventWeight definition

[4]Following the production of our samples and use in the GENIE MicroBooNE tune, issues were discovered with this knob producing nonsensically large weights. Discussion with cross section experts and the GENIE_tune group indicate the impact should not effect the validity of our analysis as anomalous weights have been removed and meson exchange current (MEC) events have a low impact on our analysis.

Table 6.4: Description of cross sections reweightable systematics used in final uncertainty calculations.

Variation Label	**Description**
All_UBGenie	All multisim mode GENIE variables combined
Min/Max Mode	Variations
NormCCCOH_UBGenie	Normilization for CC Coherent Processes (in developement)
NormNCCOH_UBGenie	Normilization for NC Coherent Processes (in developement)
RPA_CCQE_UBGenie	Strength of RPA correction for central tune
Theta_Delta2Npi_UBGenie	Variation of angle of pion with respect to detector z axis
VecFFCCQEshape_UBGenie	VecFFCCQEshape_ UBGenie
DecayAngMEC_UBGenie	Changes angular distribution of nucleon cluster
AxFFCCQEshape_UBGenie and z-expansion.	Varies CCQE axial form factor model between dipole (CV)

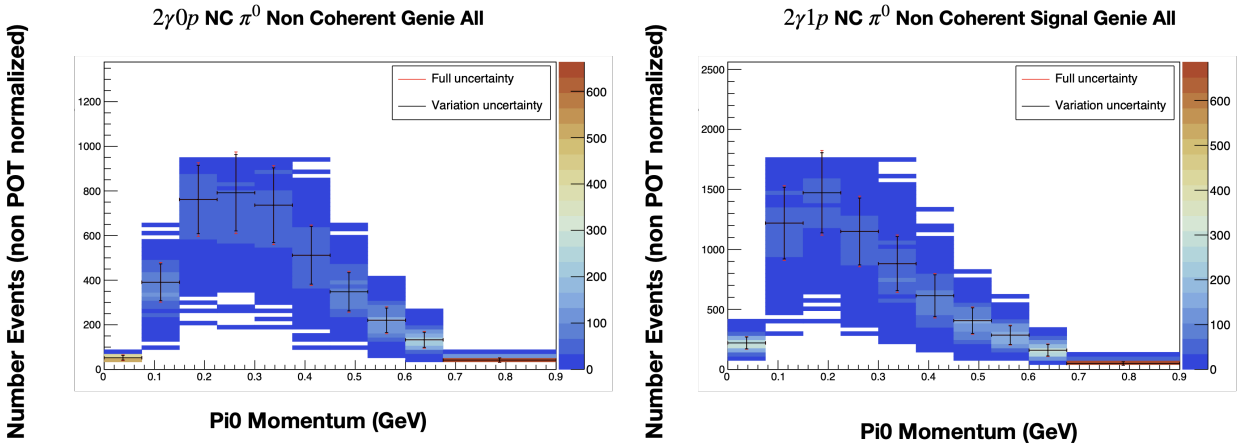

Figure 6.6: A variation plot illustrating the GENIE_all uncertainties' effect on NC π^0 non coherent component in the final $2\gamma 0p$ (left) and $2\gamma 1p$ (right) selection. The color z scale represents the density of multisims or reweighted iterations that land in that particular bin thus giving a visual representation of the spread of prediction created by this set of underlying systematic uncertainties.

variations can be found in Table 6.6. Further information on each individual variation is included in App. A where Tables 2 through 5 provide the fractional error on final stage selections from each source of systematic uncertainty for the $2\gamma 1p$ study, broken down by component sub-samples. Tables 7−14 in App. A show the variations contained within the combined GENIE variation.

Summary of Cross Section Systematics

Cross-section systematics are the dominant reweightable systematics. While not as thoroughly investigated as the flux systematics, there has been a robust effort by GENIE and MicroBooNE collaborators to improve the systematic uncertainty predictions for cross section. The highest consistent uncertainty is from GENIE systematics (GENIE_all) and more specifically $M_A^{ResAxial}$ reaching up to 30%, but we have discussed why underlying assumptions for it may be inaccurate. Unfortunately, without new data this does not itself present a method for reduction, but the constraint estimation method described in Sec. 6.4.1 is very powerful on this uncertainty in our signal region reducing it to ∼10%.

6.2.5 Total Flux and Cross Section Tables

The final values for flux and cross section systematics are shown in Tables 2, 3, 4, and 5 in App. A for each of the four samples. As previously described, the individual components of GENIE_all are also included in App. A, Tab. 7-14, but these have not been reproduced at the current iteration of our analysis as they are not essential to our final fitting. There is a large factor from the NormCCCOH (normalization charged-current coherent processes) knob in several NC π^0 coherent sub-samples. This is believed to be a result of low statistics of those particular sub-samples and that this knob would have strong effect on virtually the entirety of those types of events. It was determined to not be an issue based on its low impact to our sensitivity given its low statistics.

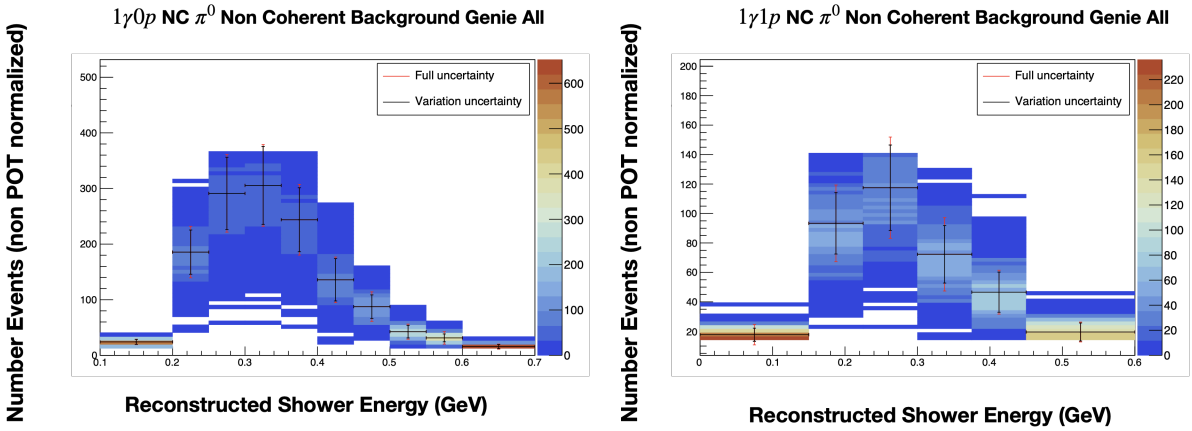

Figure 6.7: A variation plot illustrating the GENIE_all uncertainties' effect on NC π^0 non-coherent component in the final $1\gamma 0p$ (left) and $1\gamma 1p$ (right) selections. The color z scale represents the density of multisims or reweighted iterations that land in that particular bin thus giving a visual representation of the spread of prediction created by this set of underlying systematic uncertainties.

Table 6.5: Table summarising the combined GENIE systematic (GENIE_all) on each final selection subsample. A hyphen represents an empty sample, and a zero means that the sample in question was not effected by the variation.

Variation	**BNB Other**	**CC1π^0**	**Dirt**	**NCΔRad**	**NC1π^0 Coh**	**NC1π^0 NotCoh**	**CCν_e**	**OTPCinc**
$2\gamma 1p$	14.91	25.01	16.02	28.05	0.00	24.56	15.79	16.78
$2\gamma 0p$	16.11	27.19	20.29	24.93	0.00	22.12	22.36	18.22
$1\gamma 1p$	17.46	24.16	-	25.56	-	24.40	17.10	-
$1\gamma 1p$	16.56	26.89	15.34	23.26	0.00	22.60	20.01	19.63

6.2.6 Flux and Cross Section Covariance Matrices

Covariance is the joint variability between two variables as we discussed in Sec. 6.1. Covariance matrices store this information for each bin of of each signal in our samples. Correlation matrices are easily calculated from covariance matrices by dividing each entry by the product of the contributing bins' standard deviations. Correlation matrices are more visually readable defining the correlation (representing similarity in behavior under variation) between the same bins. A simple illustration of a correlation matrix is shown in Fig. 6.8.

Final covariance and correlation matrices are used to add uncertainty to our predictions and will ultimately be used for our NC π^0 constraint (estimation described in Sec. 6.4.1) and for final fits described in Sec. 6.4. For illustration, observe the produced matrices for GENIE_all in Figs. 6.9 and 6.10, which is the most dominant systematic. The combined flux and cross section fractional covariance matrix, and full covariance matrix for all four final selected samples are shown in Figs. 6.11, 6.12, and 6.13, respectively. In each of these, all sub-selections listed in Sec 6.2.2 are re-combined into larger signals i.e., $1\gamma1p$. The plotted variables and binning were chosen to optimize the constraint analysis explained in Sec. 6.4.1. A few features can be noted in the correlation matrices which are more visually readable than covariance matrices. The high correlations observed between the more populated bins of the $2\gamma1p$ and $1\gamma1p$ indicate the constraining power of the $2\gamma1p$ analysis as the most significant background. Lower correlations are generally due to lower statistics in that region. Also, the generally high correlations between bins of the same sub-sample indicate that the samples are well selected since events behave similarly under variations.

6.3 Non-Reweightable Systematics

In the previous iteration of the MC production in MicroBooNE (referred to as MCC8), detector response was defined by varying detector response associated parameters, such as ionization electron diffusion, prior to creating simulated samples. Due to the computational requirements, only samples varied with 1σ from the central value were created (known as

Table 6.6: Table of combined contribution of each min-max formatted GENIE variation on each final selection subsample. A hyphen represents an empty sample. Note while the NC1π^0Coh variation appears to have a large uncertainty, it is entirely from a single variation: NormNCCOH (see Appendix A). Due to the smallness of the sample, it should not have a large impact on final uncertainty and fitting.

Variation	**BNB Other**	**CC1π^0**	**Dirt**	**NCΔRad**	**NC1π^0 Coh**	**NC1π^0 NotCoh**	**CCν_e**	**OTPCinc**
$2\gamma 1p$	1.70	3.85	5.96	0.00	87.37	1.48	10.93	6.67
$2\gamma 0p$	4.05	4.54	13.33	0.00	20.87	1.44	22.57	3.81
$1\gamma 1p$	9.38	69.08	-	0.00	-	6.48	26.83	-
$1\gamma 0p$	4.54	5.55	7.91	0.00	33.79	0.46	14.35	5.73

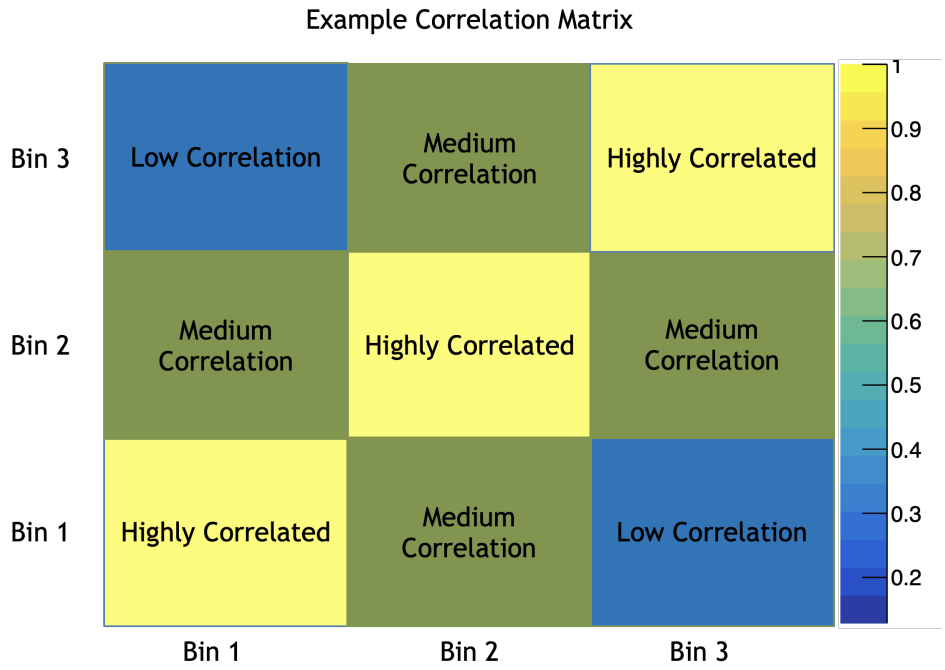

Figure 6.8: A simple illustration of a correlation matrix.

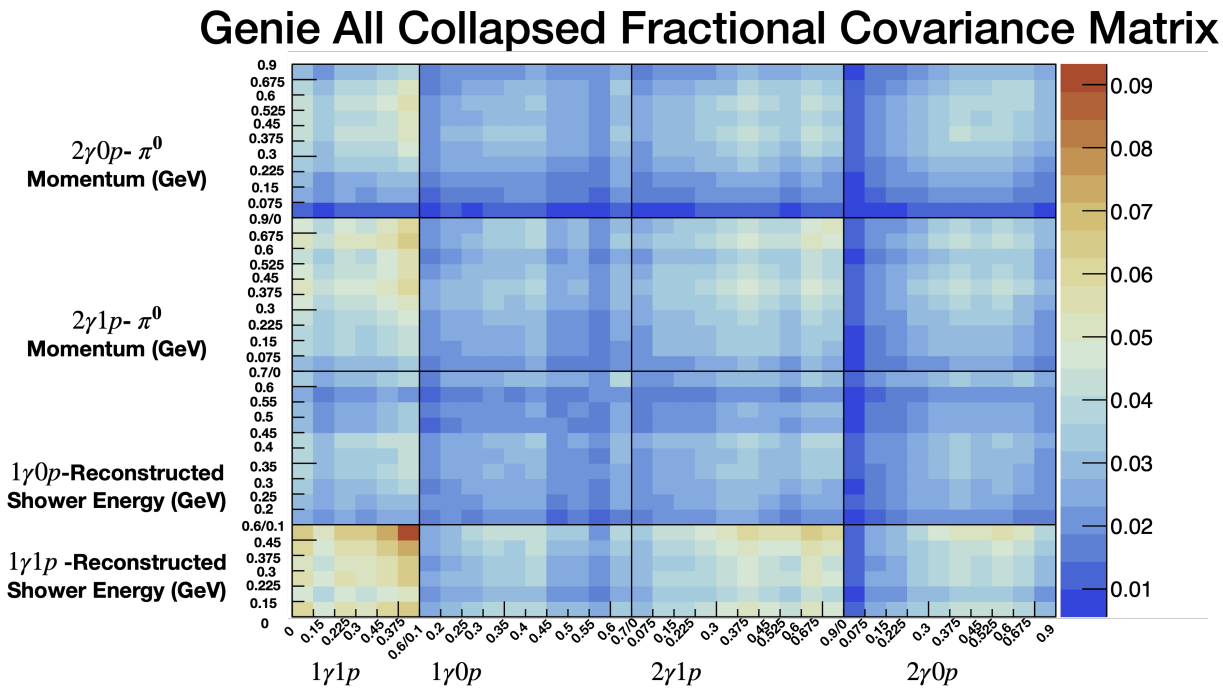

Figure 6.9: The fractional covariance matrix for the GENIE_all version of cross section systematic uncertainties, constructed for the four final selected samples side by side. Unlike a summed combination of the individual matrices, the GENIE_all covariance matrix more properly accounts for correlations among different systematic knobs. The single-photon samples are each binned in 5 and 3 bins of shower energy, for $1\gamma 0p$ and $1\gamma 1p$, respectively, and the NC π^0 samples are each binned in 8 bins of NC π^0 momentum.

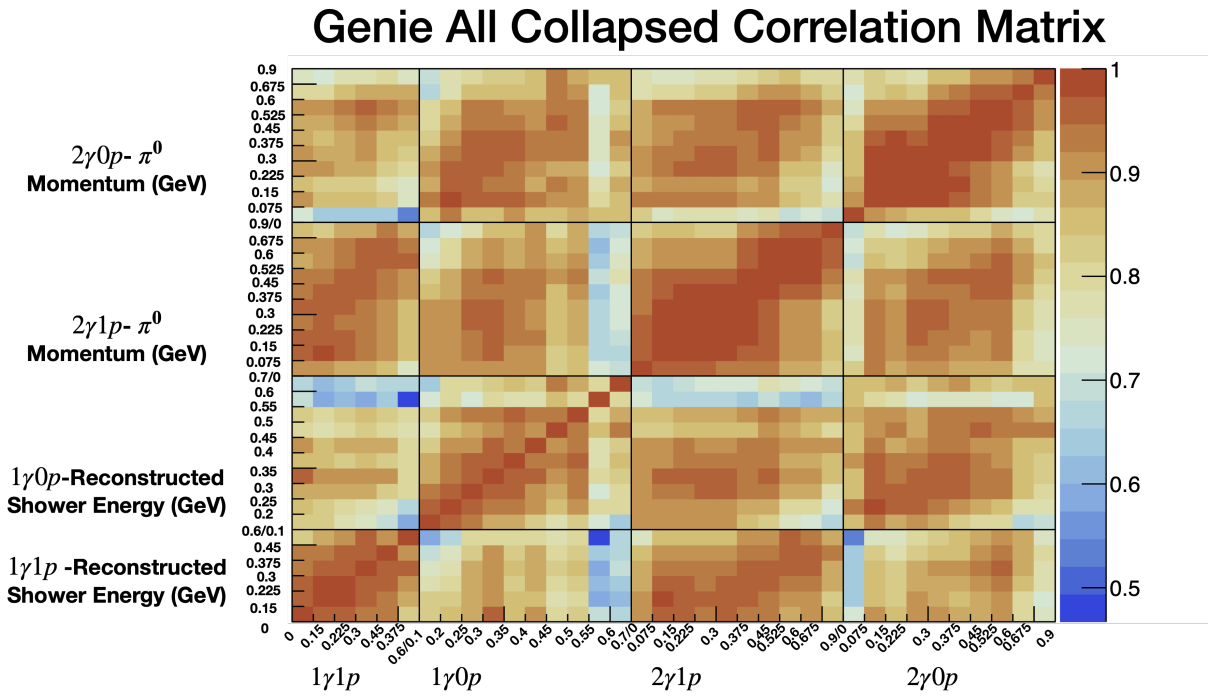

Figure 6.10: The correlation (matrix for the GENIE_all version of cross section systematic uncertainties, constructed for the four final selected samples side by side. Unlike a summed combination of the matrices, the GENIE_all correlation matrix more properly accounts for correlations among different systematic knobs. The single-photon samples are each binned in 5 and 3 bins of shower energy, for $1\gamma 0p$ and $1\gamma 1p$, respectively, and the NC π^0 samples are each binned in 8 bins of NC π^0 momentum.

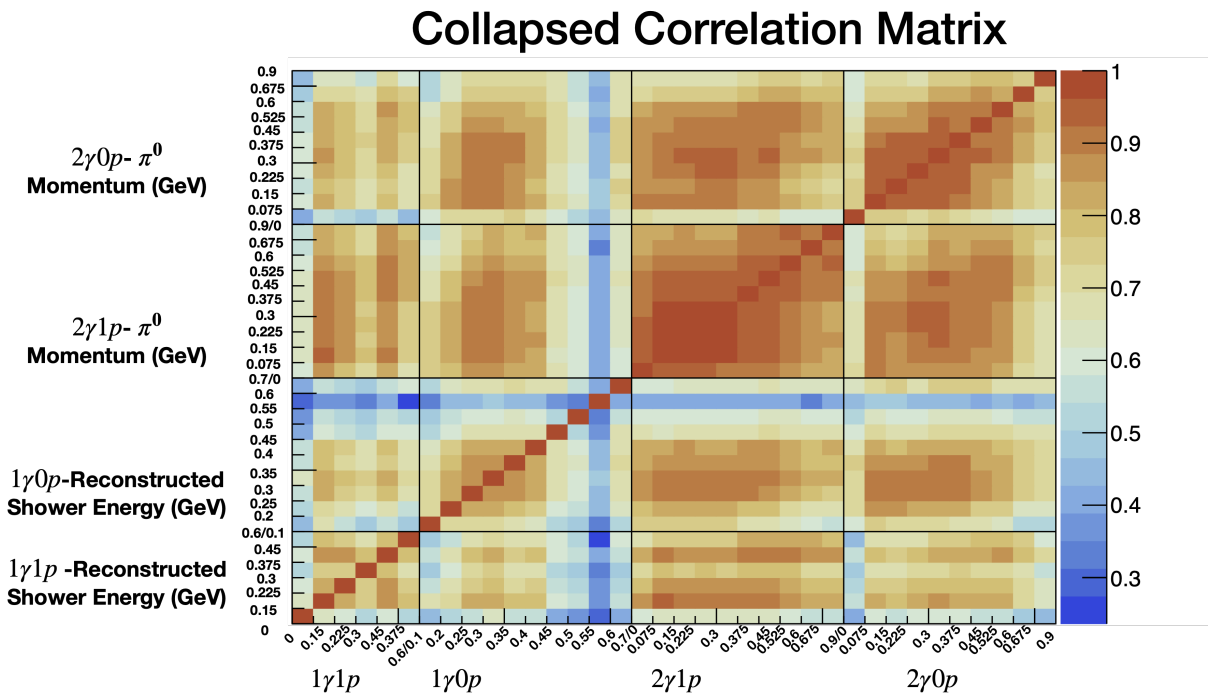

Figure 6.11: Collapsed flux and cross section correlation matrix of the final $2\gamma 1p$, $2\gamma 0p$, $1\gamma 1p$, and $1\gamma 0p$ selections. Note that the color scale (indicating the correlation strength) starts at 25% correlated, with the correlations between the primary constraint and signal channels $2\gamma 1p$ and $1\gamma 1p$ being >70% in bins, with the most populated bins being correlated by >90%. This exceptionally high correlation is what allows the dramatic reduction in flux and cross section systematics for the signal channels.

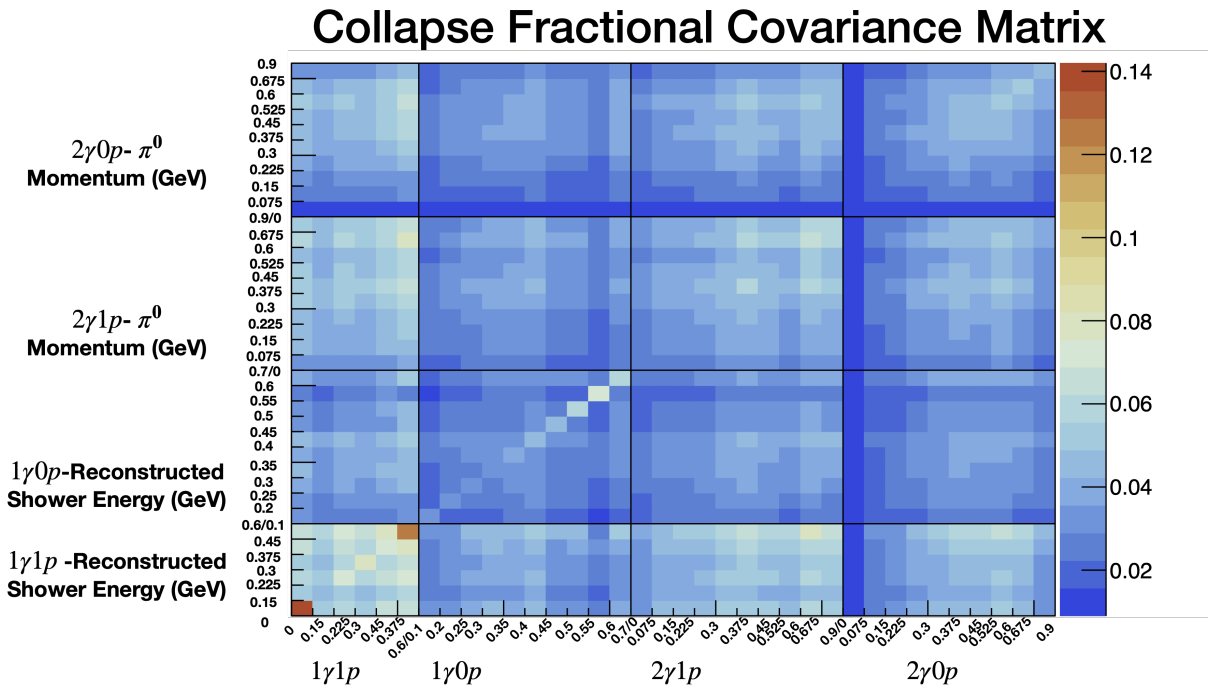

Figure 6.12: Collapsed flux and cross section fractional covariance matrix of the final combined $2\gamma 1p$, $2\gamma 0p$, $1\gamma 1p$, and $1\gamma 0p$ selections. Overall, flux and cross section systematic uncertainties never exceed $\sim$15% fractional covariance.

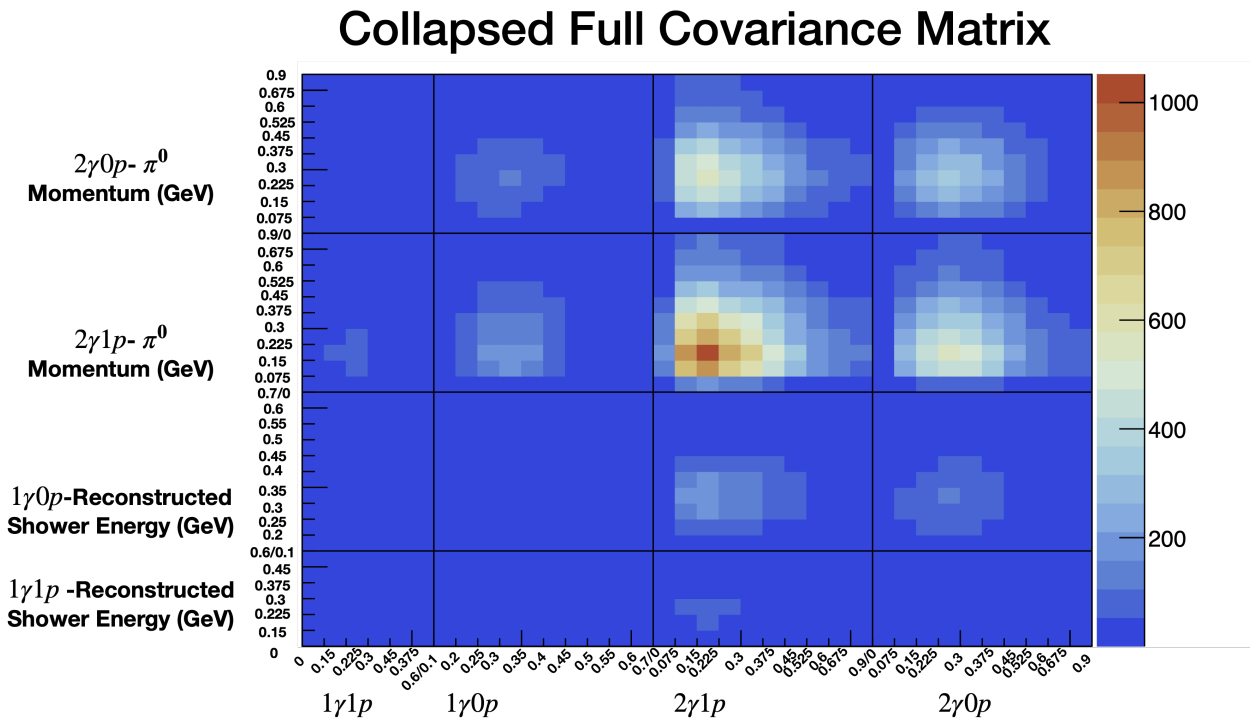

Figure 6.13: Collapsed flux and cross section full Covariance matrix of the final $2\gamma 1p$, $2\gamma 0p$, $1\gamma 1p$, and $1\gamma 0p$ selections (all sub-selection background samples combined).

unisim format). These were used to create systematic covariance matrices

$$M_{ij} = \sum_{k=1}^{S} (N_i^{CV} - N_i^k) \cdot (N_j^{CV} - N_j^k) \tag{6.4}$$

where M_{ij} is the element of covariance matrix M for row i and column j, S is the number of uni-sims, N_i (N_j) represents the number of POT weighted events in bin i (j) of the corresponding histogram, and CV refers to the central value sample. In the most recent MC production, referred to as MCC9, the novel wire-modification method allows for more complete and efficient estimation of some detector response uncertainties. The method characterizes the detectors response in terms of the charge magnitude (Q_{hit}) and width (σ_{hit}) of Gaussian hits on wires for various effects (see Fig. 6.14). These values are used to define continuous ratio functions $R_Q^{(data/MC)}$ and $R_\sigma^{(data/MC)}$ seen in Fig. 6.15. These continuous ratio functions can then be applied to Monte-Carlo events to match the data. In this way, even effects that are unknown or difficult to simulate in Monte-Carlo can still be applied. This method is also applied post-deconvolution for reduced computing time required to produce variation samples.

Naturally, systematic effects not pertaining to wires still require other methods. Thus modern detector systematics are produced in three categories: LArTPC wire related systematics, photo-multiplier light yield (LY) related systematics, and *other* systematics for any source of systematic uncertainties not included in the first two categories. These primary categories are separated into further subcategories. The wire systematics (using the wire-modification method) are defined via the detector coordinate system for the wire modification X variation defining effects related to the detector x coordinate (direction of electron drift), and then the effects on the other two coordinates are merged for the wire modification YZ variation. Likewise, angle effects are defined for the track angles θ_{XZ} and θ_{YZ}, called AngleXZ and AngleYZ. In the Light Yield (LY) category, there are samples that include a 25% reduction in light yield. Other variations are light yield attenuation (LYAtt) and light yield Rayleigh scattering length (LYRay). The category of other detector effects includes the space charge effects (SCE) variation and electron-ion recombination (Recom2) variation. Detector systematic samples have been produced for Run 1 and Run 3 of MicroBooNE.

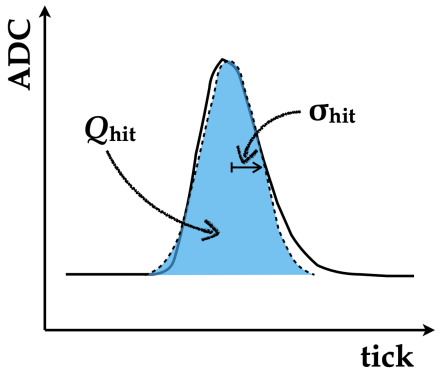

Figure 6.14: Schematic of a hit: The blue region represents fitting the hit with a Gaussian function, where Q_{hit} and σ_{hit} are the integrated area (charge) and standard deviation from the Gaussian fit, respectively.

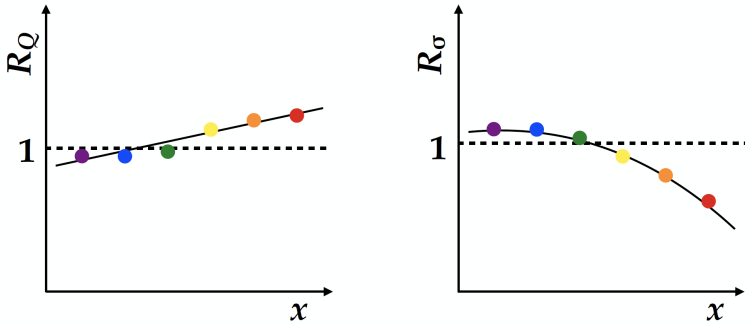

Figure 6.15: Schematics of data to MC ratio of Q_{hit} and σ_{hit} with respect to detector X coordinate. The obtained continuous functions R_Q and R_σ are used to modify the MC event hits.

However, Run 1 has an incomplete set of detector effects, and the existing samples also suffer from other issues. Most were produced before the inclusion of Space Charge and recombination, and the Light Yield variations were produced with a different central value which could introduce a bias to our analysis. Therefore, information presented here is solely from the Run 3 analysis.

6.3.1 Detector Systematics Selections

The process for producing the $1\gamma 1p$ and $1\gamma 0p$ samples is identical to what is described in Ch. 5, except it is run over smaller systematically varied samples. Table 6.7 summarizes the percentage uncertainties assessed on each 1γ sub-sample at final selection stage. Detector variations, again have small effect on the NC Δ signal with the largest individual uncertainty being 3.75% in $1\gamma 1p$ and 4.02% in $1\gamma 0p$ from Recom2. The effect for NC π^0 non-coherent is also relatively small, $\sim$5.5% from WireX is the largest contribution. For the final stage ν_e samples, low statistics begin to impact performance, and for CC π^0 and BNB-other samples, the statistics are too low for systematics to be meaningful although the values are still calculated. For Dirt (Inside Cryostat) and NC π^0 coherent, it is even impossible to extract the percentage difference, as no event survives at this stage.

The method for NC π^0 samples is identical and the results are comparable. However, the pre-selection study statistics allow for finer binned studies to explore if some of the observed data-MC disagreements are covered by any systematic in particular. The final stage systematics are shown in Tab. 6.8.

6.3.2 Detector Systematics in the Final Selections

While the flux and cross-section reweightable uncertainties are calculated using the same (high-statistics) Monte Carlo samples that make up the final selection, the detector systematics samples themselves are substantially smaller in statistics. While this is especially evident for the general BNB beam sample, even some of the dedicated high-statistics samples, such as CC π^0, have low statistics at the final selection stage. These statistics were further reduced by the requirement that we remove MC events that were included in BDT training

Table 6.7: Percent (%) shifts in number of events for each 1γ sub-sample, for each systematic variation, defined as $(N^{var} - N^{CV})/N^{CV} \times 100\%$, at the final selection stage. As noted before, the first two samples, NC Δ and NC π^0 Non-Coherent are both primary components and also the only two high statistics detector variation samples that would be most robust to statistical variations. The combined (summed in quadrature) detector normalization uncertainty for NC Δ and NC π^0 non-coherent are **6%** and **12%** respectively. For other sub-samples, the statistics are too low at this stage and although the percentage differences can be obtained for some of them, they are not usable to assert the detector systematics.

Sub-sample $1\gamma 1p$	**WireX**	**WireYZ**	**AngleXZ**	**AngleYZ**	**LY**	**LYAtt**	**LYRay**	**SCE**	**Recom2**	**Tot**
NC Δ	0.840	1.264	1.463	3.229	0.320	2.14	0.938	1.124	3.754	5.982
NC $1\pi^0$ Not Coh	5.485	2.5	2.893	0	1.24	5.085	1.282	6.881	4.741	11.98
NC $1\pi^0$ Coh	-	-	-	-	-	-	-	-	-	-
Dirt(Inside Cryostat)	-	-	-	-	-	-	-	-	-	-
CC ν_μ $1\pi^0$	30	40	10	30	20	0	0	11.11	50	80.77
Intrinsic $\nu_e/\bar{\nu}_e$	3.226	0	0	10	3.226	3.333	-	28.57	23.08	38.48
BNB Other	0	50	50	0	50	0	100	200	300	384.1

Sub-sample $1\gamma 0p$	**WireX**	**WireYZ**	**AngleXZ**	**AngleYZ**	**LY**	**LYAtt**	**LYRay**	**SCE**	**Recom2**	**Tot**
NC Δ	3.073	1.324	1.839	0	0.089	0.246	0.350	3.211	4.027	6.426
NC $1\pi^0$ Not Coh	1.716	7.453	3.226	3.39	0.614	2.24	0.161	0.169	0.162	9.267
NC $1\pi^0$ Coh	5.682	4.598	1.136	3.409	2.273	4.651	0	18.52	14.29	25.3
Dirt(Inside Cryostat)	5.128	26.83	9.524	7.317	4.762	5.128	2.564	52.94	84.21	104.1
CC ν_μ $1\pi^0$	19.15	10.42	2.128	0	21.28	23.4	2.128	9.091	19.05	43.93
Intrinsic $\nu_e/\bar{\nu}_e$	5.439	0.402	5.19	4.743	0.569	0.402	0.193	2.582	9.281	13.13
BNB Other	0	8.696	18.18	26.09	4.348	9.091	18.18	13.33	25	48.18

to avoid bias. While the NC Δ radiative samples in our 1γ selections and our most important backgrounds (NC π^0 Non-Coherent) in all selections have substantial MC statistics, all remaining backgrounds have fewer than an average of 100 MC entries per bin at the final selection, with the BNBOther sub-sample containing only a couple of MC entries in the $1\gamma 1p$ final selection. Sub-samples with less than 100 events per bin show extremely large fluctuations between detector CV and individual detector systematic variations and thus cannot reliably be used to estimate detector uncertainty on them. The strategy employed to mitigate this is to use the final selection sub-samples to estimate the uncertainties for the high-statistics signal NC Δ Radiative events, and for our primary background of NC π^0 Non-Coherent events, but for the remaining lower statistics sub-samples, we construct the covariance matrices using pre-BDT samples which have much higher statistics.

Theoretically the construction of covariance matrices from detector variation unisims, does yield meaningful correlations between bins, due to being overwhelmed by individual variations, it is likely they do not represent true correlations in our samples. It was decided to make a conservative estimate (meaning minimizing the power of the constraint) for detector systematics by treating all bins as uncorrelated. Therefore, the process for total detector uncertainty can be characterized as the bin-by-bin absolute fractional difference between an individual detector variation sample and the detector CV, summed in quadrature over all detector systematics. With this method, the final correlation matrices are shown in Fig. 6.16. The $1\gamma 1p$ selection is placed in a single bin due to low statistics, but this should be acceptable given the analysis goal of searching for a flat increased rate of NC Δ radiative decay. A comparison of the scale of detector systematic sources with others is shown in Fig. 6.17.

6.3.3 Photonocuclear Absorption Uncertainties

There is another category of systematic uncertainties provided in the Monte Carlo known as GEANT4 dealing with interactions beyond the nucleus. These determine individual final states for a given interaction which is less well modeled by adjusting the weight or likelihood of occurrence, making the EventWeight method impractical. However, it was decided to include GEANT4 photonuclear absorption uncertainties which have a potentially high impact

Table 6.8: Percent (%) shifts in number of events for each 2γ sub-sample, for each systematic variation, defined as $(N^{var} - N^{CV})/N^{CV} \times 100\%$, at the final selection stage. The *Tot* column shows the quadrature sum of all individual detector effects.

Sub-sample $2\gamma 1p$	**WireX**	**WireYZ**	**AngleXZ**	**AngleYZ**	**LY**	**LYAtt**	**LYRay**	**SCE**	**Recom2**	**Tot**
NC Δ	5.788	0.649	0.971	2.903	1.967	0.851	0.321	5.804	8.803	12.62
NC $1\pi^0$ Not Coh	2.477	0.818	1.282	0	0.083	0.713	0.238	1.092	1.138	3.392
NC $1\pi^0$ Coh	8.824	3.03	17.65	2.857	0	2.941	3.03	16.13	17.65	31.56
Dirt(Inside Cryostat)	13.46	1.923	8	13.46	20.37	15.09	5.556	66.67	63.16	97.66
CC ν_μ $1\pi^0$	3.636	0	6.115	4.762	4.676	6.939	0	2.703	8.547	14.96
Intrinsic $\nu_e/\bar{\nu}_e$	0.980	1.737	2.439	0.488	1.869	4.265	3.073	10	10.39	15.78
BNB Other	6.569	11.68	6.818	1.429	3.676	5.109	0.709	54.72	60.66	83.31
Sub-sample $2\gamma 0p$	**WireX**	**WireYZ**	**AngleXZ**	**AngleYZ**	**LY**	**LYAtt**	**LYRay**	**SCE**	**Recom2**	**Tot**
NC Δ	12.74	3.846	0	1.911	1.923	3.54	3.185	1.504	9.79	17.47
NC $1\pi^0$ Not Coh	1.231	1.553	1.004	1.2	0.421	0.751	0.817	1.031	2.566	3.928
NC $1\pi^0$ Coh	2.671	7.396	1.17	0	1.166	5.325	2.115	5.466	0.926	11.32
Dirt(Inside Cryostat)	5.618	4.494	12.5	1.205	0	3.371	3.448	15.22	4	21.92
CC ν_μ $1\pi^0$	0	2.439	2.439	10.92	6.504	10.26	3.252	23.85	3.774	29.54
Intrinsic $\nu_e/\bar{\nu}_e$	4.828	2.069	3.448	8.163	7.947	11.92	1.351	22.41	1.667	28.61
BNB Other	30.51	3.279	16.07	8.333	15	19.35	6.557	16	16	49.23

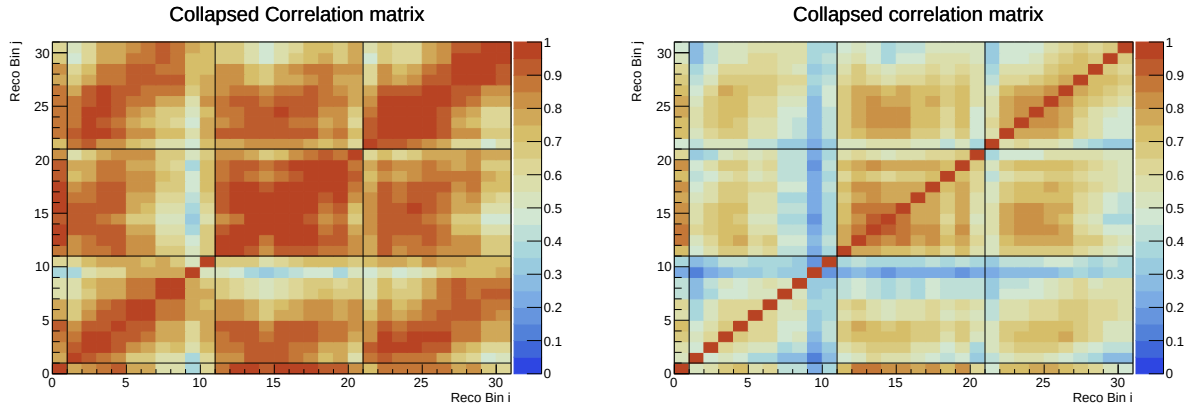

Figure 6.16: The collapsed correlation matrix between all four samples at final selection stage, $1\gamma 1p$, $1\gamma 0p$, $2\gamma 1p$, and $2\gamma 0p$, respectively, from left to right. The left matrix has only GENIE interaction and flux uncertainties included, and the right plot shows the effect of including the uncorrelated detector systematics. Higher energy bins of $1\gamma 0p$ show a significantly reduced correlation factor, due to the wash-out effect of the larger detector systematics in this region, however, the correlations between the primary signal $1\gamma 1p$ selection and the 2γ selections, although reduced, remain extremely high in the 80−90% range.

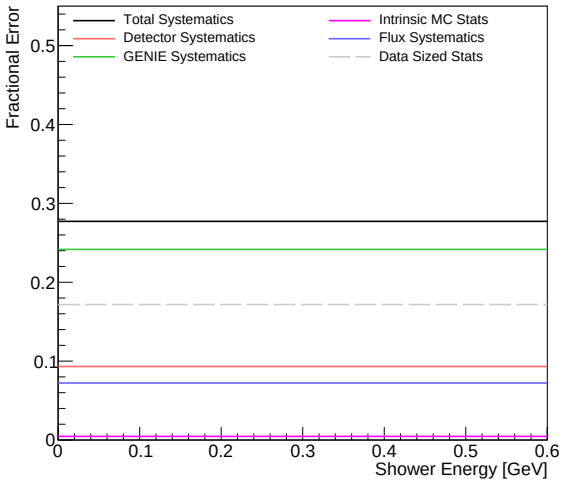

(a) $1\gamma 1p$

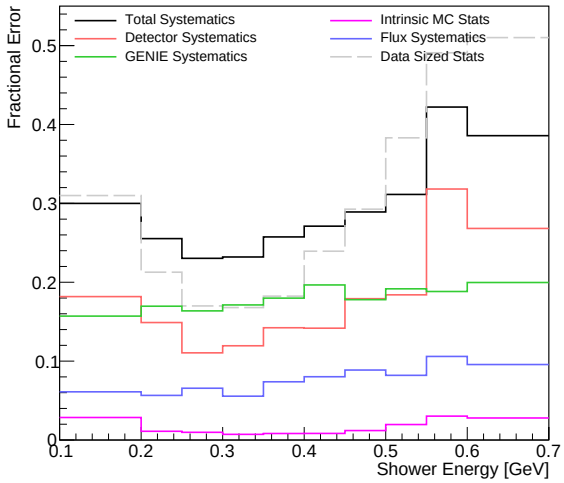

(b) $1\gamma 0p$

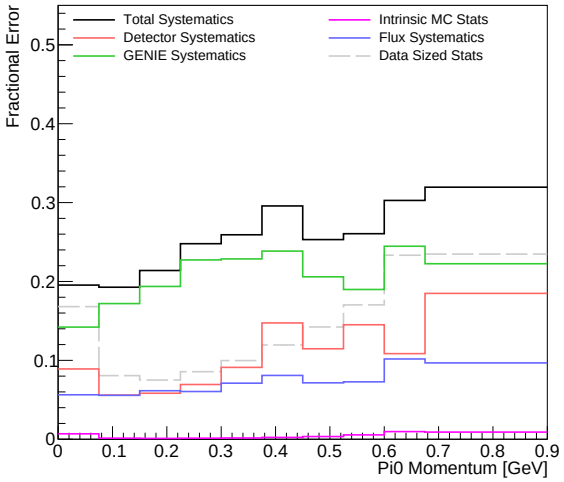

(c) $2\gamma 1p$

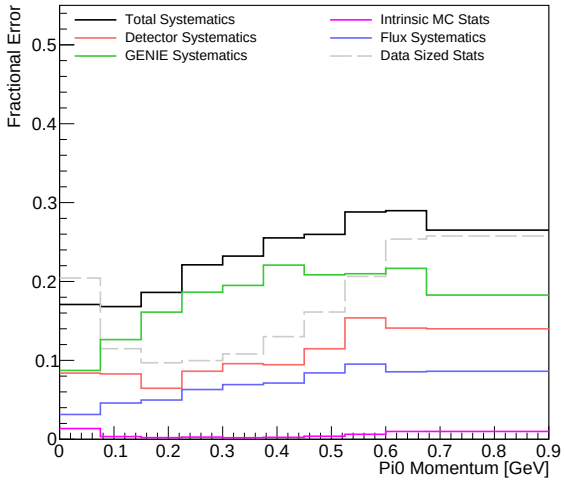

(d) $2\gamma 0p$

Figure 6.17: A summary of the systematics included on the final four selections before applying the conditional constraint. The blue, green and red curves represent flux, cross section (GENIE) and detector systematics respectively. The black curve is the total systematics. The magenta and dashed grey are intrinsic MC statistics and data sized statistical uncertainties estimated by $\sqrt{N}$, where N represents the number of events. Overall, systematics are between 20% to 30% in the primary bins of interest; however, for the main signal of the $1\gamma 1p$, the dominant systematic is the cross section uncertainty (GENIE), which is what is primarily constrained by the associated 2γ selections.

on our analysis. This effect at first order creates a topologically-irreducible background to single photons by removing one of the photons in an NC π^0 decay via nuclear absorption on Argon. The rate of this process for photon energies ranging between 0-500 MeV is 0.366%, determined using photons from the raw generated NC π^0 sample in the cryostat.

The photon energy distribution from NC π^0 decays in MicroBooNE is shown in Fig. 6.18, and the photonuclear absorption cross section dependence on photon energy is shown in Fig. 6.19. The largest contribution to single-photon backgrounds is expected from the giant dipole resonance (GDR) region. An increase in the absorption cross section would lead to an increase in NC π^0 background in our signal region. To calculate a systematic uncertainty, a custom EventWeight module is used to apply a $\pm 30\%$ variation of the photonuclear absorption cross section to a high statistics NC π^0 sample. This module allows for event level reweighting with a photon-energy-dependent modified probability of photonuclear absorption. The weighting is given by:

$$W_{event} = \Pi_{all\ primary\ photons} W_{photon\ sur}(E) W_{photon\ int}(E) \tag{6.5}$$

where

$$W_{photon\ sur}(E) = (1 - w * P_{int}(E))/(1 - P_{int}(E)) \tag{6.6}$$

is the weight on the photons which are not undergoing photonuclear absorption, and

$$W_{photon\ int}(E) = (w * P_{int}(E))/P_{int}(E) = w \tag{6.7}$$

is the weight on the photons which are undergoing photonuclear absorption. The resulting central value prediction and $\pm 1\sigma$ variations are shown in Fig. 6.20. Covariance values were about $\sim$0.09 ($=0.3^2$) across all the bins in the covariance matrix corresponding to the photonuclear subchannel making this a very sub-dominant uncertainty compared to $\sim 20-25\%$ GENIE uncertainties, and thus it was concluded this effect would be negligible to our prediction.

6.4 Systematics Constraint and Final Results

6.4.1 Estimating the Neutral Current π^0 Systematic Constraint

An estimation of the level of constraint on the uncertainty of the final 1γ signal measurement is made by considering the NC π^0 sideband (2γ) measurements, in a way analogous to how constraints were estimated for ν_e backgrounds using observed ν_μ events in the MiniBooNE and MicroBooNE experiments. This analysis is an important proof of performance, but the method for determining final fits is actually distinct.

The constraint estimation procedure is as follows: one begins with the total covariance matrix M_{ij}, containing statistical and systematic uncertainties (and correlations) for both the 1γ background samples and the 2γ signal and background samples, which is then inverted to give M_{ij}^{-1}. The Chi-square of a combined fit is then given by

$$\chi^2 = \sum_{ij}(N_i^{data} - N_i^{MC})M_{ij}^{-1}(N_j^{data} - N_j^{MC}) \tag{6.8}$$

Here N_i^{data} represents measured events and N_i^{MC} represents simulated Monte Carlo events both per bin i of data. To estimate the power of the constraint, we use N_i^{fit} instead of N_i^{data} where N_i^{fit} represents combined fit values for 1γ and 2γ per energy bin. Minimizing the chi-square for the null-hypothesis ($\chi^2 = 0$) yields.

$$N_i^{fit} = N_i^{MC} \pm \sqrt{M_{ii}} \tag{6.9}$$

We then pull a term from the chi-square function with the assumption that $N_i^{fit} = N_i^{data}$ within statistical errors ($\sigma_i^{\text{data}} = \sqrt{N_i^{\text{data}}}$) yielding

$$\chi^2 = \sum_{ij}(N_i^{fit} - N_i^{MC})M_{ij}^{-1}(N_j^{fit} - N_j^{MC}) + \sum_i \frac{(N_i^{fit} - N_i^{data})^2}{(\sigma_i^{data})^2} \tag{6.10}$$

$$\chi^2 = \sum_{ij}(N_i^{fit} - N_i^{MC})M_{ij}^{-1}(N_j^{fit} - N_j^{MC}) + \sum_i \frac{(N_i^{fit} - N_i^{data})^2}{N_i^{data}}. \tag{6.11}$$

With a further assumption that $N_i^{data} = N_i^{MC}$ for the 2γ portion of the matrix, the second term becomes $N_i^{fit} - N_i^{MC}$ such that it can be folded back into the first expression for

$$\chi^2 = \sum_{ij}(N_i^{fit} - N_i^{MC})(M_{ij}^{-1})^{new}(N_j^{fit} - N_j^{MC}) \tag{6.12}$$

where $(M_{ij}^{-1})^{new} = M_{ij}^{-1} + 1/N_i^{MC}$ for the 2γ portion of the matrix and is unchanged in the 1γ portion.

While derivation of the process is complex, implementation is a simple matter of inverting the covariance matrix applying $(M_{ij}^{-1})^{new} = M_{ij}^{-1} + 1/N_i^{MC}$ to the 2γ portion of the diagonal and re-inverting. The new diagonal 1γ portion of the matrix will be reduced in the process of re-inverting, such that the uncertainties defined by it are now constrained uncertainties. The level of constraint (i.e. the level of uncertainty reduction) grows with increased 2γ statistics.

This method of obtaining constrained systematic uncertainties is useful in foreshadowing the level of sensitivity improvement expected from a simultaneous fit to 1γ and 2γ selections, and it is useful to consider for systematic studies. We will first study the maximum constraint achievable on the Flux and GENIE systematics in the absence of detector systematics. The GENIE uncertainties represent the largest systematics that we wish to constraint, as the underlying NC π^0 model parameters, such as the neutral current resonance axial mass have high uncertainties. The results of the constraint can be seen in Fig. 6.21. Across the entire energy range of both $1\gamma 1p$ and $1\gamma 0p$, we see very large reductions. This large reduction is perhaps unsurprising when one considers that the overall correlation factor between the 1γ and 2γ spectra in the flux and cross-section correlation matrix is above 85% in the majority of bins, as was observed in Fig 6.16.

Inclusion of detector systematics both increases the uncertainty itself, but more importantly effectively reduces the correlations between the 1γ and 2γ samples, in particular for the $1\gamma 0p$ sample. Figure 6.22 (and the same information in Tab. 6.9) are the key results of this section, showing the dramatic reduction in the bin-by-bin systematic uncertainty before and after the constraint, highlighting the performance of the 2γ selections. Systematic uncertainties of 25% in the signal region of 1γ are reduced to <20% in most bins after the 2γ constraint is applied. Further detail about the exact individual GENIE systematics that are

being constrained the most can be found in the supplementary App. B, which allows us to probe which underlying uncertainties are being constrained and which are not being aided by the 2γ sideband. The level of constraint evaluated using this method suggests one should expect a promising reduction of the systematic uncertainty on the background components of $1\gamma 1p$ and $1\gamma 0p$ samples, which are highly correlated with the $2\gamma 1p$ and $2\gamma 0p$ samples.

The individual performance of each final variable can be seen in in Tab. 6.10 for flux and in Tab. 6.11 for cross section. Note the flux variations are generally less well constrained, but as their uncertainty was less initially, this is acceptable. The dominant variation, named GENIE_all, is well constrained and examination of individual variations in Fig. 15 of App. B shows this is because the highest uncertainty variations are also among those most reduced by the constraint (i.e., the neutral current axial mass), although, once again, these values are not representative of the final analysis.

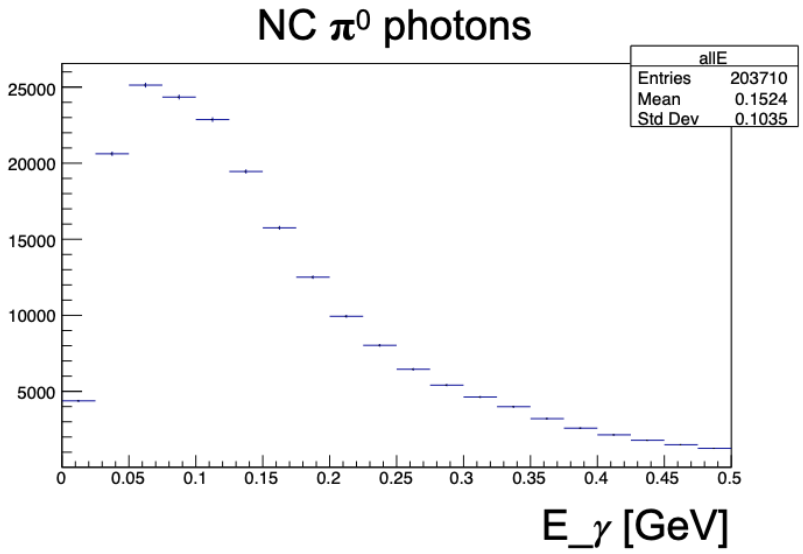

Figure 6.18: Energy distribution of photons from NC π^0 decays in MicroBooNE; the NC π^0 sample used is the generated NC π^0 sample, with no cuts applied.

Table 6.9: Effect of constraint per bin, provided in terms of a reduction factor on the total flux, cross section and detector systematic uncertainty on the backgrounds of the 1γ selections. The number of events corresponds to the available Runs 1-3 of 6.9e20 POT, however, the NC π^0 (2γ) selections that provide the constraint are fixed at the POT of the filtered samples, 5.84e20 POT and 5.89e20 POT for $2\gamma 1p$ and $2\gamma 0p$ respectively.

$1\gamma 1p$ **Bkgd. Bins of Shower Energy (GeV)**	**Events**	**Unconstrained Uncertainty**	**Constrained Uncertainty**	**Reduction Factor**
0 - 0.6	29.4339	24.55%	9.53%	2.58
$1\gamma 0p$ **Bkgd. Bins of Shower Energy (GeV)**	**Events**	**Unconstrained Uncertainty**	**Constrained Uncertainty**	**Reduction Factor**
0.1 - 0.2	10.22	17.63%	12.19%	1.45
0.2 - 0.25	21.47	17.77%	10.06%	1.77
0.25 - 0.3	33.40	17.38%	7.63%	2.28
0.3 - 0.35	34.10	18.13%	7.35%	2.47
0.35 - 0.4	28.80	19.61%	9.35%	2.10
0.4 - 0.45	16.61	21.59%	11.68%	1.85
0.45 - 0.5	11.12	20.77%	15.14%	1.37
0.5 - 0.55	6.44	23.97%	19.27%	1.24
0.55 - 0.6	3.99	28.08%	25.48%	1.102
0.6 - 0.7	3.71	24.24%	16.96%	1.43

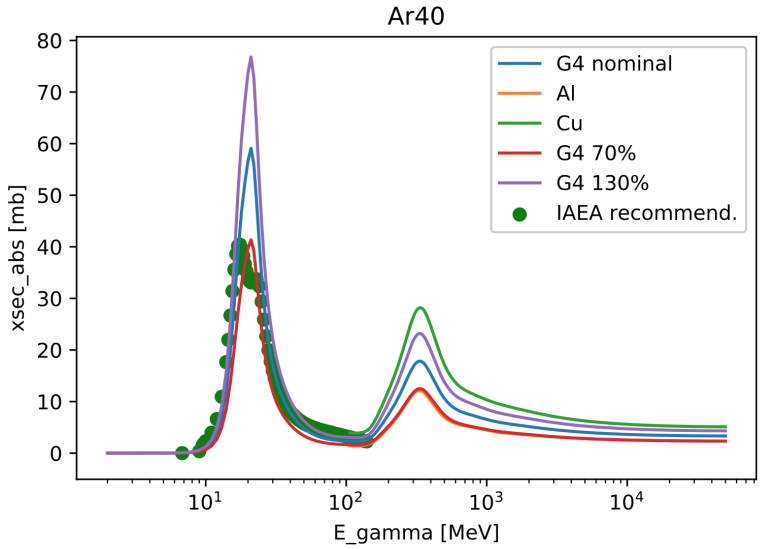

Figure 6.19: Photonuclear process cross section as a function of photon energy. The first peak in the < 100 MeV region corresponds to the Giant Dipole Resonance (GDR). The second peak in the > 100 MeV region corresponds to the Δ resonance. The solid blue line shows the photonuclear process cross section embedded in Geant4 and is used in MicroBooNE simulation. The green dotted-line represents the International Atomic Energy Agency (IAEA) [23] recommendation. The solid red line shows 30% reduction from the Geant4 nominal values. The solid purple line shows 30% increase from the Geant4 nominal values. For the second resonance region, ^{27}Al and $^{63.5}$Cu absorption cross sections are overlaid. Note that the 30% reduction graph from Geant4 is above the ^{27}Al graph.

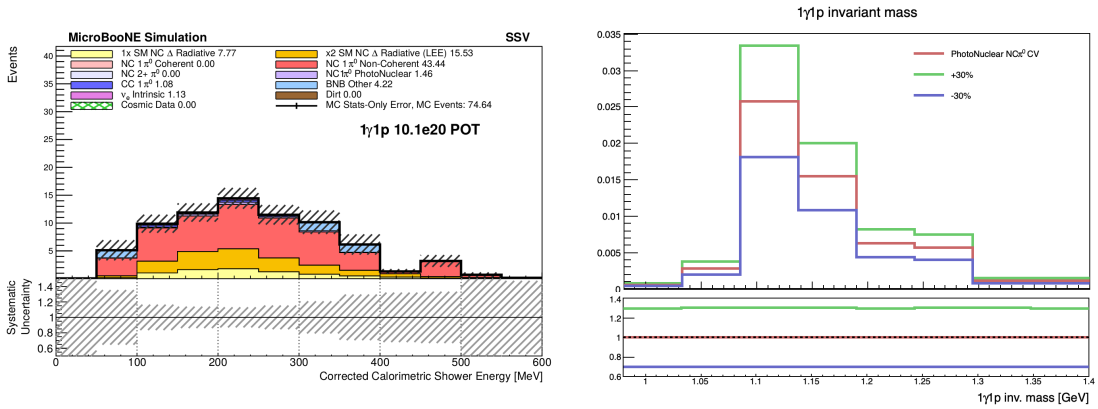

Figure 6.20: Left: Central value (CV) prediction for the final $1\gamma 1p$ selection, showing the photonuclear absorption background component. The photonuclear background is subdominant to the NC π^0 mis-identified background. Right: The same photonuclear absorption background in the $1\gamma 1p$ CV prediction as a function of $1\gamma 1p$ invariant mass, in red, contrasted with variations corresponding to a $\pm 30\%$ enhancement/reduction in photonuclear absorption cross section, in green/blue. The variations are obtained through the Geant4 reweighting scheme described in this section.

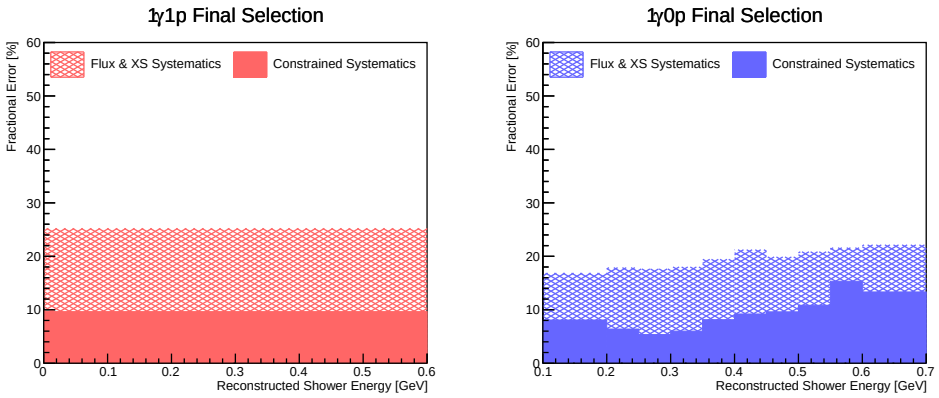

Figure 6.21: A visual representation of the reduction in flux and cross-section systematic uncertainty on the $1\gamma 1p$ and $1\gamma 0p$ final selections, due to the high statistics NC π^0 samples. See Fig. 6.22 for the effect of including detector systematics. Note that this plot is for the full final selections, including the signal channels, where as Table 6.9 is for backgrounds only.

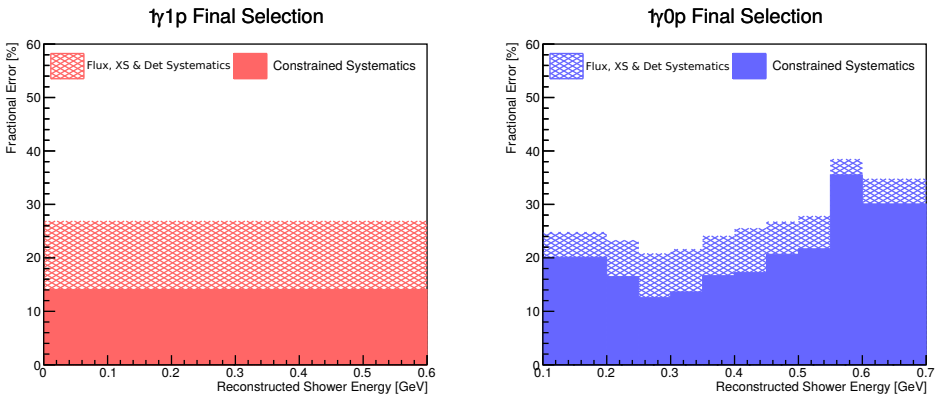

Figure 6.22: A visual representation of the reduction is systematic uncertainty on the $1\gamma 1p$ and $1\gamma 0p$ final selections, due to the high statistics NC π^0 samples. Note that this plot is for the full final selections, including the signal channels, where as Table 6.9 is for backgrounds only.

Table 6.10: Combined sum of predicted background rate in the the $1\gamma 1p$ and $1\gamma 0p$ selections, and corresponding unconstrained and constrained flux uncertainties, broken down by systematic uncertainty source. A hyphen value indicates no uncertainty.

Variation Name	**Unconstr. Error** $1\gamma 1p$	**Constr. Error** $1\gamma 1p$	**Reduction Factor** $1\gamma 1p$	**Unconstr. Error** $1\gamma 0p$	**Constr. Error** $1\gamma 0p$	**Reduction Factor** $1\gamma 0p$
expskin_FluxUnisim	4.94%	3.78%	1.31	4.17%	3.19%	1.31
horncurrent_FluxUnisim	0.68%	0.67%	1.01	0.57%	0.56%	1.01
kminus_PrimaryHadronNormalization	-	-	-	-	-	-
kplus_PrimaryHadronFeynmanScaling	0.61%	0.61%	1.00	0.51%	0.51%	1.00
kzero_PrimaryHadronSanfordWang	0.07%	0.07%	1.00	0.23%	0.23%	1.00
nucleoninexsec_FluxUnisim	0.85%	0.84%	1.01	0.77%	0.76%	1.01
nucleonqexsec_FluxUnisim	2.49%	2.28%	1.09	2.36%	2.17%	1.09
nucleontotxsec_FluxUnisim	0.74%	0.74%	1.01	0.67%	0.67%	1.01
piminus_PrimaryHadron SWCentralSplineVariation	-	-	-	0.16%	0.16%	1.00
pioninexsec_FluxUnisim	1.24%	1.21%	1.02	1.08%	1.06%	1.02
pionqexsec_FluxUnisim	0.83%	0.82%	1.01	0.75%	0.74%	1.01
piontotxsec_FluxUnisim	0.89%	0.88%	1.01	0.80%	0.79%	1.01
piplus_PrimaryHadron SWCentralSplineVariation	4.38%	3.54%	1.24	3.96%	3.11%	1.27

Table 6.11: Combined sum of predicted background rate in the the $1\gamma 1p$ and $1\gamma 0p$ selections, and corresponding unconstrained and constrained cross section uncertainties run individually. GENIE_all is a composite uncertainty and each following one is a minimum and maximum uncertainty that cannot be included as part of the composite.

Variation Name	**Unconstr. Error** $1\gamma 1p$	**Constr. Error** $1\gamma 1p$	**Reduction Factor** $1\gamma 1p$	**Unconstr. Error** $1\gamma 0p$	**Constr. Error** $1\gamma 0p$	**Reduction Factor** $1\gamma 0p$
All_UBGenie	22.66%	7.67%	2.95	15.13%	6.09%	2.48
AxFFCCQEshape_UBGenie	0.18%	0.18%	1	0.24%	0.24%	1
DecayAngMEC_UBGenie	-	-	-	0.48%	0.48%	1
NormCCCOH_UBGenie	-	-	-	0.11%	0.11%	1
NormNCCOH_UBGenie	-	-	-	1.73%	1.73%	1
RPA_CCQE_UBGenie	0.01%	0.01%	1.00	1.06%	1.06%	1.00
Theta_Delta2Npi_UBGenie	5.83%	5.83%	1	1.12%	1.12%	1
VecFFCCQEshape_UBGenie	0.55%	0.55%	1	0.27%	0.27%	1

6.4.2 Hypothesis Testing

The simplest method we plan for testing properties of the NC Δ events pertaining to the LEE is via simple two-hypothesis tests. Namely:

> *"Can we rule out, or reject, a particular hypothesis (the null hypothesis, H_0) in favour of a different hypothesis (the alternative hypothesis, H_1) with our data? And, if so, at what significance?"*

The hypotheses are simple meaning there are no free parameters or necessary relations between them. The three hypothesis of this analysis are

- $\mathcal{H}_{\text{No}\Delta}$: The No-$\Delta$ hypothesis ($x_\Delta = 0$), in which there is no NC Δ radiative decay at all.

- $\mathcal{H}_{\text{SM}}$: The SM hypothesis ($x_\Delta = 1$), in which the rate of NC Δ radiative decay is equal to the CV prediction in GENIE.

- $\mathcal{H}_{\text{LEE}}$: The LEE hypothesis ($x_\Delta = 3$), in which the rate of NC Δ radiative decay is three times the SM CV prediction in GENIE; this represents the approximate normalization increase that would be required for NC Δ radiative decay to completely explain the observed MiniBooNE excess.

With our projected sensitivity, distinguishing between the No-Δ and the SM hypothesis is beyond the scope of this analysis, but distinguishing them from the LEE hypothesis is a critical goal. Without free parameters to be used in fitting, we have to rely on a Combined-Neyman-Pearson (CNP) pseudo-experiment method. This works by simulating a large number of pseudo-experiments for each hypothesis under consideration. Each of these will require correlated distributions from the full systematic covariance matrix via Choloskey decomposition. We then sample from these pseudo-experiments via a Poisson random number around the systematic, to obtain an integer pseudo-experiment data point, D_i. Then for each such pseudo-experiment data set D, the χ^2_{CNP} is calculated between this particular pseudo-data and each hypothesis. The difference between each CNP chi-square, $\Delta\chi^2 = \chi^2_{CNP}(D, H_0) - \chi^2_{CNP}(D, H_1)$ is calculated to build a probability distribution function.

Therefore knowledge of uncertainties is crucial to this method. Median significance values can be determined by assuming the alternative hypothesis is true and calculating the p-value of the null hypothesis relative to this. The result of applying this to the final single photon selection results in a median significance of rejecting the SM hypothesis in favor of the LEE (x3 SM) hypothesis assuming LEE is true is 1.5σ (see Fig. 6.23).

6.4.3 Fitting to a Neutral Current Δ Radiative Decay Rate Parameter

Given the lack of direct measurements of SM NC Δ radiative decay on Argon, a direct measurement could be invaluable. We have settled on two fit approaches:

- **LEE search**: search for an NC Δ excess over SM-predicted NC Δ radiative decay events.
- **NC Δ radiative branching ratio measurement**: extract the enhancement of the branching ratio of NC Δ radiative decay

The fundamental difference is the decision of the fit parameter. For the LEE search method the fit factor is an NC Δ excess assuming first the SM NC Δ process. The second method fits directly the NC $\Delta \to N + \gamma$ branching ratio. The 1γ and 2γ selections are fit simultaneously to use the constraining power of the 2γ distribution.

Fit Method 1: Low Energy Excess Search

For this fit, an LEE component is added to our projected selections as effectively another subsample with a scaling factor which is varied to minimize the CNP $\Delta\chi^2$. For this analysis, systematics will need to be applied to the new LEE component treating it as extra NC Δ radiative decay events. However, because we are fitting for normalization of this component, GENIE normalization factors must be removed. So the systematic covariance matrix used in the fit includes:

- Full flux and detector uncertainties and correlations for all components, including the LEE component

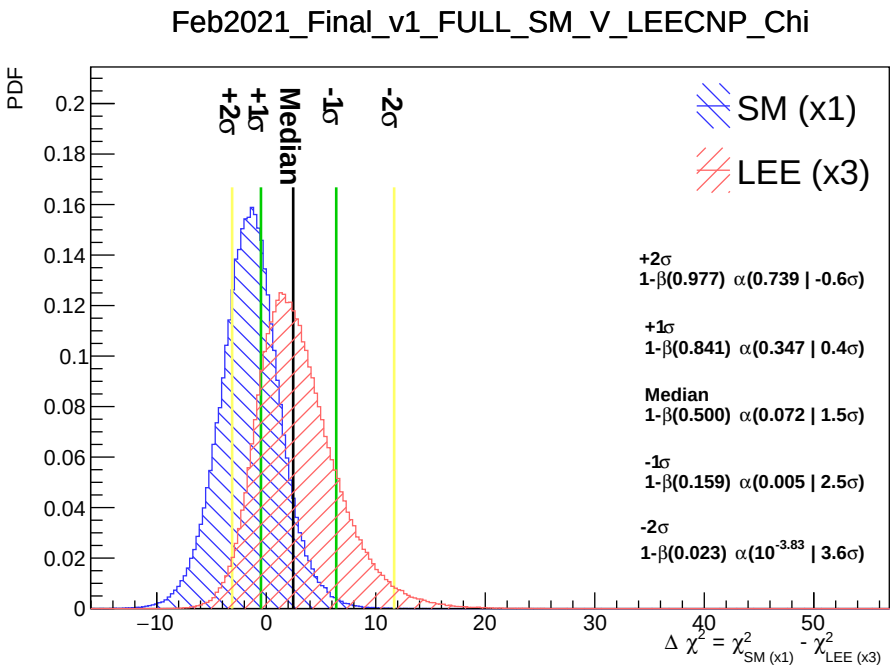

Figure 6.23: Two-hypothesis test frequentist studies for the hypothesis of Δ radiative rates of the LEE rate ($\times$3 expected) for the available Run 1-3 data set of 6.9×10^{20} POT.

- GENIE shape-only uncertainty and correlation for the LEE component, and full GENIE uncertainty and correlations for other components.

Fit Method 2: Neutral Current Δ radiative branching ratio measurement

Here a scaling factor is instead assigned directly to the SM NC Δ radiative component with no independent LEE factor introduced. The $\Delta\chi^2$ is thus determined by varying this scaling factor. Once again, we must remove relevant systematics in this case including normalization of NC Δ radiative decay. Thus the systematic covariance matrix used in the branching ratio measurement includes:

- Full flux and detector uncertainties and correlations for all components
- Almost full GENIE uncertainty and correlations for all components except: the normalization uncertainty of NC Δ radiative decay branching ratio is removed from the GENIE covariance matrix (and assumed to be uncorrelated with NC π^0).

Systematic Effect on Sensitivity

Systematic uncertainty is a defining factor of the final sensitivity of our measurements. The impact can be seen in Fig. 6.24 broken down into components. All systematic (and statistical) covariance matrices included except either cross-section, or flux, or detector, or all systematic covariance matrices removed. The left figure shows sensitivities with only one source of systematic uncertainties (in addition to statistical uncertainties) included in the fit. The plot indicates that the principle focus should be reduction of detector systematic uncertainties. The power of 2γ constraint on the of 1γ selections via correlations is shown in Fig. 6.25, illustrated by the overlaid sensitivity curves in dashed lines, where off-diagonal correlations are explicitly zeroed out during the fit. Note it is especially powerful for flux and cross-section systematics as was demonstrated in Sec. 6.4.1.

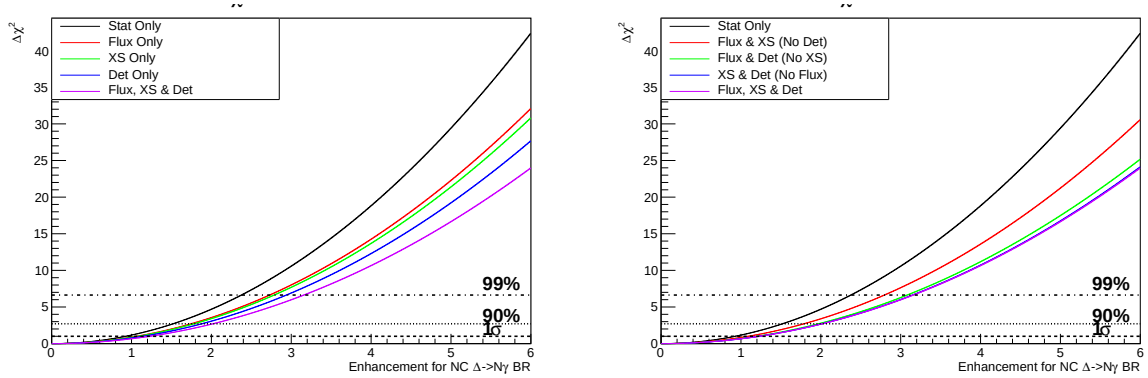

Figure 6.24: $\Delta\chi^2$ median sensitivities assuming observation of the expected spectra (the Asimov data set) under the No-Δ hypothesis, in which we fit the NC Δ radiative branching ratio enhancement. On the left plot, we show the changes in $\Delta\chi^2$ using only one class of systematics at a time (plus statistical uncertainties), and on the right plot, we show the same but removing one class of systematics at a time from the full covariance matrix (always keeping in statistical uncertainties). Note that, on the right plot, the blue line lies almost directly behind the purple line showing that flux uncertainties are negligible in this analysis, presumably due to the nearly 100% flux correlation between all (NC-dominated) samples.

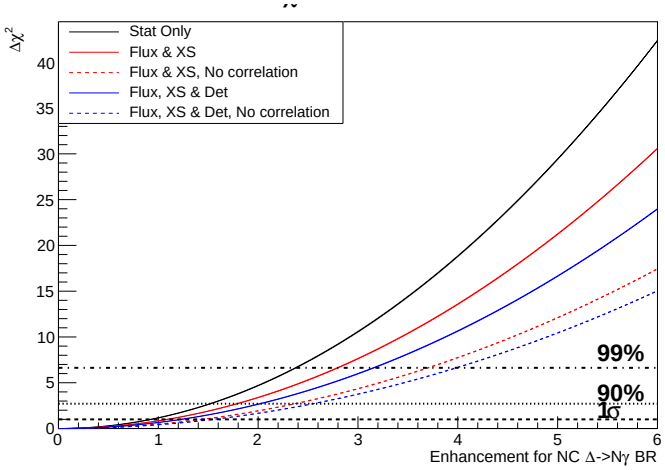

Figure 6.25: 1D $\Delta\chi^2$ median sensitivities assuming observation of the expected spectra (the Asimov data set) under the No-Δ hypothesis in the NC Δ branching ratio measurement, which illustrates the power of the NC π^0 constraint for Runs 1-3.

Chapter 7

Booster Neutrino Beam Accelerator Concepts

This chapter provides an overview of accelerator concepts in the context of the Fermilab's Booster Neutrino Beam (BNB) which are the subject of beam-related studies in Ch. 8 and the beam flux-related portion of single photon systematics described in Ch. 6. Sec. 7.1 covers basic design of accelerators, and Sec. 7.2 covers the particular details of the Fermilab accelerator complex.

7.1 Accelerator Concept

Linear accelerators rely on electrostatic forces (often alternatingly pulsed) of plates to accelerate charged particles. However, they are limited in terms of energies they can reach. To reach higher energies, the concept of accelerator rings was developed. Using magnetic fields along the beamline, the particles can be made to move circularly. Thus a few linear accelerators, called boosters, along with beamline can serve to increase the energy via the same method as above but can be used repeatedly on cycling particles. This poses the challenge of maintaining a consistent radius of cycling particles, such that the beam remains in the accelerator as the energy increases. This both shifts the variables within the basic formula ($mv^2/r = qvB$) and also can incur relativistic effects as the particles reach speeds closer to the speed of light. Synchrotrons solve this problem via increasing the magnetic

field with the increasing particle energy and maintaining a very precise radius of orbit. This means all particles within the ring must be at the same energy so synchrotons must work in spills which means all particles enter the synchrotron at the same energy, and then no further particles are injected until these particles are ejected. However, the precision of the beam allows for a much narrower magnetic field and separate quadrupole magnets serve to maintain the focus of the beam.

7.2 Fermilab Accelerator Complex

An outline of the modern Fermilab beam complex can be seen in Fig. 7.1. The most important parts to the MicroBooNE detector are the Booster Neutrino Beam (BNB) which is its primary beamline and the NuMI beam which has an off axis component in the MicroBooNE detector.

The source of the beamline is two H^- ion sources which work by filling a cavity with hydrogen gas and applying a voltage which creates an arc ionizing the hydrogen to H^+ to form a plasma. A magnetic field sends the H^+ towards the cathode such that some will capture two electrons from the plasma to create H^-. The anode and cathode are then pulsed at -35 kV transporting the H^- to a grounded extraction cone. As the raw shape of these pulses is undesirable, the pulses are chopped by an Einzel lens to 100 μs bursts with frequency 15 Hz [24], as seen in Fig. 7.2. Radio frequency quadrupoles focus, bunch, and accelerate beam to 750 keV and the Medium Energy Beam Transport (MEBT) with two quadrupole doublets and an RF buncher cavity further bunches the beam and orients to the linear accelerator (Fig. 7.3) [24].

7.2.1 Linear Accelerator

The linear accelerator (LINAC) works on the same principle of most linear accelerators: accelerating by pulsing sections between positive and negative charge. It is divided into high energy and low energy sections. The low energy portion is composed of large RF cavities which shield the beam from unwanted electric fields. Drift tube cavities accelerate the H^- ions from 750 keV to 116.5 MeV. Dipole magnets maintain beam trajectory, and quadrupole

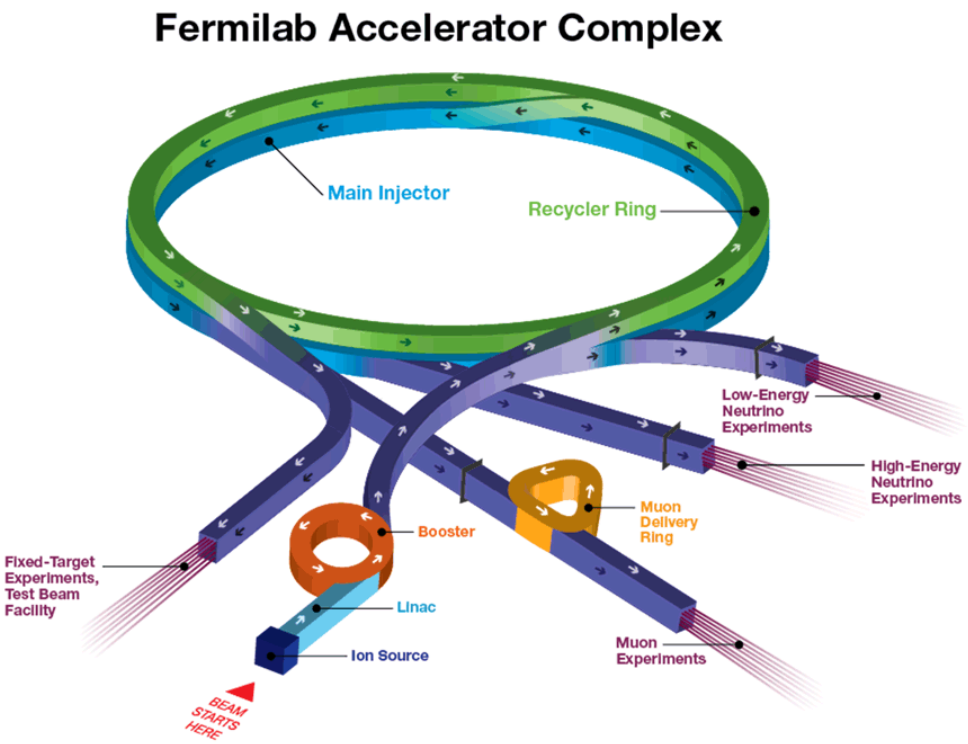

Figure 7.1: An overview of the modern Fermilab accelerator complex.

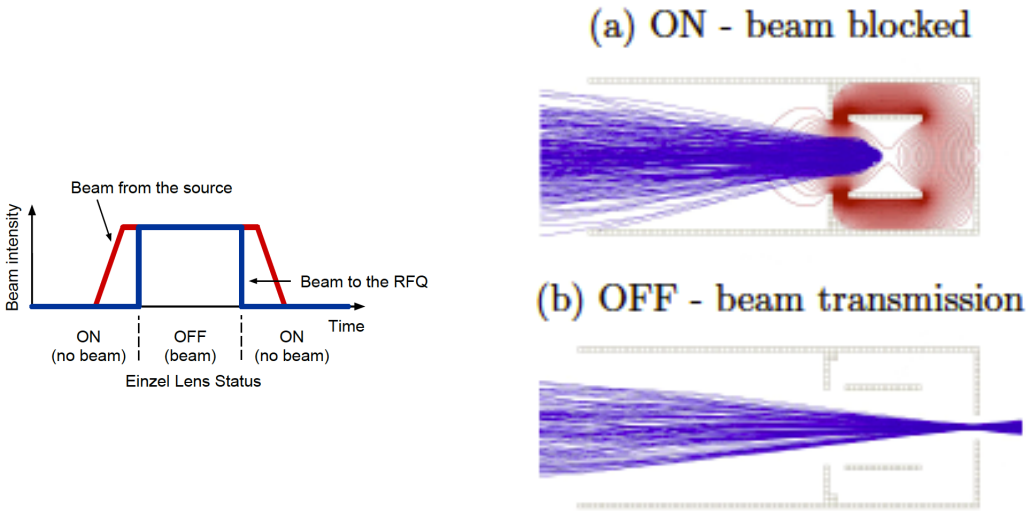

Figure 7.2: Einzel lens being used as a beam chopper that reflects the beam when on and allows it to pass when off [24].

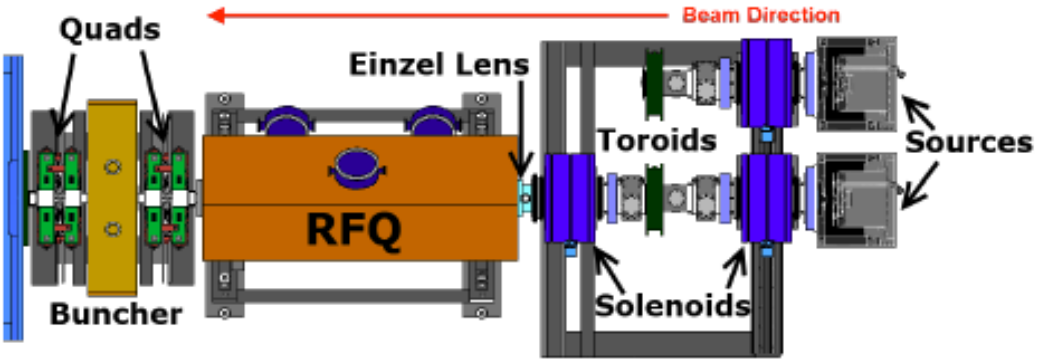

Figure 7.3: Fermilab pre-accelerator concept.

magnets maintain focus. A transition section performs longitudinal matching to transition to the new RF frequency (201.24 MHz → 804.96 MHz) of the next section using side-coupled cavity structures. The high energy section uses side-coupled structures of accelerating cells and coupling cells that accelerate the beam to 400 MeV.

7.2.2 Booster

The Booster rapid cycling synchrotron is responsible for accelerating the beam particles from 400 MeV to 8 GeV (minimum for Main Injector). Before being injected into the Booster, a stripping foil strips electrons from the H^- ions producing protons. Paraphrasing is the process by which the beam is converted from the LINAC frequency to that of the booster via RF buckets: areas in phase space where the beam is captured. Combined-function magnets along the circumference provide both the focusing quadrupole field and the orienting dipole field. The Booster RF system consists of 19 stations that accelerate the beam to 8 GeV. The ultimate result is an output in *batches* with frequency 15 Hz, with each *batch* made up of 84 *bunches* of beam each contained within *buckets*. These *batches* are then sent to either the main injector or along the Booster Neutrino Beam path. The properties of the Booster Neutrino Beam can be seen in Table 7.1. The Booster Neutrino Beam is the primary beamline of the MicroBooNE detector delivering primarily ν_μ of energy $\mathcal{O}(1)$ GeV. Along the neutrino beam path a *spill* of 4×10^{12} protons is delivered on the target for durations of about 1.6 μs. The number of protons delivered to the target is referred to as protons on target (POT) [99].

At this point the beam is separated between the Booster neutrino beam and the MI-8 line to the Main Injector.

7.2.3 Target and Horn Details

The Booster Neutrino Beam target consists of 7 cylindrical slugs of beryllium of total length 71.1 cm with 0.51 cm radius. The slugs are contained in a beryllium sleeve of 1.37 cm inner radius and 0.9 cm thickness. Three beryllium fins hold the slugs within the sleeve. The magnetic focusing horn consists of inner and outer conducting shells with inner radius

varying between 0.87 and 2.58 inches and outer diameter of 23.62 inches and a total length of 73 inches with inner shell just outside the beryllium target. It is pulsed at 174 ± 1 kA current producing a toroidal magnetic field of strength reaching 1.5 Tesla.

7.2.4 Beamline Instrumentation and Devices

The proton beam is measured and driven by a variety of devices and detectors. Toroid detectors measure the beam current that passes through them by measuring the created magnetic field. The toroids are structured comparably to a classical transformer with the source voltage replaced by the single loop of the beam passing through (see Fig. 7.4). Signal strength is estimated at 0.5 volt per ampere yielding $\sim$250 MeV. Located on either end of the beamline, toroids serve as a first check that the beam is on target and is of expected strength, and are used to normalize other monitors. The toroids are themselves normalized by measuring the output from known currents. Twenty-two beam position monitors (BPMs) are placed along the beamline each consisting of four impedance matched striplines in a cylindrical housing, two spaced vertically and two spaced horizontally. Each stripline is a section of a circle subtending an arc of 60 degrees. These position monitors detect the beam position via the difference of image currents on each stripline when the beam passes through, and are used for beam tuning and data-quality checks. Seventeen loss monitors are placed along the beamline that read intensity of radiation reflected from the target and inhibit the beam if a certain threshold is reached. Each loss monitor consists of cylindrical argon ionization proportional chambers that have high gain and fast response, tuned to the beam's 15 Hz. Finally, six low precision retractable multi-wire proportional chambers are located along the beamline. Multi-wires consist of arrays of wires: typically 48 horizontal and 48 vertical with 1 mm spacing that give a reading of the beam profile via charge induced on the wires.

Table 7.1: Booster Neutrino Beamline properties.

Property	**Value**
Injection Energy	400 MeV
Extraction Energy	8 GeV
Circumference	474.2 m
Periods	24
Revolution Period	2.2 μs/1.6 μs
RF Frequency	37.77 MHz to 52.8 MHz
Harmonic Number	84
RF Voltage Gain Per Turn	920 kV/turn

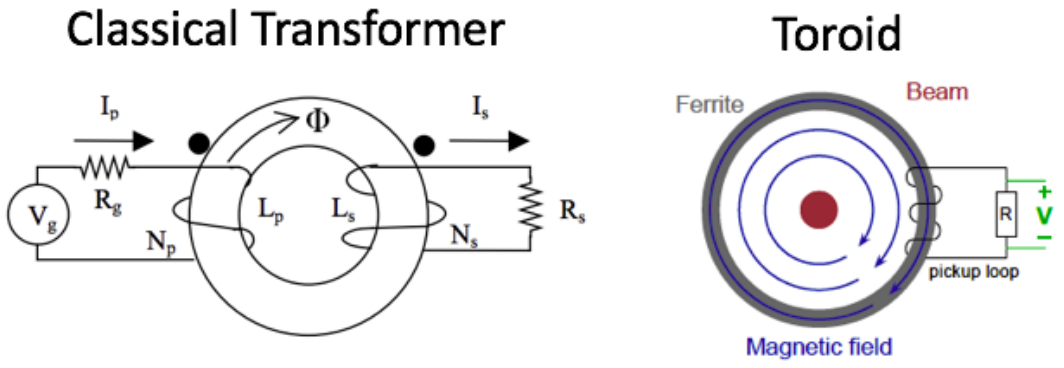

Figure 7.4: Toroid detector Structure with comparison to a classical transformer.

Chapter 8

Booster Neutrino Beam Systematic Analsysis

For precision analysis into the low energy excess (LEE) region, a robust knowledge of the neutrino beamline is necessary. While MicroBooNE has a well founded model for the beamline, as well as instrumentation to ensure consistency, I received Office of Science Graduate Student Research (SCGSR) fellowship to evaluate new methods to both improve accuracy and recover data that might otherwise be deemed unusable. Sec. 8.1 covers beam position analysis with a focus on a new method I developed that establishes a figure of merit (FOM) for data recovery. Sec. 8.2 covers an effort to fit HARP data for secondary protons in the beamline to improve our neutrino flux prediction. Preliminary results of this study were reported in the SCGSR report to the Department of Energy (DOE) and were shown at the American Physics Society (APS) meeting in April 2018.

8.1 Beam Position Study

As was covered in Sec 3.3.1, neutrino flux is produced by impinging a proton beam onto a beryllium target. The Booster Neutrino Beam (BNB) has instrumentation and software tools for ensuring the beam is consistent in targeting and intensity. However, unexplained results in a target scan and occasional technical issues motivated an expansion of methods using beamline instrumentation as well as more extensive analysis of beam data.

8.1.1 Target Scan Procedure

Target scans are the process of translating the beam across the target. A simple diagram illustrating the scans can be seen in Fig. 8.1. Three scans are typically done in succession: horizontal, vertical, and fin. Horizontal and vertical scans are both centered on the target, then translated in their respective directions to the edges of the container. The fin scan is comparable to a horizontal scan except the beam is first vertically displaced to the bottom fin, and the scan is used to more accurately determine the target center. As described in Sec. 7.2.4, loss monitors measure intensity of radiation reflected from the target. Readings from loss monitors (LMs) increase when the beam is on target or hitting the sleeve of the target. The readings can be used to identify the center position for beam position monitors (BPMs), which must periodically be re-normalized as their electrical centers drift compared to the geometrical center. Multi-wires (MWs) can also gather information during a target scan, and further uses from them are being evaluated. Finally, toroids are used to normalize loss monitor readings to the true proton flux. The position monitors used for this analysis are selected for their proximity to the target and include BPM875 and BPM876 with components referred to as HP875 and HP876 for horizontal position and VP875 and VP876 for vertical position. Likewise, loss monitors LM875A, LM875B, LM875C, multi-wires MW875 and MW876, and toroids 875 and 876 were primarily the other instruments examined in this analysis. All instruments except some loss monitors (see Fig. 8.2) are on the beamline with those labeled 875 closest to the target.

Unexplained Target Scan Reading

The initial premise of this study was an anomalous target scan. The target scan was performed on 07-14-2016 and a newer one was performed on 06-20-2017 that exhibited more expected behavior. Both can be seen in Fig. 8.3. With the goal of maximizing beam-on time (delivering measurement quality POT to the target), the number of target scans that can be performed is limited. Scans are usually taken following some interruption in beam-on time such as the regular summer shutdowns. The newer scan taken for this study has the expected behavior: dips in LM intensity corresponding to when the beam passes between the target

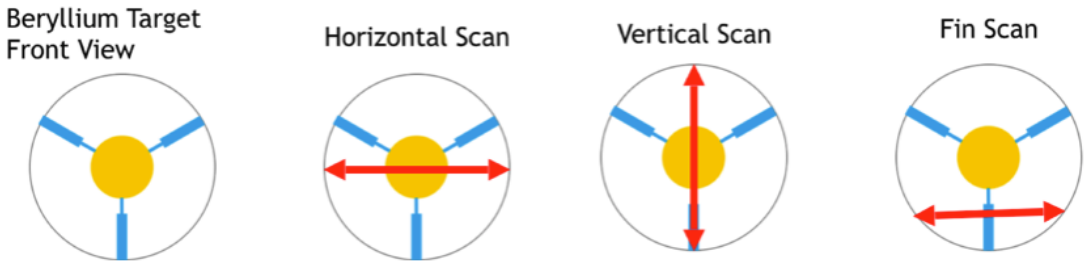

Figure 8.1: Simple diagram of target scans where the target is shown in yellow, the fins in blue, and the translation of the beam in red. The circle corresponds to the target sleeve.

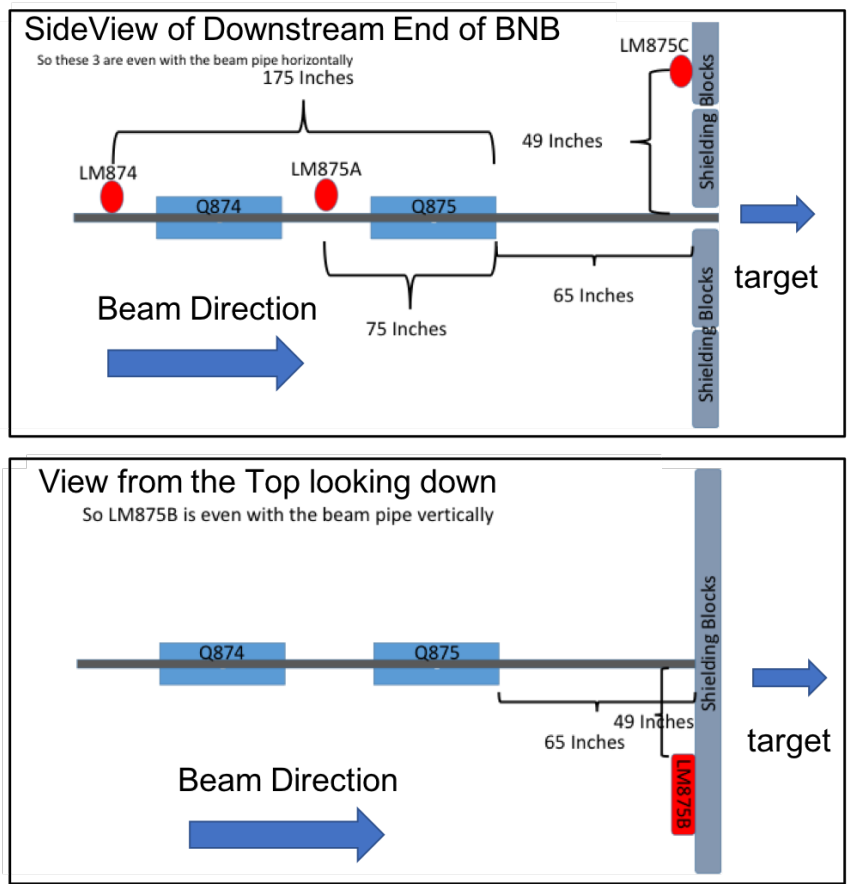

Figure 8.2: (Top) Side view of the downstream end of the BNB showing loss monitor positions. The three loss monitors shown here are inline with the beam pipe horizontally. (Bottom) View from the top (looking down) showing LM875B displaced horizontally.

and sleeve, and symmetry as expected for the symmetrical target. The older scan shows the unexpected behavior with no dip on one side and a reduced dip on the other meaning it is unexpectedly asymmetrical.

Simplified Monte-Carlo Studies

As a first look, a simplified Monte-Carlo (compared with the intensive real beam Monte-Carlo) was used for investigation. The simplified Monte-Carlo simulates loss-monitor intensities via an inverse squared relationship with points of interaction between proton beam and target and allows for easy modification of the beam or target angle. An initial hypothesis, was that the beam could have been at an angle with the target without being identified by the instruments. Several target scans were simulated with a variety of angles (examples can be seen in Figs. 8.4 and 8.5), but the simplified Monte-Carlo was unable to match the behavior of the anomalous scan even when put at angles well above what might reasonably be expected. Further analysis of beam angle would require much more intensive simulation, and with little evidence to corroborate the angle hypothesis it was decided to instead move to a more extensive analysis of beam data using multi-wires for gathering more angle information or developing new hypotheses.

8.1.2 Figure of Merit Multi-Wire Study

MW875 and MW876 are the closest functional multi-wires to the target as the former closest multi-wire (MWTGT) has degraded beyond usability likely due to radiation. A simplified diagram of the multi-wire and position monitor locations can be seen in Fig. 8.6. Given the multi-wires have access to both position and profile of the beam, they are a prime candidate for expanding knowledge of the beam-line.

A simple Gaussian is applied to fit to multi-wire data to extract the central position with a goal to use the Chi-square of the fit as a filter (see Fig. 8.7).

While angle analysis was attempted and will be covered in Sec. 8.1.2, the most significant result of the multi-wire study is the potential for a supplementary figure of merit (FOM) method. The figure of merit is the fraction of proton beam passing through the entirety of

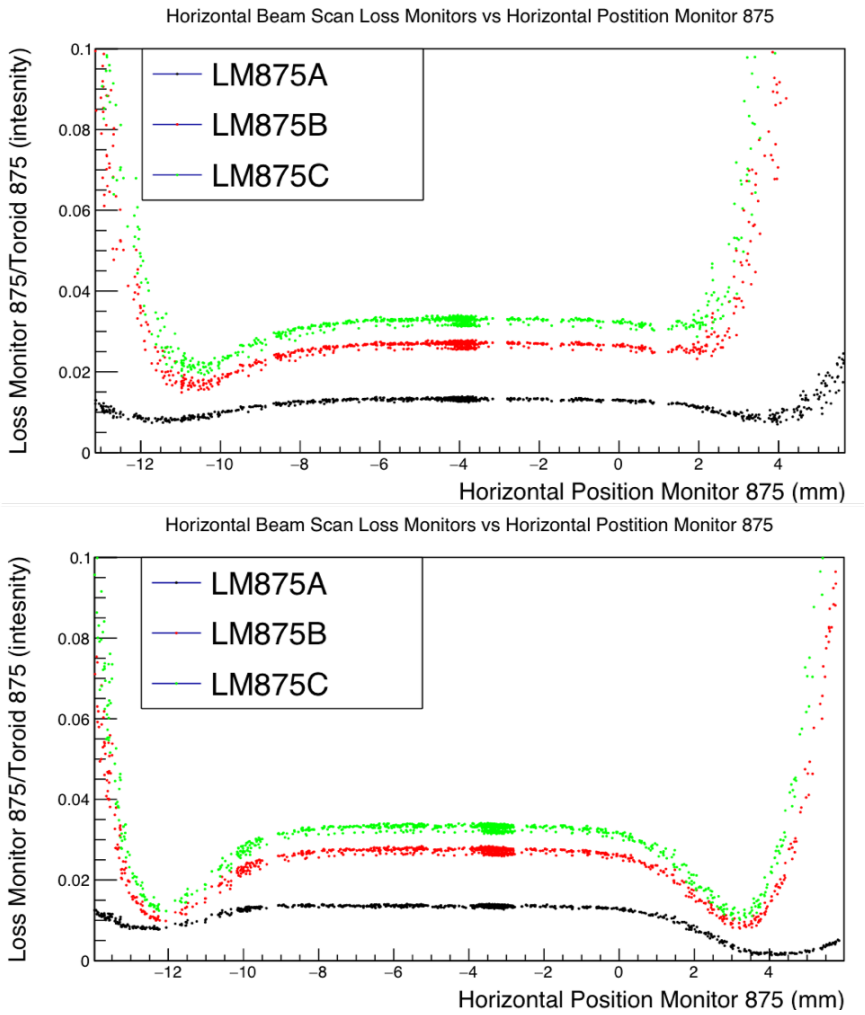

Figure 8.3: Horizontal target scans including the scan taken on 07-14-2016 (top) showing unexpected behavior with reduced dips and asymmetry and the target scan taken 06-20-2017 (bottom) showing expected reasonably symmetric behavior with significant dips when the beam is between target and shell.

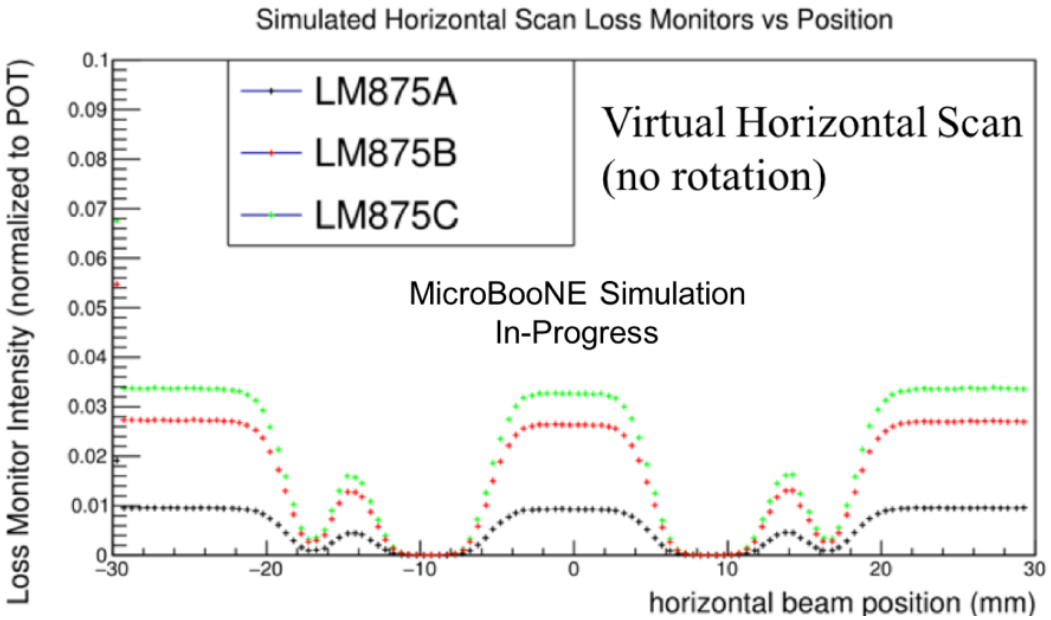

Figure 8.4: Virtual horizontal scan performed in the simplified Monte-Carlo (translating the beam horizontally). Note the shown plot goes beyond the typical bounds of a physical scan at about ±12 mm at the edge of the container and instead reaches the horn at about ±18 mm. This would not be performed physically, but it serves to show that the geometry is responding as expected. The structure at the center in the range ±15 mm is comparable to that of an actual horizontal scan.

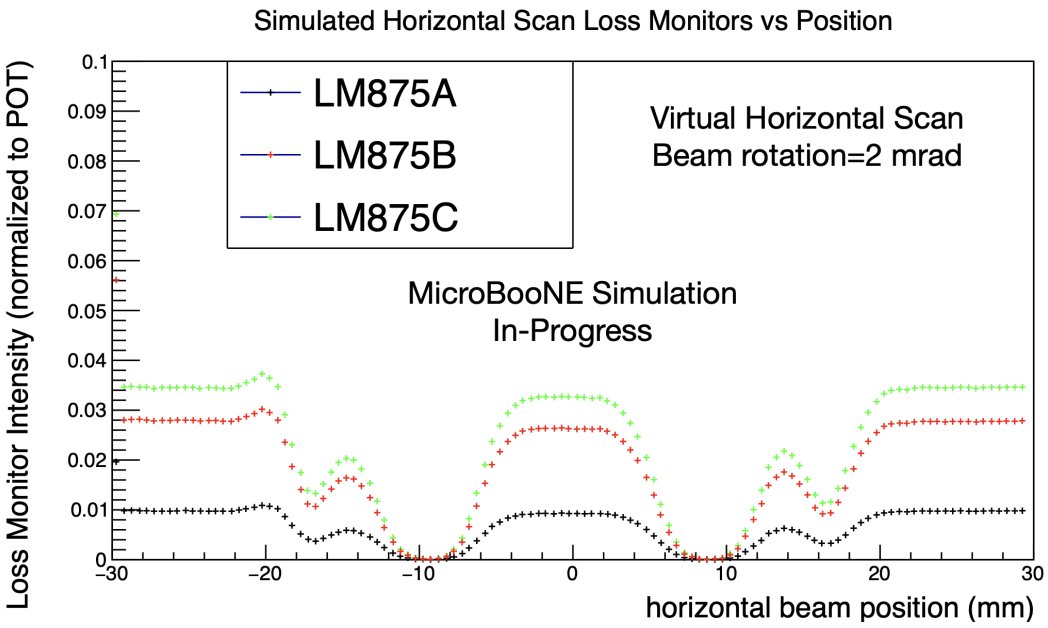

Figure 8.5: Here the simulated beam is incident at an angle of 2 mrad to the target. There are slight differences (notice the bump around −20 mm), but the desired behavior is not reproduced.

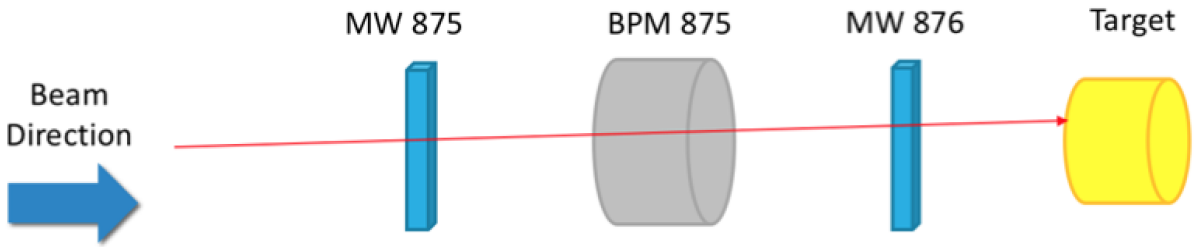

Figure 8.6: Illustration of the beam monitor positions (note: not to scale).

the beryllium target as defined by instrumentation. For a selection of MicroBooNE data to be usable, this value must be consistent and above a threshold set at 95%. The current method uses a beam transfer matrix to calculate the beam position and width at three positions along the target: beginning, center, and end of the target length. FOM values of above one will be output for known failure conditions. There have been periods of time when HP875 has suffered from technical issues. With the current method for defining FOM using HP875, the data collected while these issues were ongoing had to be deemed unfit for MicroBooNE's primary beam based measurements. Thus, a method to simulate HP875 could recover data and prevent such losses in the future, but only if it met prerequisites for precision and performance. An analysis began, to determine if a method of multi-wire interpolation could meet these prerequisites. The method works by reading beam position on MW875 and MW876 then interpolating via a linear fit to the position of BPM875. Region 1 and region 4 are discussed in detail as good and bad data regions.

To establish overall performance, first a run-by-run performance was evaluated where interpolation is calculated and averaged for each run and compared to the position monitor. For efficiency, only the first 10,000 entries were collected from each run. Because the beam position monitors' center is a virtual value set in software and can drift over time, a factor is necessary to make the interpolation value match HP985. As drift is slow, except in the case of mechanical work on the beamline, these factors should be consistent over time. This factor may also be unnecessary in the final implementation as will be explained in Sec. 8.1.2.

Regions of Stability

For testing of this method, data was sampled over the period of MicroBooNE data collection. The timespan was split into regions based on MicroBooNE downtime and stability of the shift factor needed between the HP875 value and the interpolation value. This can be seen in Fig. 8.8. While there are some anomalous runs, this was sufficient to establish the shift factors and begin analyzing performance on a region by region basis. As this study was initially performed in early 2019 the analysis stops there, but could be expanded to newer data.

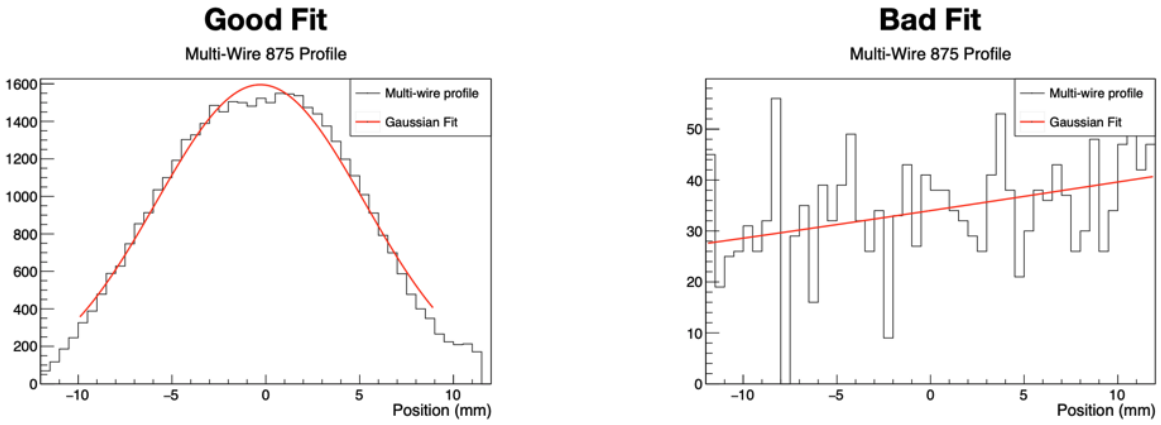

Figure 8.7: Gaussian fit to multi-wire intensity vs wire spacing. The Chi-square of the first fit was 3.04 and the bad fit was 88.32.

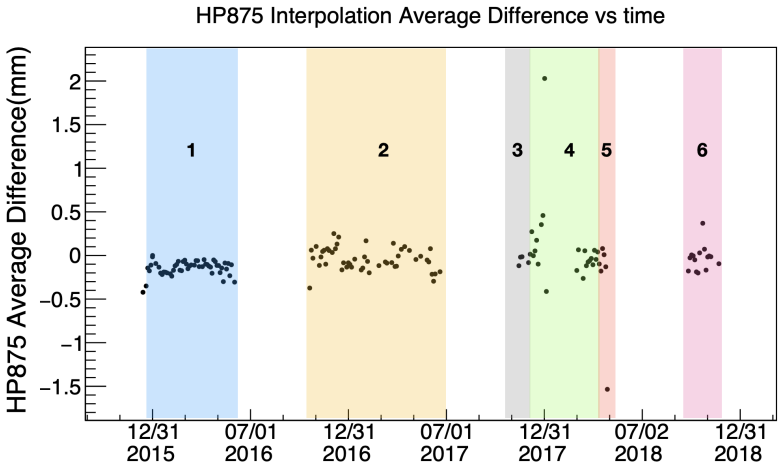

Figure 8.8: Evaluation of interpolation stability using data collected in 2015−2018. The difference between run average interpolation value and HP875 value is evaluated for a series of runs in the time span. The average interpolation remains consistent within <1 mm (often 0.5 mm) except in a few runs.

A closer investigation of Stable Region 1 can be seen in Figs. 8.9 and 8.10. Overall agreement of FOM between the methods is quite good at 97.7%. Recovery of entries when HP875 data was unavailable is 97.2%, but only internal checks on the interpolation can be performed to define if entries not recovered are truly regions where the beam performance was not within acceptable parameters or if the method failed due to other issues. There are still points of unexpected behavior, but these can largely be cut via simple filters and efforts to understand them continue.

Region 4 had dramatically less consistency in the difference between BPM and interpolation method although it should be noted it is still within 1 mm. Performance for region 4 can be seen in Fig. 8.11 and 8.12. Recovery rate is only 52.4%, although agreement remains high at 97.1%. However, the variability of the difference between the methods makes suspect any regions where HP875 lacks enough data to establish consistency, meaning this may be a region where this technique isn't applicable. This region did reveal the prospect of further tuning our cutoff for chi-square, as there are a significant number of failures due to the cut of the chi-square on the multi-wire fits. It can be seen in Fig. 8.13 that higher chi-square values may still generate fits usable for defining a central value. A summary of the performance over all regions is shown in Tab. 8.1.

A prime target for data recovery is a period of time around the 2017−2018 New Year where HP875 had mechanical issues and so the data was deemed unusable. Performance is promising as shown in Fig. 8.14. This can serve as an example for future data recovery.

Implementation

While testing of entry by entry behavior is ongoing, it was decided a test version could be implemented into the beam data collection algorithm. Thus far, the analysis has been performed in a standalone fashion after data is collected and processed. Implementation into the beam algorithm can allow for testing to continue with greater access to data not accessible via standalone methods, and without worrying that transfer of the code may cause unexpected errors. In addition, analyzers can choose to use the method accepting its current performance at their discretion. Implementation into the existing code may not need shift factors for its core function as the multi-wire value can instead be projected directly to

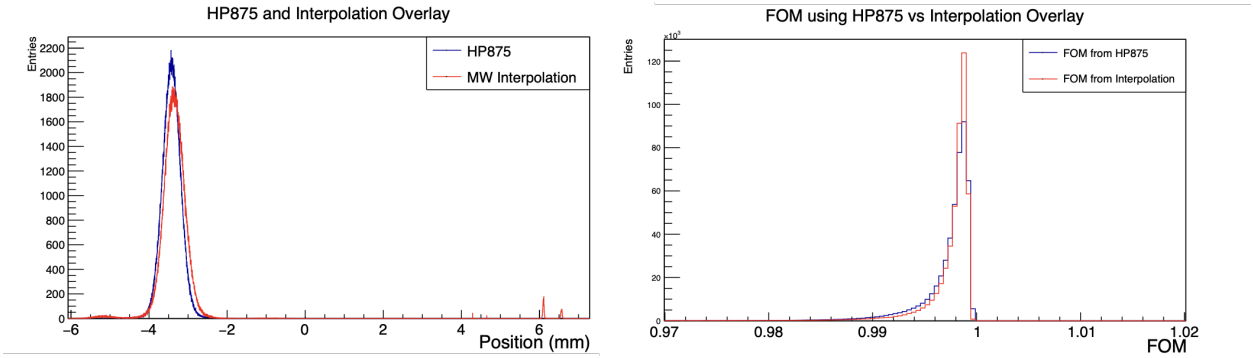

Figure 8.9: Overall performance across the entire stable region 1 as shown in Fig. 8.8, plotted in terms of entries (points of collected data with frequency 5 Hz rate on average). Data used include runs collected between 12/11/2015−06/10/2016. Regions of disagreement are obvious (the points around 6 mm) and are cut by the filter.

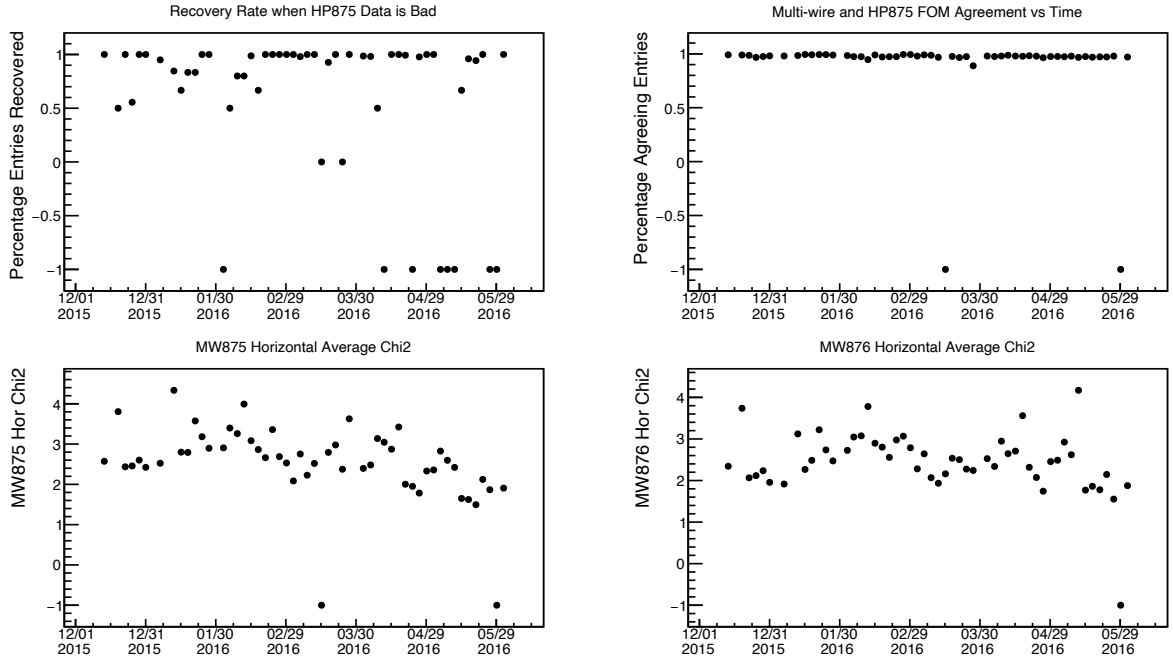

Figure 8.10: Run by run performance over stable region 1 (12/11/2015−06/10/2016). The top two plots show the run by run accuracy (right) and efficiency (left) of the stable region. The lower two plots are the run average chi-square for each multi-wire. The chi-square serves as an internal check on the Gaussian fitting to multi-wires and the run average gives good indication if the beam profile was well determined on the multi-wires.

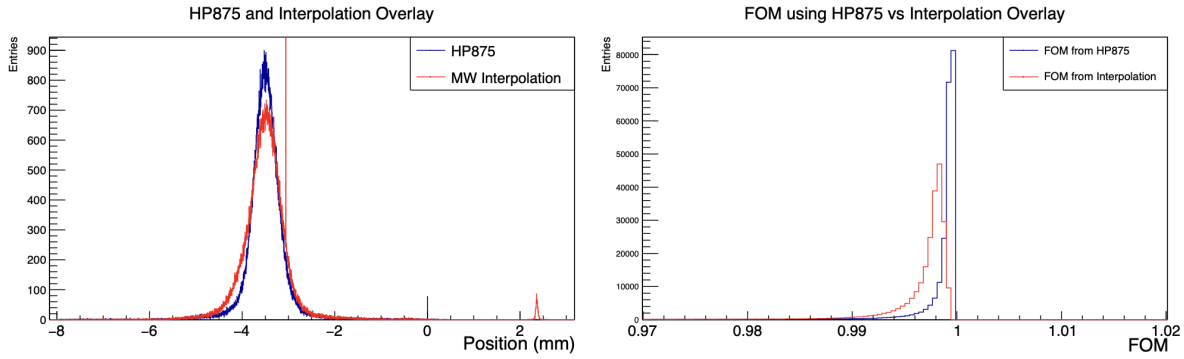

Figure 8.11: Shown is the overall performance across the entire stable region 4 plotted in terms of entries (points of collected data with frequency 5 Hz rate on average). Runs were collected from 11/30/2017−04/19/2018. Overall, the precision of the position is reduced in the interpolation method. Note the spike at −1 mm position. This is due to assignment of values that are out of bound and can be ignored. Here, the FOM disagreement is more drastic.

Table 8.1: Performance fractions of multi-wire interpolation FOM method for all regions.

Stable Regions	Region 1	Region 2	Region 3	Region 4	Region 5	Region 6
Start Date	12/11/15	10/14/16	10/27/17	11/30/17	6/2/18	9/17/18
End Date	6/10/16	7/7/17	11/30/17	4/19/18	7/6/18	12/2/18
Recovery Rate	0.97	0.81	0.00	0.52	0.00	0.48
Agreement	0.98	0.96	0.08	0.97	0.00	0.64
MW FOM Pass HP875 Fail	0.00	0.01	0.00	0.00	0.00	0.00
HP875 Fail	0.01	0.01	0.70	0.10	1.0	0.14
Both Methods Fail	2.04E-06	3.57E-05	0.511431	0.04471	1.0	0

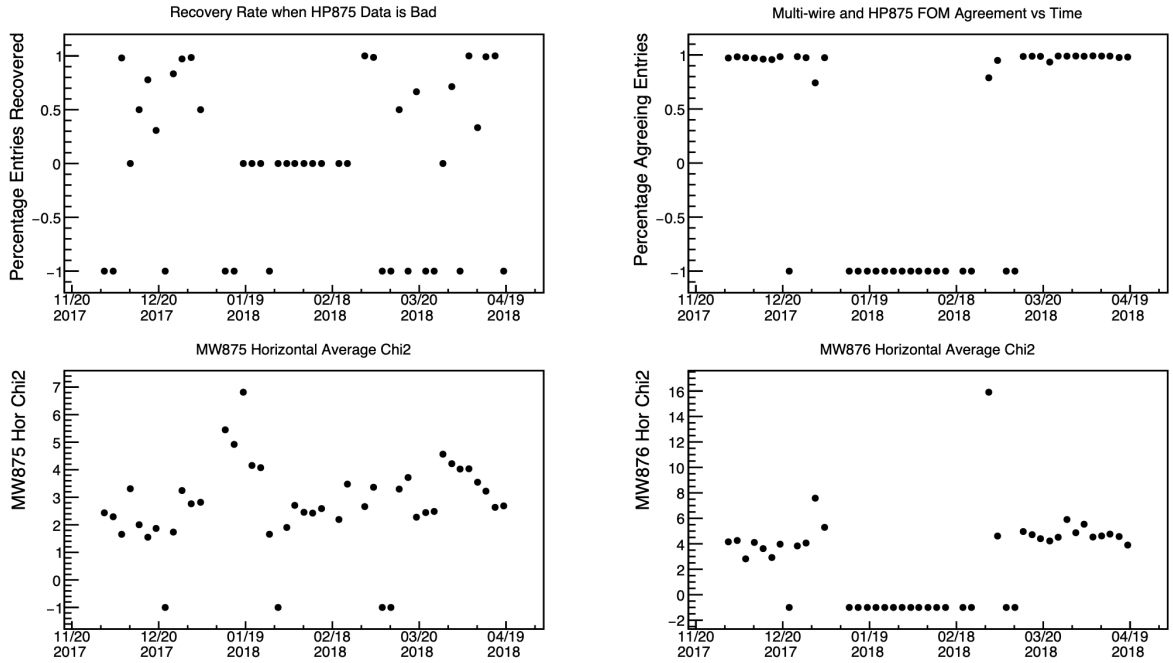

Figure 8.12: Shown is the run-by-run performance over stable region 4 (11/30/2017−04/19/2018). The top two plots show the run by run accuracy (right) and efficiency (left) on bad data. The lower two plots are the run average chi-square for each multi-wire. The chi-square serves as an internal check on the Gaussian fitting to multi-wires and the run average gives good indication if the beam profile was well determined on the multi-wires.

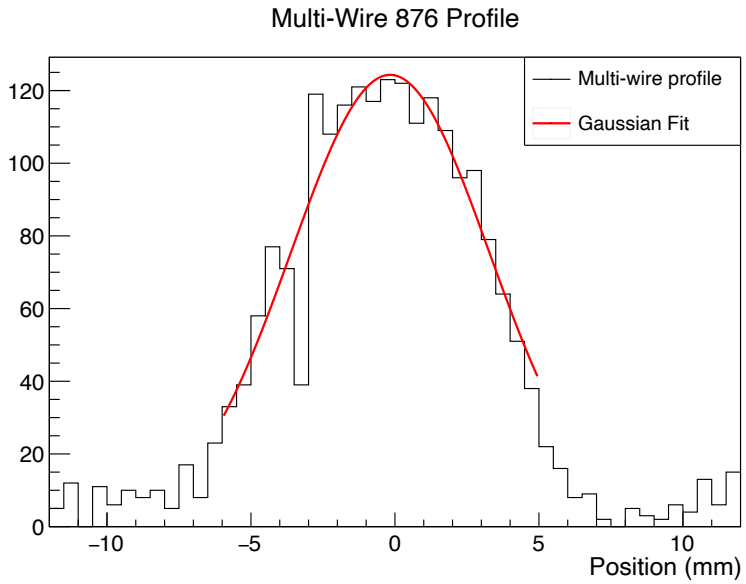

Figure 8.13: Multi-wire fit with high chi-square, but usable. Gaussian center=-0.17, gaussian sigma=3.45, gaussian chi-square=28.38.

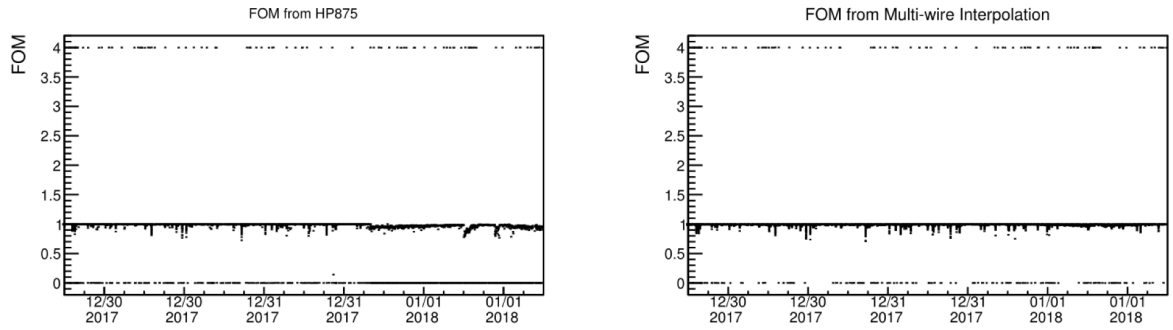

Figure 8.14: Data was collected from the end of the year 2017 to the start of 2018 when HP875 was intermittently functional. 148424 entries were recovered from a total of 152085 resulting in a recovery rate of 98.4%. Agreement on limited HP875 data near the time span is 98.5%.

the target position for FOM calculation. However, interpolating to HP875 will remain an important check on accuracy. Implementation is in progress, and testing on a small set of data showed identical FOM given by both methods. A public note is planned to accompany this implementation for accessibility to other MicroBooNE analyzers and ultimate portability to other experiments such as SBND [100] or DUNE [48].

Multi-Wire Angle

Supplementary to the figure of merit study, an effort to verify the angle of the beam using the multi-wires was developed. It uses measurements from the multi-wires and the distance between them for a simple angle calculation. By assuming the average angle between the beam and target is 0° during a normal run (as should be the case), the deviations from this central angle can be evaluated. In the lower two graphs of Fig. 8.15, it can be seen that the run average angle remaining mostly consistent (average shifted to zero) and standard deviation remaining in the range of ∼1 mrad. In addition, preliminary studies of the impact of beam angle on the neutrino flux are underway. Using the maximum beam angle from the multi-wire method, a study was performed to evaluate the impact on neutrino flux. Fig. 8.16 shows that with a significant beam angle, a great deal of protons that were expected to pass through the entire target (if not interacted) would instead have left the target region by the edges of the target. The resulting impact on flux can be seen in Fig. 8.17.

Further analysis would require use of the full beam Monte-Carlo, a much more intensive algorithm. Given both the small expected impact and the demands of further investigation, it was decided to focus on other aspects of the beam analyses, but this study remains accessible for future investigations.

8.2 Hadron Production Experiment Data Fitting and BNB Flux Prediction

The current prediction of flux coming from MiniBooNE uses the pion production cross section measurement for a thin (2 cm thick) Be target from the Hadron Production Experiment

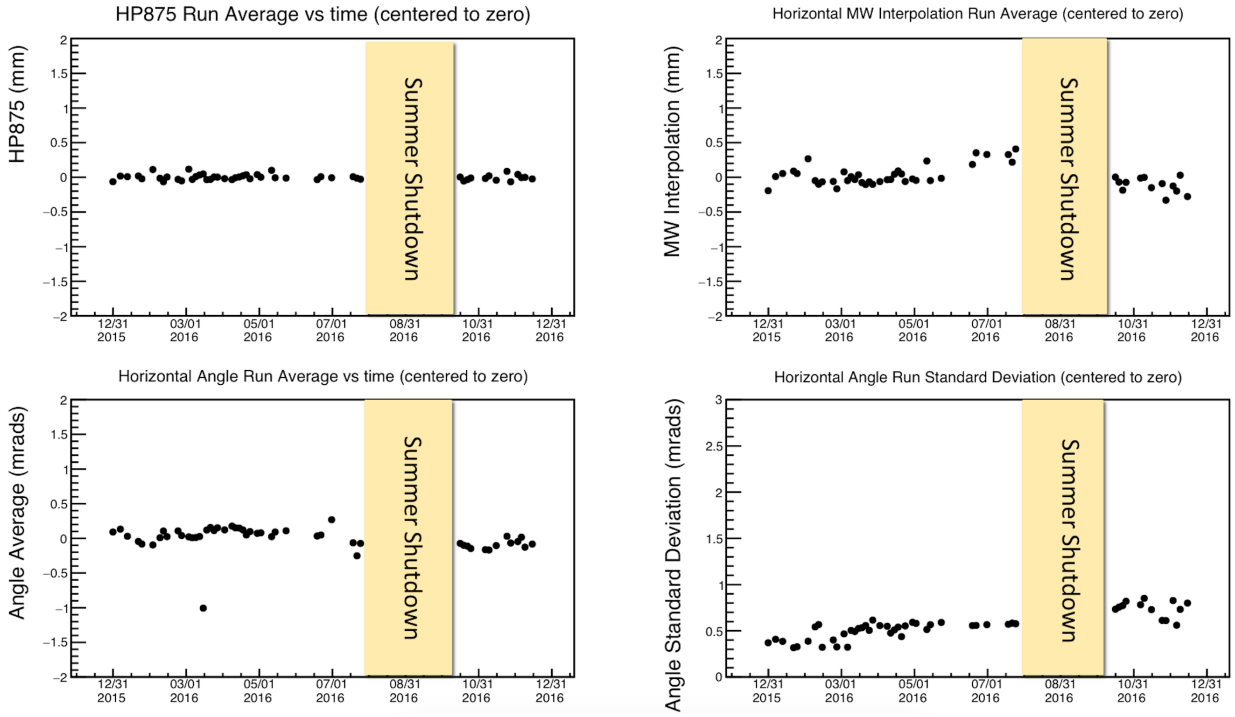

Figure 8.15: Shown are combined run average plots of Horizontal Position Monitor 875 (HP875) (top, left), multi-wire interpolation to the position of HP875 (top, right), the multi-wire angle (bottom, left), and the run standard deviation of the multi-wire angle (bottom, right). Data is collected in year 2016−2017 accepting runs with greater than 10,000 entries. Run averages are shifted such that their mean is zero.

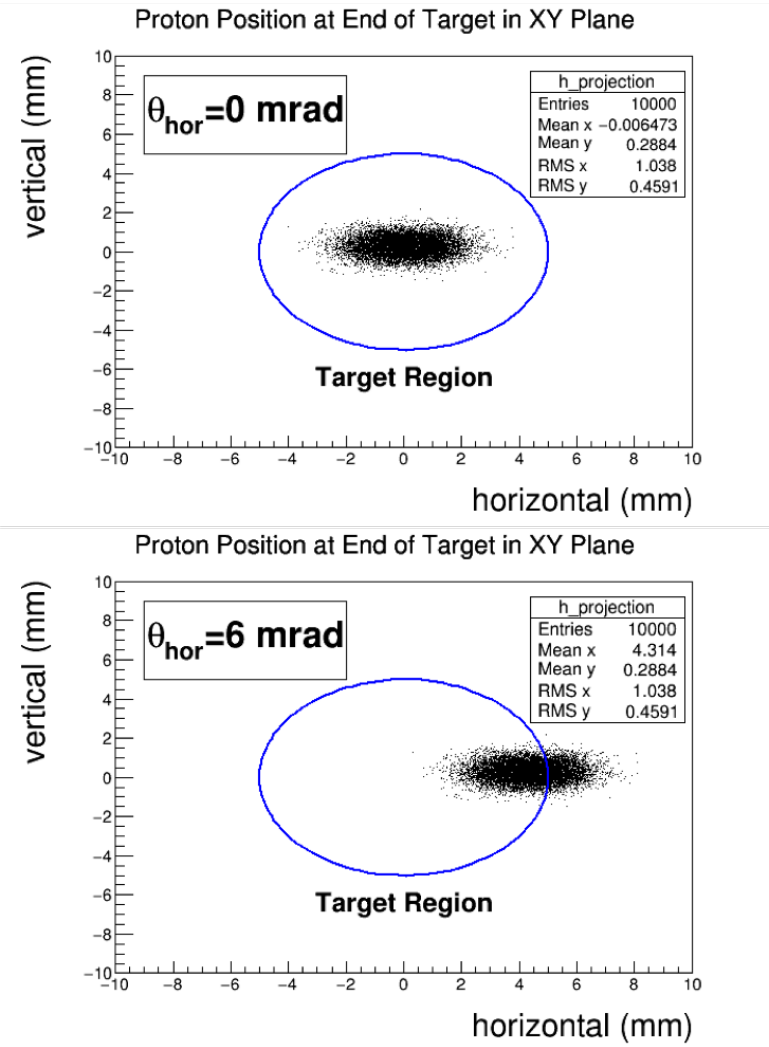

Figure 8.16: Plot of protons at the end of the target in X-Y plane generated via beam Monte-Carlo method: projected from 1 cm in front of target at nominal angle 0 mrad and with angle 6 mrad without interactions.

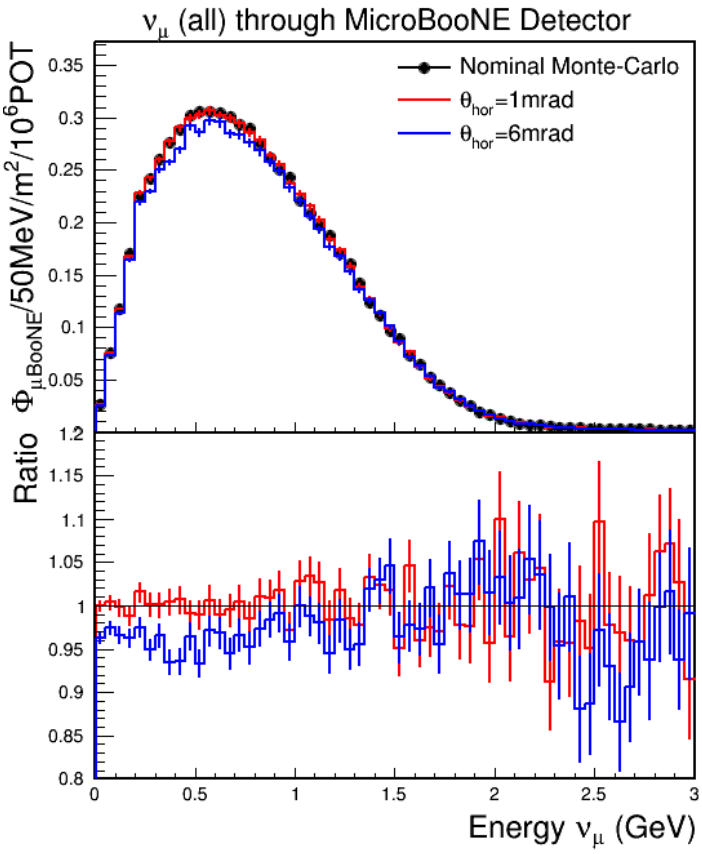

Figure 8.17: Comparison of Monte-Carlo run with nominal (zero degree angle) and chosen angles of 1 mrad and 6 mrad showing flux of ν_μ (top frame) and ratio between nominal and chosen angles (bottom frame).

(HARP). As discussed in Sec. 3.3.2, pions produce the dominant ν_μ flux while kaons produce a sub-dominant ν_e component.

The HARP experiment measured cross-sections of many particles with several targets of differing materials and thicknesses [83]. The data is well suited for use in MicroBooNE with momentum of the incoming proton beam, $p_{beam} \approx 8.89$ GeV/c comparable to that of the BNB $p_{beam} \approx 8.9$ GeV/c. The thin target proton production cross section data that is available from HARP is well suited for modeling secondary protons within the target. A quick comparison of the proton production data with the current BNB simulation shows a significant deviation, probably arising due to modeling differences of proton production processes in the simulation (see Fig. 8.18). Thus an attempt to fit the HARP thin target proton production data has been performed.

8.2.1 HARP Data

The HARP experiment was located at European Organization for Nuclear Research (CERN) in Switzerland and was an effort to measure hadron production data on a suite of targets at differing angles and momentum. It utilized the T9 beamline, and particle detection was accomplished via the HARP spectrometer as seen in Fig. 8.19.

The HARP thin target proton production data was measured with proton beam of momentum $p_{beam} \approx 8.89$ GeV/cm and beryllium target thickness $t \approx 2.046$ cm. The double differential cross section was measured in 13 momentum bins in the region $0.75 < p < 6.5$ GeV/c and six angular bins in the region $30 < \theta < 210$ mrad. The exact binning is listed below.

- p_{beam}=[0.75, 1.0, 12.5, 1.5, 2.0, 2.25, 2.5, 2.75, 3.0, 3.25, 4.0, 5.0, 6.0, 6.5]
- θ=[30, 60, 90, 120, 150, 180, 210]

8.2.2 Proton Contribution to Neutrino Flux

Secondary protons created by the initial interaction between the proton beam and beryllium target will re-interact with the potential of ultimately producing neutrinos. An example

of such an interaction chain can be seen in Fig. 8.20. The contribution of the resulting neutrinos to the net predicted neutrino flux has been analyzed to evaluate the potential impact of implementing the HARP proton data. The contribution from secondary protons compared to the total neutrino flux with cuts p <8 GeV (the region where proton data can be reasonably modelled from this fit) and to the bounds of the HARP experiment can be seen in Fig. 8.21. A table of the percentage of these cuts compared to the net predicted neutrino flux can be seen in Tab. 8.2. Small but not insignificant contribution comes from the secondary protons especially for the $\bar{\nu_\mu}$, likely because π^-s produced via secondary protons are lower in momentum and less likely to leave the target region and get subsequently filtered by the horn magnetic field. However, significant contribution also occurs in lower energy bins which is the low energy excess (LEE) area of study.

8.2.3 Sanford-Wang Parametrization

The Sanford-Wang [88] parametrization was used to model charged pion production in proton-beryllium collisions in the MiniBooNE and K2K experiments and by HARP itself. It is an empirical formula originally developed to model charged pion production of proton-beryllium interactions. In this study, its applicability to proton production was evaluated by fitting of HARP data. The formulation is shown in Eq. 8.1

$$\frac{d^2\sigma}{dp\ d\Omega} = c_1 \cdot p^{c_2}(1 - \frac{p}{p_{beam}})exp[-c_3\frac{p^{c_4}}{p_{beam}^{c_5}} - c_6\ \theta(p - c_7\ p_{beam}(cos\theta)^{c_8})] \tag{8.1}$$

where, c_i are parameters of the function for $i = 1...8$, p is the momentum of the resulting particle (in our case secondary protons), and p_{beam} is the incident proton momentum. For the parameters, c_1 is an overall normalization factor while c_2, c_3, c_4, and c_5 describe the overall momentum dependence. The paramter c_2 adjusts the direct momentum dependence while the component of $(1 - \frac{p}{p_{beam}})exp[-c_3\frac{p^{c_4}}{p_{beam}^{c_5}}]$ can be described as a shape factor dependent on the ratio of beam momentum to the resulting particle momentum. The angle and cosine term provide detailed angular structure with c_6, c_7, and c_8 defining behavior of the distribution at larger angles [101].

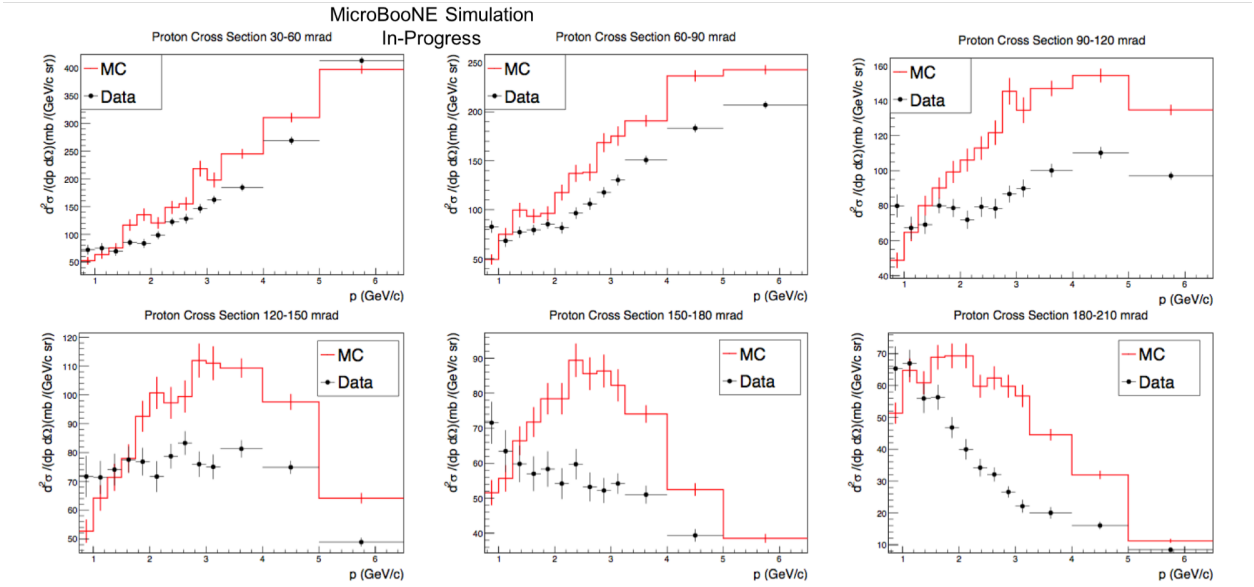

Figure 8.18: Beam Monte-Carlo estimates of proton cross section compared to the HARP data. Each individual plot is outgoing angular bin and within each plot, the double differential cross section is binned in momentum.

Table 8.2: Percentage of total flux comprised of neutrinos from secondary protons at p_p <8 GeV and with HARP bounds (0.75< p_p <6.5 GeV and 30< θ <210 mrad).

Cuts	ν_μ	$\bar{\nu_\mu}$	ν_e	$\bar{\nu_e}$
$p_p < 8\ GeV$	4.49%	11.37%	5.09%	6.75%
HARP bounds	1.67%	4.41%	1.70%	2.17%

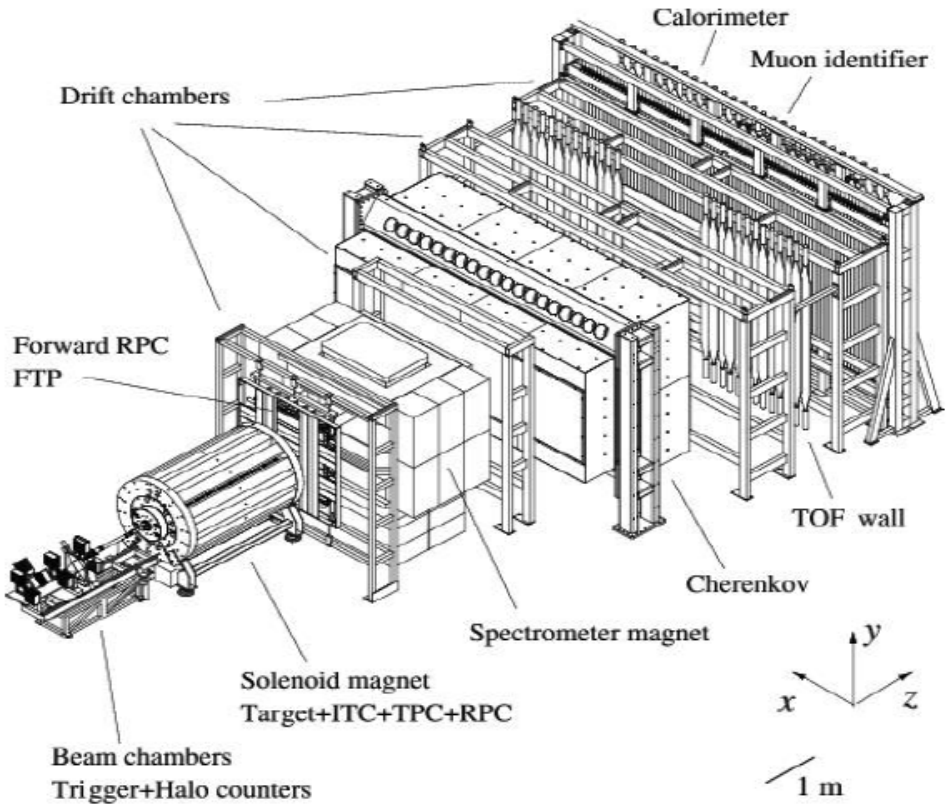

Figure 8.19: Schematic drawing of the HARP spectrometer. Particle identification at large angles is accomplished via a TPC and resistive plate chambers (RPC), and more forward going particles are identified using a Cherenkov detector, five drift chambers, and a time-of-flight scintillator wall, a muon identifier, and an electromagnetic calorimeter.

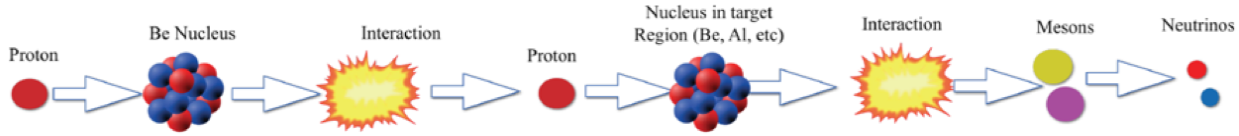

Figure 8.20: Simple illustration of secondary proton interaction chain that produces neutrinos.

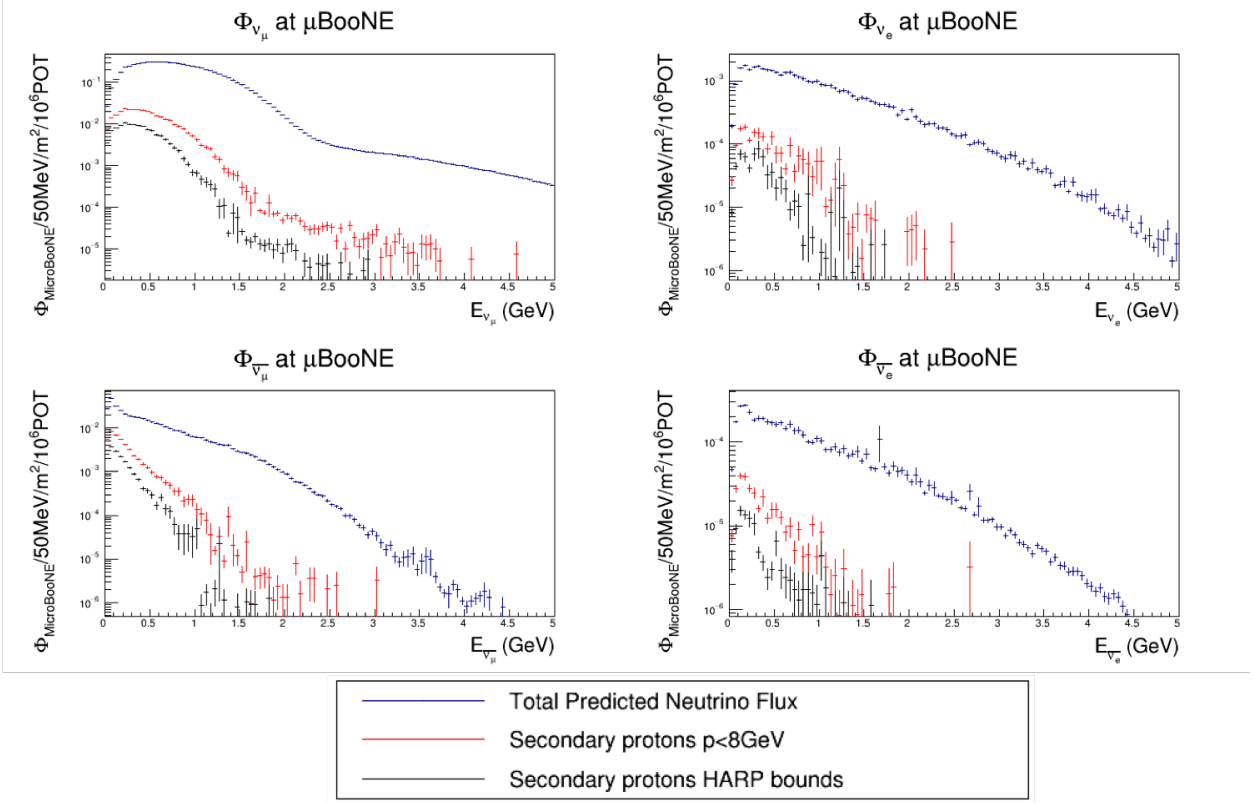

Figure 8.21: Comparison of the total neutrino flux per energy bin with the contribution of neutrino flux from secondary protons restricted to $p_p < 8$ GeV (region where it is expected to reasonably predict behavior) and to the HARP experimental bounds $0.75 < p_p < 6.5$ GeV and 0.03 rad$< \theta <$0.21 rad. Plots are made using 2000 runs with 10,000 POT per run.

8.2.4 HARP Data Fitting

To fit data, the chi-square function was minimized as shown in equation 8.2

$$\chi^2(c_1,..c_8) = \sum_i (D_i - c_9 \cdot SW_i) COV^{-1}_{i,j} (D_j - c_9 \cdot SW_i) + \frac{(c_9 - 1)^2}{\sigma_k^2} \tag{8.2}$$

The first minimizer attempted was the Nelder-Mead minimization implemented via SciPy [102] a Python-based package. The Nelder-Mead [103] algorithm is a direct search numerical method using a polytope of $n+1$ vertices where n is the number of parameters being fit which iterates by replacing worst points of the fit. The initial fitting effort also fit over only the diagonal of the covariance matrices saving processing time. The fit using this methodology can be seen in Fig. 8.22. The data fitting is good except in a few regions, but on examination of the plot, the end point behavior is not what is physically expected (see Fig. 8.23). Also, the negative values of the parameters indicate the fitting may not be physical.

Expanding the fitting algorithm to the full covariance matrix using this as a base failed to improve the endpoint behavior and indeed seemed to actually worsen the agreement as seen in Fig. 8.24.

Efforts were undertaken to improve the fit via bounding endpoints (forcing the fit to a particular value at its endpoints) and to force the parameters to be positive, but this resulted in much poorer fitting as seen in Fig. 8.25. Other attempts were made using the Extended Sanford Wang (ESW) parametrization [83] and other fitting algorithms, but nothing was produced with as good matching.

This may indicate that the intended shape of the function is incompatible with this data, but this is difficult to prove. Due to lingering issues with the fit and the low expected contribution to the flux prediction, it was decided not to implement the fit into the MicroBooNE flux prediction. However, the fit and algorithm remains available should it be desired in the future.

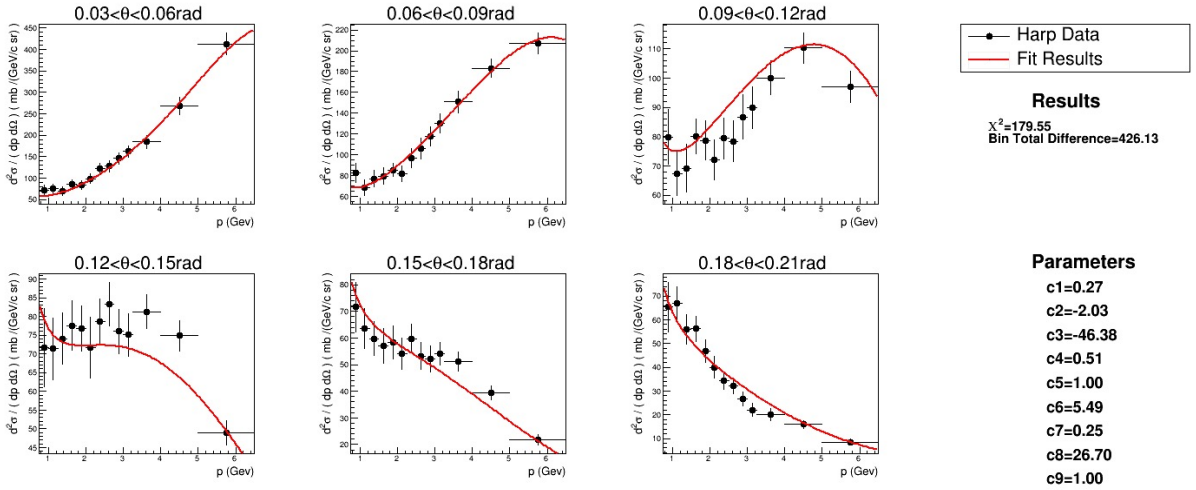

Figure 8.22: Results of fitting HARP thin beryllium target proton cross-section data with Sanford-Wang parametrization, fitting only the diagonal of the covariance matrix. As with Fig. 8.18, individual plots correspond to certain angular bins, and within each plot, the double differential cross section is binnedin momentum for the data. The Sanford-Wang fit is plotted as a function of double differential cross section vs momentum with central values of the angular bin used for each plot.

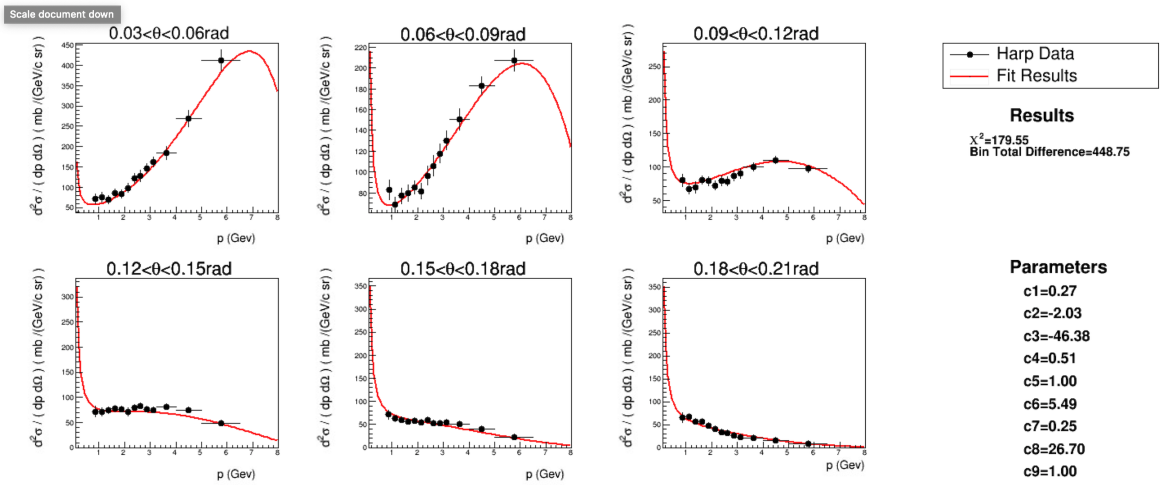

Figure 8.23: The same fit as in Fig. 8.22 is displayed here but with x-axis range extended.

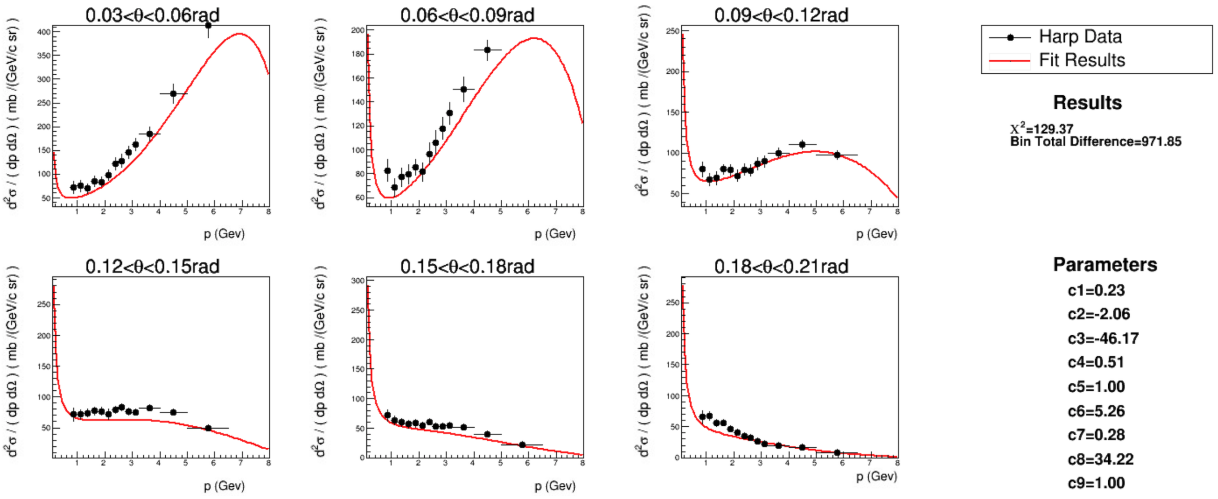

Figure 8.24: Fitting using the full covariance matrix.

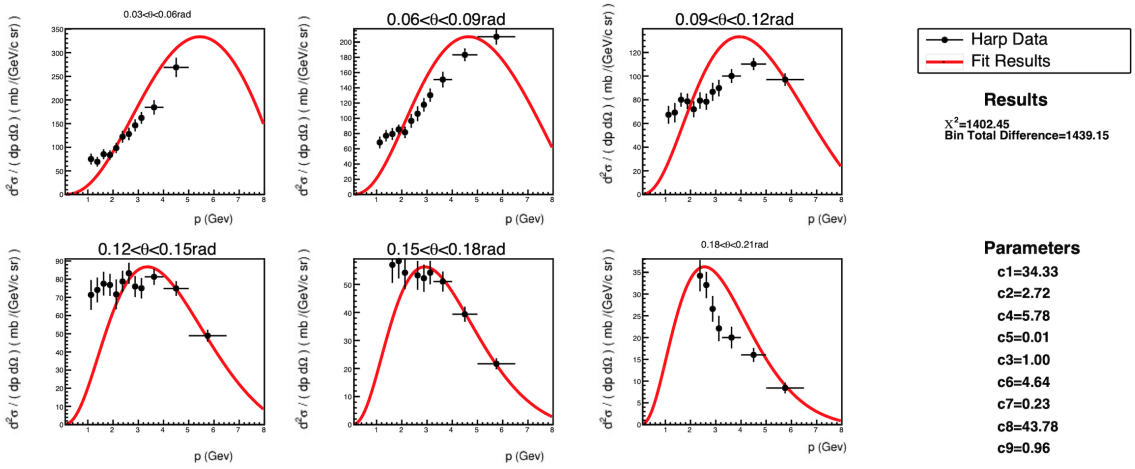

Figure 8.25: Best Fit with bounded endpoints and parameters.

Chapter 9

Summary and Outlook

This dissertation presents analysis efforts to understand the MiniBooNE Low Energy Excess (LEE) anomaly, which has broad implications to the field of particle physics including the existence of sterile neutrinos. This work focuses on analyzing a photon-like explanation for the MiniBooNE LEE by providing a complete evaluation of systematic uncertainties. This is done both in the context of the Single Photon analysis and separately through detailed studies on the Booster Neutrino Beamline.

The beam study produced a method for increasing usable data via Figure of Merit recovery. This method is being implemented into the MicroBooNE beam analysis algorithm for testing purposes. Preliminary results of this analysis were presented at the American Physical Society (APS) April 2018 meeting[1], and a public note is planned in the near future to share the concept with other collaborators and potentially other experiments with similar instrumentation. Other studies on beam angle and HARP proton production data were inconclusive, but were an important investigation into avenues for analyses. Furthermore, these analyses remain open for future explanation.

A complete set of systematic uncertainties from flux, cross-section, and detector effects were provided to the gamma LEE analysis. While improvements are still being pursued, the neutral current (NC) π^0 selection provided a powerful constraint to significantly reduce the systematics on the gamma LEE signal region. The implication of these systematic reductions to our signal sensitivity has been evaluated resulting in significant improvement.

[1] https://meetings.aps.org/Meeting/APR18/Session/J08.1

Reduction of systematic uncertainties via NC π^0 was shown to reduce overall uncertainties from $\sim$20% to $\sim$10% in high statistics regions. Without this reduction, distinguishing between our hypotheses of LEE signal would have been impossible given current data availability. Furthermore, analysis has commenced on data in the Near and Far signal-like regions. Near sidebands are naturally closer to our signal region than the Far sidebands. My most recent presentation of the systematic prediction was at the annual meeting of the APS Southeastern Section (SESAPS) in 2020[2]. First results from the gamma LEE analysis were published as a MicroBooNE public note [22] and presented at the XXIX International Conference on Neutrino Physics (Neutrino 2020) in July 2020. A more comprehensive analysis note is currently under collaboration review with an accompanying far sideband analysis note. Furthermore, two submissions to Physical Review Letters (PRL) are planned in the immediate future, for which I will author the systematics sections.

MicroBooNE is nearing its sixth year of data collection. Steps towards unblinding data have begun with analysis based on simulation and a small open data-set reaching preset thresholds for accuracy and performance. The single photon and other LEE analyses will be completed on this data in the near future shedding light on the MiniBooNE anomaly. MicroBooNE will resume running as part of the Short Baseline Neutrino program at Fermilab in the near term to further probe the phase space where there are existing hints on sterile neutrinos. The oscillation results and neutrino-Argon cross-section measurements from MicroBooNE will provide key inputs to the upcoming Deep Underground Neutrino Experiment (DUNE) [48].

Neutrino experiments continue to probe fundamental questions in the field of particle physics. Upcoming long-baseline experiments, such as DUNE [48], seek to measure potential Charge-Parity conservation violating properties of neutrinos. This factor could be crucial in explaining the matter-antimatter asymmetry of the universe. Experiments in the short-baseline region, such as the SBN program [47], seek discovery of new particles (sterile neutrinos). Sterile neutrino analyses also have the potential to resolve the issue of neutrino mass generation.

[2]https://meetings.aps.org/Meeting/SES20/Session/B05.4

Bibliography

[1] R. Acciarri, C. Adams, R. An, A. Aparicio, S. Aponte, J. Asaadi, M. Auger, N. Ayoub, L. Bagby, B. Baller, et al. Design and construction of the microboone detector. *Journal of instrumentation*, 12(02):P02017, 2017. x, xvii, 1, 37, 41, 43, 45, 56, 63

[2] F. Reines and C. L. Cowan. Detection of the free neutrino. *Phys. Rev.*, 92:830–831, Nov 1953. xiv, 8, 10

[3] J. A. Formaggio and G. P. Zeller. From ev to eev: Neutrino cross sections across energy scales. *Reviews of Modern Physics*, 84(3):1307–1341, Sep 2012. xiv, xv, 14, 24

[4] N. J. Baker, P. L. Connolly, S. A. Kahn, M. J. Murtagh, R. B. Palmer, N. P. Samios, and M. Tanaka. Total cross sections for $\nu_\mu n$ and $\nu_\mu p$ charged-current interactions in the 7-foot bubble chamber. *Phys. Rev. D*, 25:617–623, Feb 1982. xiv, 14

[5] D.S. Baranov, A.P. Bugorsky, A.A. Ivanilov, V.I. Kochetkov, V.I. Konyushko, V.M. Korablev, V.A. Korotkov, V.I. Kurbakov, E.P. Kuznetsov, V.V. Makeev, A.G. Mjagkov, A.I. Mukhin, Yu.P. Nikitin, S.N. Parshikura, A.Yu. Polyarush, Yu.G. Rjabov, A.V. Samoilov, Yu.I. Smirnov, A.A. Sokolov, Yu.M. Sviridov, A.A. Volkov, and G.G. Volkov. Measurement of the νμn total cross section at 2–30 gev in a skat neutrino experiment. *Physics Letters B*, 81(2):255–257, 1979. xiv, 14

[6] S. Ciampolillo et al. Total Cross-section for Neutrino Charged Current Interactions at 3-GeV and 9-GeV. *Phys. Lett. B*, 84:281–284, 1979. xiv, 14

[7] Y. Nakajima, J. L. Alcaraz-Aunion, S. J. Brice, L. Bugel, J. Catala-Perez, G. Cheng, J. M. Conrad, Z. Djurcic, U. Dore, D. A. Finley, and et al. Measurement of inclusive charged current interactions on carbon in a few-gev neutrino beam. *Physical Review D*, 83(1), Jan 2011. xiv, 14

[8] Stephen F King and Christoph Luhn. Neutrino mass and mixing with discrete symmetry. *Reports on Progress in Physics*, 76(5):056201, May 2013. xiv, 18, 21

[9] James Ellison, David Friant, Adam Lister, Shivesh Mandalia, and Ben Messerly. International neutrino summer 2017 school project. xv, 25

[10] A Aguilar et al. Evidence for neutrino oscillations from the observation of $\overline{\nu}_e$ appearance in a $\overline{\nu}_\mu$ beam. *Phys. Rev. D*, 64:112007, Nov 2001. xv, 19, 27, 31, 32

[11] Aguilar-Arevalo et al. Updated miniboone neutrino oscillation results with increased data and new background studies. *Phys. Rev. D*, 103:052002, Mar 2021. xv, 1, 19, 33, 34

[12] C. Adams et al. Ionization electron signal processing in single phase LArTPCs. part i. algorithm description and quantitative evaluation with MicroBooNE simulation. *Journal of Instrumentation*, 13(07):P07006–P07006, jul 2018. xvi, xvii, 48, 52, 64, 71

[13] C. Adams et al. Design and construction of the MicroBooNE cosmic ray tagger system. *Journal of Instrumentation*, 14(04):P04004–P04004, apr 2019. xvii, 54

[14] Lister A., Mogan A., and et Al. Measurement of the longitudinal diffusion of ionization electrons in the microboone detector. *https://arxiv.org/abs/2104.06551*, 2021. xvii, 61, 62

[15] V.M. Atrazhev and I.V. Timoshkin. Transport of electrons in atomic liquids in high electric fields. *IEEE Transactions on Dielectrics and Electrical Insulation*, 5(3):450–457, 1998. xvii, 62

[16] Yichen Li, Thomas Tsang, and et Al. Measurement of longitudinal electron diffusion in liquid argon. *Nuclear Instruments and Methods in Physics Research Section A: Accelerators, Spectrometers, Detectors and Associated Equipment*, 816:160–170, 2016. xvii, 62

[17] P. Cennini, S. Cittolin, and et al. Performance of a three-ton liquid argon time projection chamber. *Nuclear Instruments and Methods in Physics Research Section A: Accelerators, Spectrometers, Detectors and Associated Equipment*, 345(2):230–243, 1994. xvii, 62

[18] R. Acciarri and et al. The pandora multi-algorithm approach to automated pattern recognition of cosmic-ray muon and neutrino events in the microboone detector. *arXiv:1708.03135*, 2017. xviii, 59, 73, 74, 75

[19] Michael Mooney. The microboone experiment and the impact of space charge effects, 2015. xviii, 76

[20] MicroBooNE Collaboration. A measurement of the attenuation of drifting electrons in the microboone lartpc. *MicroBooNE Public Note 1026*. xix, 44, 78

[21] K. Abe et al. Search for neutral-current induced single photon production at the ND280 near detector in T2K. *J. Phys.*, G46(8):08LT01, 2019. xix, 9, 18, 22, 26, 60, 84

[22] MicroBooNE Collaboration. Microboone low-energy excess signal prediction from unfolding. *MicroBooNE Public Note 1043*. xix, 83, 84, 176

[23] *Handbook on Photonuclear Data for Applications Cross-sections and Spectra*. Number 1178 in TECDOC Series. INTERNATIONAL ATOMIC ENERGY AGENCY, Vienna, 2000. xxv, 132

[24] Accelerator Division — Operations Department Fermilab. Concepts rookie book. 2013. xxvii, 143, 145

[25] P. Adamson, K. Anderson, and M. et al. Andrews. The numi neutrino beam. *Nuclear Instruments and Methods in Physics Research Section A: Accelerators, Spectrometers, Detectors and Associated Equipment*, 806:279–306, Jan 2016. xxx, 207, 208

[26] S. L. Glashow. Partial Symmetries of Weak Interactions. *Nucl. Phys.*, 22:579–588, 1961. 4

[27] Steven Weinberg. A model of leptons. *Phys. Rev. Lett.*, 19:1264–1266, Nov 1967. 4, 5

[28] Abdus Salam. Weak and Electromagnetic Interactions. *Conf. Proc. C*, 680519:367–377, 1968. 4

[29] Peter W. Higgs. Broken symmetries and the masses of gauge bosons. *Phys. Rev. Lett.*, 13:508–509, Oct 1964. 7

[30] SM Bilenky. Neutrino in standard model and beyond. *Particle Data Group*, 46(4):475–496, 2015. 8, 9, 12, 19

[31] G. Aad et al.i. Observation of a new particle in the search for the standard model higgs boson with the atlas detector at the lhc. *Physics Letters B*, 716(1):1–29, 2012. 8

[32] B Pontecorvo. Inverse *beta* processes and nonconservation of lepton charge. *https://www.osti.gov/biblio/4349231*, 34, 1 1958. 8, 9

[33] G. Danby, J-M. Gaillard, K. Goulianos, L. M. Lederman, N. Mistry, M. Schwartz, and J. Steinberger. Observation of high-energy neutrino reactions and the existence of two kinds of neutrinos. *Phys. Rev. Lett.*, 9:36–44, Jul 1962. 8

[34] Bruce T. Cleveland, Timothy Daily, Jr. Raymond Davis, James R. Distel, Kenneth Lande, C. K. Lee, Paul S. Wildenhain, and Jack Ullman. Measurement of the solar electron neutrino flux with the homestake chlorine detector. *The Astrophysical Journal*, 496(1):505–526, mar 1998. 9

[35] S Turck-Chièze. The standard solar model and beyond. *Journal of Physics: Conference Series*, 665:012078, jan 2016. 9

[36] S. Fukuda et al. The super-kamiokande detector. *Nuclear Instruments and Methods in Physics Research Section A: Accelerators, Spectrometers, Detectors and Associated Equipment*, 501(2):418–462, 2003. 9

[37] K Kodama et al. Detection and analysis of tau–neutrino interactions in donut emulsion target. *Nuclear Instruments and Methods in Physics Research Section A: Accelerators, Spectrometers, Detectors and Associated Equipment*, 493(1):45–66, 2002. 9

[38] Ziro Maki, Masami Nakagawa, and Shoichi Sakata. Remarks on the Unified Model of Elementary Particles. *Progress of Theoretical Physics*, 28(5):870–880, 11 1962. 9

[39] Y Fukuda, T Hayakawa, E Ichihara, K Inoue, K Ishihara, H Ishino, Y Itow, T Kajita, J Kameda, S Kasuga, et al. Evidence for oscillation of atmospheric neutrinos. *Physical Review Letters*, 81(8):1562, 1998. 9

[40] Q Retal Ahmad, RC Allen, TC Andersen, JD Anglin, JC Barton, EW Beier, M Bercovitch, J Bigu, SD Biller, RA Black, et al. Direct evidence for neutrino flavor transformation from neutral-current interactions in the sudbury neutrino observatory. *Physical review letters*, 89(1):011301, 2002. 9

[41] T Araki, K Eguchi, S Enomoto, K Furuno, K Ichimura, H Ikeda, K Inoue, K Ishihara, T Iwamoto, T Kawashima, et al. Measurement of neutrino oscillation with kamland: Evidence of spectral distortion. *Physical Review Letters*, 94(8):081801, 2005. 9

[42] M Tanabashi. Review of particle physics. *Phys. Rev. D*, 98:030001, 2018. 12

[43] C.H. Llewellyn Smith. Neutrino reactions at accelerator energies. *Physics Reports*, 3(5):261–379, 1972. 15

[44] J. Nieves, J. E. Amaro, and M. Valverde. Erratum: Inclusive quasielastic charged-current neutrino-nucleus reactions [phys. rev. c 70, 055503 (2004)]. *Phys. Rev. C*, 72:019902, Jul 2005. 15, 60

[45] A. Bodek, M. E. Christy, and B. Coopersmith. Effective spectral function for quasielastic scattering on nuclei. *The European Physical Journal C*, 74(10):3091, 2014. 16, 60

[46] Dieter Rein and Lalit M Sehgal. Neutrino-excitation of baryon resonances and single pion production. *Annals of Physics*, 133(1):79–153, 1981. 17, 60

[47] R. Acciarri. A proposal for a three detector short-baseline neutrino oscillation program in the fermilab booster neutrino beam. *arXiv:1503.01520*, 2015. 17, 176

[48] Mehedi Masud, Animesh Chatterjee, and Poonam Mehta. Probing the cp violation signal at dune in the presence of non-standard neutrino interactions. *Journal of Physics G: Nuclear and Particle Physics*, 43(9):095005, Aug 2016. 17, 18, 22, 26, 163, 176

[49] S. P. Rosen and J. M. Gelb. Mikheyev-smirnov-wolfenstein enhancement of oscillations as a possible solution to the solar-neutrino problem. *Phys. Rev. D*, 34:969–979, Aug 1986. 18

[50] M. A. Acero et al. First Measurement of Neutrino Oscillation Parameters using Neutrinos and Antineutrinos by NOvA. *Phys. Rev. Lett.*, 123(15):151803, 2019. 18, 22, 26

[51] Kamiokande Working Group. A long baseline neutrino oscillation experiment using j-parc neutrino beam and hyper-kamiokande. *arXiv:1412.4673*, 2015. 18, 22

[52] S.M. Bilenky, C. Giunti, J.A. Grifols, and E. Massó. Absolute values of neutrino masses: status and prospects. *Physics Reports*, 379(2):69–148, May 2003. 18

[53] Ch Kraus, B. Bornschein, L. Bornschein, J. Bonn, B. Flatt, A. Kovalik, B. Ostrick, E. W. Otten, J. P. Schall, Th Thümmler, and et al. Final results from phase ii of the mainz neutrino mass searchin tritium β decay. *The European Physical Journal C*, 40(4):447–468, Apr 2005. 18

[54] V. N. Aseev, A. I. Belesev, A. I. Berlev, E. V. Geraskin, A. A. Golubev, N. A. Likhovid, V. M. Lobashev, A. A. Nozik, V. S. Pantuev, V. I. Parfenov, and et al. Upper limit on the electron antineutrino mass from the troitsk experiment. *Physical Review D*, 84(11), Dec 2011. 18

[55] M. Aker, K. Altenmüller, M. Arenz, M. Babutzka, J. Barrett, S. Bauer, M. Beck, A. Beglarian, J. Behrens, T. Bergmann, and et al. Improved upper limit on the neutrino mass from a direct kinematic method by katrin. *Physical Review Letters*, 123(22), Nov 2019. 18

[56] Walter C. Pettus. Overview of Project 8 and Progress Towards Tritium Operation. *J. Phys. Conf. Ser.*, 1342(1):012040, 2020. 19

[57] L et al. Gastaldo. The electron capture in 163ho experiment –echo. *The European Physical Journal Special Topics*, 226(8):1623–1694, 2017. 19

[58] A. Nucciotti, B. Alpert, M. Balata, D. Becker, D. Bennett, A. Bevilacqua, M. Biasotti, V. Ceriale, G. Ceruti, D. Corsini, and et al. Status of the holmes experiment to directly measure the neutrino mass. *Journal of Low Temperature Physics*, 193(5-6):1137–1145, Jul 2018. 19

[59] Davio Cianci, Andy Furmanski, Georgia Karagiorgi, and Mark Ross-Lonergan. Prospects of Light Sterile Neutrino Oscillation and CP Violation Searches at the Fermilab Short Baseline Neutrino Facility. *Phys. Rev. D*, 96(5):055001, 2017. 19, 100

[60] S. Ajimura et al. Proposal: JSNS^2-II. *arXiv:012.10807*, 2020. 19

[61] S. H. et al. Hayakawa. Observation of coulomb-assisted nuclear bound state of Ξ^- − $-^{14}$N system. *Phys. Rev. Lett.*, 126:062501, Feb 2021. 19

[62] Precision electroweak measurements on the z resonance. *Physics Reports*, 427(5-6):257–454, May 2006. 19

[63] M. Goldhaber, L. Grodzins, and A. W. Sunyar. Helicity of neutrinos. *Phys. Rev.*, 109:1015–1017, Feb 1958. 19

[64] S. Dell'Oro. Results of CUORE. *arXiv:1905.07667*, 2019. 20

[65] Jordan Myslik. Legend: The large enriched germanium experiment for neutrinoless double-beta decay, 2018. 20

[66] R. Benton Pahlka. The SuperNEMO experiment. *arXiv:0810.3169*, 2008. 20

[67] Brian Mong. nEXO - Neutrinoless double beta decay experiment. *PoS*, HQL2016:074, 2017. 20

[68] M. L. Benabderrahmane. Neutrino physics with DARWIN. *Journal of Physics: Conference Series*, 888:012048, sep 2017. 20

[69] T. D. Lee and C. N. Yang. Question of parity conservation in weak interactions. *Phys. Rev.*, 104:254–258, Oct 1956. 20

[70] C. S. Wu, E. Ambler, R. W. Hayward, D. D. Hoppes, and R. P. Hudson. Experimental test of parity conservation in beta decay. *Phys. Rev.*, 105:1413–1415, Feb 1957. 20

[71] J. H. Christenson, J. W. Cronin, V. L. Fitch, and R. Turlay. Evidence for the 2π decay of the k_2^0 meson. *Phys. Rev. Lett.*, 13:138–140, Jul 1964. 22

[72] Alavi-Harati et al. Observation of direct cp violation in $k_{s,l} \to \pi\pi$ decays. *Phys. Rev. Lett.*, 83:22–27, Jul 1999. 22

[73] V. Fanti, A. Lai, D. Marras, L. Musa, A.J. Bevan, T.J. Gershon, B. Hay, R.W. Moore, K.N. Moore, D.J. Munday, and et al. A new measurement of direct cp violation in two pion decays of the neutral kaon. *Physics Letters B*, 465(1-4):335–348, Oct 1999. 22

[74] Claus Kiefer. *CPT Theorem*, pages 138–139. Springer Berlin Heidelberg, Berlin, Heidelberg, 2009. 22

[75] Callum Wilkinson, Philip Rodrigues, Susan Cartwright, Lee Thompson, and Kevin McFarland. Reanalysis of bubble chamber measurements of muon-neutrino induced single pion production. *Physical Review D*, 90(11), Dec 2014. 23

[76] J. Bamberger, D. Brown, C. Goodzeit, D. Kassner, R. Louttit, A. Prodell, R. Shutt, and J. Sondericker. Design, construction and performance of the brookhaven national laboratory 7-foot bubble chamber. *Nuclear Instruments and Methods*, 130(2):379–425, 1975. 23

[77] L.H. Whitehead. Neutrino oscillations with MINOS and MINOS+. *Nuclear Physics B*, 908:130–150, Jul 2016. 26

[78] AA Aguilar-Arevalo, BC Brown, L Bugel, G Cheng, JM Conrad, RL Cooper, R Dharmapalan, A Diaz, Z Djurcic, DA Finley, et al. Observation of a significant excess of electron-like events in the miniboone short-baseline neutrino experiment. *arXiv preprint arXiv:1805.12028*, 2018. 27, 33

[79] Luis Salvador Miranda and Soebur Razzaque. Revisiting constraints on 3 + 1 active-sterile neutrino mixing using icecube data. *Journal of High Energy Physics*, 2019(3), Mar 2019. 31

[80] G.H. Collin, C.A. Argüelles, J.M. Conrad, and M.H. Shaevitz. Sterile neutrino fits to short baseline data. *Nuclear Physics B*, 908:354–365, Jul 2016. 31

[81] J. Allison et al. Recent developments in geant4. *Nuclear Instruments and Methods in Physics Research Section A: Accelerators, Spectrometers, Detectors and Associated Equipment*, 835:186–225, 2016. 38, 59

[82] G. et al Cheng. Measurement of K^+ production cross section by 8 gev protons using high-energy neutrino interactions in the sciboone detector. *Phys. Rev. D*, 84:012009, Jul 2011. 38, 59

[83] A. Bolshakova et al. Cross-sections of large-angle hadron production in proton- and pion-nucleus interactions i: Beryllium nuclei and beam momenta of +8.9 gev/c and -8.0 gev/c. *Eur. Phys. J.*, C62:293–317, 2009. 38, 59, 167, 172

[84] MicroBooNE Collaboration. Booster neutrino flux prediction at microboone. *MicroBooNE Public Note 1031*. 38

[85] MicroBooNE Collaboration. Single differential ν_μ charged-current cross section with the microboone detector using the cosmic ray tagger. *MicroBooNE Public Note 1069*. 44

[86] E.L. Snider and G. Petrillo. LArSoft: toolkit for simulation, reconstruction and analysis of liquid argon TPC neutrino detectors. *Journal of Physics: Conference Series*, 898:042057, oct 2017. 58

[87] C. Green, J. Kowalkowski, M. Paterno, M. Fischler, L. Garren, and Q. Lu. The Art Framework. *J. Phys. Conf. Ser.*, 396:022020, 2012. 58, 102

[88] C. Mariani, G. Cheng, J. M. Conrad, and M. H. Shaevitz. Improved parametrization ofk+production inpbecollisions at low energy using feynman scaling. *Physical Review D*, 84(11), Dec 2011. 59, 168

[89] D. Heck, J. Knapp, J. N. Capdevielle, G. Schatz, and T. Thouw. CORSIKA: A Monte Carlo code to simulate extensive air showers. *Report Number: FZKA-6019*, 2 1998. 59

[90] A Ferrari, Paola R Sala, A Fassò, and Johannes Ranft. *FLUKA: A multi-particle transport code (program version 2005)*. CERN Yellow Reports: Monographs. CERN, Geneva, 2005. 59

[91] A. Capella, U. Sukhatme, C.-I. Tan, and J. Tran Thanh Van. Dual parton model. *Physics Reports*, 236(4):225–329, 1994. 60

[92] Costas Andreopoulos, A Bell, D Bhattacharya, F Cavanna, J Dobson, S Dytman, H Gallagher, P Guzowski, R Hatcher, P Kehayias, et al. The genie neutrino monte carlo generator. *Nuclear Instruments and Methods in Physics Research Section A: Accelerators, Spectrometers, Detectors and Associated Equipment*, 614(1):87–104, 2010. 60, 101

[93] Ch. Berger and L. M. Sehgal. Lepton mass effects in single pion production by neutrinos. *Physical Review D*, 76(11), Dec 2007. 60

[94] S. Dytman K. Duffy and S. Gardiner. Microboone interaction uncertainties. *MicroBooNE Internal Notes*, 2020. 61

[95] John Stuart Marshall and Mark Andrew Thomson. The pandora software development kit for pattern recognition. *The European Physical Journal C*, 75(9):439, 2015. 64

[96] B. Baller. Liquid argon tpc signal formation, signal processing and reconstruction techniques. *Journal of Instrumentation*, 12(07):P07010–P07010, Jul 2017. 64

[97] X. Qian, C. Zhang, B. Viren, and M. Diwan. Three-dimensional imaging for large lartpcs. *Journal of Instrumentation*, 13(05):P05032–P05032, May 2018. 64

[98] R. Acciarri, C. Adams, R. An, J. Asaadi, M. Auger, L. Bagby, B. Baller, G. Barr, M. Bass, F. Bay, and et al. Convolutional neural networks applied to neutrino events in a liquid argon time projection chamber. *Journal of Instrumentation*, 12(03):P03011–P03011, Mar 2017. 64

[99] Bruce Worthel. Booster rookie book. MicroBooNE Rookie Books, 2009. 146

[100] Davio Cianci, Andy Furmanski, Georgia Karagiorgi, and Mark Ross-Lonergan. Prospects of light sterile neutrino oscillation and c p violation searches at the fermilab short baseline neutrino facility. *Physical Review D*, 96(5):055001, 2017. 163

[101] CL Wang. Pion, kaon, and antiproton production between 10 and 70 bev. *Physical Review Letters*, 25(15):1068, 1970. 168

[102] Pauli et al. Virtanen. *Nature Methods*, 17:261–272, 2020. 172

[103] John A. Nelder and Roger Mead. A simplex method for function minimization. *Computer Journal*, 7:308–313, 1965. 172

Appendices

A Appendix: Comprehensive Set of Reweightable Uncertainty Tables

Here we summarize each individual flux and cross-section variation and their contribution to the single photon LEE uncertainty. The total uncertainty of each variation on each subsample is shown. Note there are some high values in the NormNCCOH variation for the NCπ^0Coh subsample, but these are very small subsamples with very small contribution to the single photon selections. Tab. 1 describes each flux and cross section variation briefly, and Tab. 2-5 give the uncertainty values. These values correspond to the final selection stage of the gamma LEE analysis. As a study done at an earlier stage of the gamma LEE analysis, the individual elements of the combined genie variation were run individually. As these numbers are not used in final fitting or constraint, and we expect there has been no significant change, these results were not regenerated but are provided here for reference. The format is the same as previous tables in this appendix where uncertainty from each variation with different subsamples is shown. Tab. 6 gives a brief description of each cross section variation, and Tab. 7-14 list the uncertainty values calculated.

Table 1: Description of flux and cross sections reweightable systematics used in final uncertainty calculations.

Variation Label	**Description**
All_UBGenie	All multisim mode GENIE variables combined
Flux	Variations
expskin_FluxUnisim	Skin Depth for electric currents penetrating conductor
horncurrent_FluxUnisim	Horn Current in magnetic focusing horn
kminus_PrimaryHadronNormalization	K^- production normalization
kplus_PrimaryHadronFeynmanScaling	K^+ Sanford Wang Central Spline Variation
kzero_PrimaryHadronSanfordWang	K^0 Sanford Wang
nucleoninexsec_FluxUnisim	Nucleon Total Inelastic cross section on Be
nucleonqexsec_FluxUnisim	Nucleon Total Quasi-elastic cross section on Be
nucleontotxsec_FluxUnisim	Nucleon Total cross section on Be
piminus_PrimaryHadronSWCentralSplineVariation	π^- Sanford Wang Central Spline Variation
pioninexsec_FluxUnisim	Pion Total Inelastic cross section on Be
pionqexsec_FluxUnisim	Pion Total Quasi-elastic cross section on Be
piontotxsec_FluxUnisim	Pion Total cross section on Be
piplus_PrimaryHadronSWCentralSplineVariation	π^+ Sanford Wang Central Spline Variation
Min/Max Mode	Variations
NormCCCOH_UBGenie	Normilization for CC Coherent Processes (in developement)
NormNCCOH_UBGenie	Normilization for NC Coherent Processes (in developement)
RPA_CCQE_UBGenie	Strength of RPA correction for central tune
Theta_Delta2Npi_UBGenie	Variation of angle of pion with respect to detector z axis
VecFFCCQEshape_UBGenie	VecFFCCQEshape_ UBGenie
DecayAngMEC_UBGenie	Changes angular distribution of nucleon cluster
AxFFCCQEshape_UBGenie	Varies CCQE axial form factor model between dipole (CV) and z-expansion.

Table 2: Percent error on the final selection $2\gamma 1p$ subsamples from all final flux and cross section reweightable systematics. The "Combined" variation corresponds to all variations of that category added in quadrature.

Variation	**NCΔRad**	**NCπ^0 Coh**	**NCπ^0 NotCoh**	**CC1π^0**	**BNBOther Extra**	**CCν_e**	**Dirt**	**OTPCinC**
All_UBGenie	28.05	0.00	24.56	25.01	14.91	15.79	16.02	16.78
Combined Min/Max	0	87.37	1.48	3.85	1.70	10.93	5.96	6.67
AxFFCCQEshape	0.00	0.00	0.00	0.26	0.30	0.26	0.63	0.69
DecayAngMEC	0.00	0.00	0.14	0.06	0.81	6.32	2.45	4.03
NormCCCOH	0.00	0.00	0.00	0.00	0.00	0.00	0.00	1.83
NormNCCOH	0.00	87.37	0.00	0.00	0.00	0.00	0.00	0.00
RPA_CCQE	0.00	0.00	0.00	0.44	0.07	0.85	0.05	1.58
Theta_Delta2Npi	0.00	0.00	1.47	3.78	1.35	8.77	5.31	4.48
VecFFCCQEshape	0.00	0.00	0.00	0.46	0.56	1.37	0.94	1.32
Combined Flux	7.13	14.95	7.50	6.32	8.65	6.60	8.17	8.04
expskin_FluxUnisim	4.47	2.05	4.80	3.36	6.24	0.39	4.51	5.29
horncurrent_FluxUnisim	0.63	0.52	0.68	0.53	0.78	0.15	0.57	0.68
K^- PrimaryHadronNormalization	0.00	0.00	0.01	0.00	0.12	0.00	0.00	0.00
K^+ PrimaryHadronFeynmanScaling	0.30	0.00	0.32	0.20	0.58	2.13	1.48	0.81
K^0 PrimaryHadronSanfordWang	0.00	0.00	0.05	0.01	0.00	3.11	0.00	0.26
nucleoninexsec_FluxUnisim	0.83	0.90	0.84	0.88	0.75	0.61	0.82	0.85
nucleonqexsec_FluxUnisim	2.49	2.52	2.47	2.50	2.46	2.73	2.61	2.54
nucleontotxsec_FluxUnisim	0.73	0.80	0.75	0.77	0.70	0.57	0.75	0.74
π^- Primary SW CV SplineVar	0.19	0.00	0.16	0.00	0.20	0.00	0.72	0.00
pioninexsec_FluxUnisim	1.27	1.31	1.28	1.23	1.25	0.22	0.97	1.21
pionqexsec_FluxUnisim	0.85	0.86	0.87	0.87	0.85	0.47	0.69	0.80
piontotxsec_FluxUnisim	0.89	0.87	0.95	0.82	0.93	0.28	0.75	0.85
π^+ Primary SW CV SplineVar	4.45	14.43	4.68	4.21	4.97	4.55	5.78	5.00

Table 3: Percent error on the final selection $2\gamma 0p$ subsamples from all final flux and cross section reweightable systematics. The "Combined" variation corresponds to all variations of that category added in quadrature.

Variation	**NCΔRad**	**NCπ^0 Coh**	**NCπ^0 NotCoh**	**CC1π^0**	**BNBOther Extra**	**CCν_e**	**Dirt**	**OTPCinC**
All_UBGenie	24.93	0.00	22.12	27.19	16.11	22.36	20.29	18.22
Combined Min/Max	0.00	20.87	1.44	4.54	4.05	22.57	13.33	3.81
AxFFCCQEshape	0.00	0.00	0.00	0.24	0.30	2.29	0.44	0.17
DecayAngMEC	0.00	0.00	0.00	1.20	1.57	15.45	10.20	0.82
NormCCCOH	0.00	0.00	0.00	0.00	0.00	0.00	0.00	1.03
NormNCCOH	0.00	20.87	0.00	0.00	0.00	0.00	0.00	0.80
RPA_CCQE	0.00	0.00	0.00	0.40	0.51	3.53	0.77	0.51
Theta_Delta2Npi	0.00	0.00	1.44	4.32	3.64	15.65	8.51	3.41
VecFFCCQEshape	0.00	0.00	0.00	0.51	0.61	2.87	0.55	0.40
Combined Flux	6.59	8.21	7.20	6.11	8.73	6.31	5.15	7.89
expskin_FluxUnisim	3.92	4.62	4.52	3.22	5.99	0.57	2.79	5.24
horncurrent_FluxUnisim	0.56	0.64	0.65	0.52	0.76	0.35	0.45	0.65
K^- PrimaryHadronNormalization	0.00	0.00	0.00	0.00	0.00	0.00	0.00	0.00
K^+ PrimaryHadronFeynmanScaling	0.59	0.22	0.36	0.27	0.56	2.27	0.74	0.97
K^0 PrimaryHadronSanfordWang	0.00	0.00	0.04	0.09	0.24	3.80	0.00	0.00
nucleoninexsec_FluxUnisim	0.84	0.86	0.84	0.90	0.77	0.73	1.03	0.85
nucleonqexsec_FluxUnisim	2.51	2.49	2.49	2.51	2.55	2.89	2.82	2.51
nucleontotxsec_FluxUnisim	0.73	0.75	0.76	0.77	0.75	1.05	0.76	0.76
π^- Primary SW CV SplineVar	0.26	0.25	0.11	0.00	0.09	0.00	0.00	0.13
pioninexsec_FluxUnisim	1.23	1.29	1.25	1.24	1.31	0.54	0.79	1.19
pionqexsec_FluxUnisim	0.80	0.88	0.86	0.85	0.88	0.30	0.71	0.79
piontotxsec_FluxUnisim	0.86	0.93	0.91	0.80	0.98	0.45	0.47	0.89
π^+ Primary SW CV SplineVar	4.10	5.89	4.49	4.00	5.32	3.05	2.65	4.80

Table 4: Percent error of $1\gamma 1p$ subsamples at the final selection stage from all final flux and cross section reweightable systematics. The "Combined" variation corresponds to all variations of that category added in quadrature.

Variation	**NCΔRad**	**NCπ^0 Coh**	**NCπ^0 NotCoh**	**CC1π^0**	**BNBOther Extra**	**CCν_e**	**Dirt**	**OTPCinC**
All_UBGenie	25.56	-	24.40	24.16	17.46	17.10	-	-
Combined Min/Max	0.00	-	6.48	69.08	9.38	26.83	-	-
AxFFCCQEshape	0.00	-	0.00	0.00	1.48	7.98	-	-
DecayAngMEC	0.00	-	0.00	0.00	0.00	0.00	-	-
NormCCCOH	0.00	-	0.00	0.00	0.00	0.00	-	-
NormNCCOH	0.00	-	0.00	0.00	0.00	0.00	-	-
RPA_CCQE	0.00	-	0.00	0.00	0.51	3.06	-	-
Theta_Delta2Npi	0.00	-	6.48	69.08	7.75	19.33	-	-
VecFFCCQEshape	0.00	-	0.00	0.00	5.05	16.52	-	-
Combined Flux	6.45	-	7.35	7.16	9.07	10.87	-	-
expskin_FluxUnisim	3.65	-	4.83	4.43	6.68	0.83	-	-
horncurrent_FluxUnisim	0.58	-	0.69	0.50	0.80	1.54	-	-
K^- PrimaryHadronNormalization	0.00	-	0.00	0.00	0.00	0.00	-	-
K^+ PrimaryHadronFeynmanScaling	0.19	-	0.64	0.54	0.26	1.62	-	-
K^0 PrimaryHadronSanfordWang	0.07	-	0.00	0.00	0.00	5.52	-	-
nucleoninexsec_FluxUnisim	0.88	-	0.86	0.68	0.78	1.96	-	-
nucleonqexsec_FluxUnisim	2.49	-	2.49	2.56	2.38	3.16	-	-
nucleontotxsec_FluxUnisim	0.78	-	0.75	0.66	0.64	2.50	-	-
π^- Primary SW CV SplineVar	0.16	-	0.00	0.00	0.00	0.00	-	-
pioninexsec_FluxUnisim	1.26	-	1.25	1.01	1.24	0.97	-	-
pionqexsec_FluxUnisim	0.88	-	0.83	0.81	0.90	0.26	-	-
piontotxsec_FluxUnisim	0.87	-	0.89	0.88	0.99	0.85	-	-
π^+ Primary SW CV SplineVar	4.15	-	4.39	4.60	5.18	7.76	-	-

Table 5: Percent error of $1\gamma 0p$ subsamples at the final selection stage from all final flux and cross section reweightable systematics. The "Combined" variation corresponds to all variations of that category added in quadrature.

Variation	**NCΔRad**	**NCπ^0 Coh**	**NCπ^0 NotCoh**	**CC1π^0**	**BNBOther Extra**	**CCν_e**	**Dirt**	**OTPCinC**
All_UBGenie	23.26	0.00	22.60	26.89	16.56	20.01	15.34	19.63
Combined Min/Max	0.00	33.79	0.46	5.55	4.54	14.35	7.91	5.73
AxFFCCQEshape	0.00	0.00	0.00	0.68	0.53	0.77	5.35	0.52
DecayAngMEC	0.00	0.00	0.00	2.47	3.51	1.70	0.00	0.96
NormCCCOH	0.00	0.00	0.00	0.00	0.00	1.57	0.00	0.00
NormNCCOH	0.00	33.79	0.00	0.00	0.00	0.00	0.00	0.00
RPA_CCQE	0.00	0.00	0.00	0.66	1.10	13.98	1.04	0.00
Theta_Delta2Npi	0.00	0.00	0.46	4.73	2.35	0.25	4.14	5.60
VecFFCCQEshape	0.00	0.00	0.00	1.21	1.12	2.11	3.97	0.50
Combined Flux	6.59	7.27	7.04	7.20	7.81	8.42	7.63	8.86
expskin_FluxUnisim	3.68	4.22	4.41	4.44	4.91	0.29	4.32	6.02
horncurrent_FluxUnisim	0.57	0.62	0.63	0.62	0.65	0.16	0.56	0.78
K^- PrimaryHadronNormalization	0.00	0.00	0.00	0.00	0.00	0.00	0.00	0.00
K^+ PrimaryHadronFeynmanScaling	0.21	0.19	0.31	0.49	0.34	1.67	2.42	0.58
K^0 PrimaryHadronSanfordWang	0.01	0.00	0.00	0.00	0.00	3.38	0.00	0.00
nucleoninexsec_FluxUnisim	0.87	0.81	0.86	0.87	0.87	0.77	0.53	0.85
nucleonqexsec_FluxUnisim	2.49	2.50	2.48	2.53	2.47	2.92	2.90	2.44
nucleontotxsec_FluxUnisim	0.79	0.71	0.75	0.78	0.73	0.66	0.52	0.72
π^- Primary SW CV SplineVar	0.20	0.67	0.19	0.00	0.39	0.04	0.00	0.15
pioninexsec_FluxUnisim	1.26	1.30	1.26	1.27	1.24	0.36	1.03	1.32
pionqexsec_FluxUnisim	0.87	0.85	0.87	0.85	0.87	0.26	0.54	0.88
piontotxsec_FluxUnisim	0.89	0.98	0.89	0.83	0.87	0.40	0.77	0.93
π^+ Primary SW CV SplineVar	4.33	4.84	4.36	4.54	5.07	6.83	4.74	5.54

Table 6: Description of GENIE cross section reweightable systematics.

Variation Label	**Description**
AGKYpT1pi_UBGenie	Pion transverse momentum for Nπ states in AGKY
AGKYxF1pi_UBGenie	Pion Feynman x for Nπ states in AGKY
AhtBY_UBGenie	A_HT higher twist param in BY model scaling variable ξ_w $\pm$25 %
BhtBY_UBGenie	B_HT higher twist param in BY model scaling variable ξ_w
CV1uBY_UBGenie	C_V1u u valence GRV98 PDF correction param in BY model
CV2uBY_UBGenie	C_V2u u valence GRV98 PDF correction param in BY model
CoulombCCQE_UBGenie	Changes angular distribution of nucleon cluster
EtaNCEL_UBGenie	Strange axial form factor η for NC elastic
FrAbs_N_UBGenie	Nucleon absorption probability.
FrAbs_pi_UBGenie	Pi absorption probability
FrCEx_N_UBGenie	Fractional cross section for nucleon charge exchange
FrCEx_pi_UBGenie	Fractional cross section for πcharge exchange
FrInel_N_UBGenie	Nucleon fractional cross section for inelastic scatting
FrInel_pi_UBGenie	π fractional cross section for inelastic scatting
FracDelta_CCMEC_UBGenie	Varies relative ontribution of δ diagram to total MEC cross setion
FracPN_CCMEC_UBGenie	Varies fraction of initial nucleon pairs that are pn
MFP_N_UBGenie	Nucleon mean free path (total rescattering probability)
MFP_pi_UBGenie	π mean free path (total rescattering probability)
MaCCQE_UBGenie	Axial Mass for CCQE
MaCCRES_UBGenie	Axial mass for CC resoce neutrino production
MaNCEL_UBGenie	Axial mass for NC elastic
MaNCRES_UBGenie	Axial mass for NC resoce neutrino production
MvCCRES_UBGenie	Vector mass for CC resoce neutrino production
MvNCRES_UBGenie	Vector mass for NC resoce neutrino production
NonRESBGvbarnCC1pi_UBGenie	Non-Res background normalization $\bar{\nu}$ neutron $CC1\pi$ scattering
NonRESBGvbarnCC2pi_UBGenie	Non-Res background normalization $\bar{\nu}$ neutron $CC2\pi$ scattering
NonRESBGvbarnNC1pi_UBGenie	Non-Res background normalization $\bar{\nu}$ neutron $NC1\pi$ scattering
NonRESBGvbarnNC2pi_UBGenie	Non-Res background normalization $\bar{\nu}$ neutron $NC2\pi$ scattering
NonRESBGvbarpCC1pi_UBGenie	Non-Res background normalization $\bar{\nu}$ proton $CC1\pi$ scattering
NonRESBGvbarpCC2pi_UBGenie	Non-Res background normalization $\bar{\nu}$ proton $CC2\pi$ scattering
NonRESBGvbarpNC1pi_UBGenie	Non-Res background normalization $\bar{\nu}$ proton $NC1\pi$ scattering
NonRESBGvbarpNC2pi_UBGenie	Non-Res background normalization $\bar{\nu}$ proton $NC2\pi$ scattering
NonRESBGvnCC1pi_UBGenie	Non-Res background normalization ν neutron $CC1\pi$ scattering
NonRESBGvnCC2pi_UBGenie	Non-Res background normalization ν neutron $CC2\pi$ scattering
NonRESBGvnNC1pi_UBGenie	Non-Res background normalization ν neutron $NC1\pi$ scattering
NonRESBGvnNC2pi_UBGenie	Non-Res background normalization ν neutron $NC2\pi$ scattering
NonRESBGvpCC1pi_UBGenie	Non-Res background normalization ν proton $CC1\pi$ scattering
NonRESBGvpCC2pi_UBGenie	Non-Res background normalization ν proton $CC2\pi$ scattering
NonRESBGvpNC1pi_UBGenie	Non-Res background normalization ν proton $NC1\pi$ scattering
NonRESBGvpNC2pi_UBGenie	Non-Res background normalization ν proton $NC2\pi$ scattering

Table 7: Percent error of $2\gamma 1p$ subsamples at the final selection stage from cross section (GENIE) reweightable systematics (Table 1 of 2). Genie_All uses multisims while individual variations use $\pm 1\sigma$.

Variation	**BNB Other**	**CC1π^0**	**Dirt**	**NCΔRad**	**NCMultiπ^0**	**NC1π^0 Coh**	**NC1π^0 NotCoh**	**CCν_e**
Genie All	14.44	24.22	14.93	27.71	25.30	0.00	23.49	15.12
AGKYpT1pi	0.16	0.48	0.92	0.00	0.50	0.00	0.16	0.50
AGKYxF1pi	0.06	0.11	0.35	0.00	0.22	0.00	0.68	0.30
AhtBY	0.01	0.04	0.21	0.00	0.06	0.00	0.00	0.31
BhtBY	0.03	0.04	0.39	0.00	0.09	0.00	0.01	0.32
CV1uBY	0.02	0.04	0.27	0.00	0.00	0.00	0.00	0.31
CV2uBY	0.02	0.04	0.25	0.00	0.00	0.00	0.00	0.31
CoulombCCQE	0.17	0.01	0.12	0.00	0.00	0.00	0.00	0.52
EtaNCEL	0.15	0.00	0.20	0.00	0.00	0.00	0.00	0.31
FrAbs_N	5.68	6.64	5.05	6.60	3.11	0.00	5.21	5.49
FrAbs_pi	3.18	12.03	3.22	0.43	6.80	0.00	6.12	2.76
FrCEx_N	5.62	5.82	2.15	5.31	0.10	0.00	5.28	1.19
FrCEx_pi	0.09	20.94	1.62	0.54	12.23	0.00	10.07	1.26
FrInel_N	2.60	9.90	4.61	3.25	2.85	0.00	1.85	4.99
FrInel_pi	2.92	6.76	3.25	0.12	4.41	0.00	3.24	3.56
FracDelta_CCMEC	0.49	0.08	0.82	0.00	0.00	0.00	0.00	1.87
FracPN_CCMEC	0.38	0.09	0.39	0.00	0.00	0.00	0.00	1.21
MFP_N	3.03	2.86	3.87	3.11	3.49	0.00	2.42	2.34
MFP_pi	1.21	1.84	2.32	0.18	4.72	0.00	1.50	0.92
MaCCQE	0.77	0.11	0.70	0.00	0.00	0.00	0.00	1.28
MaCCRES	5.57	11.98	4.61	0.00	0.00	0.00	0.00	4.90
MaNCEL	4.29	0.00	0.43	0.00	0.00	0.00	0.81	0.31
MaNCRES	4.44	0.00	4.99	24.95	16.96	0.00	20.25	0.31
MvCCRES	5.41	10.40	3.71	0.00	0.00	0.00	0.00	4.36
MvNCRES	2.46	0.00	1.69	9.90	7.39	0.00	8.20	0.31

Table 8: Percent error of $2\gamma 1p$ subsamples at the final selection stage from cross section (GENIE) reweightable systematics (Table 2 of 2). Genie_All uses multisims while individual variations use $\pm 1\sigma$. Min/Max variations are not included in Genie_All.

Variation	**BNB Other**	**CC1π^0**	**Dirt**	**NCΔRad**	**NCMultiπ^0**	**NC1π^0 Coh**	**NC1π^0 NotCoh**	**CCν_e**
NonRESBGvbarnCC1pi	0.00	0.00	0.00	0.00	0.00	0.00	0.00	0.31
NonRESBGvbarnCC2pi	0.00	0.00	0.00	0.00	0.00	0.00	0.00	0.31
NonRESBGvbarnNC1pi	0.00	0.00	0.00	0.00	0.00	0.00	0.01	0.31
NonRESBGvbarnNC2pi	0.00	0.00	0.00	0.00	0.00	0.00	0.04	0.31
NonRESBGvbarpCC1pi	0.00	0.00	0.00	0.00	0.00	0.00	0.00	0.31
NonRESBGvbarpCC2pi	0.00	0.00	0.00	0.00	0.00	0.00	0.00	0.31
NonRESBGvbarpNC1pi	0.21	0.00	0.00	0.00	0.00	0.00	0.07	0.31
NonRESBGvbarpNC2pi	0.00	0.00	0.00	0.00	0.00	0.00	0.00	0.31
NonRESBGvnCC1pi	1.31	4.98	3.69	0.00	0.00	0.00	0.00	0.76
NonRESBGvnCC2pi	1.45	3.18	2.02	0.00	0.00	0.00	0.00	2.09
NonRESBGvnNC1pi	0.96	0.00	0.00	0.00	2.19	0.00	3.25	0.31
NonRESBGvnNC2pi	0.21	0.00	1.01	0.00	1.67	0.00	0.55	0.31
NonRESBGvpCC1pi	0.49	0.04	0.00	0.00	0.00	0.00	0.00	0.31
NonRESBGvpCC2pi	0.00	1.30	0.00	0.00	0.00	0.00	0.00	0.34
NonRESBGvpNC1pi	0.55	0.00	0.00	0.00	0.81	0.00	1.25	0.31
NonRESBGvpNC2pi	0.55	0.00	0.00	0.00	13.63	0.00	1.34	0.31

Table 9: Percent error of $2\gamma 0p$ subsamples at the final selection stage from cross section (GENIE) reweightable systematics (Table 1 of 2). Genie_All uses multisims while individual variations use $\pm 1\sigma$.

Variation	**BNB Other**	**CC1π^0**	**Dirt**	**NCΔRad**	**NCMultiπ^0**	**NC1π^0 Coh**	**NC1π^0 NotCoh**	**CCν_e**
Genie All	15.66	24.22	18.53	24.46	23.90	0.00	21.00	16.95
AGKYpT1pi	0.23	0.48	0.12	0.00	0.48	0.00	0.10	4.59
AGKYxF1pi	0.87	0.11	0.44	0.00	0.74	0.00	0.34	4.49
AhtBY	0.01	0.04	0.00	0.00	0.10	0.00	0.00	4.65
BhtBY	0.02	0.04	0.00	0.00	0.31	0.00	0.00	4.65
CV1uBY	0.03	0.04	0.00	0.00	0.00	0.00	0.00	4.64
CV2uBY	0.03	0.04	0.00	0.00	0.00	0.00	0.00	4.65
CoulombCCQE	0.33	0.01	0.11	0.00	0.00	0.00	0.00	4.62
EtaNCEL	0.01	0.00	0.24	0.00	0.00	0.00	0.01	4.58
FrAbs_N	6.82	6.64	2.55	6.08	3.46	0.00	5.38	9.92
FrAbs_pi	3.60	12.03	1.82	0.08	9.18	0.00	3.24	4.58
FrCEx_N	1.67	5.82	3.16	3.14	1.83	0.00	4.99	6.14
FrCEx_pi	1.52	20.94	1.02	0.19	9.07	0.00	5.92	4.75
FrInel_N	8.31	9.90	4.05	7.86	2.02	0.00	8.09	11.97
FrInel_pi	1.83	6.76	0.12	0.08	0.92	0.00	1.94	4.66
FracDelta_CCMEC	0.17	0.08	3.76	0.00	0.00	0.00	0.00	4.78
FracPN_CCMEC	0.20	0.09	2.71	0.00	0.00	0.00	0.00	4.61
MFP_N	2.71	2.86	1.35	2.30	2.61	0.00	1.94	5.66
MFP_pi	0.93	1.84	1.23	0.04	3.27	0.00	0.96	4.59
MaCCQE	0.53	0.11	0.66	0.00	0.00	0.00	0.00	4.76
MaCCRES	5.39	11.98	2.04	0.00	0.00	0.00	0.00	5.53
MaNCEL	4.02	0.00	0.29	0.00	0.00	0.00	0.24	4.58
MaNCRES	4.77	0.00	0.50	21.41	12.61	0.00	17.81	4.58
MvCCRES	5.12	10.40	1.71	0.00	0.00	0.00	0.00	5.17
MvNCRES	2.68	0.00	0.18	8.65	7.59	0.00	7.08	4.58

Table 10: Percent error of $2\gamma 0p$ subsamples at the final selection stage from cross section (GENIE) reweightable systematics (Table 2 of 2). Genie_All uses multisims while individual variations use $\pm 1\sigma$.

Variation	**BNB Other**	**CC1π^0**	**Dirt**	**NCΔRad**	**NCMultiπ^0**	**NC1π^0 Coh**	**NC1π^0 NotCoh**	**CCν_e**
NonRESBGvbarnCC1pi	0.00	0.00	0.00	0.00	0.00	0.00	0.00	4.58
NonRESBGvbarnCC2pi	0.00	0.00	0.00	0.00	0.00	0.00	0.00	4.58
NonRESBGvbarnNC1pi	0.00	0.00	0.00	0.00	0.00	0.00	0.01	4.58
NonRESBGvbarnNC2pi	0.00	0.00	0.00	0.00	0.00	0.00	0.00	4.58
NonRESBGvbarpCC1pi	0.00	0.00	0.00	0.00	0.00	0.00	0.00	4.58
NonRESBGvbarpCC2pi	0.00	0.00	0.00	0.00	0.00	0.00	0.00	4.58
NonRESBGvbarpNC1pi	0.00	0.00	0.00	0.00	0.00	0.00	0.01	4.58
NonRESBGvbarpNC2pi	0.00	0.00	0.00	0.00	1.79	0.00	0.00	4.58
NonRESBGvnCC1pi	1.92	4.98	1.48	0.00	0.00	0.00	0.00	4.67
NonRESBGvnCC2pi	1.17	3.18	1.48	0.00	0.00	0.00	0.00	4.60
NonRESBGvnNC1pi	0.34	0.00	0.00	0.00	1.33	0.00	4.98	4.58
NonRESBGvnNC2pi	0.00	0.00	0.00	0.00	1.79	0.00	0.39	4.58
NonRESBGvpCC1pi	0.00	0.04	0.00	0.00	0.00	0.00	0.00	4.58
NonRESBGvpCC2pi	0.00	1.30	0.00	0.00	0.00	0.00	0.00	4.58
NonRESBGvpNC1pi	0.25	0.00	0.00	0.00	0.00	0.00	0.74	4.58
NonRESBGvpNC2pi	0.00	0.00	0.00	0.00	16.07	0.00	1.03	4.58

Table 11: Percent error of $1\gamma 1p$ subsamples at the final selection stage from cross section (GENIE) reweightable systematics (Table 1 of 2). Genie_All uses multisims while individual variations use $\pm 1\sigma$. A hyphen represents an empty subchannel. Note that the Dirt, NC $1\pi^0$ Coherent and NC Multi π^0 subsamples are missing as they have no surviving events in the final selection.

Variation	**BNB Other**	**CC1π^0**	**Dirt**	**NCΔRad**	**NCMultiπ^0**	**NC1π^0 Coh**	**NC1π^0 NotCoh**	**CCν_e**
Genie All	19.17	30.03	-	25.27	-	-	24.22	14.51
AGKYpT1pi	0.36	0.00	-	0.00	-	-	0.55	0.00
AGKYxF1pi	1.10	0.00	-	0.00	-	-	0.28	0.00
AhtBY	0.00	0.00	-	0.00	-	-	0.01	0.00
BhtBY	0.00	0.00	-	0.00	-	-	0.02	0.00
CV1uBY	0.00	0.00	-	0.00	-	-	0.03	0.00
CV2uBY	0.00	0.00	-	0.00	-	-	0.03	0.00
CoulombCCQE	0.16	0.00	-	0.00	-	-	0.00	0.59
EtaNCEL	0.31	0.00	-	0.00	-	-	0.02	0.00
FrAbs_N	5.56	6.47	-	5.58	-	-	4.78	5.76
FrAbs_pi	1.16	19.38	-	0.08	-	-	5.44	3.11
FrCEx_N	14.31	20.37	-	11.42	-	-	8.73	12.46
FrCEx_pi	3.26	20.40	-	0.07	-	-	10.24	2.25
FrInel_N	3.61	5.44	-	1.58	-	-	0.70	1.97
FrInel_pi	1.47	1.65	-	0.14	-	-	3.61	4.69
FracDelta_CCMEC	0.00	0.00	-	0.00	-	-	0.00	1.89
FracPN_CCMEC	0.00	0.00	-	0.00	-	-	0.00	1.13
MFP_N	2.73	3.97	-	2.13	-	-	2.40	3.08
MFP_pi	3.22	1.92	-	0.01	-	-	1.58	0.32
MaCCQE	0.50	0.00	-	0.00	-	-	0.00	1.55
MaCCRES	4.42	9.07	-	0.00	-	-	0.00	2.55
MaNCEL	2.40	0.00	-	0.00	-	-	0.19	0.00
MaNCRES	11.79	0.00	-	22.64	-	-	20.69	0.00
MvCCRES	4.93	7.32	-	0.00	-	-	0.00	2.01
MvNCRES	5.69	0.00	-	9.08	-	-	8.72	0.00

Table 12: Percent error of $1\gamma 1p$ subsamples at the final selection stage from cross section (GENIE) reweightable systematics (Table 2 of 2). Genie_All uses multisims while individual variations use $\pm 1\sigma$. A hyphen represents an empty subchannel. Min/Max variations are not included in Genie_All.

Variation	**BNB Other**	**CC1π^0**	**Dirt**	**NCΔRad**	**NCMultiπ^0**	**NC1π^0 Coh**	**NC1π^0 NotCoh**	**CCν_e**
NonRESBGvbarnCC1pi	0.00	0.00	-	0.00	-	-	0.00	0.00
NonRESBGvbarnCC2pi	0.00	0.00	-	0.00	-	-	0.00	0.00
NonRESBGvbarnNC1pi	0.00	0.00	-	0.00	-	-	0.19	0.00
NonRESBGvbarnNC2pi	0.00	0.00	-	0.00	-	-	0.00	0.00
NonRESBGvbarpCC1pi	0.00	0.00	-	0.00	-	-	0.00	0.00
NonRESBGvbarpCC2pi	0.00	0.00	-	0.00	-	-	0.00	0.00
NonRESBGvbarpNC1pi	0.00	0.00	-	0.00	-	-	0.00	0.00
NonRESBGvbarpNC2pi	0.00	0.00	-	0.00	-	-	0.00	0.00
NonRESBGvnCC1pi	0.00	0.00	-	0.00	-	-	0.00	0.00
NonRESBGvnCC2pi	0.00	9.25	-	0.00	-	-	0.00	0.00
NonRESBGvnNC1pi	0.00	0.00	-	0.00	-	-	3.53	0.00
NonRESBGvnNC2pi	0.00	0.00	-	0.00	-	-	0.00	0.00
NonRESBGvpCC1pi	3.26	0.00	-	0.00	-	-	0.00	0.00
NonRESBGvpCC2pi	0.00	9.25	-	0.00	-	-	0.00	0.00
NonRESBGvpNC1pi	0.00	0.00	-	0.00	-	-	1.22	0.00
NonRESBGvpNC2pi	0.00	0.00	-	0.00	-	-	0.64	0.00

Table 13: Percent error of $1\gamma 0p$ subsamples at the final selection stage from cross section (GENIE) reweightable systematics (Table 1 of 2). Genie_All uses multisims while individual variations use $\pm 1\sigma$.

Variation	**BNB Other**	**CC1π^0**	**Dirt**	**NCΔRad**	**NCMultiπ^0**	**NC1π^0 Coh**	**NC1π^0 NotCoh**	**CCν_e**
Genie All	15.07	25.08	16.05	22.89	36.63	0.00	21.56	16.74
AGKYpT1pi	0.59	0.32	2.25	0.00	1.61	0.00	0.23	2.93
AGKYxF1pi	0.69	0.33	5.47	0.00	5.11	0.00	0.17	2.91
AhtBY	0.00	0.06	0.38	0.00	0.00	0.00	0.00	2.91
BhtBY	0.00	0.07	0.41	0.00	0.00	0.00	0.01	2.91
CV1uBY	0.00	0.08	0.41	0.00	0.00	0.00	0.01	2.91
CV2uBY	0.00	0.08	0.41	0.00	0.00	0.00	0.01	2.91
CoulombCCQE	0.09	0.02	0.18	0.00	0.00	0.00	0.00	2.96
EtaNCEL	0.04	0.00	0.18	0.00	0.00	0.00	0.02	2.91
FrAbs_N	6.55	7.01	1.29	5.41	0.00	0.00	4.49	9.06
FrAbs_pi	3.84	9.73	1.36	0.05	0.00	0.00	3.37	3.28
FrCEx_N	3.45	0.56	0.05	2.28	0.00	0.00	1.61	4.15
FrCEx_pi	0.21	18.64	0.73	0.08	0.00	0.00	5.17	2.99
FrInel_N	8.19	7.18	1.45	6.60	0.00	0.00	5.28	10.47
FrInel_pi	4.25	5.49	1.15	0.12	0.00	0.00	1.25	3.57
FracDelta_CCMEC	0.96	0.08	0.00	0.00	0.00	0.00	0.00	3.00
FracPN_CCMEC	1.24	0.08	0.00	0.00	0.00	0.00	0.00	3.35
MFP_N	3.71	3.46	0.50	1.29	1.63	0.00	1.75	3.39
MFP_pi	0.52	2.46	1.30	0.01	5.20	0.00	1.09	2.92
MaCCQE	0.59	0.18	2.40	0.00	0.00	0.00	0.00	3.02
MaCCRES	5.69	13.85	5.35	0.00	0.00	0.00	0.00	3.10
MaNCEL	0.44	0.00	0.66	0.00	0.00	0.00	0.23	2.91
MaNCRES	3.93	0.00	0.85	20.25	27.93	0.00	18.94	2.91
MvCCRES	5.21	12.21	6.02	0.00	0.00	0.00	0.00	2.96
MvNCRES	2.15	0.00	0.72	7.83	10.35	0.00	7.85	2.91

Table 14: Percent error of $1\gamma 0p$ at the subsamples at the final selection stage from cross section (GENIE) reweightable systematics (Table 2 of 2). Genie_All uses multisims while individual variations use $\pm 1\sigma$.

Variation	**BNB Other**	**CC1π^0**	**Dirt**	**NCΔRad**	**NCMultiπ^0**	**NC1π^0 Coh**	**NC1π^0 NotCoh**	**CCν_e**
NonRESBGvbarnCC1pi	0.00	0.00	0.00	0.00	0.00	0.00	0.00	2.91
NonRESBGvbarnCC2pi	0.00	0.00	0.00	0.00	0.00	0.00	0.00	2.91
NonRESBGvbarnNC1pi	0.00	0.00	0.00	0.00	0.00	0.00	0.00	2.91
NonRESBGvbarnNC2pi	0.00	0.00	0.00	0.00	0.00	0.00	0.00	2.91
NonRESBGvbarpCC1pi	0.00	0.00	0.00	0.00	0.00	0.00	0.00	2.91
NonRESBGvbarpCC2pi	0.00	0.00	0.00	0.00	0.00	0.00	0.00	2.91
NonRESBGvbarpNC1pi	0.00	0.00	2.03	0.00	8.45	0.00	0.00	2.91
NonRESBGvbarpNC2pi	0.00	0.00	0.00	0.00	0.00	0.00	0.00	2.91
NonRESBGvnCC1pi	3.38	4.42	0.00	0.00	0.00	0.00	0.00	2.91
NonRESBGvnCC2pi	1.94	3.06	4.07	0.00	0.00	0.00	0.00	2.91
NonRESBGvnNC1pi	1.94	0.00	0.00	0.00	0.00	0.00	5.18	2.91
NonRESBGvnNC2pi	0.00	0.00	0.00	0.00	0.00	0.00	0.42	2.91
NonRESBGvpCC1pi	0.00	0.00	0.00	0.00	0.00	0.00	0.00	2.91
NonRESBGvpCC2pi	0.95	1.29	0.00	0.00	0.00	0.00	0.00	2.91
NonRESBGvpNC1pi	0.50	0.00	0.00	0.00	0.00	0.00	0.53	2.91
NonRESBGvpNC2pi	0.95	0.00	0.00	0.00	16.19	0.00	0.90	2.91

B Constraint Tables

Here we provide Tab. 15 of the constraint performance on independently varied genie variations for the gamma LEE analysis. These results have not been reprocessed for the latest iteration of the analysis as they are not used to build the final covariance matrices and are contained within Genie_All. They are included here for illustrative purposes to inform which underlying physics is driving the uncertainties. As can be seen from the table, the Ma NC Resonant variation, highlighted in bold, is one of the primary uncertainties on the NC π^0 backgrounds and is reduced by a factor of 3.5 with the constraint.

Table 15: Combined sum of predicted background rate in the the $1\gamma 1p$ and $1\gamma 0p$ selections, and corresponding unconstrained and constrained individually run cross section uncertainties, broken down by systematic uncertainty source.

Variation Name	**Uncon. Error** $1\gamma 1p$	**Con. Error** $1\gamma 1p$	**Reduc. Factor** $1\gamma 1p$	**Uncon. Error** $1\gamma 0p$	**Con. Error** $1\gamma 0p$	**Reduc. Factor** $1\gamma 0p$
AGKYpT1pi	0.43%	0.43%	1.00	0.36%	0.36%	1.00
AGKYxF1pi	0.34%	0.34%	1.00	0.18%	0.18%	1.01
AhtBY	0.00%	0.00%	1.00	0.23%	0.23%	1.00
BhtBY	0.01%	0.01%	1.00	0.23%	0.23%	1.00
CV1uBY	0.03%	0.03%	1.00	0.23%	0.23%	1.00
CV2uBY	0.03%	0.03%	1.00	0.23%	0.23%	1.00
CoulombCCQE	0.03%	0.03%	1.00	0.22%	0.22%	1.00
EtaNCEL	0.02%	0.02%	1.00	0.21%	0.21%	1.00
FrAbs_N	4.91%	3.21%	1.53	4.61%	3.02%	1.53
FrAbs_pi	5.12%	3.26%	1.57	3.33%	2.13%	1.57
FrCEx_N	9.58%	6.69%	1.43	1.58%	1.10%	1.43
FrCEx_pi	9.32%	4.36%	2.14	4.18%	1.96%	2.13
FrInel_N	1.11%	0.74%	1.50	5.39%	3.60%	1.50
FrInel_pi	3.14%	2.78%	1.13	0.30%	0.28%	1.07
FracDelta_CCMEC	0.05%	0.05%	1.00	0.32%	0.32%	1.00
FracPN_CCMEC	0.03%	0.03%	1.00	0.22%	0.22%	1.00
MFP_N	2.47%	2.19%	1.13	1.94%	1.72%	1.13
MFP_pi	1.73%	1.65%	1.05	0.97%	0.93%	1.05
MaCCQE	0.09%	0.09%	1.00	0.34%	0.34%	1.00
MaCCRES	0.66%	0.60%	1.10	2.41%	2.20%	1.10
MaNCEL	0.42%	0.41%	1.02	0.28%	0.28%	1.01
MaNCRES	**18.94%**	**5.45%**	**3.48**	**10.44%**	**3.01%**	**3.47**
MvCCRES	0.68%	0.63%	1.08	2.18%	2.02%	1.08
MvNCRES	8.06%	4.77%	1.69	4.41%	2.61%	1.69
NonRESBGvbarnCC1pi	-	-	-	0.21%	0.21%	1.00
NonRESBGvbarnCC2pi	-	-	-	0.21%	0.21%	1.00
NonRESBGvbarnNC1pi	0.16%	0.16%	1.00	0.21%	0.21%	1.00
NonRESBGvbarnNC2pi	-	-	-	0.21%	0.21%	1.00
NonRESBGvbarpCC1pi	-	-	-	0.21%	0.21%	1.00
NonRESBGvbarpCC2pi	-	-	-	0.21%	0.21%	1.00
NonRESBGvbarpNC1pi	-	-	-	0.27%	0.27%	1.00
NonRESBGvbarpNC2pi	-	-	-	0.21%	0.21%	1.00
NonRESBGvnCC1pi	-	-	-	0.97%	0.96%	1.01
NonRESBGvnCC2pi	0.13%	0.13%	1.00	0.78%	0.78%	1.00
NonRESBGvnNC1pi	3.01%	2.51%	1.20	2.92%	2.44%	1.20
NonRESBGvnNC2pi	-	-	-	0.30%	0.30%	1.00
NonRESBGvpCC1pi	0.35%	0.35%	1.00	0.21%	0.21%	1.00
NonRESBGvpCC2pi	0.13%	0.13%	1.00	0.35%	0.35%	1.00
NonRESBGvpNC1pi	1.04%	1.02%	1.02	0.40%	0.40%	1.01
NonRESBGvpNC2pi	0.55%	0.52%	1.04	0.79%	0.76%	1.04

C Neutrinos at the Main Injector Beamline

The MicroBooNE detector also sees an off axis component of the Neutrinos at the Main Injector (NuMI) beamline. The NuMI target hall is shown in Fig. 1. This shares the same beam path as the BNB until leaving the booster where it is sent to the Main Injector ring and protons are accelerated to 120 GeV. The target consists of carbon plates instead of the BNB solid beryllium but works on the same principle by producing mesons which decay producing neutrinos. It is focused via a pair of magnetic focusing horns where the first one diverts particles with the wrong charge sign away and sends the correctly charged particles to the second horn which more properly orients them along the desired beam path. However, sometimes particles of opposite charge, particularly forward going ones, make it through the beam path creating an undesired background. The most common decay is $\pi^+ \rightarrow \mu^+ + \nu_\mu$ in the neutrino mode which is used predominately. There are also a large number of kaons which decay to produce electron neutrinos in three body decays given by $K^+ \rightarrow \nu_e + e^+ + \pi^0$ and $K_L^0 \rightarrow \nu_e + e^+ + \pi^-$. This creates a significant ν_e component which is actually useful for MicroBooNE, as the BNB produces fewer of these. To reach MicroBooNE, a particle must deviate approximately 8° from the center. This produces the flux distribution as seen in Fig. 2. The NuMI beam systematics are less well known compared to the BNB [25].

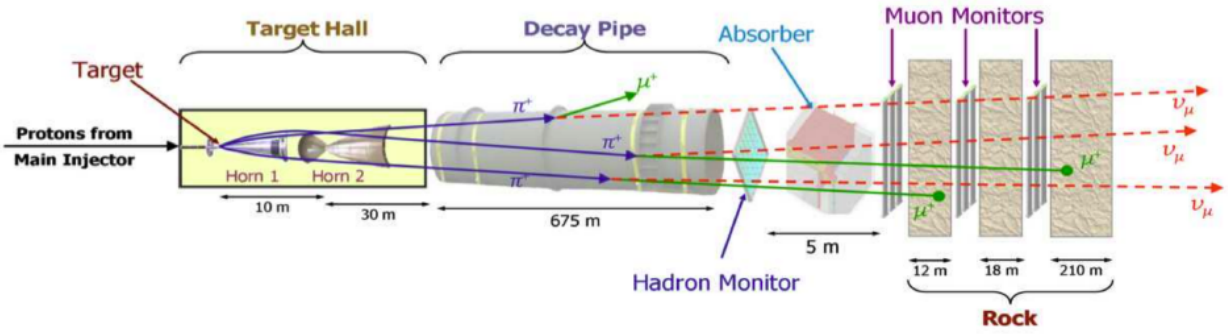

Figure 1: NuMI target hall and decay region along with its instrumentation [25].

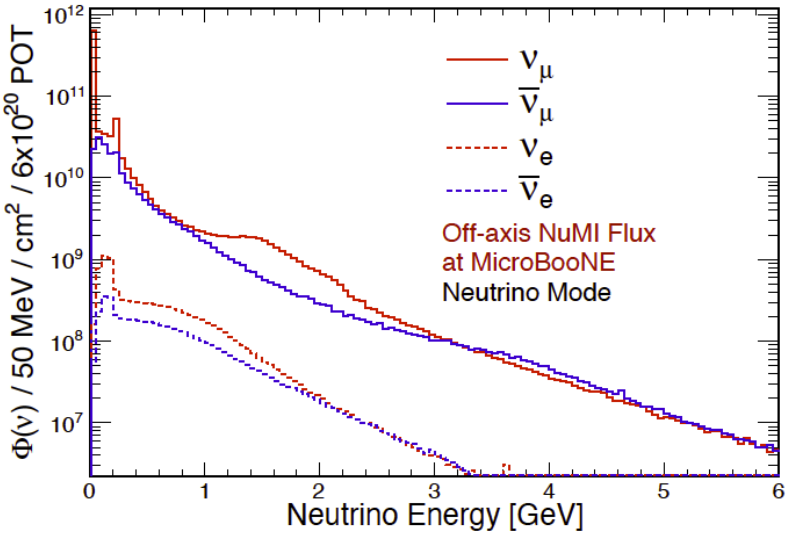

Figure 2: Flux from NuMI received by the MicroBooNE detector. NuMI has 200 MeV higher average energy compared to the BNB but has a significant low energy component as well.

Vita

Born in North Carolina and raised in Tennessee, Gray Yarbrough attended University School of Nashville for High School. He was accepted to Davidson College, completing a double major in Mathematics and Physics and receiving his BS in 2015. After this, he attended the University of Tennessee, Knoxville (UTK) as part of the PhD program. For the first two years, he was a graduate teaching assistant to several professors. He received a Neutrino Physics Center (NPC) fellowship for the summer of 2017 to travel and conduct his research at Fermilab. Then, in 2018 he would transfer to full time work at Fermilab, as part of the MicroBooNE collaboration, as a graduate research assistant funded by an award from the Office of Science Graduate Student Research Program (SCGSR). The project consisted of analysis on the neutrino beam-line and preliminary results were presented at the American Physical Society (APS) 2018. Concluding this work, he would move to primarily focus on the Single Photon analysis continuing as part of the MicroBooNE collaboration aimed at addressing the long-standing MiniBooNE anomaly. As part of the single photon group, Gray developed expertise in evaluating systematics uncertainties related to neutrino flux and cross sections in neutrino experiments. His systematics work would be included in a collaboration reviewed public note in 2020 accompanying a presentation at the International Conference on Neutrino Physics in 2020. At the time of the writing of this thesis, an internal analysis note is nearing completion to which he contributed with his extensive systematics work, and authored corresponding sections. Two publications on the single photon analysis are planned to be submitted to Physical Review Letters in the summer of 2021.